

**PETROLOGY AND GEOCHRONOLOGY OF THE IGNEOUS ROCKS  
FROM THE ÇANGALDAĞ METAMORPHIC COMPLEX AND THE  
ÇANGALDAĞ PLUTON (CENTRAL PONTIDES, TURKEY)**

A THESIS SUBMITTED TO  
THE GRADUATE SCHOOL OF NATURAL AND APPLIED SCIENCES  
OF  
MIDDLE EAST TECHNICAL UNIVERSITY

BY

OKAY ÇİMEN

IN PARTIAL FULFILLMENT OF THE REQUIREMENTS  
FOR  
THE DEGREE OF DOCTOR OF PHILOSOPHY  
IN  
GEOLOGICAL ENGINEERING

AUGUST 2016



Approval of the thesis:

**PETROLOGY AND GEOCHRONOLOGY OF THE IGNEOUS ROCKS  
FROM THE ÇANGALDAĞ METAMORPHIC COMPLEX AND THE  
ÇANGALDAĞ PLUTON (CENTRAL PONTIDES, TURKEY)**

submitted by **OKAY ÇİMEN** in partial fulfillment of the requirements for the degree of **Doctor of Philosophy in Geological Engineering Department, Middle East Technical University** by,

Prof. Dr. Gülbin Dural Ünver

Dean, **Graduate School of Natural and Applied Sciences**

---

Prof. Dr. Erdin Bozkurt

Head of Department, **Geological Engineering**

---

Prof. Dr. M. Cemal Göncüoğlu,

Supervisor, **Geological Engineering Dept., METU**

---

Assoc. Prof. Dr. Kaan Sayıt,

Co-Supervisor, **Geological Engineering Dept., METU**

---

Examining Committee Members:

Prof. Dr. Mehmet Arslan

Geological Engineering Dept., KTU

---

Prof. Dr. M. Cemal Göncüoğlu

Geological Engineering Dept., METU

---

Prof. Dr. Asuman G. Türkmenoğlu

Geological Engineering Dept., METU

---

Assoc. Prof. Dr. Biltan Kürkçüoğlu

Geological Engineering Dept., HU

---

Assist. Prof. Dr. Fatma Toksoy Köksal

Geological Engineering Dept., METU

---

**Date:** 10/08/2016

**I hereby declare that all information in this document has been obtained and presented in accordance with academic rules and ethical conduct. I also declare that, as requested by these rules and conduct, I have fully cited and referenced all material and results that are not original to this work.**

Name, Last Name: Okay ÇİMEN

Signature:

## ABSTRACT

### **PETROLOGY AND GEOCHRONOLOGY OF THE IGNEOUS ROCKS FROM THE ÇANGALDAĞ METAMORPHIC COMPLEX AND THE ÇANGALDAĞ PLUTON (CENTRAL PONTIDES, TURKEY)**

Çimen, Okay

Ph.D., Department of Geological Engineering

Supervisor: Prof. M. Cemal Göncüoğlu

Co-supervisor: Assoc.Prof. Kaan Sayıt

August 2016, 254 pages

The Central Pontide Structural Complex (CPSC) in northern Turkey forms an imbricated unit that consists of a number of variable metamorphic oceanic assemblages between the Istanbul-Zonguldak and Sakarya Composite terranes. The Çangaldağ Complex comprising the Çangaldağ Metamorphic Complex and the Çangaldağ Pluton is one of the members of this body and occurs as an E-W trending 30 km long and 15 km wide belt to the north of the Kastamonu-Boyabat Tertiary basin. The Çangaldağ Metamorphic Complex consists predominantly of variably deformed and metamorphosed igneous rocks ranging from felsic to mafic in composition. The main volcanic lithologies are basalt, tuff, diabase, andesite and rhyodacite associated with sediments. The mafic and intermediate volcanic rocks were mainly subjected to greenschist facies metamorphism as evidenced by the assemblage of alb+act+chl+ep. The felsic phases exhibit blastoporphyratic textures with musc+ alb+ chl as the metamorphic parageneses. Geochemically, all metavolcanic rocks display the typical features of subduction-related magmas as evidenced by variable enrichment in LREE over HFSE. LA-ICP-MS U-Pb geochronological data from zircons of three different meta-rhyodacite samples yield

Middle Jurassic ages between  $156 \pm 3$  Ma and  $176 \pm 6$  Ma. Additionally, in-situ  $^{176}\text{Hf}/^{177}\text{Hf}$  initial ratios (between  $0.28281 \pm 0.00003$  and  $0.28276 \pm 0.00003$ ) on the same zircons correspond to  $T_{\text{DM}}$  model ages between 538 and 678 Ma, which suggest partial melting of a depleted mantle, affected by the Cadomian arc magmatism. This Cadomian signature is common in Gondwana-derived terranes.

The Çangaldağ Pluton to the northeast of the Çangaldağ Complex is bounded by a strike-slip fault towards the Çangaldağ Metamorphic Complex. The pluton comprises non-metamorphic diorite, dacite porphyry, and lesser amount of granitic rocks. The dioritic rocks are surrounded by dacite porphyries, which indicate a zoned nature (mafic core with felsic rim) of the complex. Geochemically, various rock types from this pluton exhibit calc-alkaline features and are akin to volcanic arc magmatics displaying LILE/HFSE enrichment coupled with Nb depletion. The available data from the pluton suggest derivation primarily from partial melting of an amphibolitic source. The diorites and dacite porphyries exhibit geochemical features of I-type granites, whereas the granitic rocks show typical features of S-type granites. LA-ICP-MS U-Pb dating of zircons from dacite porphyry and granite samples yielded ages of  $161 \pm 6$  Ma and  $170 \pm 2$  Ma, respectively. Corresponding in-situ  $^{176}\text{Hf}/^{177}\text{Hf}$  initial ratios are  $0.28276 \pm 0.00003$  and  $0.28213 \pm 0.00002$  for the dacite porphyry and granite, respectively. These results support their generation in a marginal arc system with the involvement of a subduction-modified mantle source.  $T_{\text{DM}}$  model ages vary between 674 and 1512 Ma and suggest that the Çangaldağ Pluton magmatism has formed by partial melting of Neoproterozoic/Mesoproterozoic crustal rocks, which are common in Gondwana-derived terranes.

Overall the geochemical and geochronological data confirm the presence of an island-arc (Çangaldağ Metamorphic Complex) and a continental-arc (Çangaldağ Pluton) system during the Middle Jurassic period formed by the partial closing within the Intra-Pontide Ocean.

**Keywords:** Çangaldağ Metamorphic Complex, Çangaldağ Pluton, Central Pontides, Geochemistry, Geochronology, Intra-Pontide

## ÖZ

### ÇANGALDAĞ METAMORFİK KOMPLEKSİ VE ÇANGALDAĞ PLUTONU (ORTA PONTİTLER, TÜRKİYE) İÇERİSİNDEKİ MAGMATİK KAYAÇLARIN PETROLOJİSİ VE JEOKRONOLOJİSİ

Çimen, Okay

Doktora, Jeoloji Mühendisliği Bölümü

Danışman: Prof. Dr. M. Cemal Göncüoğlu

Eş Danışman: Doç.Dr. Kaan Sayıt

Ağustos 2016, 254 sayfa

Türkiye'nin kuzeyinde bulunan Orta Pontid Yapısal Kompleksi (OPYK); İstanbul-Zonguldak ve Sakarya Tektonik Birlikleri arasında yer alan birtakım metamorfik okyanusal birimleri içermekte ve üstüste binmiş bir yapısal kompleksi oluşturmaktadır. Çangaldağ Metamorfik Kompleksi ve Çangaldağ Plutonunu içeren Çangaldağ Kompleksi bu birimin bir üyesi olup, Kastamonu-Boyabat Tersiyer havzası'nın kuzeyinde 30 km uzunluğunda ve 15 km genişliğindeki D-B yönlü bir magmatik kuşağı oluşturmaktadır. Çangaldağ Metamorfik Kompleksi genellikle felsikten mafik'e değişen kompozisyona sahip, çeşitli derecede deformasyona ve metamorfizmaya uğramış magmatik kayalardan oluşmaktadır. Ana volkanik litolojiler sedimanlar ile birlikte bulunan bazalt, tuf, diyabaz, andezit ve riyodasitten oluşmaktadır. Mafik ve ortaç metavolkanik kayalar alb+akt+klr+ep mineral birlikteliğinin gösterdiği üzere genellikle yeşilist fasiyesi metamorfizmasına maruz kalmışlardır. Felsik fazlar ise ince taneli matriks tarafından çevrelenmiş kuvars ve feldispat fenokristleri ile blastoporfiritik doku göstermektedir. Jeokimyasal olarak tüm volkanik kayalar LREE'lerin HFSE'lere göre zenginleşmesi ile dalma-batma ilişkili magmaların tipik özelliklerini sergilemektedir. Üç farklı metariyodasit örneğinden elde edilen zirkonlar üzerindeki LA-ICP-MS U-Pb yaşlandırma sonuçları  $156 \pm 3$  My ve  $176 \pm 6$  My arasında değişen Orta-Jura yaşları vermektedir. Ek

olarak, aynı zirkon minerallerindeki 'in-situ' ilksel  $^{176}\text{Hf}/^{177}\text{Hf}$  oranları ( $0.28281 \pm 0.00003$  ve  $0.28276 \pm 0.00003$  arasında) 538 ve 678 My'ları arasındaki  $T_{\text{TM}}$  model yaşlarına karşılık gelmekte ve bu sonuç Kadomiyen yay magmatizmasından etkilenmiş bir tüketilmiş mantonun kısmi ergimesine işaret etmektedir. Bu tür Kadomiyen magmatizmasının izleri genellikle Gondwana kökenli tektonik birliklerde gözlenmektedir.

Çangaldağ Kompleksi'nin kuzeydoğusunda yeralan Çangaldağ Plutonu doğrultu atımlı bir fay ile Çangaldağ Metamorfik Komplexine bağlanmaktadır. Bu pluton genellikle metamorfik olmayan diyorit, dasit porfiri ve az oranda granitik kayalardan oluşmaktadır. Diyoritik kayalar, dasit porfiriler tarafından çevrelenmekte ve kompleksin zonlu (felsik halkalı mafik çekirdek) yapısına işaret etmektedir. Jeokimyasal olarak ise bu plutondaki çeşitli kayaç türleri kalk-alkalen özellik sergilemekte ve Nb tüketilmesi ile birlikte LILE/HFSE zenginleşmesi göstererek volkanik yay magmatiklerine benzemektedir. Elde edilen veriler öncelikle amfibolitik bir kaynağın kısmi ergimesi ile türemeyi işaret etmektedir. Diyoritler ve dasit porfiriler I-tipi granitlerin jeokimyasal karakteristiklerini sunarken, granitik kayalar S-tipi granitlerinin tipik özelliklerini göstermektedir. Dasit porfiri ve granit örneklerindeki zirkonların LA-ICP-MS U-Pb metodu ile yaşlandırılması sırasıyla  $161 \pm 6$  My ve  $170 \pm 2$  My yaşlarını vermektedir. Ek olarak, 'in-situ' ilksel  $^{176}\text{Hf}/^{177}\text{Hf}$  oranları dasit porfiri ve granit için sırasıyla  $0.28276 \pm 0.00003$  ve  $0.28213 \pm 0.00002$  şeklindedir. Bu sonuçlar kayaların yitim ile modifiye edilmiş manto kaynağının karışımı ile bir kıtasal yay sistemi içerisinde türetildiğini desteklemektedir.  $T_{\text{TM}}$  model yaşları 674 ve 1512 My arasında olup, Çangaldağ Plutonunu oluşturan magmatizmanın, Gondwana kökenli tektonik birliklerde yaygın olarak gözlenen Neoproterozoyik/Mesoproterozoyik yaşlı kıtasal kayaların kısmi ergimesi ile oluşabileceğine işaret etmektedir.

Tüm jeokimyasal ve jeokronolojik veriler Orta-Jura dönemi boyunca Pontid-içi okyanusun içerisinde yeralan ve bu okyanus kapanması ile oluşan bir ada yayı (Çangaldağ Metamorfik Kompleksi) ve kıtasal yay (Çangaldağ Plutonu) sisteminin varlığını doğrulamaktadır.

**Anahtar Kelimeler:** angaldađ Metamorfik Kompleksi, angaldađ Plutonu, Orta Pontidler, Jeokimya, Jeokronoloji, Pontid-ii

**To My Mother!**

## ACKNOWLEDGEMENTS

First of all, I would like to thank my supervisor Prof. M. Cemal Göncüođlu since he has supported me with his huge improving and constructive efforts during this research. I have learnt so many things for my academic future. It is really a great honor for me to be last PhD student of Prof. Göncüođlu!

I also gratefully acknowledge my co-supervisor Assoc. Prof. Kaan Sayıt for his detailed and thoughtful comments which scientifically improved my thesis! Then, I am extremely grateful to Prof. Antonio Simonetti for accepting me as a research scholar at University of Notre Dame. I have also learnt many things from him, particularly, in relation to geochronology and isotope geochemistry!

Special thanks to Prof. Asuman Türkmenođlu and Assoc.Prof. Biltan Kürkçüođlu for their discussion and comments who were members of the thesis monitoring committee.

I wish to thank Zehra Deveci, Orhan Karaman, Dr. Elizabeth Koeman, Dr. Ian Steele and Dr. Enrica Balboni for their assistance during the laboratory studies at METU and Notre Dame.

I would like to sincerely thank my family and friends Çađrı Alperen İnan, Uđur Balci, Alican Aktađ, Mustafa Kaplan, Faruk Berber, Mustafa Yücel Kaya, Yavuz Kaya, Zehra Deveci, Sanem Elidemir, Felat Dursun, Serdar Görkem Atasoy, David Burney, Karl Cronberger, Fabrizio Bob Sabba, Tylor Spano, Corrine Dorais etc. (I am so sorry if I forgot some names :-)) for their continuous supports, patience and encouragements!

Finally, many thanks go to the TUBITAK 2214-A Research Fellowship Programme, TUBITAK-1002 Project (144Y422) and YÖK-ÖYP Programme. I would not be able to complete this research without these grants!

## TABLE OF CONTENTS

ABSTRACT.....	v
ÖZ.....	vii
ACKNOWLEDGEMENTS .....	xi
LIST OF TABLES .....	xvii
TABLES.....	xvii
LIST OF FIGURES .....	xviii
FIGURES .....	xviii
CHAPTERS	
1. INTRODUCTION .....	1
1.1. General Overview: Contradictions and Problems.....	1
1.1.1. Central Pontides / Central Pontide Structural Complex (CPSC) .....	3
1.1.2. Çangaldağ Metamorphic Complex (CMC).....	5
1.1.3. Problems related to generation within the Paleotethyan Ocean / Karakaya Complex .....	8
1.1.4. Problems related to generation within the Intra-Pontide Ocean (IPO) ....	11
1.1.5. Problems related to generation within the Izmir-Ankara-Erzincan Branch of Neotethys .....	13
1.1.6. Purpose and Scope .....	15
1.2. Geographic Location.....	16
1.3. Methods of Study .....	17
1.3.1. Field Work .....	17
1.3.2. Laboratory Work.....	18
2. GEOLOGY .....	21
2.1. Regional Geology.....	21

2.1.1. Istanbul-Zonguldak Terrane (IZT) .....	22
2.1.2. Sakarya Composite Terrane (SCT) .....	23
2.1.3. Tectonic units of the Central Pontide Structural Complex .....	26
2.2. Local Geology .....	31
2.2.1. Çangaldağ Metamorphic Complex (CMC) .....	32
2.2.2. Çangaldağ Pluton (CP).....	51
2.2.3. Devrekani Units.....	55
2.2.4. Devrekani Granitoid.....	58
2.2.5. Cover Units .....	59
3. PETROGRAPHY .....	67
3.1. Çangaldağ Metamorphic Complex (CMC).....	67
3.1.1. Metabasalts.....	67
3.1.2. Metadiabase.....	70
3.1.3. Metaandesites .....	72
3.1.4. Metarhyodacites .....	74
3.1.5. Metavolcaniclastics .....	77
3.1.6. Metatuff.....	79
3.1.7. Metapelites .....	80
3.2. Çangaldağ Pluton (CP).....	83
3.2.1. Diorites .....	83
3.2.2. Dacite Porphyries .....	85
3.2.3. Granites .....	87
4. GEOCHEMISTRY.....	91
4.1. Introduction .....	91
4.2. Major and Trace Element Geochemistry of the Metavolcanic/subvolcanic Rocks within the Çangaldağ Metamorphic Complex .....	91

4.2.1. Effects of the Post Magmatic Processes.....	91
4.2.2. Geochemical Classification.....	93
4.2.3. Petrogenesis .....	98
4.3. Major and Trace Element Geochemistry of the Çangaldağ Pluton.....	105
4.3.1. Geochemical Classification.....	105
4.3.2. Petrogenesis .....	108
4.3.3. Tectonomagmatic Characteristics .....	112
5. U-Pb GEOCHRONOLOGY and Hf ISOTOPE SYSTEMATICS .....	115
5.1. U-Pb Geochronology .....	115
5.1.1. Instrumentation and Data Acquisition .....	117
5.1.2. Çangaldağ Metamorphic Complex (CMC).....	118
5.1.3. Çangaldağ Pluton (CP).....	121
5.1.4. Devrekani Orthogneiss.....	123
5.1.5. Metadiorite intruding Devrekani Metaophiolite .....	125
5.1.6. Devrekani Granitoid.....	126
5.2. Lu-Hf isotope Systematics .....	128
5.2.1. Instrumentation and Data Acquisition .....	129
5.2.2. Çangaldağ Metamorphic Complex .....	129
5.2.3. Çangaldağ Pluton .....	133
5.2.4. Metadiorite intruding Devrekani Metaophiolite .....	135
5.2.5. Devrekani Granitoid.....	137
6. DISCUSSION .....	139
6.1. New Insights into the Geological Evolution of the Çangaldağ Metamorphic Complex (CMC) .....	139
6.1.1. Geochemical Characteristics.....	139
6.1.2. U-Pb Geochronology .....	141

6.1.3. Hf Isotope Systematics.....	141
6.2. New Insights into the Geological Evolution of the Çangaldağ Pluton (CP).	142
6.2.1. Geochemical Characteristics .....	142
6.2.2. U-Pb Geochronology.....	142
6.2.3. Hf Isotope Systematics.....	144
6.3. Overall Geodynamic Evolution.....	146
7. CONCLUSIONS.....	153
7.1. Concluding remarks for the Çangaldağ Metamorphic Complex .....	153
7.2. Concluding remarks for the Çangaldağ Pluton .....	154
REFERENCES.....	155
APPENDICES A.....	173
APPENDICES B .....	175
APPENDICES C .....	182
APPENDICES D.....	187
APPENDICES E .....	239
Standards for U-Pb Geochronology .....	243
Standards for Hf Isotope Analysis .....	248
CURRICULUM VITAE .....	249

## LIST OF TABLES

### TABLES

Table 1: Differing interpretations about the Çangaldağ Metamorphic Complex .....	7
Table 2: Number of Zircon Grains .....	117

## LIST OF FIGURES

### FIGURES

Figure 1-1: a. Distribution of the main Alpine terranes in central North Anatolia (modified from Göncüoğlu, 2010). b. The main structural units of the Central Pontides (modified after Okay et al., 2015; Göncüoğlu et al., 2012, 2014; Ustaömer and Robertson, 1999). .....	2
Figure 1-2: Controversial views on the Çangaldağ Metamorphic Complex.....	8
Figure 1-3: Subduction accretion model of Okay (2000) for the Karakaya Complex (taken from Sayıt and Göncüoğlu, 2012) .....	9
Figure 1-4: Island Arc Magmatic model of the Paleotethyan Ocean (taken from Ustaömer and Robertson, 1999).....	10
Figure 1-5: Late Triassic paleogeography (taken from Robertson et al., 2012) .....	11
Figure 1-6: Middle Jurassic paleogeographical reconstruction of the Neotethys Ocean Ib: Iberia; Ad: Adria; Tz: Tizia; Ms: Moesia (taken from Marroni et al., 2014) .....	13
Figure 1-7: The paleographic positions of the Çangaldağ Metamorphic Complex during Late Jurassic-Early Cretaceous time (taken from Okay et al., 2013) .....	15
Figure 1-8: Location of the study area (modified from Saygılı, 2015) .....	17
Figure 2-1: The stratigraphic section of the Istanbul and Sakarya Zones in the Central Pontides (taken from Okay et al., 2014).....	25
Figure 2-2: Simplified cross section of the Central Pontides (modified from Ustaömer and Robertson, 1999).....	26
Figure 2-3: Sketch of the stratigraphy of the tectonic units within the Central Pontide Structural Complex (taken from Sayıt et al., 2016) .....	31
Figure 2-4: a. Distribution of the main alpine terranes in central North Anatolia (modified from Göncüoğlu, 2010) b. Geological map of the study area (modified	

from Konya et al., 1988). Blue samples: metarhyodacites, green samples: metaandesites; red samples: metabasalts/diabases (just analyzed samples). .....	33
Figure 2-5: Simplified cross sections of the Çangaldağ Metamorphic Complex (modified from Konya et al., 1988). .....	35
Figure 2-6: Field view of the foliated metaclastic rocks (pelitic schist) within the Çangaldağ Metamorphic Complex. Muscovite-rich parts are easily distinguished with their lighter colors from the biotite-rich darker parts. Both types display very nice foliation planes and microstructures.....	36
Figure 2-7: Field view of the small foldings on the metaclastic rocks (pelitic schist) within the Çangaldağ Metamorphic Complex. They display multi-deformation signatures. ....	37
Figure 2-8: Field view of the foliated metacarbonate rocks (calc-schist) within the Çangaldağ Metamorphic Complex. They have approximately 5 cm thicknesses and found with the pelitic schists.....	37
Figure 2-9: Field view of the metavolcaniclastic rocks within the Çangaldağ Metamorphic Complex. ....	38
Figure 2-10: Field view of the foliated metatuffs within the Çangaldağ Metamorphic Complex. They are mostly found with other metavolcaniclastic rocks and could be distinguished with very fine grained matrix. ....	38
Figure 2-11: a. Image of the small folding within an olistostromal black shale unit rocks within the Çangaldağ Complex. They show complex multi-deformational structures in small scale. b. Image of the small foldings from the metavolcaniclastic rocks within the Çangaldağ Complex. They exhibit complex multi-deformation structures in small scale. ....	39
Figure 2-12: Field view of the foliated metabasic rocks (metabasalts) within the Çangaldağ Metamorphic Complex. ....	42
Figure 2-13: Field view of the metavolcanic breccia (metabasalts). Note the relict vesicular texture of the clasts. ....	42
Figure 2-14: Field view of the foliated metabasic rocks (metabasalts) within the Çangaldağ Metamorphic Complex where white lensoidal parts are carbonates.....	43
Figure 2-15: Image of the pyrite and chalcopyrite minerals within the metavolcanic rocks. ....	43

Figure 2-16: Field view of the metaintermediate rocks (metaandesites) within the Çangaldağ Metamorphic Complex. They have lighter colors than metabasic rocks and found as non-foliated or foliated types in the field..... 44

Figure 2-17: a. Field view of the altered metafelsic (metarhyodacite) rocks within the Çangaldağ Metamorphic Complex. They have whitish colors in the field. The mafic products are cut by these felsic rocks. b. Another field view of altered metarhyodacite. .... 45

Figure 2-18: Field view of the metafelsic rocks (metarhyodacite) including metabasic enclaves within the Çangaldağ Metamorphic Complex..... 46

Figure 2-19: Field view of the contact relation between metaclastic and metavolcanic rocks within the Çangaldağ Metamorphic Complex. Mostly, metavolcanic rocks are thrust onto the metaclastic rocks. The primary relations are masked by secondary intense tectonic activities. .... 46

Figure 2-20: Field view of the contact relation between metaclastic and metavolcanic rocks within the Çangaldağ Metamorphic Complex. The metavolcanic rocks are mostly thrust onto the metaclastic rocks. .... 47

Figure 2-21: Field view of the tectonic contact relation between metaclastic and metavolcanic rocks within the Çangaldağ Metamorphic Complex. .... 47

Figure 2-22: Field view of the cross-cutting relation between a metarhyodacite and metaclastic rock within the Çangaldağ Metamorphic Complex. Dark colored part at the contact is the hornfelsic contact zone. The other units including metavolcanics, metavolcaniclastics and metaclastics are cut by these felsic rocks..... 48

Figure 2-23: Field view of the cross-cutting relation between a metarhyodacite and metabasic rock within the Çangaldağ Metamorphic Complex. .... 48

Figure 2-24: Field view of the tectonic contact relation between a metarhyodacite and metabasic rock within the Çangaldağ Metamorphic Complex..... 49

Figure 2-25: Field view of the slickensides (strike-slip: N80E, 68SE) within a shear zone between Çangaldağ Metamorphic Complex and Çangaldağ Pluton. There is a regional strike-slip fault between these units. .... 49

Figure 2-26: Field view of the cutting relation between a felsic intrusion and metaclastic rocks within the Çangaldağ Metamorphic Complex. The primary relation is erased by overprinting mylonitic deformation. .... 50

Figure 2-27: Field view of the cutting relation between a felsic intrusion and metabasic rocks within the Çangaldağ Metamorphic Complex. They show different petrographical characteristics than metavolcanic rocks of the CMC. They belong to a later magmatic event. ....	50
Figure 2-28: View of the field relations between Çangaldağ Pluton, Küre Complex and İnaltı Formation. This pluton cuts the Triassic Küre Complex and overlain by Upper Jurassic İnaltı Formation. ....	52
Figure 2-29: Closer view of the cutting relation between Çangaldağ Pluton and Küre Complex. ....	53
Figure 2-30: Field view of the dacite porphyry body within the Çangaldağ Pluton (the surface is highly altered).....	53
Figure 2-31: Field view of a granitic rock including a mafic enclave within the Çangaldağ Pluton. ....	54
Figure 2-32: Field view of the cutting relation between the granitic veins and diorite body within the Çangaldağ Pluton. ....	54
Figure 2-33: Field view of the cutting relation between orthogneiss and the Devrekani Metamorphics (paragneiss). ....	56
Figure 2-34: Field view of the cutting relation between orthogneiss and the Devrekani Metamorphics (paragneiss). ....	56
Figure 2-35: Field view of the cutting relation between orthogneiss/aplitic dyke and the Devrekani Metamorphics (paragneiss). ....	57
Figure 2-36: Field view of the cutting relation between a metadiorite body and the Devrekani Metaophiolite (found as tectonic slice within the Devrekani Metamorphics). ....	57
Figure 2-37: Field view of the cutting relation between a metadiorite body and the Devrekani Metaophiolite.....	58
Figure 2-38: Field view of the Devrekani Granitoid (Diorite).....	59
Figure 2-39: General view of the İnaltı Formation (unconformably overlies the Küre Complex and the Çangaldağ Pluton) .....	60
Figure 2-40: View of the field relation (tectonic) between the Çangaldağ Pluton and the İnaltı Formation.....	61

Figure 2-41: View of the field relation (tectonic) between the Çangaldağ Pluton and the Çangaldağ Metamorphic Complex. Also, there is a sheared limestone knocker (black boundary) between these units. ....	61
Figure 2-42: Field view of the Çağlayan Formation (thicker sandstone beds). It is composed of sandstone and shale alternations. ....	63
Figure 2-43: Field view of volcanic fragments in the Gökçeadağ Formation.....	64
Figure 2-44: The Tertiary sedimentary units unconformably overly the Çangaldağ Metamorphic Complex.....	65
Figure 2-45: General view of the Tertiary units in the Taşköprü-Boyabat Basin.....	65
Figure 3-1: Development of epidote and chlorite minerals in a fine grained groundmass of a foliated metabasalt (Sample 13, a. PPL b. XPL) .....	69
Figure 3-2: Development of epidote and actinolite minerals in a fine grained groundmass of non-foliated metabasalt (Sample BLV-11, a. PPL b. XPL) .....	69
Figure 3-3: Relict clinopyroxene and plagioclase crystals in a non-foliated metadiabase. Development of chlorite minerals on the pyroxene and amphibole crystals (Sample 47, a. PPL b. XPL).....	71
Figure 3-4: Relict amphibole and plagioclase crystals in a non-foliated metadiabase. Development of chlorite and epidote minerals (greenschist facies) on the pyroxene and amphibole crystals (Sample DVK-10, a. PPL b. XPL) .....	71
Figure 3-5: Development of chlorite crystals in a fine grained groundmass of foliated metaandesite (Sample 48, a. PPL b. XPL) .....	73
Figure 3-6: Development of chlorite and epidote crystals (greenschist facies) in a fine grained groundmass of non-foliated metaandesite (Sample 21, a. PPL b. XPL).....	73
Figure 3-7: Development of chlorite, epidote and actinolite crystals (greenschist facies) in a fine grained groundmass of slightly foliated metaandesite (Sample DRN-10, a. PPL b. XPL) .....	74
Figure 3-8: Development of small epidote crystals in a fine grained groundmass of non-foliated metarhyodacite (Sample 19, a. PPL b. XPL).....	75
Figure 3-9: Development of an epidote crystal in a fine grained groundmass of foliated metarhyodacite (Sample AK-10, a. PPL b. XPL) .....	76
Figure 3-10: Quartz phenocryst in a fine grained groundmass of non-foliated metarhyodacite (Sample AK-14, a. PPL b. XPL) .....	76

Figure 3-11: Development of small epidote and sericite crystals (on the feldspars) in a fine grained groundmass of non-foliated metarhyodacite. Also, the corroded quartz mineral can be observed (Sample AK-22, a. PPL b. XPL).....	77
Figure 3-12: The quartz grains and development of chlorite minerals within a non-foliated metavolcaniclastic rock (Sample DRN-15, a. PPL b. XPL).....	78
Figure 3-13: The quartz fragments and development of chlorite/epidote crystals (greenschist facies) within a slightly foliated metavolcaniclastic rock (Sample DRN-3, a. PPL b. XPL) .....	78
Figure 3-14: Development of epidote, chlorite and actinolite crystals (greenschist facies) in a fine grained groundmass of metatuff (Sample AK-5, a. PPL b. XPL)....	79
Figure 3-15: Development of chlorite and actinolite crystals (greenschist facies) in a fine grained groundmass of metatuff (Sample DRN-8, a. PPL b. XPL).....	80
Figure 3-16: The quartz fragments and development of muscovite / biotite crystals within a foliated metapelitic rock (Sample DRN-7, a. PPL b. XPL).....	81
Figure 3-17: The quartz fragments and development of muscovite / biotite crystals within a foliated metapelitic rock (Sampe SCH-1, a. PPL b. XPL).....	82
Figure 3-18: Development of muscovite / biotite / graphite crystals and S1 / S2 cleavage planes within a foliated metapelitic rock (Sample 9, a. PPL b. XPL).....	82
Figure 3-19: Clinopyroxene, Amphibole and plagioclase crystals in a diorite (Sample CN-1, a. PPL b. XPL) .....	84
Figure 3-20: Amphibole, plagioclase and small quartz crystals in diorite (Sample CN-9, a. PPL b. XPL) .....	84
Figure 3-21: Amphibole, plagioclase, clinopyroxene and quartz crystals in a qtz-diorite (Sample CN11, a. PPL b. XPL).....	85
Figure 3-22: Development of chlorite and sericite crystals (on the plagioclase crystals) in a fine grained groundmass of dacite porphyry (Sample CN-3, a. PPL b. XPL).....	86
Figure 3-23: Quartz and biotite phenocrysts in a fine grained groundmass of dacite porphyry (Sample CN-5, a. PPL b. XPL) .....	86
Figure 3-24: Quartz phenocrysts and development of chlorite and sericite crystals (on the feldspars) in a fine grained groundmass of dacite porphyry (Sample CN-8, a. PPL b. XPL).....	87

Figure 3-25: Quartz and amphibole crystals in a granite (Sample SL-2, a. PPL b. XPL).....	88
Figure 3-26: Secondary quartz vein, plagioclase and hornblende crystals in a granite (Sample SL-3, a. PPL b. XPL).....	88
Figure 3-27: Biotite, muscovite and secondary sericite crystals (on the feldspars) in a granite (Sample SL-5, a. PPL b. XPL).....	89
Figure 4-1: Plots of selected major and trace elements vs Zr. Group 1-2-3: Basalts and diabases; Group 4: Metaandesites; Group 5: Metarhyodacites .....	92
Figure 4-2: Zr–Ti v. Nb–Y (after Pearce 1996) diagram for the metavolcanic rocks of the Çangaldağ Metamorphic Complex. Group 1-2-3: Basalts and diabases; Group 4: Metaandesites; Group 5: Metarhyodacites.....	94
Figure 4-3: N-MORB normalized multi element spider diagrams (Sun and McDonough, 1989); the data of Mariana and Lau arc-back arc basin samples taken from Pearce et al. (1995, 2005). a. Group 1: Boninites; b-c. Group 2: Island arcs; d-e. Group 3: Back-arc basin basalts; f. Group 4: Metaandesites; g. Group 5: Metarhyodacites .....	96
Figure 4-4: Chondrite normalized REE spider diagrams (Sun and McDonough, 1989); the data of Mariana and Lau arc-back arc basin samples taken from Pearce et al. (1995, 2005). a. Group 1: Boninites; b-c. Group 2: Island arcs; d-e. Group 3: Back-arc basin basalts; f. Group 4: Metaandesites; g. Group 5: Metarhyodacites. ...	97
Figure 4-5: a. Nb/Y vs Zr/Y (Sayit et al., 2016) and b. La/Yb vs Zr/Nb (Aldanmaz et al., 2008) diagrams for the metavolcanic rocks of the CMC; the data of Mariana and Lau arc-back arc basin samples taken from Pearce et al. (1995, 2005). Group 1: Boninites; Group 2: Island arcs; Group 3: Back arc basalts .....	100
Figure 4-6: a. TiO <sub>2</sub> – Yb (Gribble et al., 1998) and b. Sm vs Sm/Yb (Sayit et al., 2016) partial melting diagrams for the primitive metavolcanic rocks of the Çangaldağ Metamorphic Complex.....	103
Figure 4-7: Geotectonic discrimination diagrams a) after Shervais (1982), b) after Meschede (1986).....	105
Figure 4-8: Geochemical classification of the Çangaldağ Pluton (Middlemost, 1985) .....	106

Figure 4-9: Geochemical discrimination diagram for the Çangaldağ Pluton a. Total alkali silica diagram b. K <sub>2</sub> O vs SiO <sub>2</sub> diagram (Peccerillo and Taylor, 1976) c. FeO <sub>t</sub> / (FeO <sub>t</sub> +MgO) vs SiO <sub>2</sub> diagram (Frost et al., 2001) d. Na <sub>2</sub> O vs K <sub>2</sub> O diagram (Chappell and White, 2001).	107
Figure 4-10: a. N-MORB normalized multi-element diagram b. Chondrite normalized rare earth element diagram. N-MORB and Chondrite normalization values are from Sun and McDonough (1989). Volcanic arc granites data from Pearce et al. (1984).	108
Figure 4-11: Harker variation diagrams for selected major (wt %) and trace (ppm) elements	110
Figure 4-12: Plots showing compositional fields of experimental melts derived from partial melting of pelite, grewake and amphibolite. Data from Patino Douce (1999)	111
Figure 4-13: Geotectonic discrimination diagrams for the Çangaldağ Pluton a. Pearce et al., 1984 b. Schandl and Gorton (2002).	113
Figure 4-14: Nb/Y vs Zr/Y and Th/Yb vs Nb/Yb diagrams. Oceanic Arc and Continental Arcs values are from Condie and Kröner (2013). Average N-MORB and E-MORB values are from Sun and McDonough (1989)	114
Figure 5-1: <sup>206</sup> Pb / <sup>238</sup> U vs <sup>207</sup> Pb / <sup>235</sup> U diagram and concordia age for AK-7 (metarhyodacite)	119
Figure 5-2: <sup>206</sup> Pb / <sup>238</sup> U vs <sup>207</sup> Pb / <sup>235</sup> U diagram and lower intercept age for AK-14 (metarhyodacite)	119
Figure 5-3: <sup>206</sup> Pb / <sup>238</sup> U vs <sup>207</sup> Pb / <sup>235</sup> U diagram and weighted mean age for AK-22 (metarhyodacite)	120
Figure 5-4: <sup>206</sup> Pb/ <sup>238</sup> U (weighted mean age) data for AK-22 (metarhyodacite)	120
Figure 5-5: <sup>206</sup> Pb / <sup>238</sup> U vs <sup>207</sup> Pb / <sup>235</sup> U diagram and concordia age for CN-3 (daciteporphyry)	121
Figure 5-6: <sup>206</sup> Pb / <sup>238</sup> U vs <sup>207</sup> Pb / <sup>235</sup> U diagram and concordia age for CN-3 (dacite porphyry)	122
Figure 5-7: <sup>206</sup> Pb / <sup>238</sup> U vs <sup>207</sup> Pb / <sup>235</sup> U diagram and lower intercept age for SL-3 (S-type granite)	122

Figure 5-8: $^{206}\text{Pb} / ^{238}\text{U}$ vs $^{207}\text{Pb} / ^{235}\text{U}$ diagram and concordia age for SL-3 (S-type granite) .....	123
Figure 5-9: $^{206}\text{Pb} / ^{238}\text{U}$ vs $^{207}\text{Pb} / ^{235}\text{U}$ diagram and Pb-loss for DVK-4A (orthogneiss).....	124
Figure 5-10: $^{206}\text{Pb} / ^{238}\text{U}$ vs $^{207}\text{Pb} / ^{235}\text{U}$ diagram and lower intercept age for DVK-4A (orthogneiss).....	125
Figure 5-11: $^{206}\text{Pb} / ^{238}\text{U}$ vs $^{207}\text{Pb} / ^{235}\text{U}$ diagram and lower intercept age for DV-11 (metadiorite).....	126
Figure 5-12: $^{206}\text{Pb} / ^{238}\text{U}$ vs $^{207}\text{Pb} / ^{235}\text{U}$ diagram and weighted age for DVK-13 (granite).....	127
Figure 5-13: $^{206}\text{Pb}/^{238}\text{U}$ (weighted mean age) data for DVK-13 (granite) .....	127
Figure 5-14: $^{176}\text{Hf}/^{177}\text{Hf}$ vs Time for AK-7 (metarhyodacite) .....	130
Figure 5-15: $\epsilon\text{Hf}$ vs Time for AK-7 (metarhyodacite).....	130
Figure 5-16: $^{176}\text{Hf}/^{177}\text{Hf}$ vs Time for AK-14 (metarhyodacite) .....	131
Figure 5-17: $\epsilon\text{Hf}$ vs Time for AK-14 (metarhyodacite).....	131
Figure 5-18: $^{176}\text{Hf}/^{177}\text{Hf}$ vs Time for AK-22 (metarhyodacite) .....	132
Figure 5-19: $\epsilon\text{Hf}$ vs Time for AK-22 (metarhyodacite).....	132
Figure 5-20: $^{176}\text{Hf}/^{177}\text{Hf}$ vs Time for CN-3 (dacite porphyry).....	133
Figure 5-21: $\epsilon\text{Hf}$ vs Time for CN-3 (dacite porphyry).....	134
Figure 5-22: $^{176}\text{Hf}/^{177}\text{Hf}$ vs Time for SL-3 (S-type granite).....	134
Figure 5-23: $\epsilon\text{Hf}$ vs Time for SL-3 (S-type granite) .....	135
Figure 5-24: $^{176}\text{Hf}/^{177}\text{Hf}$ vs Time for DV-11 (metadiorite).....	136
Figure 5-25: $\epsilon\text{Hf}$ vs Time for DV-11 (metadiorite) .....	136
Figure 5-26: $^{176}\text{Hf}/^{177}\text{Hf}$ vs Time for DVK-13 (granite).....	137
Figure 5-27: $\epsilon\text{Hf}$ vs Time for DVK-13 (granite).....	138
Figure 6-1: Distributions of the different ages from SL-3 (granite sample) .....	144
Figure 6-2: Possible geodynamic model for the Çangaldağ Metamorphic Complex and Çangaldağ Pluton (Prism 1: Aylı Dağ Ophiolite and Arkot Dağ Melange; Prism 2: Domuzdağ, Daday and Saka Units; Variscan Basement: Devrekani Units, Geme Complex, Sivrikaya and Deliktaş Granitoids; LM: Lithospheric Mantle; IA: Island Arcs; BAB: Back-arc Basalts; LC: Lower Crust) .....	151

## LIST OF ABBREVIATIONS

**CMC:** Çangaldağ Metamorphic Complex

**CP:** Çangaldağ Pluton

**CPSC:** Central Pontide Structural Complex

**CPMS:** Central Pontide Metamorphic Supercomplex

**SCT:** Sakarya Composite Terrane

**IZT:** İstanbul Zonguldak Terrane

**ATT:** Anatolide-Tauride Terrane

**IPOB:** Intra-Pontide Ocean Basin

**IPS:** Intra-Pontide Suture

**IAESASB:** İzmir-Ankara-Erzincan-Sevan-Akera Suture Belt

**MC-LA-ICP-MS:** Multi Collector Laser Ablation Inductively Coupled Plasma Mass Spectrometer

**ICP-OES:** Inductively Coupled Plasma Optical Emission Spectrometer

**NMORB:** Normal Mid-Ocean Ridge Basalts

**EMORB:** Enriched Mid-Ocean Ridge Basalts

**CHUR:** Chondritic Uniform Reservoir

**DM:** Depleted Mantle

**VAG:** Volcanic Arc Granites

**LREE:** Light Rare Earth Elements

**HREE:** Heavy Rare Earth Elements

**LILE:** Large Ion Lithophile Elements

**HFSE:** High Field Strength Elements

**Chl:** Chlorite

**Act:** Actinolite

**Alb:** Albite

**Ep:** Epidote

**Cpx:** Clinopyroxene

**Qtz:** Quartz

**Kfs:** K-feldspar

**Plg:** Plagioclase

**Musc:** Muscovite

**Bio:** Biotite

**Amp:** Amphibole

**Src:** Sericite

**Grp:** Graphite

**Spi:** Spinel

## CHAPTER 1

### INTRODUCTION

#### 1.1. General Overview: Contradictions and Problems

Turkey is a part of Alpine-Himalayan orogenic belt, and the commonly accepted view regarding the northern part of Turkey is that a number of terranes or continental micro-plates (Fig. 1-1a) were amalgamated during the closure of the Neotethyan oceanic branches (Şengör and Yılmaz, 1981; Göncüoğlu et al., 1997; Göncüoğlu et al., 2006; Aldanmaz et al., 2008; Göncüoğlu, 2010; Robertson et al., 2014).

The northern terrane is the Istanbul-Zonduldak Terrane that has separated from the Sakarya Composite Terrane (SCT) in the south by the Intra-Pontide Suture Belt (IPSB; Fig. 1-1a; Göncüoğlu et al., 1997, Göncüoğlu, 2010). In the south, the third microcontinent, that is Anatolid-Tauride Terrane (ATT), separated from the SCT by the Izmir-Ankara-Erzincan-Sevan-Akera Suture Belt (IAESASB; Fig.1-1a; Şengör and Yılmaz, 1981; Okay and Şahintürk, 1997; Göncüoğlu et al., 1997, Göncüoğlu, 2010; Aldanmaz et al., 2008; Parlak et al., 2013; Robertson et al., 2014). The continuation of this suture belt extends from Armenia (Galoyan, 2008; Galoyan et al., 2009; Rolland et al., 2010; Hässig et al., 2013) to northern Iran.

To identify and clarify the current problems on the geodynamic evolution of Northern Turkey, firstly, the Tethyan events must be discussed by detailed literature survey. After that, the problematic units, which have critical importance, can be determined to solve unclear points in relation to regional geology of Turkey.

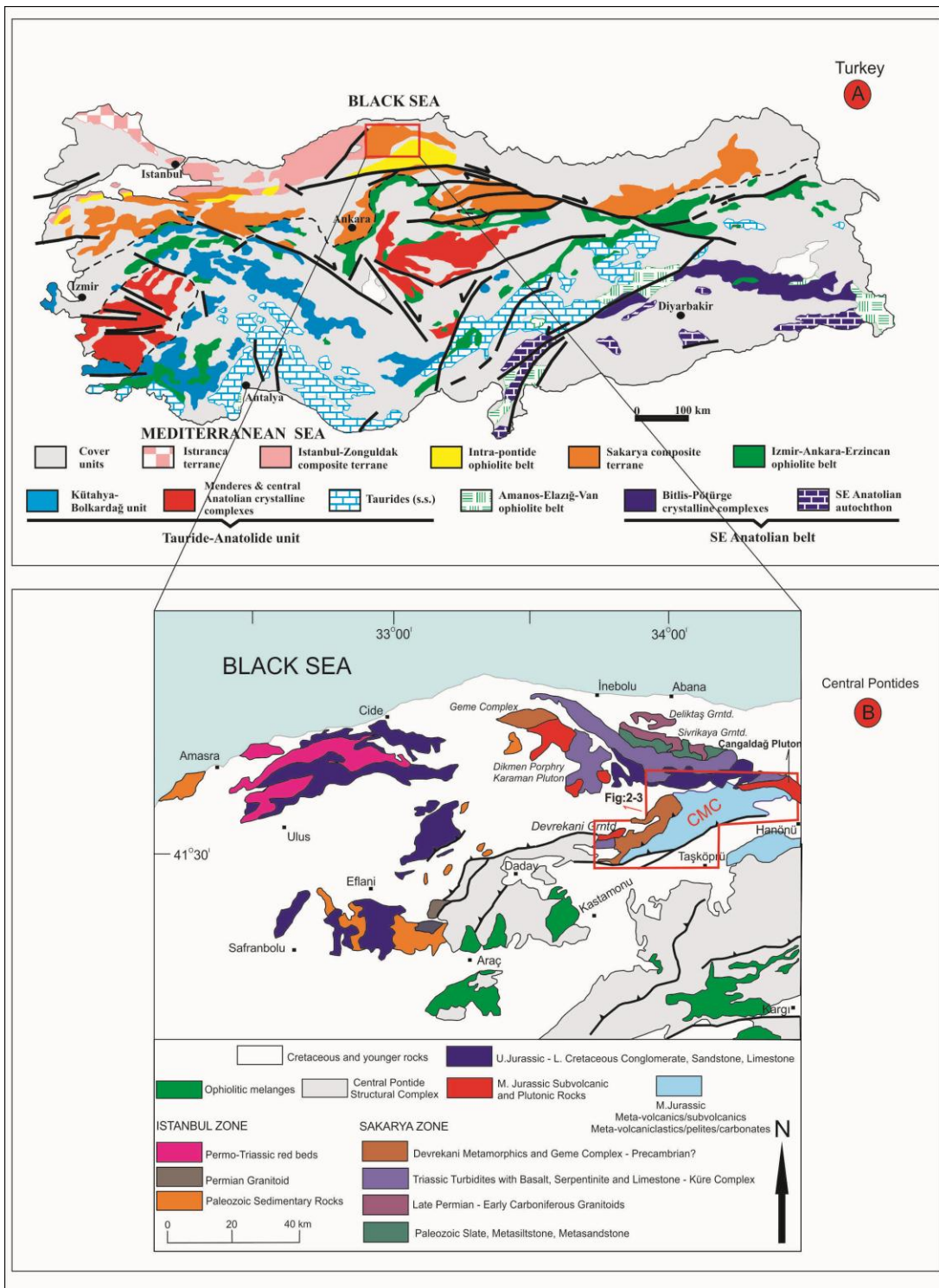


Figure 1-1: a. Distribution of the main Alpine terranes in central North Anatolia (modified from Göncüoğlu, 2010). b. The main structural units of the Central Pontides (modified after Okay et al., 2015; Göncüoğlu et al., 2012, 2014; Ustaömer and Robertson, 1999).

For this, we will start to discuss the problematic regions and hence the aim and scope of this study by evaluating the geological models for the Çangaldağ Metamorphic Complex proposed in previous studies.

### **1.1.1. Central Pontides / Central Pontide Structural Complex (CPSC)**

In Turkey, the Central Pontides includes the boundary between two important Gondwana-derived tectonic terranes, which are Istanbul-Zonguldak Terrane (IZT) and SCT (Fig. 1-1b). The Central Pontides and its geodynamic evolution, particularly in the Mesozoic, are hotly debated since long time. There is no consensus yet on the origin of the Central Pontides, which is of crucial importance to understand the geodynamic evolution of northern Turkey. The region has been studied by many researchers over a long period (e.g. Yılmaz, 1980, 1981, 1983; Boztuğ, 1983, 1988, 1992; Boztuğ and Yılmaz, 1983; Yılmaz and Tüysüz, 1984, 1991; Tüysüz, 1985, 1990, 1993, 1999; Yılmaz and Şengör, 1985; Aydın et al., 1986, 1995; Yılmaz and Boztuğ, 1986, 1987; Şengün et al., 1988; Tüysüz et al., 1989; Ustaömer and Robertson, 1993, 1994, 1999; Boztuğ et al., 1995; Yılmaz et al., 1997; Nzegge et al., 2006; Uğuz and Sevin, 2007; Göncüoğlu et al., 2008, 2012, 2014; Nzegge, 2008; Okay et al., 2006, 2013, 2014; Sayıt et al., 2016; Aygül et al., 2016; Gücer et al., 2016; Çimen et al., 2016a, b).

Recently, the large area of the metamorphic rocks in the southern part of the Central Pontides has been defined as the Central Pontide Supercomplex (CPS) or Central Pontide Metamorphic Supercomplex (CPMS; Okay et al., 2013) also known as CPSC (Tekin et al., 2012) which contains the Daday Massif in the west, the Elekdağ-Domuzdağ and Kargı massifs in the east and the Çangaldağ Complex (CMC) in the north (Fig. 1-1b). On the other hand, the “Central Pontides” is a geographical term comprising several units with geographical (e.g. Devrekani Massif, Kargı Massif, Daday Massif, Ilgaz Massif) or tectonic (e.g. Küre Complex, Geme Complex, Devrekani Metamorphics, CMC, Elekdağ Complex, Domuzdağ-Saraycık Complex)

origin (Yılmaz and Tüysüz; 1984; Ustaömer and Robertson, 1999; Kozur et al., 2000; Göncüoğlu et al., 2012, 2014; Okay et al., 2006, 2013, 2014, 2015; Okay and Nikishin, 2015; Aygül et al., 2016; Sayıt et al., 2016; Çimen et al., 2016a, b; Gücer et al., 2016) units (Fig. 1-1b).

The detailed investigation of the previous studies reveals significant differences that have been put forward about the Central Pontides. The first one is related to the presence or absence of the Intra-Pontide Ocean (IPO) between the IZT and SCT during the Mid to Late Mesozoic (Şengör and Yılmaz, 1981; Yılmaz et al., 1995; Tüysüz, 1999; Elmas and Yiğitbaş, 2001; Robertson and Ustaömer, 2004; Okay et al., 2006, 2008; Kaya, 1977, Kaya and Kozur, 1987; Göncüoğlu et al., 2008, 2012, 2014; Akbayram et al., 2013; Marroni et al., 2014). The second problem is concentrated on that the Central Pontides has formed as result of accretionary prisms developing in the Paleotethyan, Neotethyan or Intra-Pontide (a northern branch of Neotethyan) oceans (Ustaömer and Robertson, 1993, 1994, 1999; Okay et al., 2006, 2013, 2014, 2015; Göncüoğlu et al., 2012, 2014; Marroni et al., 2014). The third problem discusses the presence of the Cimmeria microcontinent in Turkey which is considered to be reason of the Cimmeride Orogeny in the southern Laurasian margin during Late Triassic - Early Jurassic (Şengör, 1984; Okay et al., 2014, 2015; Çelik et al., 2011; Topuz et al., 2013).

From the numerous tectonic units making up the CPSC the Çangaldağ Complex comprises two main units: the Çangaldağ Metamorphic Complex (CMC) mainly consisting of metavolcanics with meta-sedimentary and metavolcanoclastic rocks, and the Çangaldağ Pluton mainly made of non-metamorphic diorites, dacite porphyries and granites. The CMC and Çangaldağ Pluton (CP) play a critical role for evaluating the major geological events which have occurred during the geodynamic evolution of the Central Pontides.

### 1.1.2. Çangaldağ Metamorphic Complex (CMC)

Although the CMC has been studied by many researchers over a long period of time (Yılmaz, 1980, 1983; Tüysüz, 1985; Şengün et al., 1988; Yılmaz, 1988; Tüysüz, 1990; Ustaömer and Robertson, 1993, 1994, 1999; Okay et al., 2006, 2013, 2014), there is no consensus yet on the origin of the CMC.

There are important contradictions and problems in the literature about the origin of the CMC. Three different models can be considered for this metamorphic complex (Fig. 1-2 and Table 1). First of them suggests that the CMC is a meta-ophiolitic body related to the southernly Elekdağ meta-ophiolite (Fig. 1-2a; Yılmaz, 1980, 1983; Şengün et al., 1988; Yılmaz, 1988; Tüysüz, 1985, 1990; Uğuz and Sevin, 2007). The second opinion (Ustaömer and Robertson, 1993, 1994, 1999) indicates that the CMC was formed as the result of arc volcanism developing in a pre-late Jurassic ocean (Paleotethyan; Fig. 1-2b). However, these previous studies are based upon the whole rock geochemical analyses of volcanic rocks by using XRF method. As results of these studies, the volcanic rocks within the CMC have been determined as andesite, basaltic andesite and rhyo-dacite and plotted into the island arc tholeiite and mid-ocean ridge basalt fields on the geotectonic classification diagram (Ustaömer and Robertson, 1999; Çimen et al., 2015). The last view is that the CMC is the conjugate of the Nilüfer Unit of the Karakaya Complex (Fig. 1-2c; Okay et al., 2006). In this study without any geochemical data, the volcanic rocks of the CMC have been accepted as an oceanic plateau and ocean island series rather than island arc volcanics (Table 1). Later on, this opinion was revised by the author (Okay et al., 2013, 2014) as “arc magmatism” considering the previous studies including geochemical data of Ustaömer and Robertson (1999).

In brief, the main point is the absence of detailed field (relations, systematically sampling etc.) and petrological studies (e.g. isotope geochemistry and geochronology). The outstanding problems, contradictions and deficient information have been summarized in the Figure 1-2 and Table 1.

Regarding the age, the CMC is intruded by mid-Jurassic granitic rocks (CP) that provides a relative pre-Mid-Jurassic age (Yılmaz, 1980; Yılmaz and Boztuğ, 1986; Aydın et al., 1995). In relation to the radiometric dating methods, firstly, the Middle Jurassic (153 Ma) and Early Cretaceous metamorphism (126-110 Ma) ages were assigned for the metabasic rocks and phyllites, respectively (Yılmaz and Bonhomme, 1991) by using the K-Ar methods. These Early Cretaceous metamorphic ages have been confirmed by Okay et al. (2013) for the metamorphic complex based upon the Ar-Ar mica dating of phyllite samples (136 and 125 Ma). The contradictions in these ages are;

1- How can a Middle Jurassic non-metamorphic intrusion (CP) cut the Metamorphic Complex metamorphosed at Lower Cretaceous?

2- How can the CMC with a Lower Cretaceous metamorphism be disconformably overlain by the non-metamorphic Upper Jurassic-Lower Cretaceous Limestone (the İnaltı Formation)?

Table 1: Differing interpretations about the Çangaldağ Metamorphic Complex

<b>Previous Studies</b>	Şengün et al.,1988; Tüysüz, 1985, 1990; Uğuz and Sevin, 2007; Yılmaz, 1980,1983; Yılmaz, 1988	Ustaömer and Robertson, 1993, 1994, 1999	Okay et al., 2006, Okay et al., 2013,2014
<b>Definition</b>	Meta-ophiolite	Paleotethyan Volcanic Arc	Paleotethyan oceanic plateau (2006), volcanic arc (2013, 2014)
<b>Isotope Systems</b>	no	no	no
<b>Protholith Age</b>	no	no	169 Ma-Middle Jurassic (2014)
<b>Relative Age</b>	Pre-Jurassic (cut by Middle Jurassic Granitoid and overlain by Late Jurassic Conglomerates)	Pre-Jurassic (cut by Middle Jurassic Granitoid and overlain by Late Jurassic Conglomerates)	Pre-Jurassic (cut by Middle Jurassic Granitoid and overlain by Late Jurassic Conglomerates- 2006)

As mentioned above, the interpretations on the origin and geodynamic evolution of the CMC have various problems in regard to the petrogenesis, origin and geochronology. Moreover, the different magmatic and geodynamic reconstructions regarding the Paleotethys, and Neotethyan oceans must be re-evaluated.

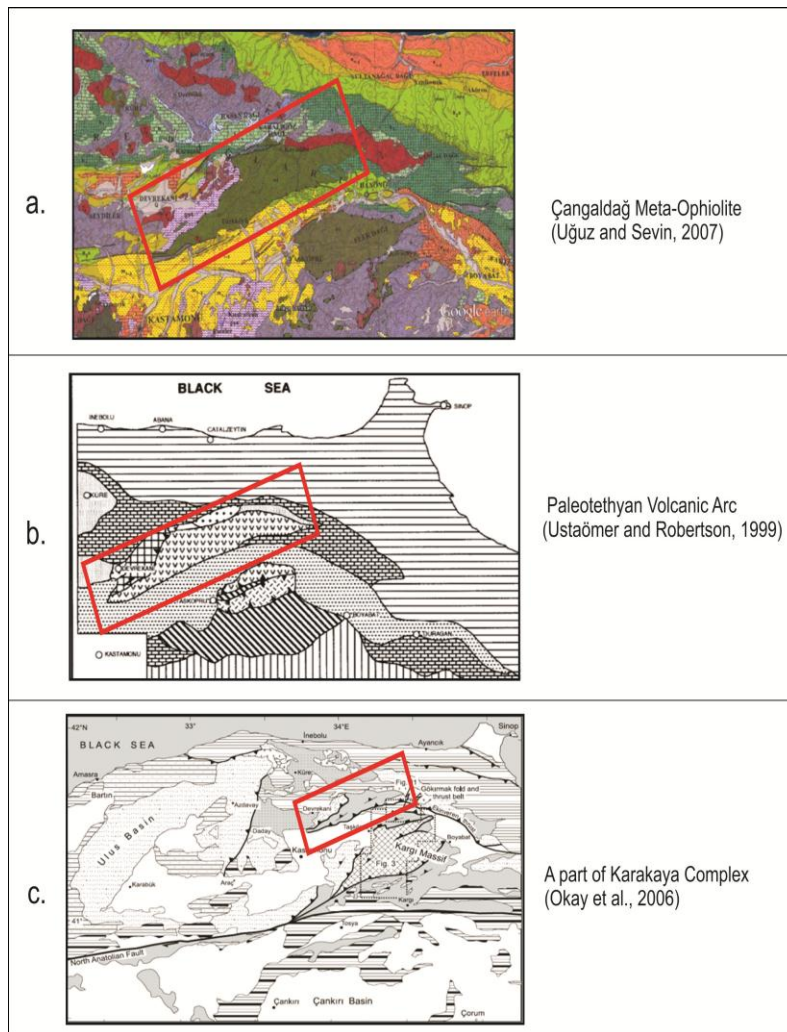


Figure 1-2: Controversial views on the Çangaldağ Metamorphic Complex

### 1.1.3. Problems related to generation within the Paleotethyan Ocean / Karakaya Complex

The paleogeographic position and geodynamic evolution of the Paleotethyan Ocean and Karakaya Complex play an important role to understand the evolution of the CMC and Central Pontides. In relation to the origin of the CMC, so far, two different models were proposed. The first one is that CMC is the conjugate of Nilüfer Volcanics in SCT which corresponds to a Triassic oceanic plateau within the

Paleotethyan Ocean (Okay et al., 2006; Fig. 1-3). The second model by Ustaömer and Robertson (1994, 1999), Robertson et al. (2012) and Okay et al. (2013) suggests island arc magmatism within the Paleotethyan Ocean (Figs. 1-4, 1-5). If the CMC had been the remnant of the Paleotethyan Ocean, its age must have been older than the Middle Jurassic. These models are mainly based on the pre-Mid Jurassic relative age (Yılmaz, 1980; Yılmaz and Boztuğ, 1986; Aydın et al., 1995). This relative age has been given regarding the cross-cutting relation between the CMC and CP in the study area. The Mid-Jurassic relative age is accepted (there is no radiometric age data) for the formation of CP on the basis of the field relations, as CP intrudes the Triassic Küre Complex and is overlain by Upper Jurassic İnaltı Limestone. However, the recently assigned Middle Jurassic age (1 dacite sample) for the CMC by Okay et al. (2014) invalidates the Paleotethyan models. Therefore, it is significant to determine more reliably the radiometric age (from several samples) for the CMC and CP.

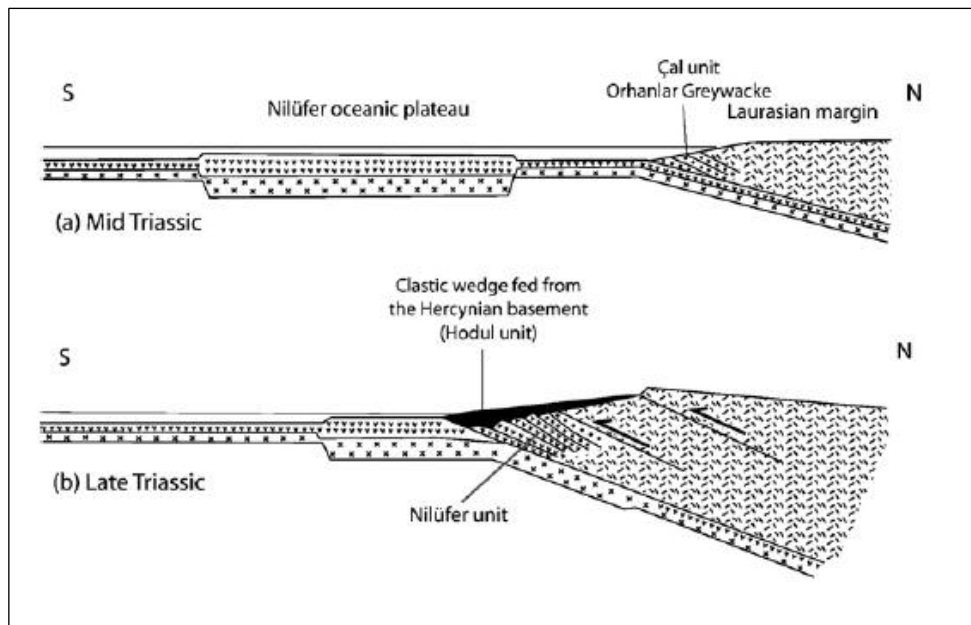


Figure 1-3: Subduction accretion model of Okay (2000) for the Karakaya Complex (taken from Sayıt and Göncüoğlu, 2012)

The other important point related to the formation of CMC and CP is the subduction polarity of the Paleotethyan Ocean, provided that they are products of the Cimmerian events. As seen in the previous studies both northward (beneath Laurasia margin; Robertson and Dixon, 1984; Dercourt et al., 1993; Ustaömer and Robertson, 1997; Okay, 2000; Stampfli, 2000; Dercourt et al., 2000; Stampfli et al., 2001; Eren et al., 2004) and southward (beneath the SCT, Özcan et al., 1990; Göncüoğlu et al., 2000, 2007; Sayit and Göncüoğlu, 2013) subduction is proposed. Considering the recent geographic configuration and that CP indeed intrude the Küre Complex of the SCT, the subduction should be northward but beneath the SCT. This is another result that refutes to the geodynamic models yet proposed.

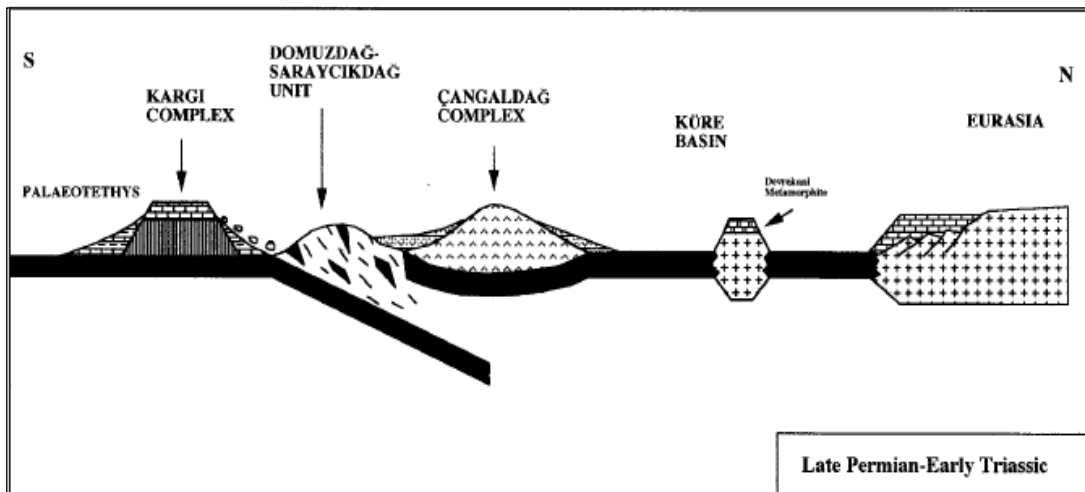


Figure 1-4: Island Arc Magmatic model of the Paleotethyan Ocean (taken from Ustaömer and Robertson, 1999)

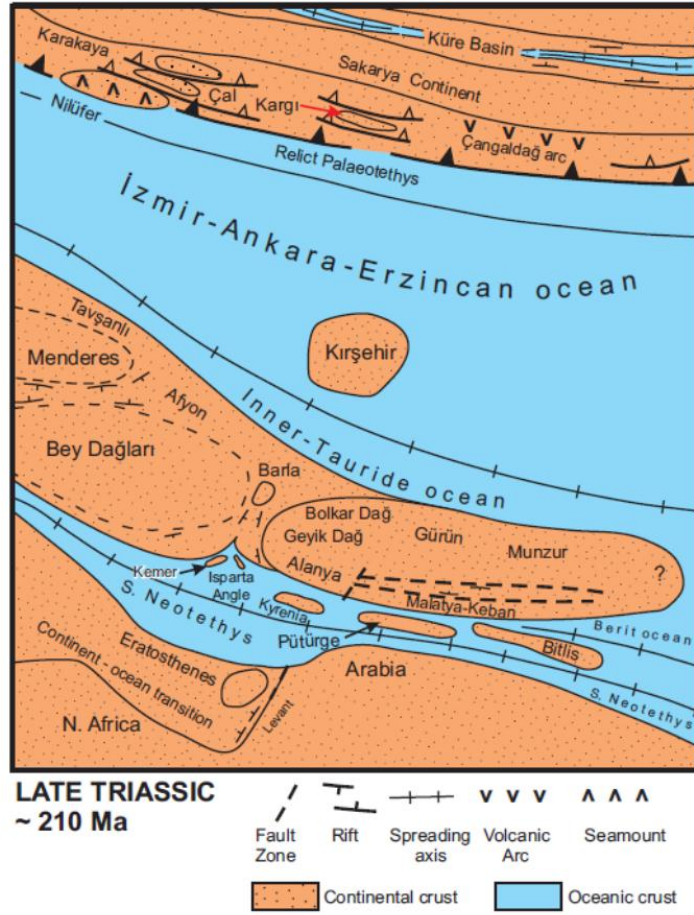


Figure 1-5: Late Triassic paleogeography (taken from Robertson et al., 2012)

#### 1.1.4. Problems related to generation within the Intra-Pontide Ocean (IPO)

The CMC is interpreted as one of the tectonic units formed in relation to the Intra-Pontide Ocean Basin (IPOB) between the SCT and IZT (e.g. Göncüoğlu et al. 1997). However, the presence or absence of the IPO between these two terranes during the Mid to Late Mesozoic is also hotly debated in the literature (Şengör and Yılmaz, 1981; Yılmaz et al., 1995; Tüysüz, 1999; Elmas and Yiğitbaş, 2001; Robertson and Ustaömer, 2004; Okay et al., 2006, 2008; Kaya, 1977; Kaya and Kozur, 1987; Göncüoğlu et al., 2008, 2012, 2014; Akbayram et al., 2013; Marroni et al., 2014; Sayıt et al., 2016; Çimen et al., 2016a, b).

There are several models which have been proposed for the suture zone of this ocean. The first model suggests a multiple branch model for the Neotethyan Ocean during the Mesozoic time and advocates the presence of the IPO (Fig. 1-6; Şengör and Yılmaz, 1981; Yılmaz et al., 1995; Okay et al., 1996, 2006; Robertson and Ustaömer, 2004; Göncüoğlu et al., 2008, 2012, 2014, Akbayram et al., 2013; Marroni et al., 2014; Sayıt et al., 2016; Çimen et al., 2016a, b) especially in NW Anatolia. In this model, there are different ideas about the time of opening and closure of this ocean. The second model suggests that the ophiolitic melanges belong to the Izmir-Ankara-Erzincan branch of the Neotethyan Ocean (single-strand model) and strike slip faulting during the Late Cretaceous time has caused the replacement of the Izmir-Ankara-Erzincan oceanic units to their present locations (Elmas and Yiğitbaş, 2001). The third model suggests that these ophiolitic rocks are related to the Permo-Triassic rifting events and ignores any Neotethyan oceanic involvement (e.g. Kaya, 1977; Kaya and Kozur, 1987; Kaya et al., 1986, 1988). The last model states that the IPSB can be continuation of the Rheic Ocean in Turkey (Okay et al., 2008; Stampfli and Borel, 2002) or remnants of the Paleotethyan Ocean (Bozkurt et al., 2012, 2013).

The geochemical data from the CMC indicate an ancient arc-back arc basin environment (Ustaömer and Robertson, 1999; Çimen et al., 2015) that was formed during the Mid-Jurassic time regarding the recent radiometric age data (Okay et al., 2014; Çimen et al., 2016a). The IPOB was already open prior to the Early Jurassic (Göncüoğlu et al., 2014). In addition, the ophiolitic blocks and Ayli Dag ophiolite support the presence of a supra subduction zone which has begun to form during the Middle Jurassic (Göncüoğlu et al., 2012, 2014). Hence, the CMC can correspond to the island arc and back arc systems of this supra subduction zone (Fig. 1-6) that were formed during the Mid-Jurassic (Çimen et al., 2015, 2016a). In addition, the presence of Mid-Late Jurassic Island Arc, BABB and MORB-type basalts in the CPSC melanges (Göncüoğlu et al., 2008, 2012; Sayıt et al., 2016) also support an intra-oceanic subduction.

The Ar-Ar single-grain ages of phyllites from the CMC (125 Ma and 136 Ma) indicate an Early Cretaceous (Valanginian-Barremian) age for the regional metamorphism (Okay et al., 2013). This age may correspond to the collision of an island arc with a marginal arc represented by the CP.

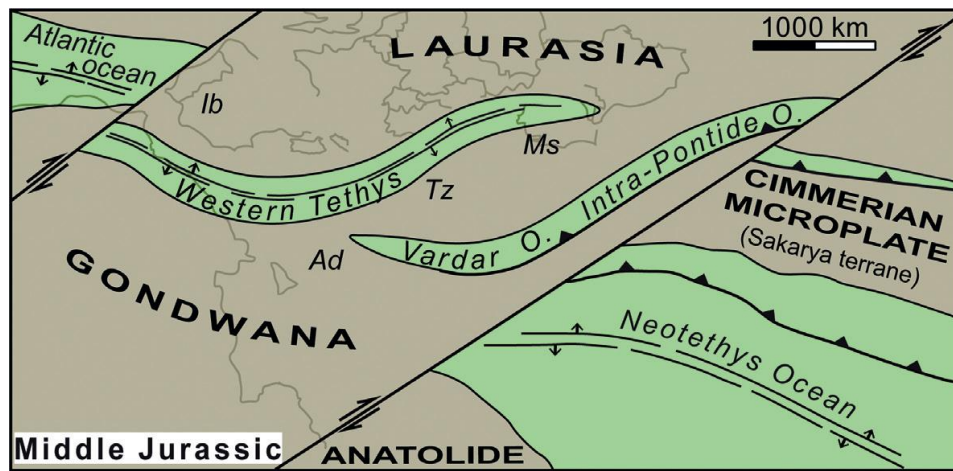


Figure 1-6: Middle Jurassic paleogeographical reconstruction of the Neotethys Ocean Ib: Iberia; Ad: Adria; Tz: Tizia; Ms: Moesia (taken from Marroni et al., 2014)

### 1.1.5. Problems related to generation within the Izmir-Ankara-Erzincan Branch of Neotethys

The suture of the northern Neotethyan Ocean with ophiolites and melanges was located between the Anatolide-Tauride Terrane (ATT) in the south and the SCT in the north (Göncüoğlu et al., 2000). They have been derived from a complex subduction-accretion system during the closure of the Neotethyan ocean (Şengör and Yılmaz, 1981; Okay and Şahintürk, 1997; Aldanmaz et al., 2008). The ages of these oceanic assemblages range from Late Triassic to Early Cretaceous (Tekin et al., 2002; Göncüoğlu et al., 2006; Dilek and Thy, 2006; Topuz et al., 2013), whereas the formation of the mélangé complexes were assigned to Late Cretaceous (Yılmaz et

al., 1997; Robertson and Ustaömer, 2006; Okay et al., 2006; Parlak et al., 2013; Robertson et al., 2014, Göncüoğlu et al., 2014). The geochemical characteristics of the oceanic lithologies indicate the presence of various tectonic settings such as mid-ocean ridge, oceanic island; island arc and back arc basin (Yalınız et al., 2000; Floyd et al., 2003; Göncüoğlu et al., 2006a, b; Aldanmaz et al., 2008; Parlak et al., 2013; Çimen et al., 2014). Lastly, their emplacements onto the Tauride-Anatolide margin has started at the beginning of Maastrichtian and continued until Early Eocene (Şengör and Yılmaz, 1981; Yılmaz et al., 1997; Floyd et al., 2000; Göncüoğlu et al., 2000).

This overall paleogeographic distribution and geodynamic models work well in the western part of the IPS. However, in the Central Pontide area, the SCT pinches out because of intensive strike-slip tectonics, so that a critical duplication occurs along a N-S traverse from the Black Sea to Ankara. This configuration impedes the lateral correlation of the main tectonic units of the CPSC. Therefore, the detailed evaluation of the regional scale structures and the boundaries of the studied units may shed light to the problem whether CMC and CP are products of the IPS or the Izmir-Ankara-Erzincan Ocean. In recent studies (e.g. Okay et al., 2013) only the name “Northern Neotethys” is used (Figure 1-7) without specifying which one.

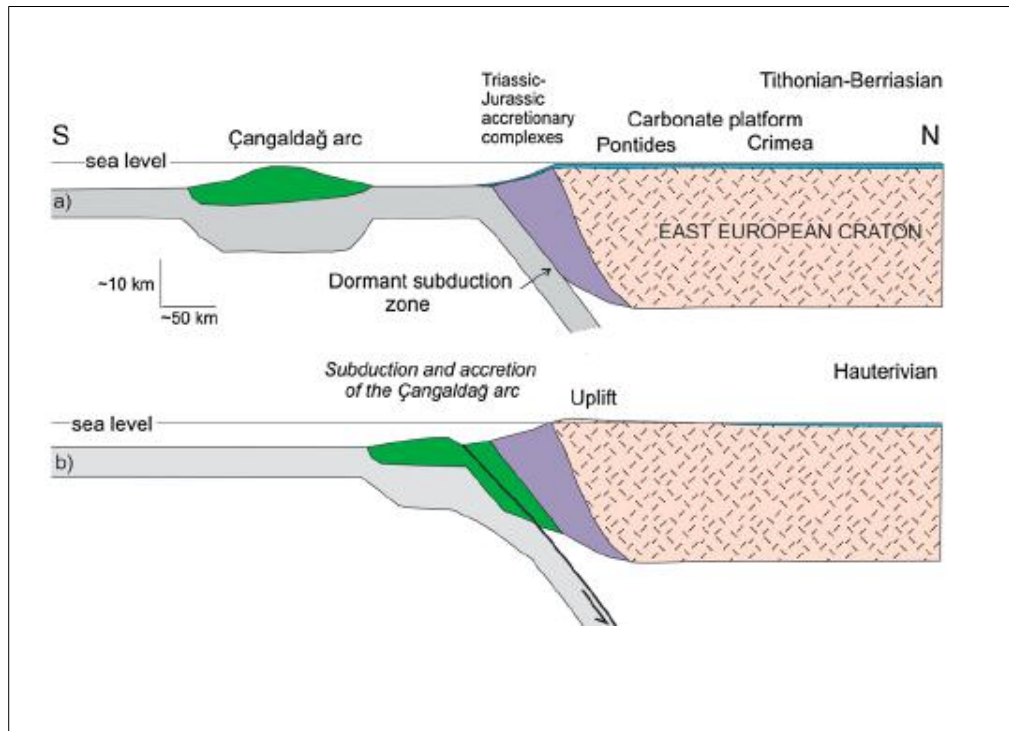


Figure 1-7: The paleogeographic positions of the Çangaldağ Metamorphic Complex during Late Jurassic-Early Cretaceous time (taken from Okay et al., 2013)

### 1.1.6. Purpose and Scope

The brief evaluation in the previous chapter demonstrates the presence of conflicting views and problems on the Central Pontides and CMC. By this, the detailed study of the CMC plays an important role to test the validity of the models (as mentioned in this chapter) which have been proposed by the previous researchers (Yılmaz, 1980, 1983; Tüysüz, 1985; Şengün et al., 1988; Yılmaz, 1988; Tüysüz, 1990; Ustaömer and Robertson, 1993, 1994, 1999; Uğuz and Sevin, 2007; Okay et al., 2006, 2013, 2014). These problems can be summarized as:

1- Is the CMC a meta-ophiolitic body related to the southernly Elekdağ meta-ophiolite?

- 2- Was the CMC formed as the result of arc volcanism developing in a pre-late Jurassic ocean (Paleotethyan)?
- 3- Is the CMC the conjugate of the Nilüfer Unit of the Karakaya Complex?

However, the most important goal of this study is to solve the current contradictions and problems by using detailed field (mapping, field relations, systematical sampling) and laboratory (petrographical, geochemical and geochronological) studies. After furthermore studies; the possible genesis and evolution of the metavolcanic rocks from the CMC and surrounding important units (e.g. CP) will be clearly understood which will definitely help to reconstruct a more accurate model for the study area. In addition to the CMC, the CP plays an important role in order to understand geodynamic evolution of the Central Pontides.

## **1.2. Geographic Location**

The CMC and CP, which are the subjects of this study, are located between the Devrekani and Taşköprü towns (Fig. 1-8; northeast of Kastamonu). The geographic coordinates of CMC are approximately  $41^{\circ}39'$  N and  $34^{\circ}09'$  E. The size of CMC is about  $600 \text{ km}^2$  (40 km long and 15 km wide) and it is located in E31: c3-c4; E32: c1-c2-d1-d2-d3-d4; E33: d1 (Kastamonu and Sinop) quadrangles of the 1:25.000 scaled topographic maps of Turkey.

The CP is located at northeast part of the CMC and the geographic coordinates are approximately  $41^{\circ}43'$  N and  $34^{\circ}12'$  E. The size of this pluton is about  $240 \text{ km}^2$  (30 km long and 8 km wide). It is mostly located in E32: c1-c2 quadrangles of the 1:25.000 scaled topographic maps of Turkey.

The study area is mostly covered by intense forests. There are many high and rugged hills in the study area. Therefore, it is really difficult to observe clearly the primary field relations of the units. There are more than 20 villages on the CMC and the

geological units can be observed through the roads of these villages. The distance between Ankara (the capital city of Turkey) and Kastamonu is about 260 km and it takes approximately 3 hours by driving.

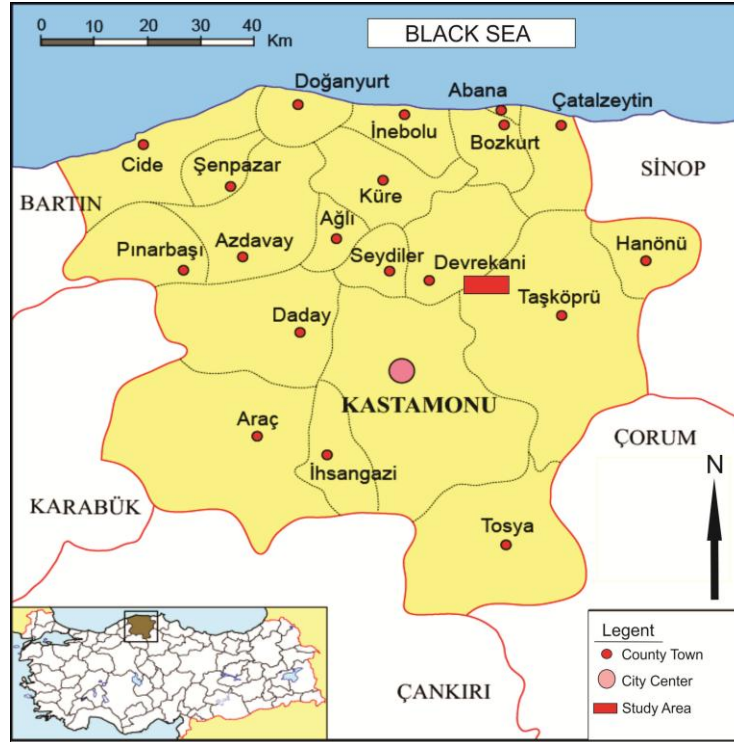


Figure 1-8: Location of the study area (modified from Saygılı, 2015)

### 1.3. Methods of Study

This study was mainly completed in two stages: a) Field Work and b) Laboratory Work

#### 1.3.1. Field Work

To solve the current problems on the field relations of the CMC, the available geological map (Konya et al., 1988) was modified, the distinct geological units were

identified, the relationships between lithostratigraphic units were determined and finally systematical sampling was realized along the three selected traverses. These traverses were selected from N to S due to distributions of the geological units and structural characteristics of the tectonic units (Fig. 2-4).

Approximately 200 samples were collected from the CMC during field studies. In addition to that, more than 50 samples were collected from the surrounding units (from the CP and Devrekani orthogneiss) in order to figure out the possible relations in the region. The Google Earth images and topographic maps were also used to observe the field characteristics of the CMC.

### **1.3.2. Laboratory Work**

The laboratory work comprises petrographic, geochemical, radiogenic isotope and radiometric dating studies;

- a) Approximately 150 thin sections were prepared from the selected rocks which had been collected along representative three traverses. These studies were performed at the laboratories of the Department of Geological Engineering in Middle East Technical University (METU, Turkey). The petrographic thin sections were examined and grouped by using transmitted light microscope at the same department. The images of thin section were taken by using analyzer image program at the Department of Civil and Environmental Engineering and Earth Sciences at the University of Notre Dame (ND), South Bend, Indiana, United States.
  
- b) 32 whole rock samples were selected for the geochemical analyses from the representative groups which had been identified based on the petrographical observations. Major and trace element concentrations were determined by Inductively Coupled Plasma-Optical Emission Spectrometer (ICP-OES) and

Inductively Coupled Plasma-Mass Spectrometer (ICP-MS), respectively, with lithium metaborate/tetraborate fusion and dilute nitric acid digestion methods at the Acme Analytical Laboratories (Canada). Also, some duplicated samples were analyzed in order to confirm the accuracy of the analyses.

- c) Mineral separation processes were conducted at the Department of Geological Engineering (Sample preparation and Mineral Separation Laboratory) in METU. Firstly, the rocks were crushed in a jaw crusher and sieved between 63 and 500 microns by using different sieves. After the samples reduced to a small grain size, the wilfley table was used in order to separate the more heavy fractions of the minerals. Subsequently, the heavy liquid process was performed to obtain the heavy minerals by using Bromoform. These heavy minerals were separated as magnetic and non-magnetic minerals using a Franz magnetic separator. The zircon crystals were hand-picked among the non-magnetic heavy minerals under the binocular microscope for the isotopic and geochronological analyses.
  
- d) The U-Pb radiometric dating was conducted on the zircon minerals in order to get geochronological data by using Multi Collector-Laser Ablation Inductively Coupled Plasma-Mass Spectrometer (MC-LA-ICP-MS) at the Midwest Isotope and Trace Element Research Analytical Center (MITERAC), University of Notre Dame (USA); (the detailed procedure and data are given in the Chapter 5 and Appendices E).
  
- e) The Hf isotopes were analyzed from the same zircon minerals at the MITERAC in the University of Notre Dame by using the MC-LA-ICP-MS; (the detailed procedure and data are given in the Chapter 5 and Appendices E).



## CHAPTER 2

### GEOLOGY

#### 2.1. Regional Geology

The Central Pontides has a complex geology with signatures of the Variscan, Cimmeride and Alpin events (Tüysüz, 1985; Yılmaz and Şengör, 1985; Tüysüz, 1990; Boztuğ, 1992; Ustaömer and Robertson, 1993, 1994; Aydın et al., 1995; Ustaömer and Robertson, 1999; Nzegge et al., 2006; Nzegge, 2008; Uğuz and Sevin, 2007; Okay et al., 2006, 2013, 2014, 2015; Göncüoğlu et al., 2008, 2012, 2014). This region comprises different terranes such as the Istanbul-Zonguldak Terrane (IZT), the Sakarya Composite Terrane (SCT (Fig. 1-1) and a subduction-accretion complex, known as the CPSC, representing the remnants of the IPS. From these, the IZT is a distinct unit with its typical non-metamorphic Palaeozoic successions overlying a Cadomian basement. The IZT is mainly located to the west and southwest of Central Pontides and overthrusts the SCT as well as the CPSC. The initial juxtaposition of CPSC and the SCT is of pre Middle Jurassic age. The recent configuration, however, is of post- Late Cretaceous/pre Eocene (Catanzariti et al., 2013).

In the Central Pontides area, on the other hand, the tectonic units Sivrikaya-Deliktaş, Geme, Devrekani and Küre resemble the SCT with their Variscan Basement-Karakaya mélangé pair. The Middle Jurassic CP and its counterparts intrude different parts of these tectonic units. Similar Variscan Terranes such as Kazdağ, Uludağ, Söğüt, Pulur and Hasdere massifs are found in the SCT and they are characterized by Late Carboniferous to Early Permian calc-alkaline magmatism (Göncüoğlu, 2010). The earliest common cover of these tectonic units and the Middle Jurassic intrusions is the Late Jurassic Bürnük and/or İnaltı formations (Okay et al., 2015). On the other hand, the CMC should be considered as a part of the CPSC, as it is one of the

elements of the IPS. Other members of the CPSC and hence the IPS are Daday, Saka, Emir, Domuzdağ, Aylıdağ and Arkotdağ units (Sayit et al., 2016; Frassi et al., 2016).

The tectonic units displaying different pre-Jurassic geological histories (Okay et al., 2014) have similar stratigraphic features after the Late Jurassic indicates the existence in the same depositional environment.

### **2.1.1. Istanbul-Zonguldak Terrane (IZT)**

This terrane displays a well-developed Paleozoic sequence (Fig. 2-1) from the Early Ordovician to the Late Carboniferous (including coal measures; Görür et al., 1997; Okay et al., 2015) which unconformably overlies the Neoproterozoic crystalline basement (Ustaömer et al., 2005; Göncüoğlu et al., 1997; Göncüoğlu, 2010). This crystalline basement is composed of accreted intra-oceanic island arc, oceanic and continental crust with signatures of Cadomian orogeny. The differences in Middle-Late Paleozoic successions suggest that the Istanbul and Zonguldak units were distinct terranes and attached at the end of the Permian. The Permian granitoids locally cut these Paleozoic units (Şahin et al., 2009; Okay et al., 2013). They were unconformably overlain by the Late Permian-Triassic red-beds and the Middle Jurassic lacustrine limestones (Okay et al., 2015). This succession is intruded by the Middle Jurassic granitoids (Yılmaz and Boztuğ, 1986). Lastly, the Upper Jurassic-Lower Cretaceous limestones and the Lower Cretaceous turbidites unconformably overlie this succession (Uğuz and Sevin, 2007).

The opening of the Black Sea has caused the deposition of the volcano-sedimentary rift sediments from the Berriasian to the Campanian (Görür, 1988; Derman, 1990). The Early Tertiary carbonates and clastics with volcanic intercalations cover both terranes (Göncüoğlu, 2010).

### **2.1.2. Sakarya Composite Terrane (SCT)**

Göncüoğlu et al. (1997) describes this unit as “Composite Terrane” due to the presence of several pre-Alpine terranes in its basement which have signatures of the different geological events (Fig. 1-1). This microcontinent was rifted off from the Gondwanian Tauride-Anatolide unit by southward subduction of the Paleotethyan ocean during the Early Carboniferous (Özcan et al., 1990; Göncüoğlu et al., 2000, 2007). It is considered as an Armonica type block together with the Greater and Lesser Caucasus and Strandja Massif which were accreted to the East European Platform during the Carboniferous (Okay and Nikishin, 2015). The rifting age of these Armorican terranes from the Gondwana is assumed as the Late Silurian (Stampfli and Borel, 2002). Geologically, this terrane consists of the Pre-Jurassic assemblages (Variscan Terranes and Cimmerian Terranes) and their Jurassic-Late Cretaceous cover units (Göncüoğlu, 2010). The Variscan Terranes are represented in the Central Pontides by several metamorphic massifs such as the Devrekani and Geme complexes (Okay et al., 2015) in the Central Pontides (Fig. 2-1).

This Devrekani unit is located between the Küre and CMC. It comprises medium to high grade metamorphic rocks such as gneiss, amphibolite and metacarbonates which have been metamorphosed under amphibolite and granulite facies (Yılmaz and Boztuğ, 1995; Boztuğ et al., 1995; Ustaömer and Robertson, 1999). The two different mappable units were differentiated in this metamorphic body such as the Gürleyik Gneiss and Başakpınar metacarbonates (Yılmaz, 1980). Yılmaz and Bonhomme (1991) suggested that the age of the Gürleyik Gneiss is approximately between Early and Middle Jurassic based upon the K-Ar mica and amphibole ages (149 Ma to 170 Ma). Later, the similar Jurassic metamorphism ages, 150 Ma and 156 Ma by using Ar-Ar method, have been confirmed by Okay et al. (2014) and Gücer et al. (2016), respectively. Moreover, Gücer and Arslan (2015) suggested that the protoliths of the amphibolites, orthogneisses (Permo-Carboniferous) and paragneisses are island-arc tholeiitic basalts, I-type calc-alkaline volcanic arc granitoids and clastic sediments (shale-wackestone), respectively. Recently, the

Devrekani metamorphic rocks have been interpreted as the products of Permo-Carboniferous continental arc magmatism overprinted by the Jurassic metamorphism in the northern Central Pontides (Gücer et al., 2016).

The significant geological and geochronological data about the Geme Complex has been given by Okay et al. (2014). It consists mostly of gneiss and migmatite with minor amphibolite, marble and cross-cutting granitic veins and stocks. This complex is intruded by the Middle Jurassic (163 Ma) Dikmen Porphyry and unconformably overlain by Lower Cretaceous sandstone and shale. This field relations indicate a pre-Callovian metamorphic age for this complex. The Central Pontides is characterized by a late Neoproterozoic and Hercynian basement and Geme Complex represents the remobilized basement of the Central Pontides based upon the zircon ages (Okay et al., 2014). Subsequently, the Cimmerian compound of the SCT is represented by the Karakaya Complex. It represents the subduction accretionary prism of the Paleotethyan Ocean and Triassic olistostroms with the Permo-Carboniferous limestone blocks (Okay and Göncüoğlu, 2004; Sayıt, 2010; Sayıt and Göncüoğlu, 2013).

In Central Pontides, the Karakaya Complex is represented by the Küre Complex, Geologically, Ustaömer and Robertson (1999) has defined the Küre Complex as dismembered ophiolite bearing thrust-imbricated deep-sea sediments. The ophiolitic rocks include serpentized harzburgite, massive gabbro, sheeted dykes and basic volcanics. According to the Kozur et al. (2000); this complex comprises three main tectonostratigraphic units which are Küre Ridge Unit (low grade metamorphics, a Lower and Middle Triassic shallow water sequence, Küre Ocean Unit (siliciclastic turbidites and olistostromes, Middle Jurassic molasse type shallow-water sandstone, siltstone and shale, thick oceanic basalt and ophiolite) and Çalca Unit (Pelsonian to upper Norian Hallstat Limestone and Lower Jurassic deep-water shale and marl).

The Mesozoic cover of the SCT in the west comprises a Lower Jurassic basal conglomerate followed first by middle Jurassic neritic carbonates, and then by Upper Jurassic-Lower Cretaceous slope-type carbonates (Soğukçam Limestone) and Late Cretaceous turbidites and ophiolite-bearing units.

In the Central Pontides, the oldest cover units of the SCT are the Upper Jurassic Bürnük clastics and Inaltı Limestone (Okay et al., 2014, 2015; Fig 2-1). These sedimentary units also cover the IZT and its primary contact with the SCT.

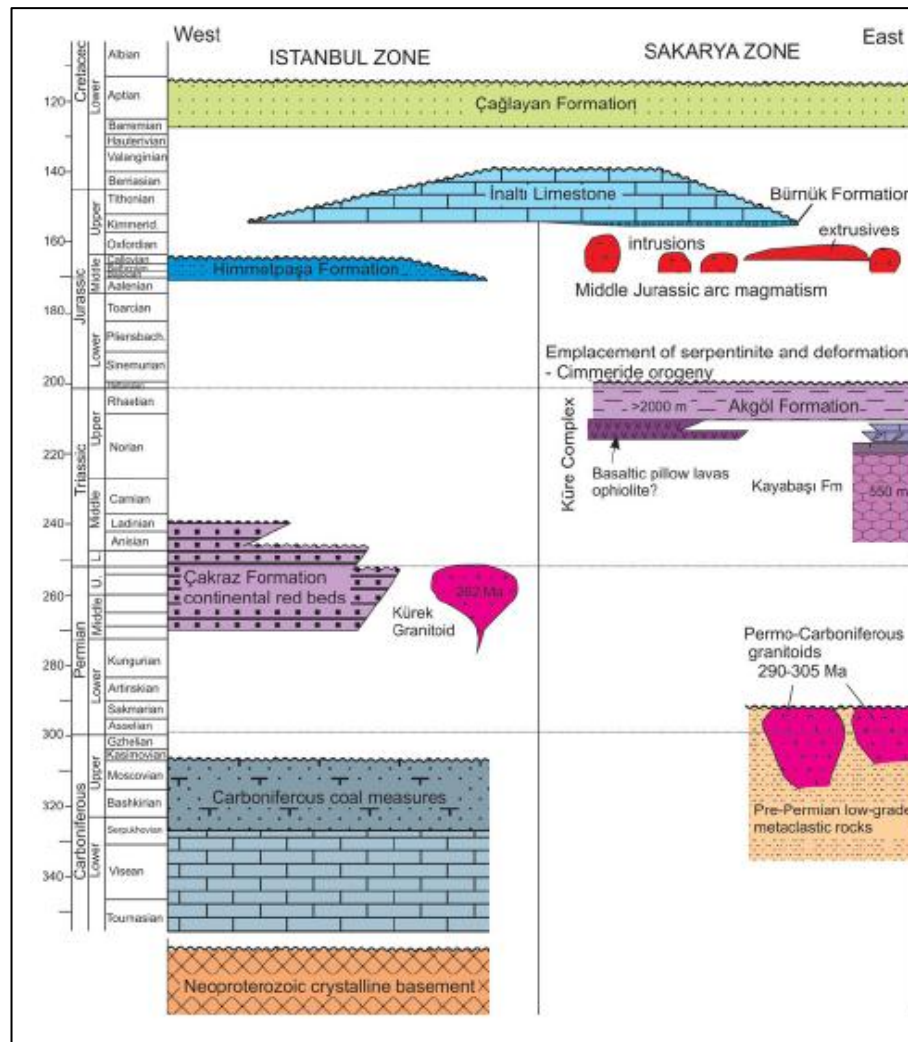


Figure 2-1: The stratigraphic section of the Istanbul and Sakarya Zones in the Central Pontides (taken from Okay et al., 2014).

The last unit of the SCT in the Central Pontides is the Çangaldağ Pluton, which is one of the topics of the present thesis and will be evaluated in the following chapters. A brief account based on previous data (Yılmaz and Boztuğ, 1986; Aydın et al., 1995) suggests that CP intrudes all members of the SCT and is Middle Jurassic in age, based on geological constraints. The oldest cover of the CP and its contact with the SCT units is the Lower Cretaceous (Barremian) Çağlayan Formation (Konya et al., 1988; Uğuz and Sevin, 2007).

### 2.1.3. Tectonic units of the Central Pontide Structural Complex

The CPSC consists of the several tectonic units (Figs. 2-2, 2-3). The nomenclature used for these tectonic units differs in previous studies (e.g. Ustaömer and Robertson, 1999; Okay et al., 2006, 2013, Göncüoğlu et al. 2012, 2014; Marroni et al, 2014; Sayıt et al, 2016). In this thesis we will mainly follow the nomenclature of Sayıt et al. (2016) and Frassi et al. (2016).

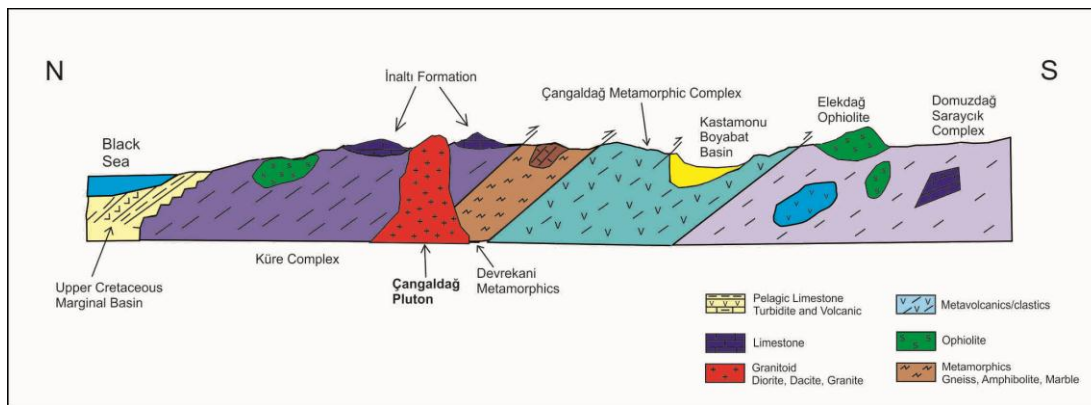


Figure 2-2: Simplified cross section of the Central Pontides (modified from Ustaömer and Robertson, 1999).

### **2.1.3.1. Çangaldağ Metamorphic Complex (CMC)**

The CMC is located between the Devrekani and Taşköprü towns (northeast of Kastamonu, Central Pontides). Okay et al. (2006) regarded this complex as a pre-Jurassic metabasite-phyllite-marble unit that forms several crustal-scale tectonic slices in the north and south. Ustaömer and Robertson (1999) described the complex as a structurally thickened pile of mainly volcanic rocks and subordinate volcanoclastic sedimentary rocks that overlie a basement of sheeted dykes in the north and basic extrusives in the south. The complex was also considered as a meta-ophiolitic body by several authors (Yılmaz, 1980, 1983; Yılmaz and Tüysüz, 1984; Şengün et al., 1988; Tüysüz, 1985, 1990; Boztuğ and Yılmaz, 1995).

In the previous studies, the Middle Jurassic (153 Ma) and Early Cretaceous metamorphic (126-110 Ma) ages were assigned for the metabasic rocks and phyllites, respectively (Yılmaz and Bonhomme, 1991) by using mineral K-Ar methods. These Early Cretaceous metamorphic ages have also been confirmed by Okay et al. (2013) for the complex based upon the Ar-Ar mica dating of phyllite samples (136 and 125 Ma). Recently, a single radiometric age finding for the protolith of the CMC (U-Pb zircon dating from a metadacite sample) indicating a Middle Jurassic age was reported (Okay et al., 2014). Our preliminary radiometric data (in-situ U-Pb dating of many zircon grains from several metadacites) confirm the Middle Jurassic magmatic ages (Çimen et al., 2016a).

### **2.1.3.2. Domuz Dağ Unit**

Okay et al. (2006) describes the Domuzdağ Complex as a north-west dipping crustal slice that is extending in a north-east and south-west direction. Tectonically, the Permo-Triassic metabasite - phyllite and slightly metamorphosed Cretaceous flysch overly this complex in the north and west, respectively. A Late Cretaceous foreland basin and the Kargı Complex are overlain by this complex in the south (Okay et al.,

2006). The Domuzdağ-Saraycık Complex, metamorphosed under blueschist facies, is mostly composed of metabasite, serpentinite and sedimentary rocks (Ustaömer and Robertson, 1999). The metamorphism age of this unit has been determined as Early Cretaceous (105 Ma) by using Ar-Ar dating method (Okay et al., 2006). Later, Sayıt et al. (2016) has used the name Domuzdağ Unit with a broader sense according to the distributions of marbles, micaschist and amphibolites in the study area. The Domuzdağ Unit displays polyphase deformation signatures that are similar to those of the Saka Unit. The last three deformational phases exhibit characteristics of the retrograde metamorphism ranging from greenschist to very low grade metamorphism conditions (Sayıt et al., 2016). The thickness of this unit is approximately 800-1200 m (Frassi et al., 2016). The geochemical data from amphibolites provide E-MORB, OIB, BABB and IAT-type signatures (Sayıt et al., 2016). Overall tectono-metamorphic characteristics of the Domuzdağ Unit indicate that it could have formed as a subduction-related tectonic *mélange* (Okay et al., 2006, 2013; Sayıt et al., 2016; Frassi et al., 2016).

### **2.1.3.3. Emirköy Unit**

This unit is described by Sayıt et al. (2016) as a monotonous succession of metaturbidites represented by alternation of fine grained metasandstones, metasiltsstones and metapelites. The thickness of this unit is approximately 300-400 m (Frassi et al., 2016). It partially resembles the turbidite dominated Martin Complex of Okay et al. (2013) but has a lower grade metamorphism (Sayıt et al., 2016). Therefore, this unit could be deformed and slightly metamorphosed part of the Çağlayan Formation. However, it does not include any magmatic rocks which are common in the Çağlayan Formation (Sayıt et al., 2016). Additionally, the polyphase (three different deformational phases) deformation history could be observed in the Emirköy Unit (Sayıt et al., 2016).

#### **2.1.3.4. Aylı Dağ Unit**

Aylı Dağ Unit corresponds to the Kirazbaşı Complex of Aygül et al. (2015). This unit mostly consists of slices of serpentized peridotites, dunites and pyroxenites (Sayıt et al., 2016). Also, Göncüoğlu et al. (2012) has described a more extensive ophiolite sequence in the south of Siragözü village in the Aylı Dağ area. The lower part of this sequence is composed of peridotites (less than 3 km), layered gabbros (approximately 500-600 m) alternating with spinel bearing dunites, melatroctolites, troctolites, ol-gabbros and leucogabbros (Sayıt et al., 2016). This thick gabbro sequence is followed by a sheeted dyke complex that is overlain by massive basaltic lava flows (100-200 m). Finally, the massive and pillow lavas and breccias alternating with ophiolite-bearing arenites and cherts (600-800 m) overlies this succession. From the Middle Bathonian to Callovian ages have been obtained from the radiolarian cherts (Sayıt et al., 2016). The oceanic assemblages of this unit represent the fragments of back arc type oceanic lithosphere (Göncüoğlu et al., 2012, 2014; Sayıt et al., 2016, Frassi et al., 2016).

#### **2.1.3.5. Arkot Dağ Unit**

The Arkot Dağ Unit is composed of slide blocks within a sedimentary matrix that is resperented by shales, coarse grained arenites, pebbly-mudstones and pebbly-sandstones (Göncüoğlu et al., 2014; Sayıt et al., 2016). The amount of this matrix is mostly less than that of the slide blocks and it is locally completely absent (Sayıt et al., 2016). The size of these slide blocks ranging from few meters to several hundred square meters and they include sedimentary, metamorphic and ophiolite rocks (Sayıt et al., 2016). It consists Late Jurassic to Early Cretaceous neritic and pelagic limestones, dolostones, Late Cretaceous marly-limestones and ophiolite-bearing arenites, gneisses and micaschists (Sayıt et al., 2016). These units are thrust over the sedimentary cover of SCT whose top is represented by Late Cretaceous-Middle Paleocene Taraklı Flysch (Catanzariti et al., 2013; Göncüoğlu et al., 2014). The

Arkot Dağ Unit could have been derived as an imbricate stack of deformed and metamorphosed oceanic and continental-derived slices (Göncüoğlu et al., 2014). The age of this unit could be accepted as the Late Santonian based on the nannofossil data from some soft clasts of marls (Sayıt et al., 2016).

#### **2.1.3.6. Saka Unit**

According to the Okay et al. (2013); the large amount (about 80%) of the Saka Complex consists of micaschists and the rest includes marble, calc-schist, metabasite and small serpentine slivers. It crops out mostly in the Daday Massif. Geochronologically, the Middle Jurassic cooling ages have been determined from the micaschists by using single grain Ar-Ar dating method (Okay et al., 2013). Then, the name Saka Unit has been used by Sayıt et al. (2016). According to this study, it is always sandwiched between Arkot Dağ Melange and the Daday Unit. The thickness of this unit is not higher than 300 m and it is characterized by garnet-bearing amphibolites, coarse grained banded amphibolites, garnet bearing micaschist and coarse grained impure marble (Sayıt et al., 2016). Also, the Saka Unit has the polyphase deformation history which developed under decreasing P and T conditions (Sayıt et al., 2016). The garnet bearing amphibolites provide the Late Jurassic age (163 Ma, Ar-Ar dating; Marroni et al., 2014). Moreover, they display the signatures of retrograde metamorphism ranging from greenschist to sub-greenschist facies conditions (Marroni et al., 2014).

#### **2.1.3.7. Daday Unit**

This unit (Kargı Complex of Okay et al., 2006) includes the slices of fine grained actinolite bearing schists, fine grained marbles, paragneiss, mica bearing schists and black quartzites (Sayıt et al., 2016). The age of this unit has been assigned as Early Cretaceous (between 102 and 112 Ma; using Ar-Ar dating method) by Okay et al.

(2013). Around the Tuzaklı Dam, it partially corresponds to the Martin, Esenler and Domuzdağ Complexes of Okay et al. (2013) and Esenler unit of Aygül et al. (2015), characterized by a succession of sandstones, shales, limestones and lydites associated with mafic rocks (Sayıt et al., 2016). The thickness of this unit is approximately 400-500 m (Frassi et al., 2016). Geochemically, the actinolite-bearing schist exhibit E-MORB, OIB, BABB and IAT signatures (Sayıt et al., 2016; Frassi et al., 2016). Moreover, the Daday Unit displays a similar deformation history with the Saka and Domuzdağ Units which indicates the presence of retrograde P and T metamorphic conditions ranging from blueschist to sub-greenschist (Sayıt et al., 2016).

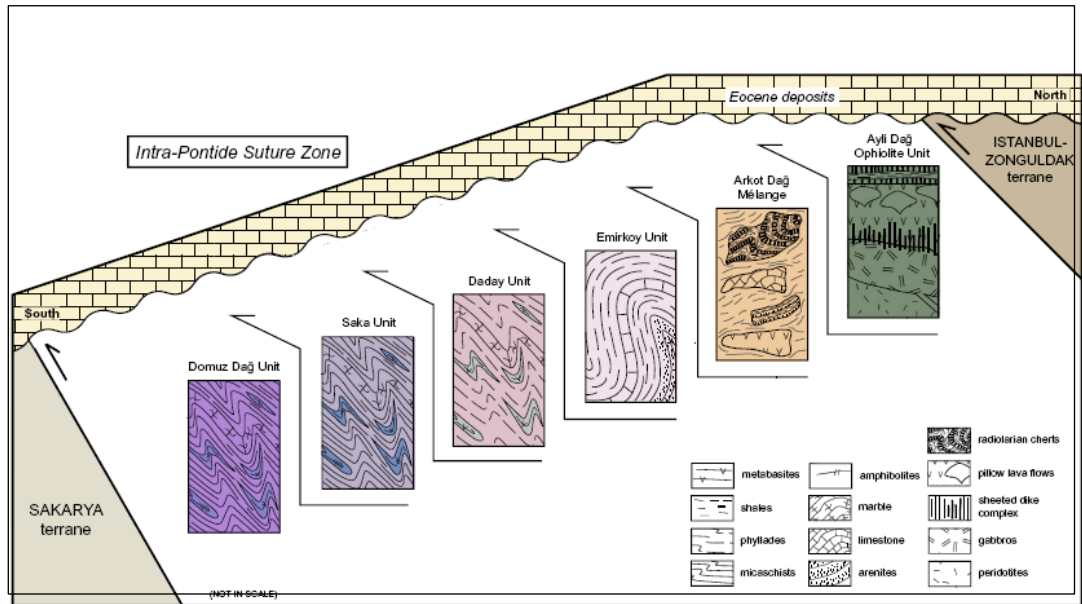


Figure 2-3: Sketch of the stratigraphy of the tectonic units within the Central Pontide Structural Complex (taken from Sayıt et al., 2016)

## 2.2. Local Geology

The field observations on the local geological units (CMC, CP, Devrekani Units and Younger Cover Units) will be explained in this part.

### 2.2.1. Çangaldağ Metamorphic Complex (CMC)

The CMC is tectonically located between the Devrekani Metamorphics and Domuz Dağ Unit (Fig. 2-2). It covers approximately area of 600 km<sup>2</sup>. The sedimentary units of the Taşköprü-Boyabat Basin unconformably overlie the southern boundary of this metamorphic complex. It is overthrust by the Devrekani Metamorphics in the northwest. The Çağlayan Formation is the oldest cover unit (Fig. 2-4). Yılmaz and Boztuğ (1986) and Aydın et al. (1995) report that CMC is intruded by the Çangaldağ Pluton. However, it is observed that the northern contact of the unit is a regional-scale steep fault with strike-slip component.

Overall, the CMC comprises a number of NW-dipping thrust planes separating different rock-packages of low-grade metamorphic rocks dominated by metavolcanics and volcanoclastics in the west and metasediments and volcanoclastic rocks in the east. The foliation planes dip in general to NW.

To figure out the possible field relations, three north-south cross sections have been prepared (Fig. 2-5). In these cross sections, most of the primary contact relations between the main tectonic units are thrusts or strike slip faults that display the signatures of polyphase deformation including a compressional and a strike-slip system (Fig. 2-5).

Considering the rock types, the CMC is mostly composed of metavolcanic, metavolcaniclastics and metaclastic/carbonate rocks. The metavolcanic rocks comprise mafic, intermediate and felsic phases. Metavolcanic rocks are characterized by schistose textures and only locally ghost dyke or pillowed structures are preserved. The volcanic protolith is mainly recognized by blastoporphyratic textures. Differences in color and structures are the only features to map different lithological units.

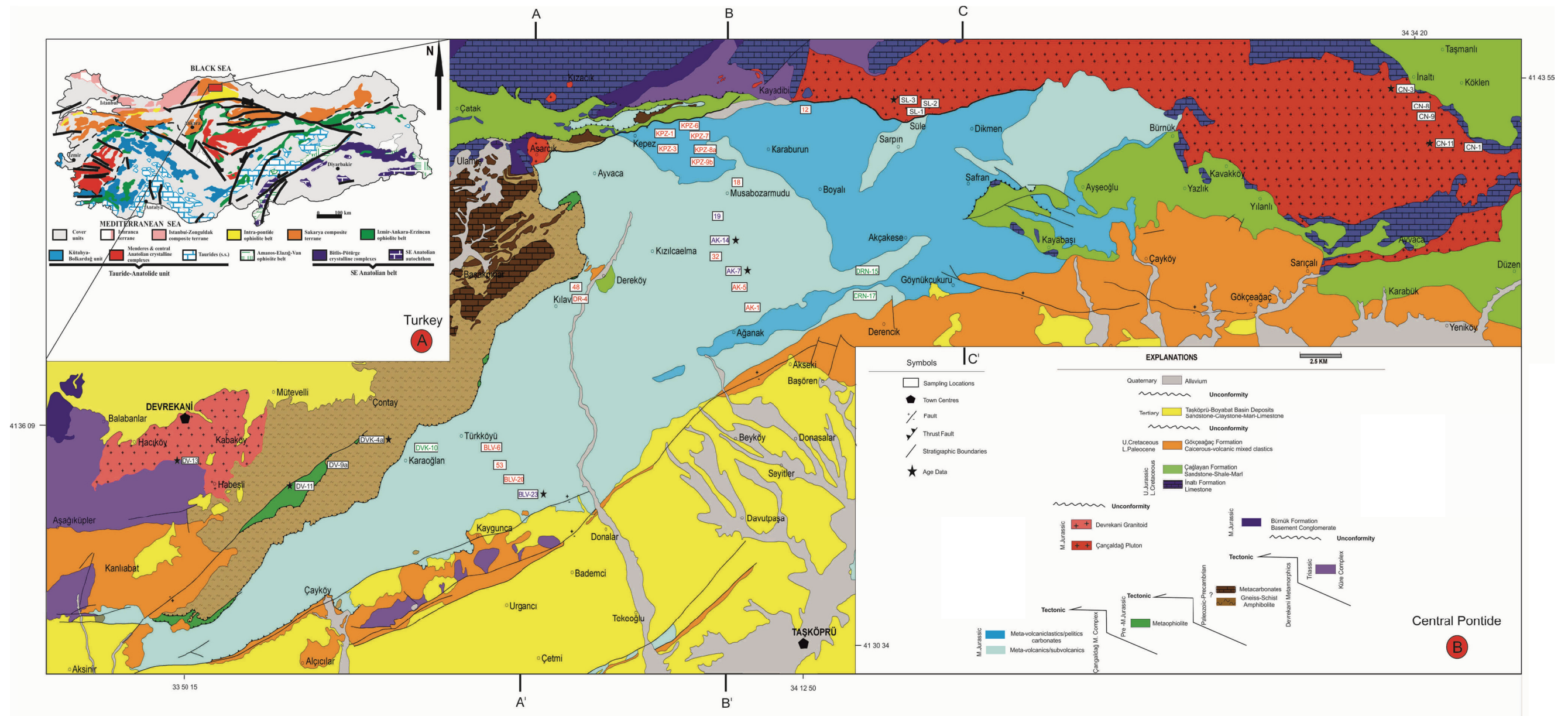


Figure 2-4: a. Distribution of the main alpine terranes in central North Anatolia (modified from Göncüoğlu, 2010) b. Geological map of the study area (modified from Konya et al., 1988). Blue samples: metarhyodacites, green samples: metaandesites; red samples: metabasalts/diabases (just analyzed samples).



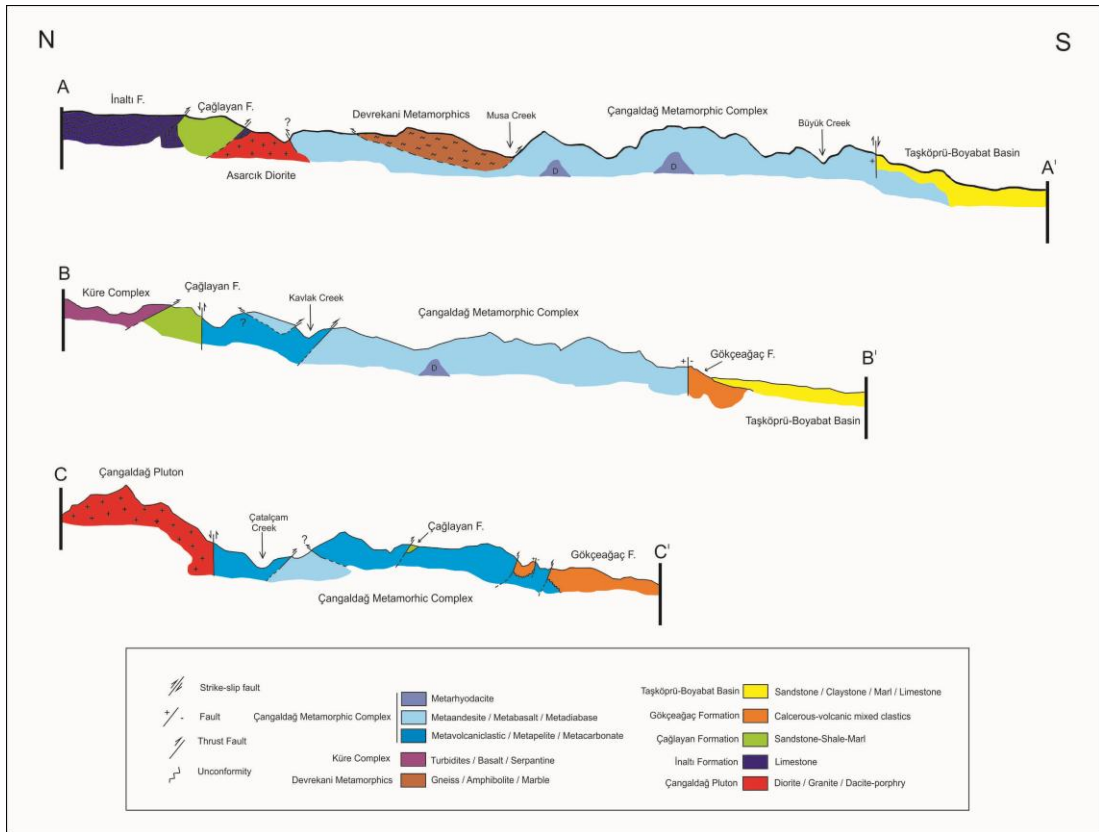


Figure 2-5: Simplified cross sections of the Çangaldağ Metamorphic Complex (modified from Konya et al., 1988).

### 2.2.1.1. Metaclastics/carbonates and Metavolcaniclastics

The metaclastic rocks consist of pelitic schists in the study area. They are highly deformed and have well-developed schistosity planes (Fig. 2-6). Some of them display crenulation cleavages in macroscale which indicate the presence of the different deformation processes (Fig. 2-7). The effect of deformation can be seen in macro-scale.

Mineralogically, the quartz and mica minerals can be identified in handspecimens. Particularly, the orientation of the phyllosilicate minerals can be clearly traced on the surface of these rocks. These pelitic schists were mostly determined in the northeast part of the study area (around of the Karaburun and Boyalı villages; Fig. 2-4).

They can be easily identified by their lighter colors (white and gray, dark shades) and shiny surfaces in the field. In addition, most of them have well-developed foliation planes and small folds (Figs. 2-6, 2-7) which support the effects of different deformation processes. Also, some metacarbonates (calc-schist) were identified within the metaclastic rocks at the south of Süle village (Fig. 2-4). They have approximately 5 cm thicknesses and found within the pelitic schists (Fig. 2-8). No fossils were found within the metacarbonates due to the effect of deformation and metamorphism. The metavolcaniclastic rocks include mainly the tuffaceous materials which are mostly products of the basic-intermediate volcanism. They are greenish in color due to the presence of secondary mineral assemblages such as epidote, actinolite and chlorite (Figs. 2-9, 2-10). Also, they mostly show well-developed foliation and small-scale folding (Fig. 2-11).



Figure 2-6: Field view of the foliated metaclastic rocks (pelitic schist) within the Çangaldağ Metamorphic Complex. Muscovite-rich parts are easily distinguished with their lighter colors from the biotite-rich darker parts. Both types display very nice foliation planes and microstructures.

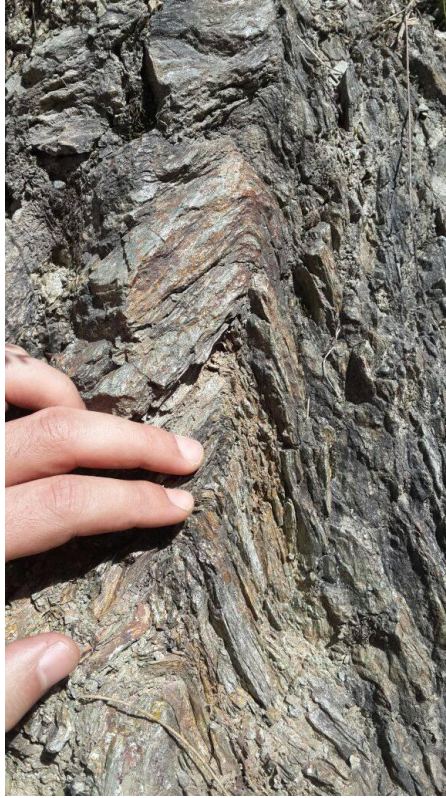


Figure 2-7: Field view of the small foldings on the metaclastic rocks (pelitic schist) within the Çangaldağ Metamorphic Complex. They display multi-deformation signatures.



Figure 2-8: Field view of the foliated metacarbonate rocks (calc-schist) within the Çangaldağ Metamorphic Complex. They have approximately 5 cm thicknesses and found with the pelitic schists.



Figure 2-9: Field view of the metavolcaniclastic rocks within the Çangaldağ Metamorphic Complex.



Figure 2-10: Field view of the foliated metatuffs within the Çangaldağ Metamorphic Complex. They are mostly found with other metavolcaniclastic rocks and could be distinguished with very fine grained matrix.



Figure 2-11: a. Image of the small folding within an olistostromal black shale unit rocks within the Çangaldağ Complex. They show complex multi-deformational structures in small scale. b. Image of the small foldings from the metavolcaniclastic rocks within the Çangaldağ Complex. They exhibit complex multi-deformation structures in small scale.

#### 2.2.1.2. Metavolcanic rocks

Three different metavolcanic phases were determined during the field studies. They are metabasic, metaintermadiate and metafelsic rocks, the first two being the major types. The basalts, basaltic andesites, andesites and rhyo-dacites are the volcanic and subvolcanic products of these magmatic phases. In addition to these types, the meta-

diabase dykes and pillow lavas were also locally found in the north-west of the CMC (Fig. 2-4; around of the Karaođlan village).

The felsic metavolcanic rocks are mostly found near Musabozarmudu village (approximately in the central region of the study area; Fig. 2-4). In the field, these metavolcanic rocks are more resistant and have sharp outcrops. On the other side, the metaclastics and metavolcaniclastic rocks display more smooth surfaces due to the secondary alteration processes. In terms of the metavolcanic rocks, there are both foliated and non-foliated types within the complex (Figs. 2-12, 2-13). The grade of deformation is variable on these rocks. Also, some of these foliated metavolcanic rocks can show small folds, as in the metaclastics and metavolcaniclastics, which suggest the presence of different deformation processes during the evolution of this metamorphic complex. In some cases, the carbonate-rich boudens are observed within the metabasic rocks (Fig. 2-14). Also, some metabasic rocks include significant pyrite and chalcopyrite minerals which are responsible from the Cu-mineralization within the CMC (Fig. 2-15). The metaandesites and metarhyodacites can be distinguished by their lighter colors in the field (Figs. 2-16, 2-17). In particular, some metarhyodacites can contain mafic enclaves which might be involved during the felsic magmatism within the CMC (Fig. 2-18).

The field relationship between the metavolcanic and metaclastic rocks is tectonic (thrust) that could be seen in some locations (Figs. 2-19, 2-20, 2-21). However, all of these units are cut by the felsic volcanic rocks (metarhyodacites) in different localities (for instance, south of the Musabozarmudu village; Figs. 2-4, 2-22, 2-23, 2-24). Some of these primary contact relations have been masked by tectonic activities under the effect of the compressional regime after the magmatism (Fig. 2-24). The significant cutting relation reveals that the metarhyodacite rocks are relatively younger than the other units within the CMC. In particular, the age of these metarhyodacites play an important role in order to determine the relative age of the other metavolcanic rocks in the study area.

The contact of different types of CMC to CP is tectonic as well. There is a regional-scale strike slip fault between these units (Fig. 2-4, 2-25). Moreover, some younger non-metamorphic dykes which cut the CMC at different localities were identified during the field studies (Figs. 2-26, 2-27). They display completely different petrographical characteristics than the volcanic rocks of the CMC and they should be related to a later magmatic activity.

The presence of the greenschist facies minerals indicates that the members of this complex have undergone the same metamorphism event. Most of the meta-basic and intermediate volcanic rocks exhibit the characteristics of the greenschist facies including epidote, actinolite and chlorite as the metamorphic minerals. The color of these metavolcanic rocks is greenish as well due to the development of this secondary mineral paragenesis. The primary mineral assemblages cannot be observed in hand specimen size because of the metamorphism and alteration. Although there are foliated and non-foliated basic metavolcanic rocks, the mineral paragenesis of the typical greenschist facies can be observed on the both meta-basic and intermediate rock types. While the foliated rocks display the effects of ductile deformation (Fig. 2-12), the non-foliated volcanic rocks could have preserved their original massive textures. On the other hand, the felsic rocks (metarhyodacite) exhibit white and slightly brownish colors in the field. They have highly altered surfaces. Macroscopically, the presence of quartz grains helps to identify these rocks in the field.



Figure 2-12: Field view of the foliated metabasic rocks (metabasalts) within the Çangaldağ Metamorphic Complex.



Figure 2-13: Field view of the metavolcanic breccia (metabasalts). Note the relict vesicular texture of the clasts.



Figure 2-14: Field view of the foliated metabasic rocks (metabasalts) within the Çangaldağ Metamorphic Complex where white lensoidal parts are carbonates.

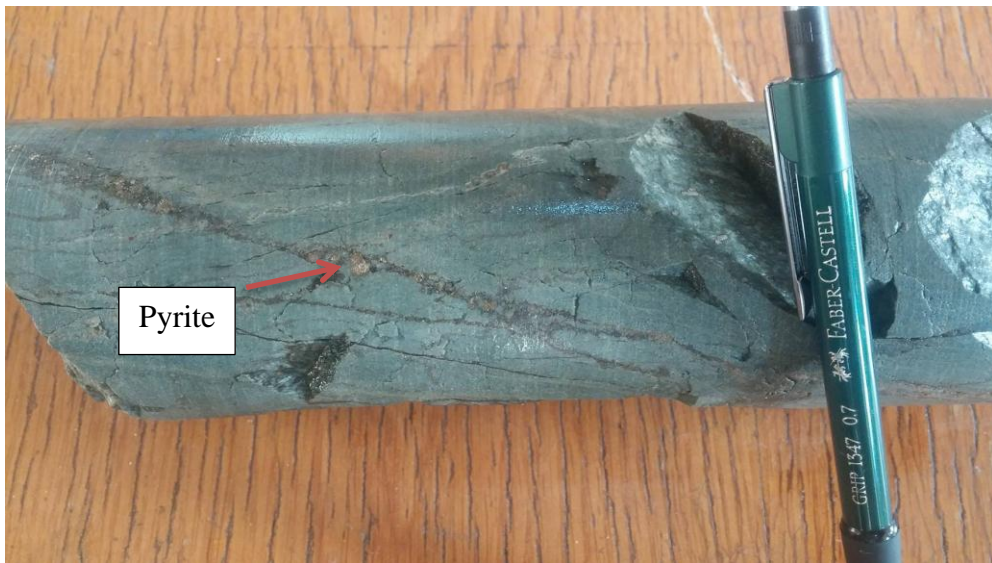


Figure 2-15: Image of the pyrite and chalcopyrite minerals within the metavolcanic rocks.



Figure 2-16: Field view of the metaintermediate rocks (metaandesites) within the Çangaldağ Metamorphic Complex. They have lighter colors than metabasic rocks and found as non-foliated or foliated types in the field.

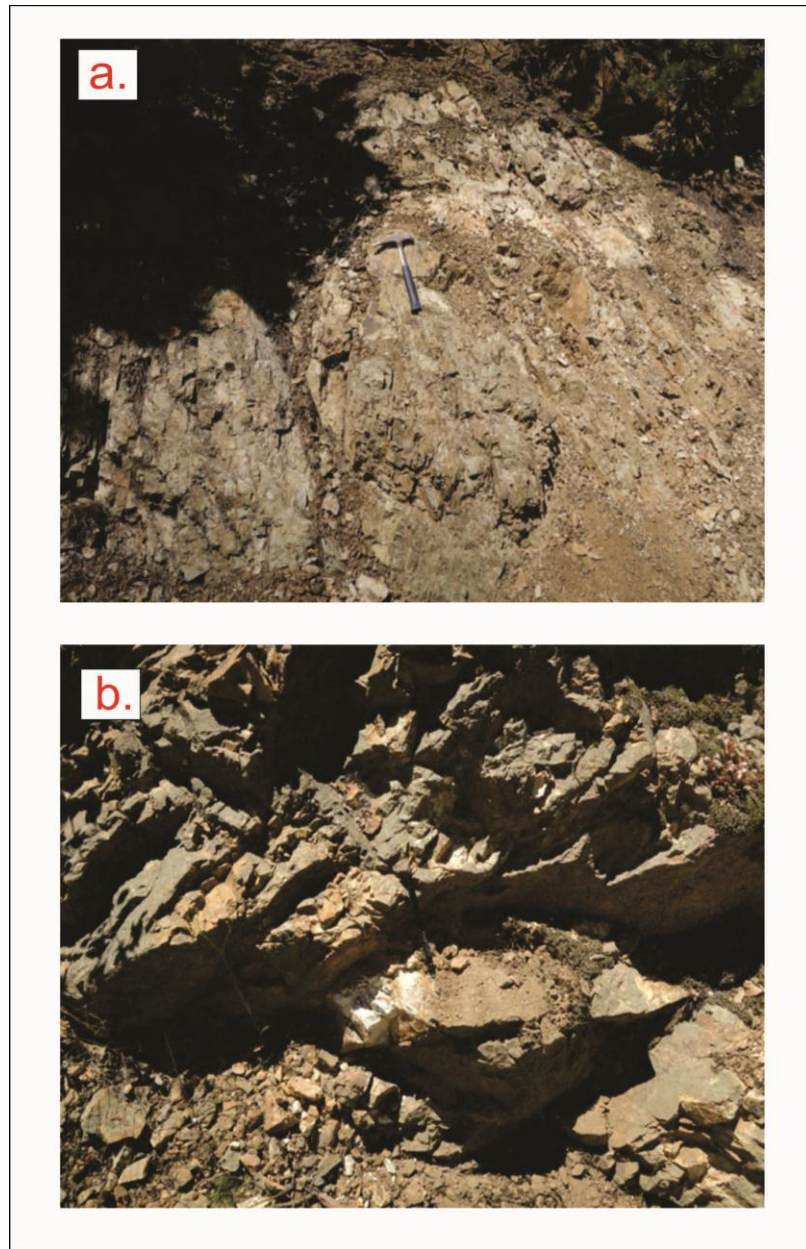


Figure 2-17: a. Field view of the altered metafelsic (metarhyodacite) rocks within the Çangaldağ Metamorphic Complex. They have whitish colors in the field. The mafic products are cut by these felsic rocks. b. Another field view of altered metarhyodacite.



Figure 2-18: Field view of the metafelsic rocks (metarhyodacite) including metabasic enclaves within the Çangaldağ Metamorphic Complex.

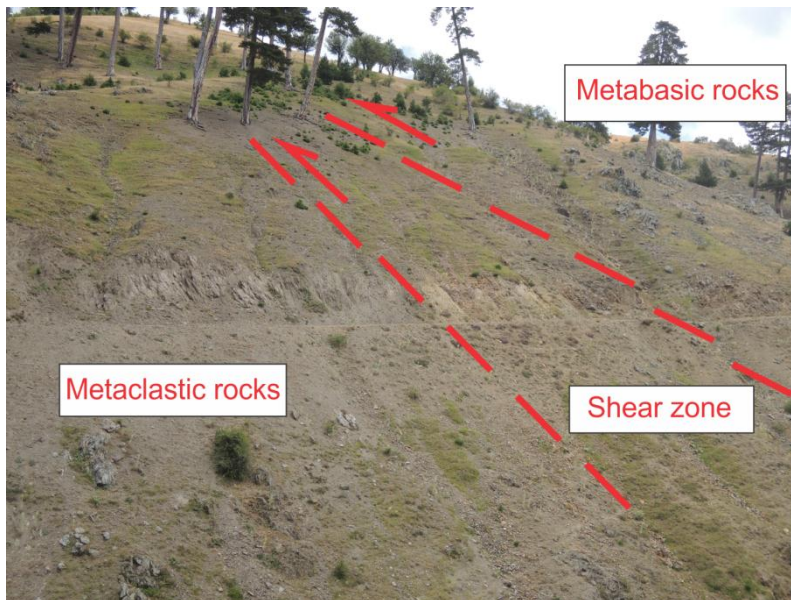


Figure 2-19: Field view of the contact relation between metaclastic and metavolcanic rocks within the Çangaldağ Metamorphic Complex. Mostly, metavolcanic rocks are thrust onto the metaclastic rocks. The primary relations are masked by secondary intense tectonic activities.

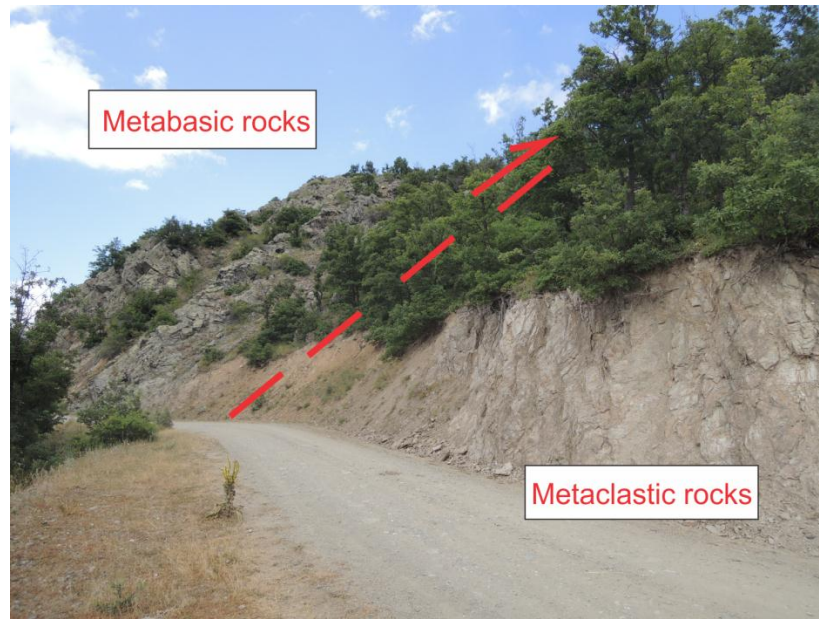


Figure 2-20: Field view of the contact relation between metaclastic and metavolcanic rocks within the Çangaldağ Metamorphic Complex. The metavolcanic rocks are mostly thrust onto the metaclastic rocks.

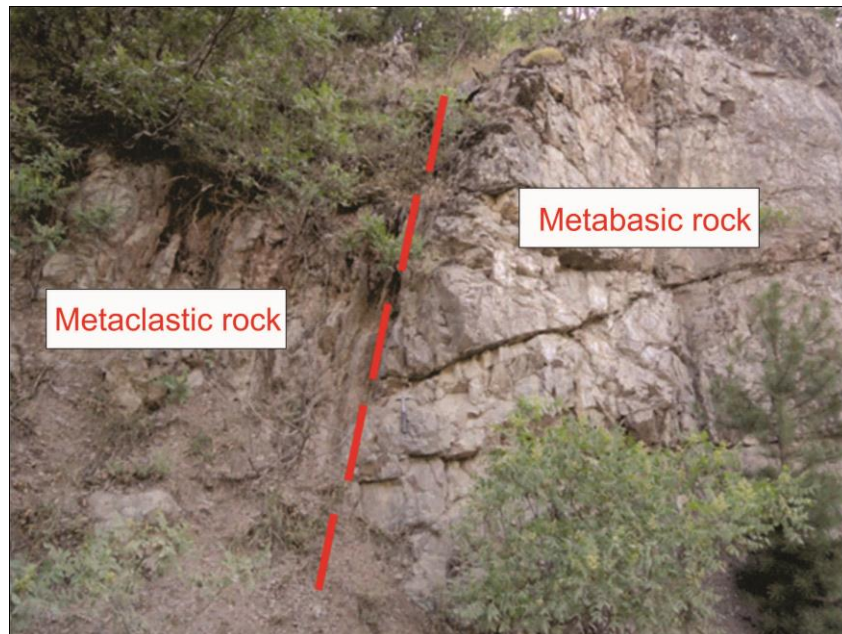


Figure 2-21: Field view of the tectonic contact relation between metaclastic and metavolcanic rocks within the Çangaldağ Metamorphic Complex.

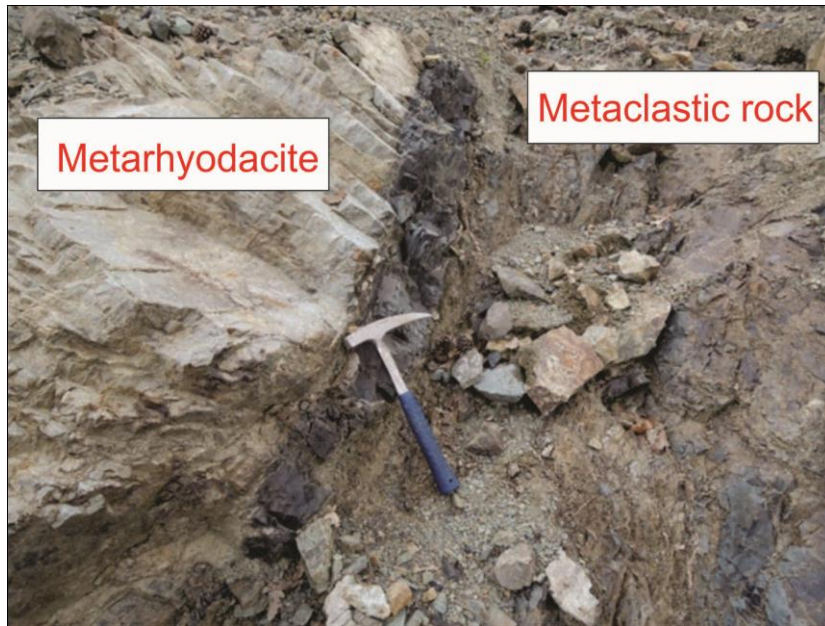


Figure 2-22: Field view of the cross-cutting relation between a metarhyodacite and metaclastic rock within the Çangaldağ Metamorphic Complex. Dark colored part at the contact is the hornfelsic contact zone. The other units including metavolcanics, metavolcaniclastics and metaclastics are cut by these felsic rocks.



Figure 2-23: Field view of the cross-cutting relation between a metarhyodacite and metabasic rock within the Çangaldağ Metamorphic Complex.

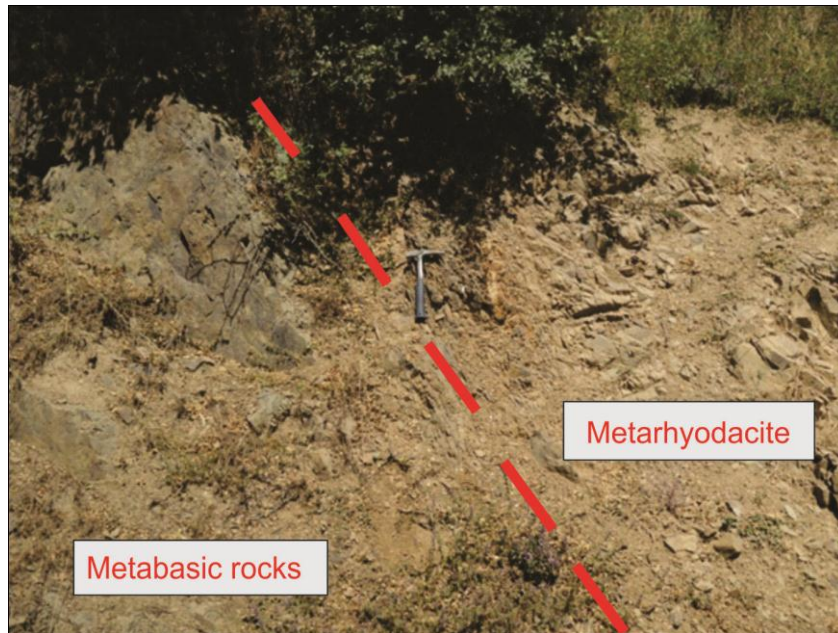


Figure 2-24: Field view of the tectonic contact relation between a metarhyodacite and metabasic rock within the Çangaldağ Metamorphic Complex.

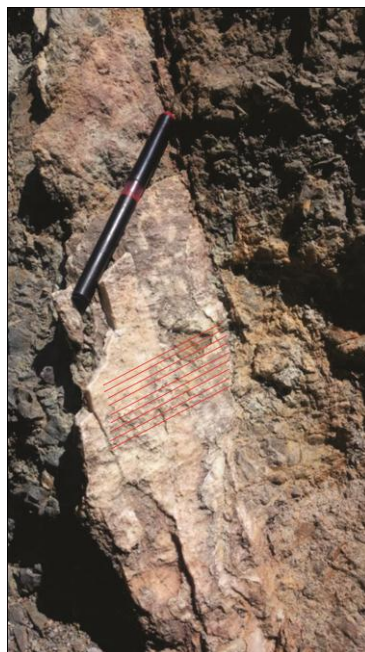


Figure 2-25: Field view of the slickensides (strike-slip: N80E, 68SE) within a shear zone between Çangaldağ Metamorphic Complex and Çangaldağ Pluton. There is a regional strike-slip fault between these units.



Figure 2-26: Field view of the cutting relation between a felsic intrusion and metaclastic rocks within the Çangaldağ Metamorphic Complex. The primary relation is erased by overprinting mylonitic deformation.



Figure 2-27: Field view of the cutting relation between a felsic intrusion and metabasic rocks within the Çangaldağ Metamorphic Complex. They show different petrographical characteristics than metavolcanic rocks of the CMC. They belong to a later magmatic event.

### **2.2.2. Çangaldağ Pluton (CP)**

Three different rock groups were determined within the CP such as granite, diorite and dacite porphyry. According to the some previous studies, this intrusive body intrudes the CMC (Yılmaz and Boztuğ, 1986; Aydın et al., 1995) in the south and Triassic Küre Complex in the east. The former interpretation is not confirmed by the field observations. It is overlain by the Upper Jurassic İnaltı Formation at several locations. These field relations suggest that the age of CP must be between the Triassic and Upper Jurassic.

The contact relation between the CP and CMC is important for further geological evaluation. It is therefore studied the contact in detail in locations where the outcrop conditions are preferable. Generally this contact is covered by intense vegetation in the north of the CMC. According to the field observation along a number of road-cuts, as mentioned above, there is a strike-slip fault between these units (Fig. 2-25). The reported contact relations between this pluton, Küre Complex and İnaltı formation have been confirmed during the field studies (Figs. 2-28, 2-29).

The pluton is mostly composed of diorite in the west and east. The dacite porphyries are mostly determined in the east and they can represent the marginal parts of this large dioritic body (Fig. 2-30). The field relation between diorite and dacite-porphyries are only observed in limited areas.

The rocks of the pluton are mostly whitish, greenish and pinkish based upon the mineral constituents. The mineral paragenesis of the some dioritic rocks can be seen on the hand specimens which mostly include plagioclase, mica and amphibole minerals. On the other side, the feldspar phenocrysts can be identified in the dacite porphyry samples by naked eye.

At the western part (in the north of the Süle village, Fig. 2-4) of the pluton, the felsic phases (Figs. 2-31, 2-32) are dominated. Also, they can include some mafic enclaves

(Fig. 2-31). Macroscopically, the granites include feldspar, quartz, mica minerals. Except for mylonitic deformation zones, there is no indication for metamorphism on the CP. The mylonitic zones are also characterized by intensive alteration and mineralization. The effects of the surface alteration can be observed on these plutonic rocks.

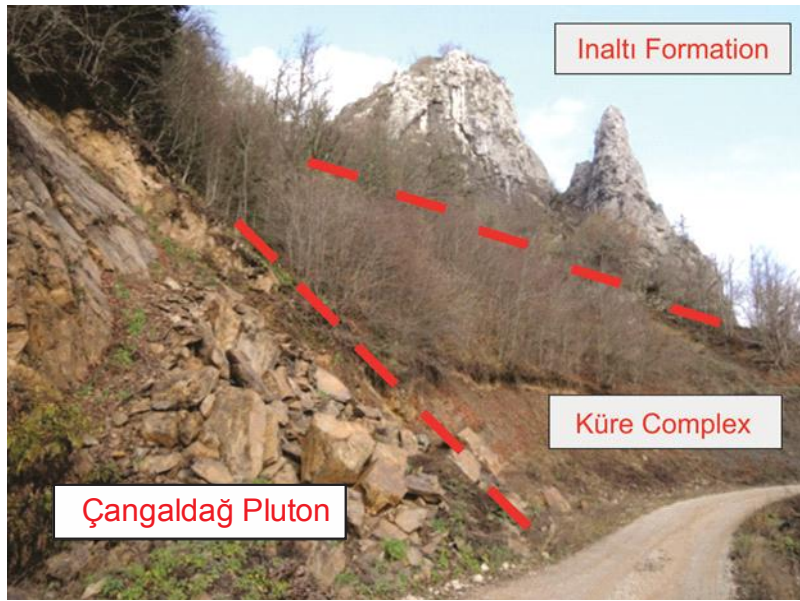


Figure 2-28: View of the field relations between Çangaldağ Pluton, Küre Complex and İnaltı Formation. This pluton cuts the Triassic Küre Complex and overlain by Upper Jurassic İnaltı Formation.



Figure 2-29: Closer view of the cutting relation between Çangaldağ Pluton and Küre Complex.



Figure 2-30: Field view of the dacite porphyry body within the Çangaldağ Pluton (the surface is highly altered)



Figure 2-31: Field view of a granitic rock including a mafic enclave within the Çangaldağ Pluton.



Figure 2-32: Field view of the cutting relation between the granitic veins and diorite body within the Çangaldağ Pluton.

### **2.2.3. Devrekani Units**

The Devrekani Metamorphics comprise mostly a basement made of ortho- and paragneisses, amphibolites, and metacarbonates. They are intruded by orthogneisses in the eastern part of this unit. (Figs. 2-33, 2-34, 2-35). These field relations could be clearly observed along the roadcuts which were opened for a chromite pit in the study area.

In addition to these lithologies, there are a few metaophiolite slices within the Devrekani Metamorphics (Figs. 2-4, 2-36). Some of them (between Devrekani Metamorphics and CMC) have been named as Dibekdere metaophiolite by Yılmaz (1980). According to the field observations, some of the Devrekani Metamorphics are found as tectonic klippe over the CMC. In other words, they can be probably connected to the metavolcanic rocks of the CMC under this klippe. These metaophiolites are restricted by a fault in the west (near of the Sıpacı village; Fig. 2-4).

The age of these metaophiolites are unknown. There is no radiometric age data yet in the literature. However, two meta-diorite bodies were determined within a metaophiolite which is shown in the Figure 2-4. It is cut by these intrusive metadiorites (Figs. 2-36, 2-37) at different locations which will provide a relative age for these metaophiolite bodies.



Figure 2-33: Field view of the cutting relation between orthogneiss and the Devrekani Metamorphics (paragneiss).

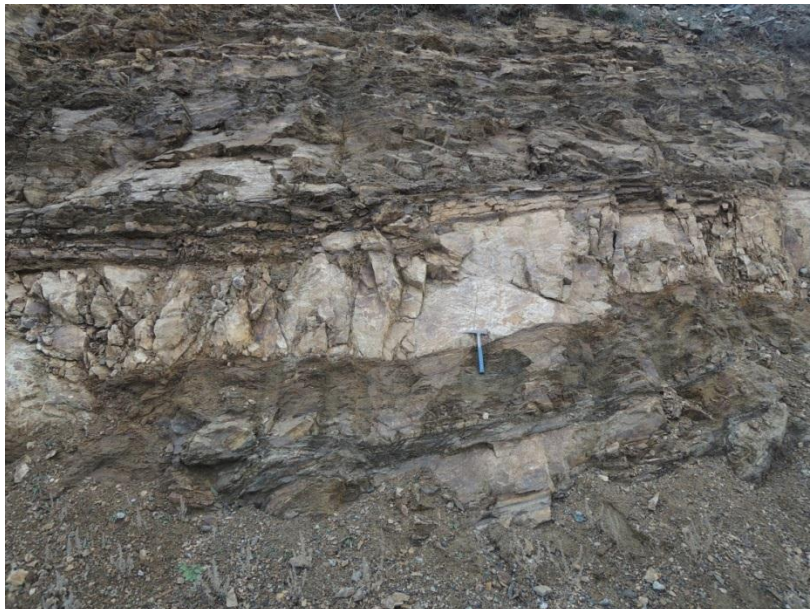


Figure 2-34: Field view of the cutting relation between orthogneiss and the Devrekani Metamorphics (paragneiss).



Figure 2-35: Field view of the cutting relation between orthogneiss/aplitic dyke and the Devrekani Metamorphics (paragneiss).

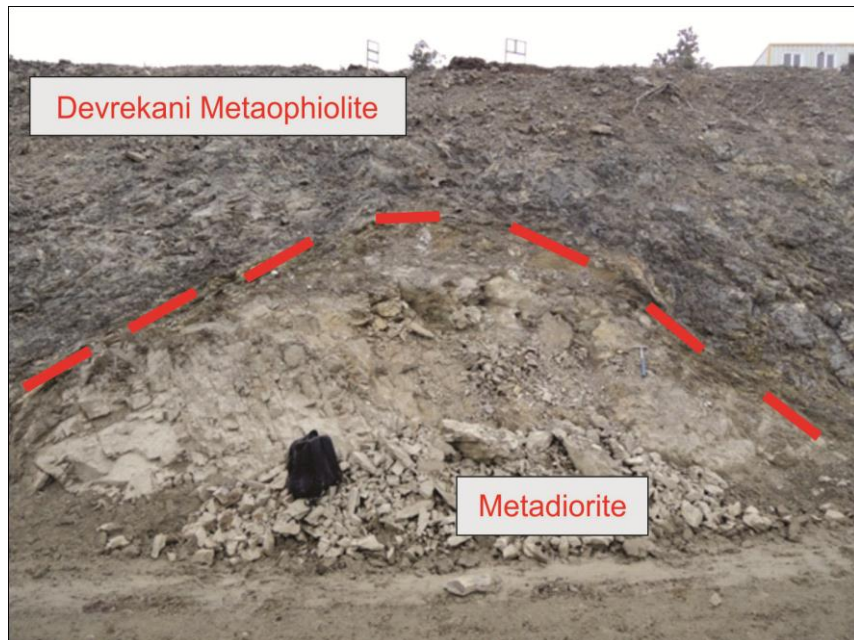


Figure 2-36: Field view of the cutting relation between a metadiorite body and the Devrekani Metaophiolite (found as tectonic slice within the Devrekani Metamorphics).

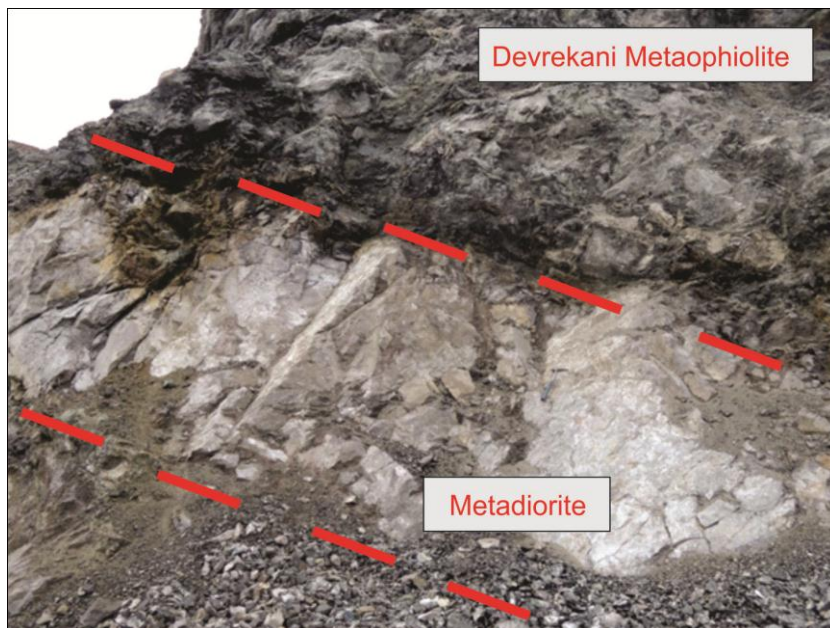


Figure 2-37: Field view of the cutting relation between a metadiorite body and the Devrekani Metaophiolite.

#### 2.2.4. Devrekani Granitoid

The Devrekani Granitoid is outcropping in the Devrekani town of Kastamonu. It mainly composed of diorites and granites (Fig. 2-38). In addition to these observations, Nzegge (2008) has identified the presence of the tonalite bodies within the Devrekani Granitoid. They have medium grain sizes and whitish/greenish colors. Most of them were affected by the intense alteration processes. Therefore, in some cases, it is difficult to differentiate them in the field.

These intrusive bodies cut the Triassic Küre Complex in the south and overlain by younger Tertiary cover units in the north (Fig. 2-4). The field relation between this granitoid and Devrekani Metamorphics could not be observed at the eastern part of the study area since it is covered by younger sedimentary units and farm lands.

The age of this granitoid was assigned as the Middle Jurassic (from 170 to 165 Ma) by using radiometric U-Pb dating method (Nzegge, 2008). It is consistent with the field relationships which were mentioned in the previous paragraph.



Figure 2-38: Field view of the Devrekani Granitoid (Diorite).

### **2.2.5. Cover Units**

The sedimentary cover units are grouped as the “first allochthonous cover” comprising the Upper Jurassic Brnk and İnalıtı formations, the “second allochthonous cover” comprising the Early Cretaceous ađlayan and Late Cretaceous / Early Paleocene Gkeađa formations and the Tertiary cover of the Tařkpr-Boyabat Basin (Fig. 2-4).

#### **2.2.5.1. Brnk Formation**

The oldest sedimentary cover of the Central Pontides is Brnk formation and its age is probably Middle-Late Jurassic (Hippolyte et al., 2016). It is composed of

alternation of conglomerate, sandstone and mudstone. Its name was given by Ketin and Gümüş (1963) and type locality is the around of Bürnük village where is located in the north of Boyabat country (Uğuz and Sevin, 2007). The thickness of this unit is approximately ranging between 300-400 m (Yılmaz and Tüysüz, 1984). The Upper Jurassic-Lower Cretaceous İnaltı formation overlies the Bürnük formation at the several locations in the Central Pontides.

### 2.2.5.2. İnaltı Formation

The İnaltı formation is mostly outcropping in the north of study area. It overlies the Küre Complex and CP (Fig. 2-39). However, these relations can be questionable due to the presence of the intense tectonic activities in the study area. For instance, along the strike-slip fault zone between the CMC and the CP highly sheared knockers of İnaltı Formation are observed (Figs. 2-40, 2-41).

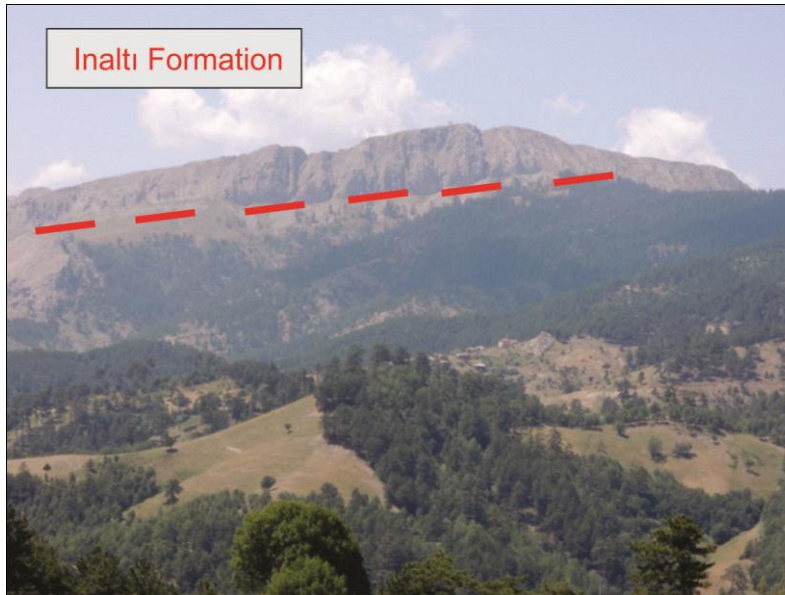


Figure 2-39: General view of the İnaltı Formation (unconformably overlies the Küre Complex and the Çangaldağ Pluton)

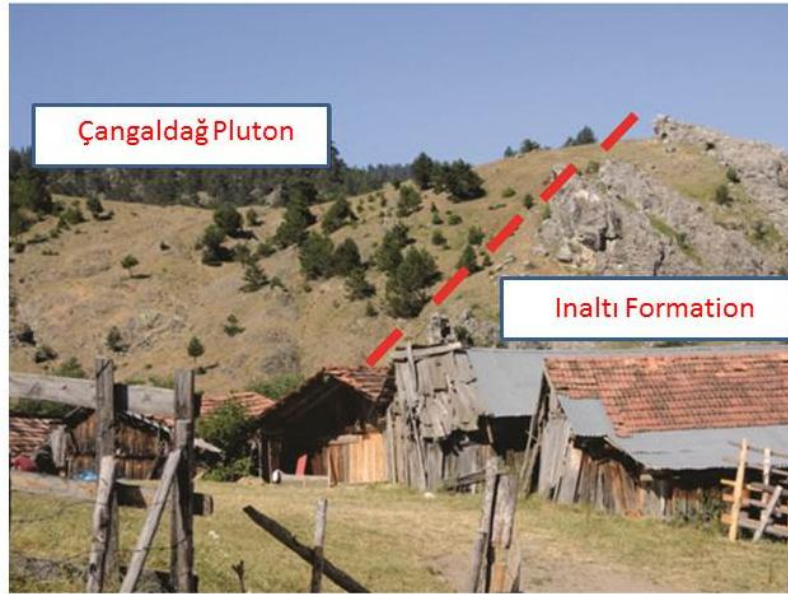


Figure 2-40: View of the field relation (tectonic) between the Çangaldağ Pluton and the İnaltı Formation

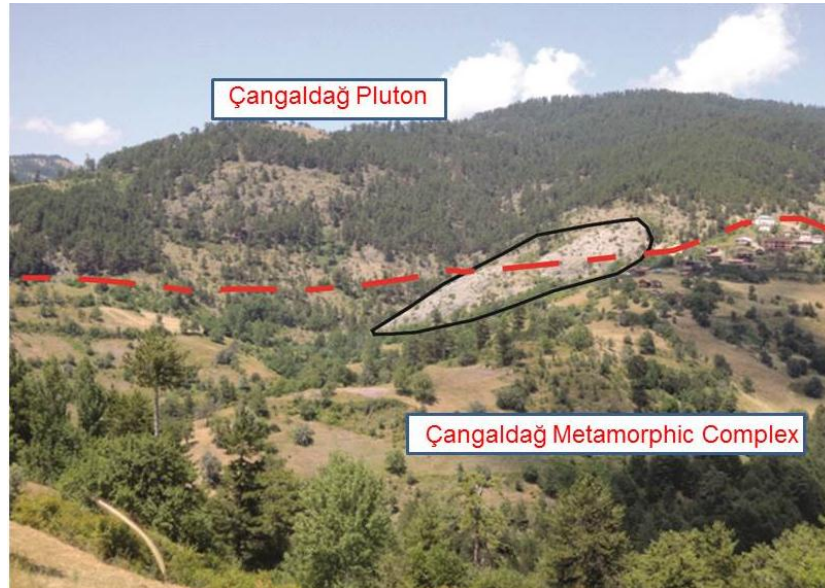


Figure 2-41: View of the field relation (tectonic) between the Çangaldağ Pluton and the Çangaldağ Metamorphic Complex. Also, there is a sheared limestone knocker (black boundary) between these units.

The type locality where stratigraphic relations are observed, is the around of İnalti village (Ketin and Gümüş 1963). The thickness of the limestone unit was measured as approximately 395 m. Kaya and Altıner (2014) suggested shallow water and reefal/fore-reefal character and Upper Jurassic-Lower Cretaceous (Kimmeridgian-Berriasian) age for the deposition of the carbonates. They are mostly white and lighter gray recrystallized limestones.

### **2.2.5.3. Çağlayan Formation**

The Çağlayan Formation mostly comprises alternation of the sandstone, siltstone and shale beds (Fig. 2-42). The sandstone beds are gray to yellowish and their thicknesses change from thin to thick based upon the depositional environments. The shale beds are mostly thinner and gray color. It unconformably overlies the CMC, mostly, in the south.

Şen (2013) has proposed that the maximum thickness of this unit is approximately 3000 m. The Çağlayan formation shows typical turbidite characteristics which have graded bedding, flute casts, grooves, slump structures etc. (Okay et al., 2013). It is unconformably overlain by the Upper Cretaceous pelagic limestones (Okay et al., 2006, 2013).



Figure 2-42: Field view of the Çağlayan Formation (thicker sandstone beds). It is composed of sandstone and shale alternations.

#### **2.2.5.4. Gökçeğaç Formation**

The Gökçeğaç Formation mostly includes andesitic and basaltic clasts and blocks in a volcanoclastic matrix (Fig. 2-43). The color of this unit is mostly green and greenish black. Generally, it has massive structure and overlies unconformably the CMC in the south of the study area (Fig. 2-4). This formation is also considered as a volcanic fragments-bearing member of the Cankurtaran Formation that comprises the sandstone, siltstone, claystone and sandy limestone alternations (Uğuz and Sevin, 2007).



Figure 2-43: Field view of volcanic fragments in the Gökçeada Formation

#### **2.2.5.5. Tertiary Units**

The NE-SW trending Boyabat-Taşköprü Basin is filled by the Tertiary deposits (Fig. 2-4). This basin is restricted by the Ekinveren fault in the north. In this basin, three different sedimentary units were determined which are Pervanekaya Formation, Ilıca Formation and Sakızdağı Formation (Uğuz and Sevin, 2007). All of these units are mostly composed of conglomerate, sandstone, sandy limestone, limestone. In the southern part of the study area, the Tertiary units unconformably overlie the CMC and the other older units (Figs. 2-4, 2-44, 2-45). Towards west, the contact becomes steeper, and is overturned, or the CMC thrusts onto the Tertiary units.



Figure 2-44: The Tertiary sedimentary units unconformably overly the Çangaldağ Metamorphic Complex

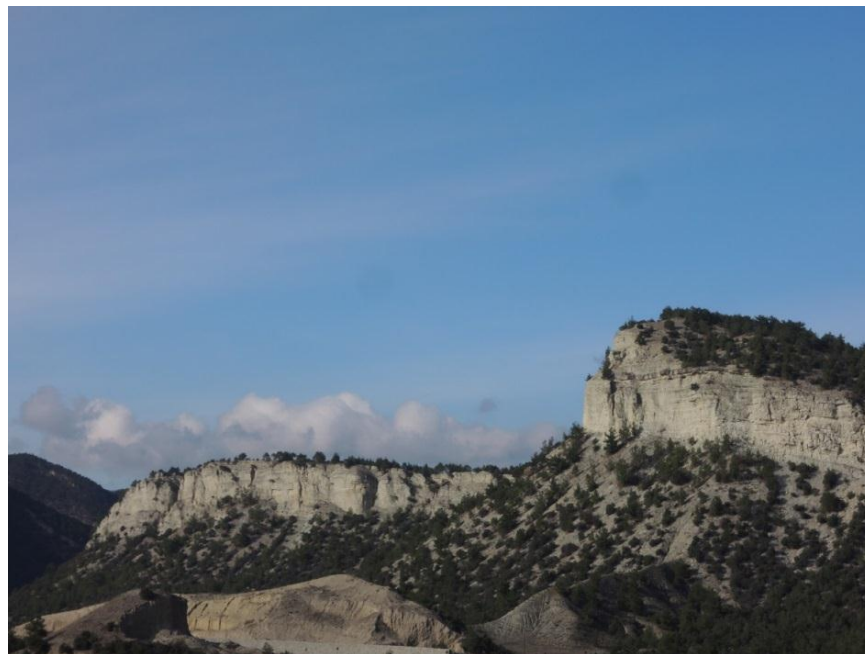


Figure 2-45: General view of the Tertiary units in the Taşköprü-Boyabat Basin



## CHAPTER 3

### PETROGRAPHY

Approximately 100 thin sections were prepared after grouping the hand-specimens based upon their macroscopic features. As grouped through the field studies, here, 8 different rock types for the CMC and 3 different rock types for the CP were identified according to their modal compositions. The thin sections were carefully examined under the polarized microscope in order to identify the characteristics of the rock types from the CMC and CP.

The CMC includes metabasalts, metadiabases, metatuffs, metaandesites, metarhyodacites, metavolcaniclasticss, metaclastics and metacarbonates. In particular, the low-grade metamorphic parageneses and micro-textures indicate the presence of different deformational processes. On the other hand, the CP is represented by diorites, dacite porphyries and granites which do not display any metamorphic textures but only alteration signatures (e.g. sericitation of feldspars).

The mineralogical contents, textural characteristics and metamorphism/deformation signatures of these different rock types have been described in detail in this chapter.

#### **3.1. Çangaldağ Metamorphic Complex (CMC)**

##### **3.1.1. Metabasalts**

Firstly, it should be noted that the primary mineral paragenesis of the metabasalts are hardly observed due to the presence of low grade metamorphism. Both foliated and

non-foliated types are found among the collected samples. The metabasalts have generally aphanitic and porphyritic texture (Figs. 3-1, 3-2). The porphyritic texture could be explained by slow cooling in the deeper parts and then rapid cooling can cause the forming of fine-grained groundmass. Rarely preserved primary phenocrysts are clinopyroxenes, plagioclases and a few serpentinized olivines (Fig. 3-1).

The clinopyroxene phenocrysts display glomeroporphyritic texture. They are subhedral to euhedral and marginally replaced by actinolite and chlorite. The preserved clinopyroxene crystals exhibit moderate birefringences (Fig. 3-1). The extinction angle of clinopyroxene minerals are ranging from 30 to 45°. Some clinopyroxene minerals show glomeroporphyritic texture by forming clusters.

In some samples, the plagioclase phenocrysts exhibit seriate texture by the presence of randomly oriented interlocking laths. The plagioclase minerals show simple and multiple twinning. They have mostly subhedral outlines. Olivine has been completely replaced by serpentine and chlorite. Lastly, the cubic opaque minerals in these rocks may represent pyrite and magnetite.

As metamorphic minerals, the chlorite minerals can be identified by their pleochroism and pale greenish colors. They display low-angle oblique extinction. Also, they are characterized by anomalous interference colors (Figs. 3-1, 3-2). Chlorites are developed parallel to the foliation planes. The second common metamorphic mineral is epidote, and it displays high relief and yellowish/greenish colors. In addition to that, the patchy birefringence is characteristic for the epidote minerals (Fig. 3-2). The last common metamorphic mineral is actinolite which can be distinguished by acicular (needle) / bladed forms. Some sericite minerals are seen as an alteration product of the plagioclase minerals which could be defined by their high birefringences under XPL (crossed polars). The epidote, chlorite and actinolite minerals may have been formed by metamorphic transformation of primary mafic minerals (e.g. clinopyroxene minerals) and/or groundmass glass.

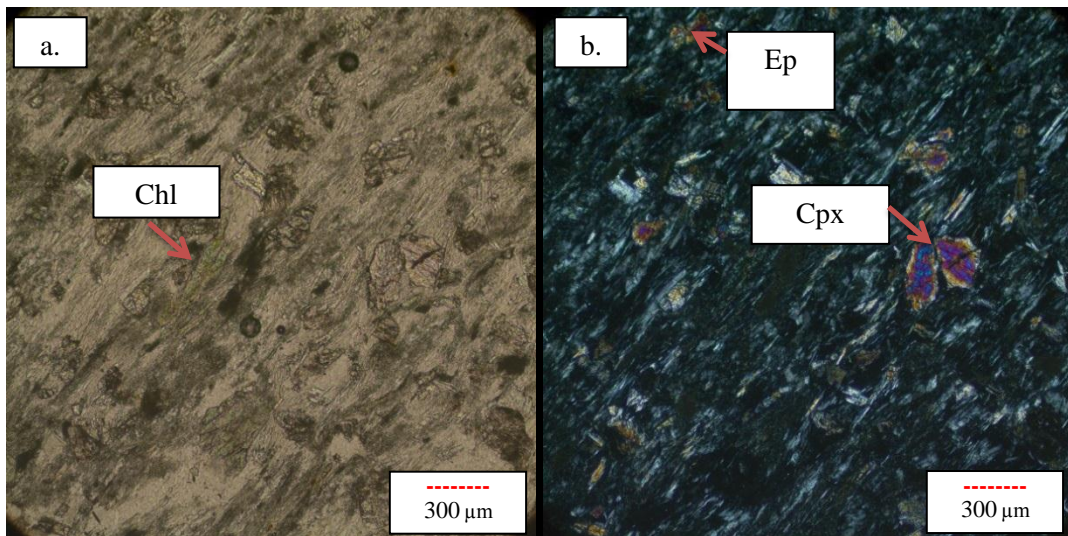


Figure 3-1: Development of epidote and chlorite minerals in a fine grained groundmass of a foliated metabasalt (Sample 13, a. PPL b. XPL)

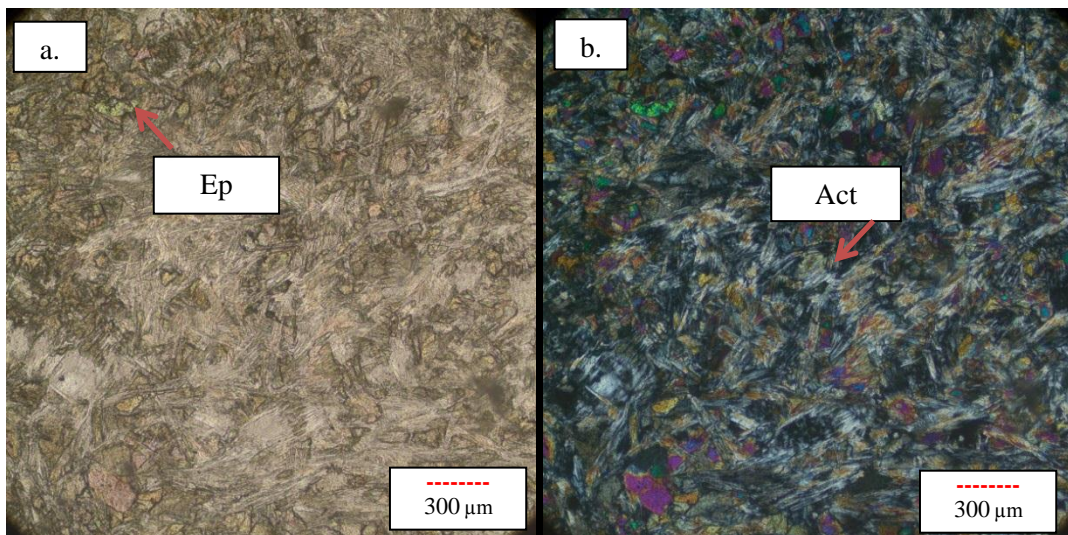


Figure 3-2: Development of epidote and actinolite minerals in a fine grained groundmass of non-foliated metabasalt (Sample BLV-11, a. PPL b. XPL)

### 3.1.2. Metadiabase

The metadiabases essentially comprise clinopyroxene, amphibole and plagioclase as primary igneous minerals (Figs. 3-3, 3-4). They are characterized by porphyritic texture and include fine and coarse grains of the minerals. Almost all of olivine minerals have been altered to the serpentine minerals. The clinopyroxene crystals exhibit oblique extinction and the angles change between  $35^{\circ}$  and  $45^{\circ}$ . Subofitic texture can be seen by gathering large clinopyroxene crystals and plagioclase laths. The amphibole crystals can be distinguished by their pleochroism and greenish colors. Also, they display high order interference colors. They are mostly anhedral and subhedral crystals. In some cases, the cleavages can be seen of the amphibole crystals. The plagioclase crystals have mostly subhedral shapes and exhibit simple and multiple twinnings (Figs. 3-3, 3-4). The presence of some fractures on these crystals indicates the effect of ductile deformation. However, most of the mafic minerals have been altered to chlorite and epidote (Figs. 3-4).

Similar to the metabasalts, as metamorphic minerals, the chlorite, actinolite and epidote minerals have been determined for the metadiabase samples which can be identified by their diagnostic optical characteristics (as explained above in the metabasalt part). In brief, the chlorite minerals can be distinguished by their pleochroism and anomalous interference colors. The presence of epidote minerals can be confirmed by higher relief and slightly greenish colors. Lastly, the actinolites display less pleochroism than amphiboles and acicular / bladed forms. All of these secondary minerals suggest the effect of low-grade metamorphism conditions (greenschist).

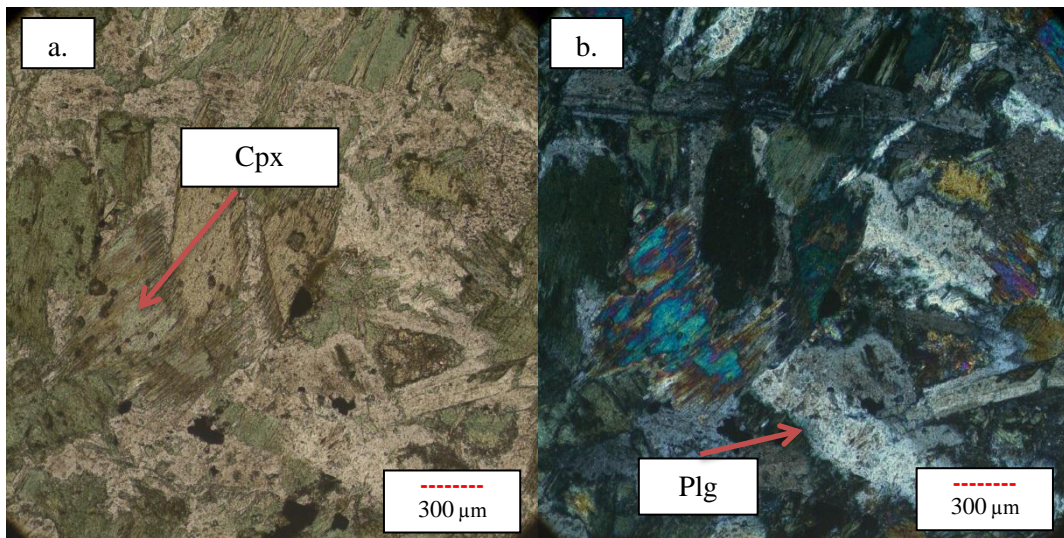


Figure 3-3: Relict clinopyroxene and plagioclase crystals in a non-foliated metadiabase. Development of chlorite minerals on the pyroxene and amphibole crystals (Sample 47, a. PPL b. XPL)

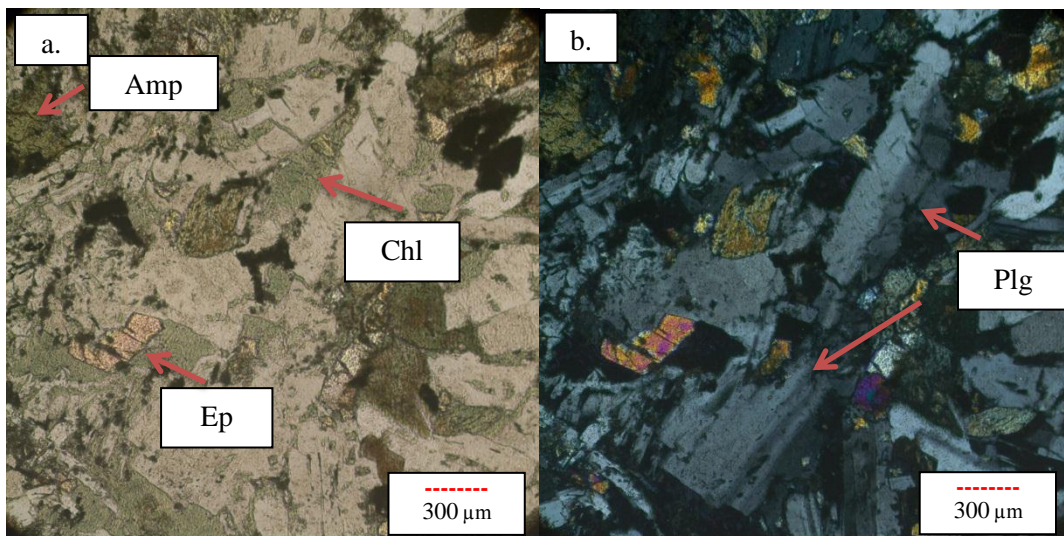


Figure 3-4: Relict amphibole and plagioclase crystals in a non-foliated metadiabase. Development of chlorite and epidote minerals (greenschist facies) on the pyroxene and amphibole crystals (Sample DVK-10, a. PPL b. XPL)

### 3.1.3. Metaandesites

Metaandesites represent the other common metavolcanic rock type among the samples. They have aphanitic and porphyritic texture. The foliated and non-foliated types are found for the metaandesite samples. As in the metabasalt samples, the primary igneous minerals of the metaandesites are mostly plagioclase and minor clinopyroxene. The plagioclase minerals obviously display flow texture (Fig. 3-5). They have subhedral and anhedral shapes. The presence of relict plagioclase as porphyroclasts within the fine-grained groundmass may indicate the effect of ductile deformation process.

Most of the mafic minerals have been altered to secondary metamorphic minerals such as epidote, chlorite and actinolite (Figs. 3-5, 3-6, 3-7). The epidote minerals could be identified by their high relief and yellowish/greenish colors. Also, the characteristic patchy birefringence is obviously observed for the epidote minerals (Fig. 3-6).

The chlorite crystals have oblique extinction and show low-angle extinction angles. Additionally, the characteristic anomalous interference colors of the chlorite crystals can be seen for identifying them under the microscope (Figs. 3-5, 3-6, 3-7). The other metamorphic mineral is actinolite which exhibits acicular (needle-like) / bladed forms. These metamorphic minerals may mainly have been formed by transformation of plagioclase and clinopyroxene minerals. In some samples, the sericite crystals are found on the plagioclase crystals which may indicate the presence of hydrothermal alteration.

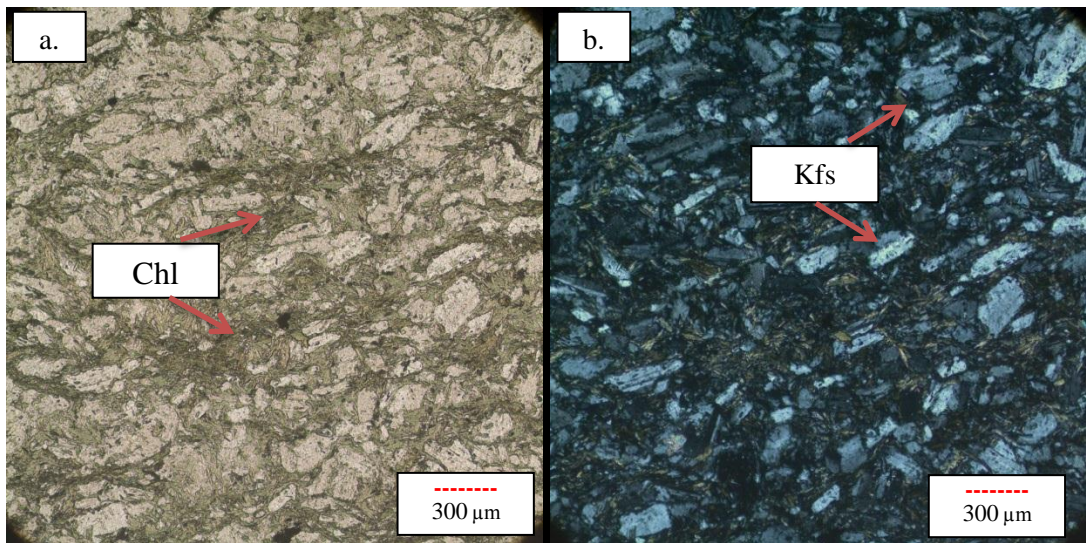


Figure 3-5: Development of chlorite crystals in a fine grained groundmass of foliated metaandesite (Sample 48, a. PPL b. XPL)

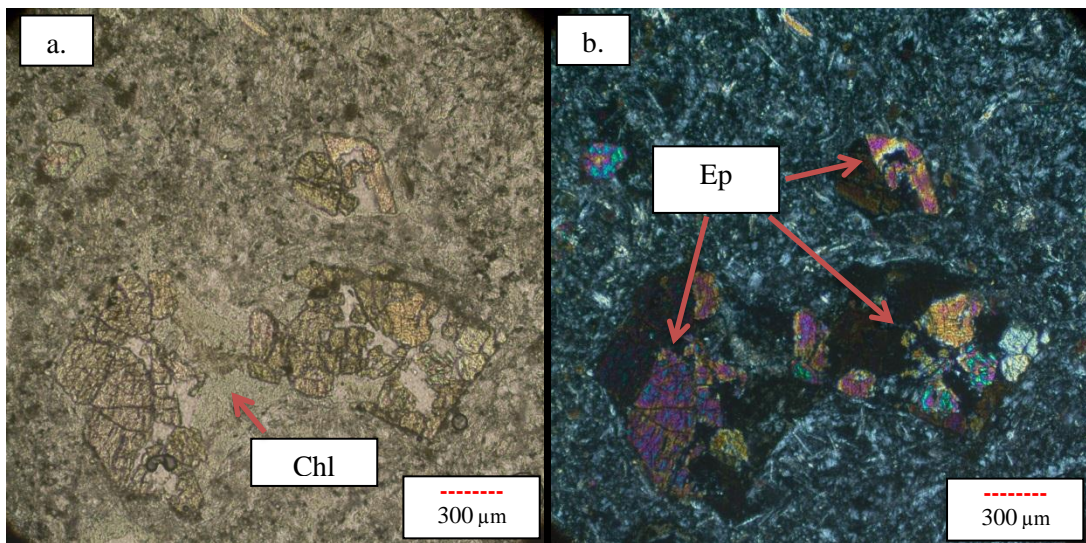


Figure 3-6: Development of chlorite and epidote crystals (greenschist facies) in a fine grained groundmass of non-foliated metaandesite (Sample 21, a. PPL b. XPL)

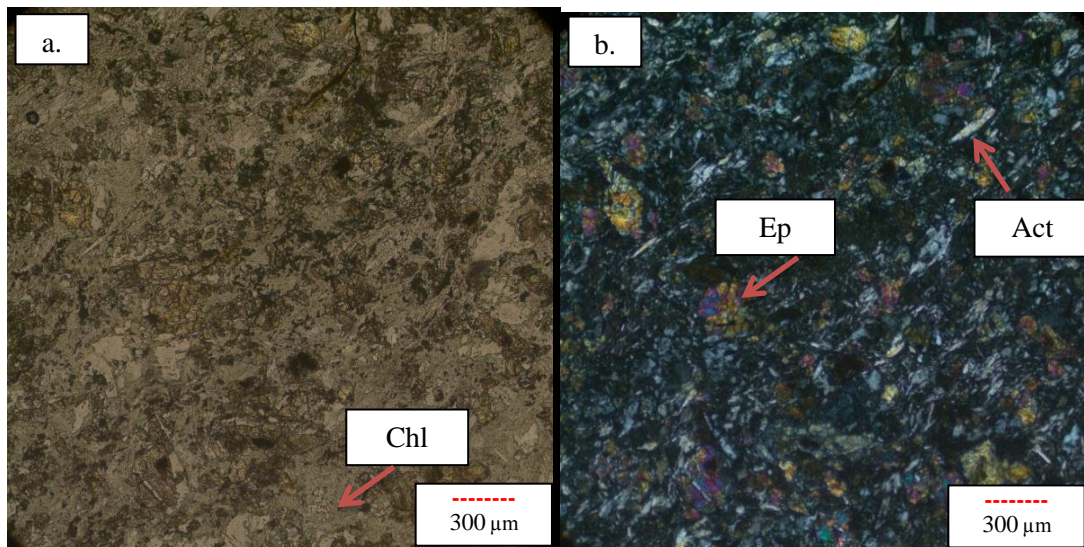


Figure 3-7: Development of chlorite, epidote and actinolite crystals (greenschist facies) in a fine grained groundmass of slightly foliated metaandesite (Sample DRN-10, a. PPL b. XPL)

### 3.1.4. Metarhyodacites

The felsic volcanic rocks of the CMC, such as the metarhyodacites, exhibit mostly porphyritic and microcrystalline textures. The phenocryst phases are characterized by quartz, feldspar and minor biotite in a fine grained groundmass. The quartz and feldspar crystals are mostly anhedral to subhedral (Figs. 3-8, 3-9, 3-10, 3-11).

The quartz crystals display undulatory extinction and can be seen quite fresh due to their high resistance (Figs. 3-10, 3-11). They are mostly found as anhedral crystals. On the other hand, the feldspar minerals (K-feldspar and plagioclase) mostly have been altered to sericite (Fig. 3-11). These feldspar crystals show simple and polysynthetic twinnings. They have subhedral and anhedral shapes. Additionally, the biotite crystals can be identified by brownish colors and mottled extinction under crossed polars (Fig. 3-9). In some samples, the plagioclase crystals are enveloped by biotite minerals which may indicate the presence of mylonitic texture after ductile deformation process.

The stable minerals may transform to unstable minerals by increasing of temperature and pressure during the magmatic evolution. The presence of corroded quartz crystals (Fig. 3-11) may indicate the interaction between these crystals and melt during the magmatism (magmatic corrosion). In some samples, the plagioclase crystals have been replaced by calcite crystals which can be defined by their high order interference colors. As an indicator the presence of low-grade metamorphism conditions, the epidote crystals may have formed from the mafic minerals and plagioclases which can be easily distinguished by high relief, yellowish / greenish colors and patchy birefringence (Figs. 3-8, 3-9, 3-11). The mafic phases in the metarhyodacites have been replaced by epidote and chlorite minerals. In some samples, the epidote minerals are surrounded by finer-grained quartz minerals that indicate the mortar texture (Fig. 3-9).

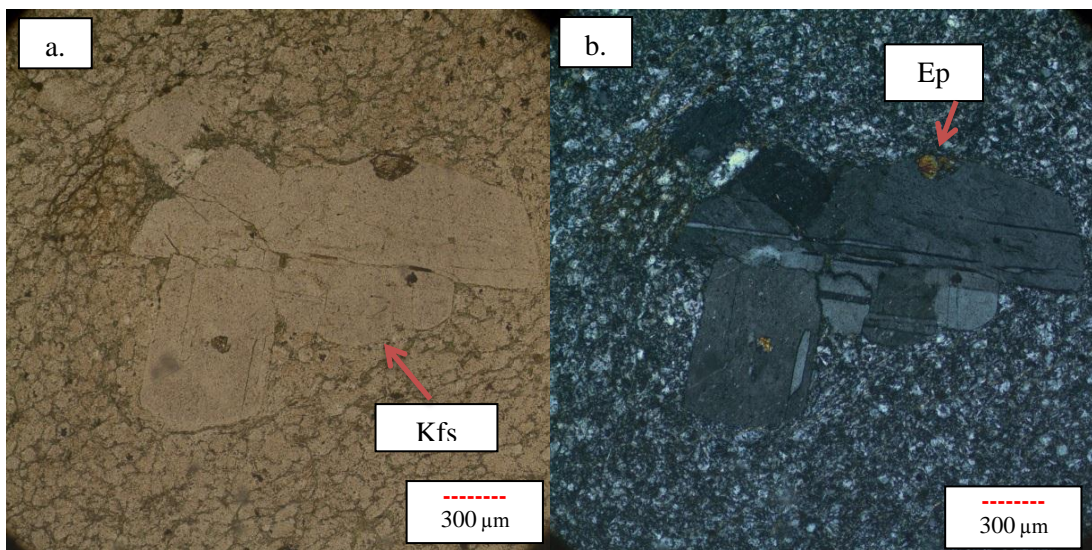


Figure 3-8: Development of small epidote crystals in a fine grained groundmass of non-foliated metarhyodacite (Sample 19, a. PPL b. XPL)

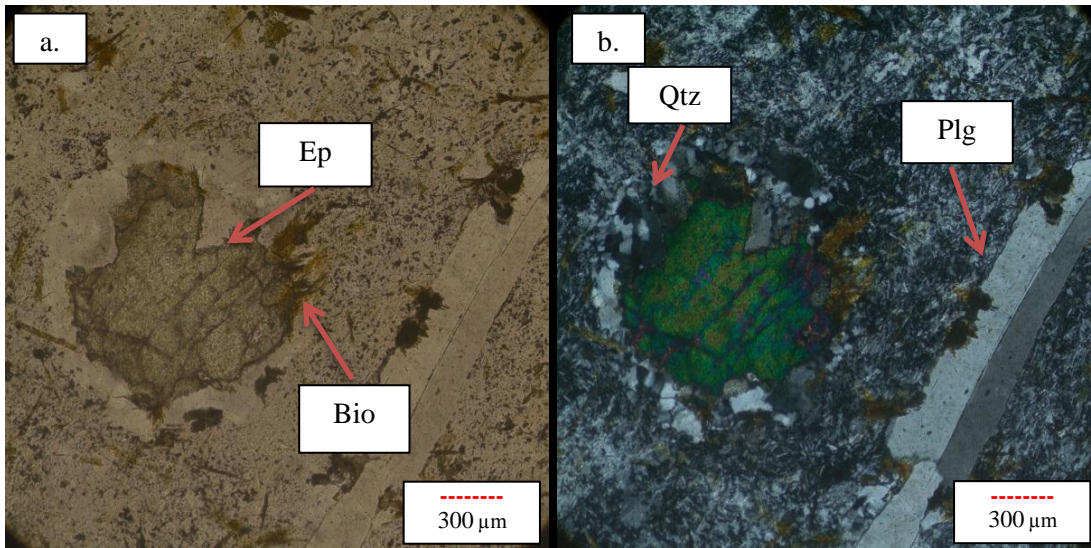


Figure 3-9: Development of an epidote crystal in a fine grained groundmass of foliated metarhyodacite (Sample AK-10, a. PPL b. XPL)

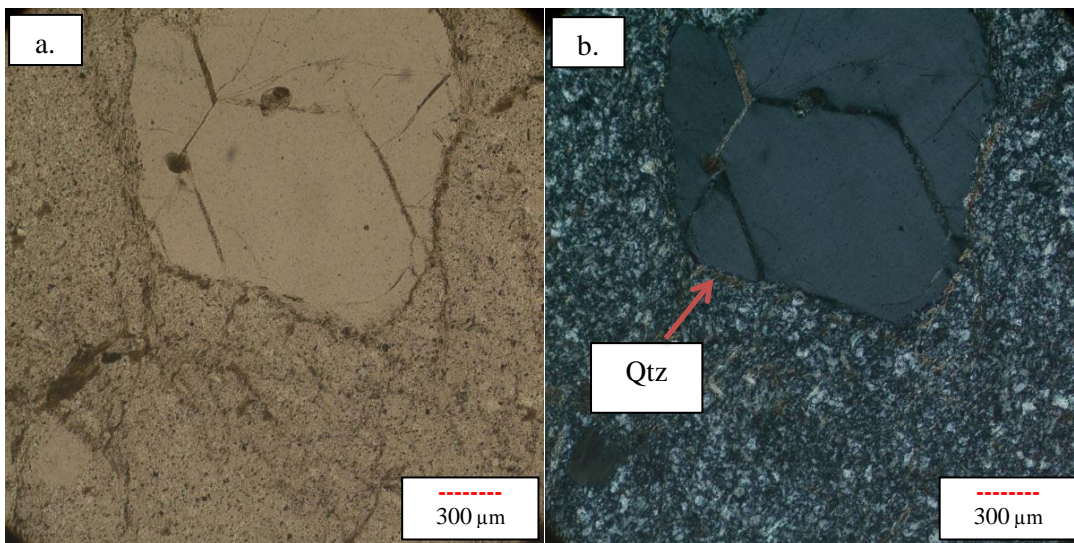


Figure 3-10: Quartz phenocryst in a fine grained groundmass of non-foliated metarhyodacite (Sample AK-14, a. PPL b. XPL)

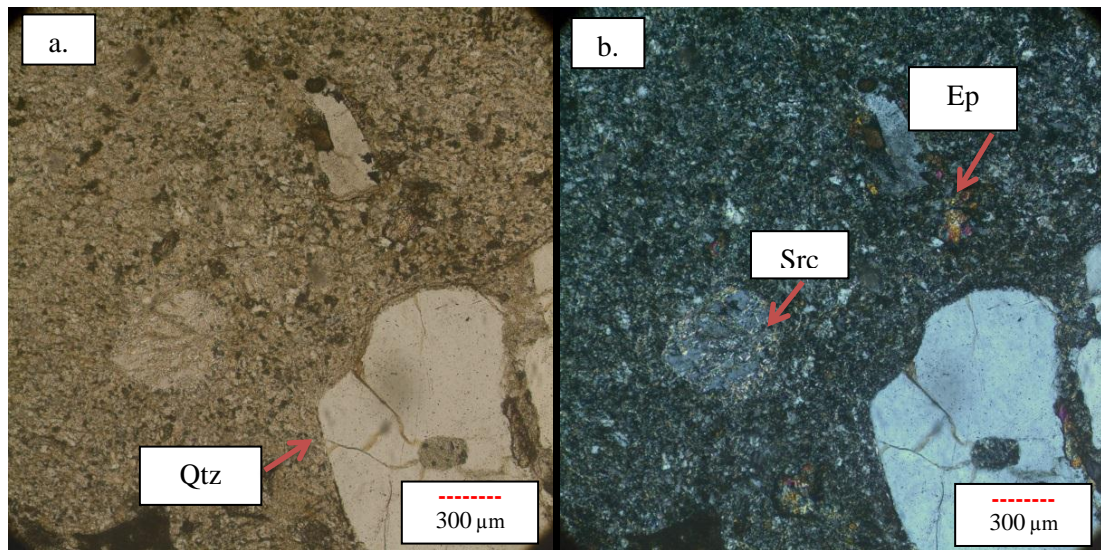


Figure 3-11: Development of small epidote and sericite crystals (on the feldspars) in a fine grained groundmass of non-foliated metarhyodacite. Also, the corroded quartz mineral can be observed (Sample AK-22, a. PPL b. XPL)

### 3.1.5. Metavolcaniclastics

The metavolcaniclastic rocks contain many mineral fragments. They are mostly composed of quartz / feldspar grains and metamorphic chlorite / epidote / actinolite minerals (Figs. 3-12, 3-13). The quartz crystals have mostly anhedral shapes and are seen fresh due to the high resistance. The foliated and non-foliated types are found for these samples at the different localities.

In detail, the relict mineral fragments (e.g. quartz) have been surrounded by metamorphic minerals (e.g. chlorite, epidote) during the metamorphism which indicate the presence of low-grade metamorphism conditions for these rocks as well. (Figs. 3-12, 3-13). For instance, the chlorite crystals are identified by their pleochroism / greenish colors and anomalous interference colors. Also, the other metamorphic mineral is epidote, and it shows typical patchy birefringence and high relief.

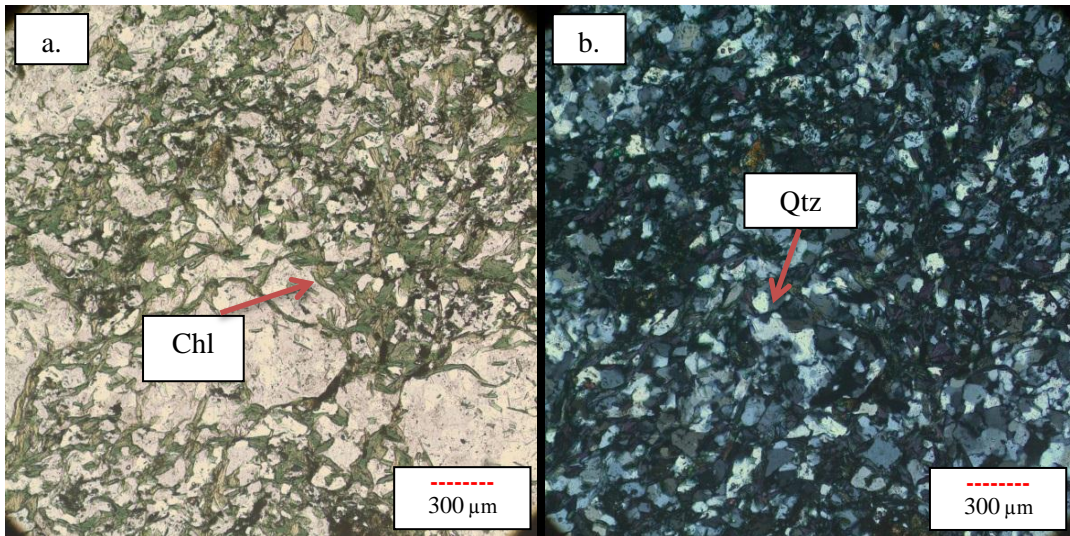


Figure 3-12: The quartz grains and development of chlorite minerals within a non-foliated metavolcaniclastic rock (Sample DRN-15, a. PPL b. XPL)

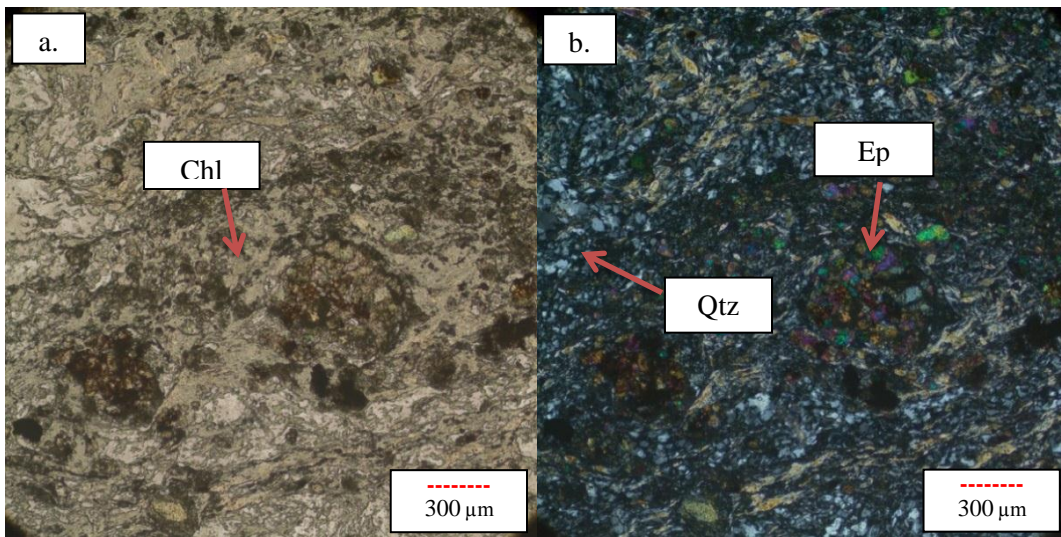


Figure 3-13: The quartz fragments and development of chlorite/epidote crystals (greenschist facies) within a slightly foliated metavolcaniclastic rock (Sample DRN-3, a. PPL b. XPL)

### 3.1.6. Metatuff

The metatuff samples are characterized by fine grained groundmass (Figs. 3-14, 3-15). Therefore, it is really hard to observe primary mineral paragenesis. However, the quartz crystals can be defined in some thin sections (Fig. 3-9). These metatuff samples include well-oriented metamorphic minerals such as chlorite, epidote and actinolite (Figs. 3-14, 3-15).

The epidotes are characterized by higher relief, slightly greenish colors and patchy birefringence. The chlorites show greenish colors and anomalous interference colors. The actinolites can be easily observed by needle-like shapes. Once again, the presence of this metamorphic mineral paragenesis indicates the low-grade metamorphism conditions for metatuff samples as well.

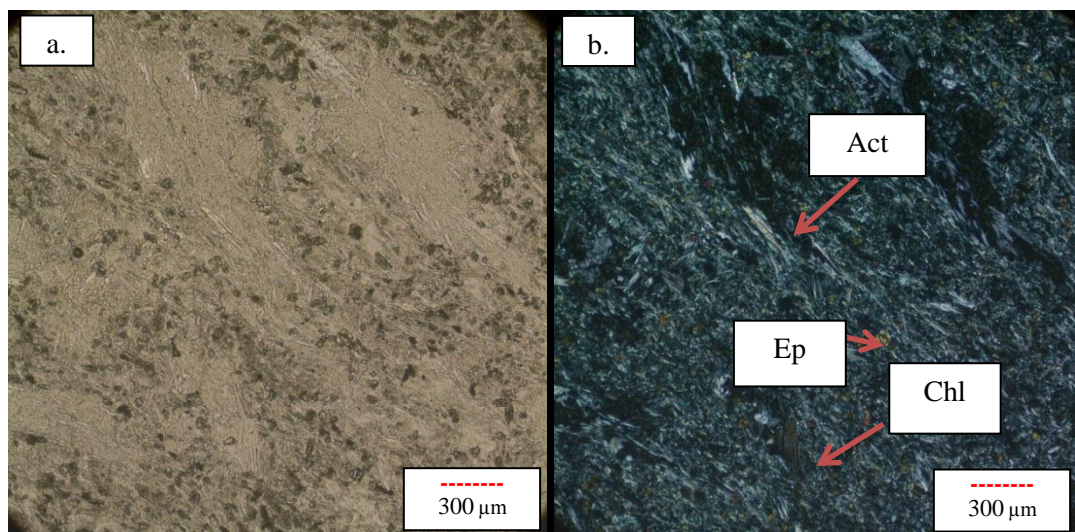


Figure 3-14: Development of epidote, chlorite and actinolite crystals (greenschist facies) in a fine grained groundmass of metatuff (Sample AK-5, a. PPL b. XPL)

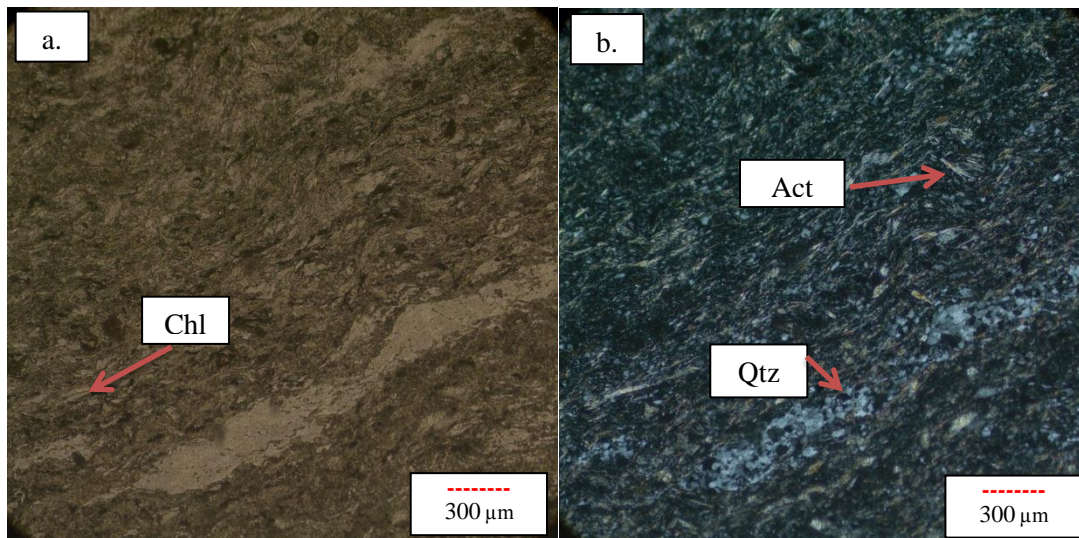


Figure 3-15: Development of chlorite and actinolite crystals (greenschist facies) in a fine grained groundmass of metatuff (Sample DRN-8, a. PPL b. XPL)

### 3.1.7. Metapelites

The pelitic schists have very distinctive mineral paragenesis of the low-grade metamorphism. They consist mostly of muscovite, biotite, feldspar and quartz (Figs. 3-16, 3-17, 3-18). The schistosity can be defined by lepidoblastic mica minerals and elongated recrystallized feldspar and quartz.

The presence of sub-grain development, undulatory extinction and sutured boundaries between recrystallized grains may indicate the effect of dynamic recrystallization. These assemblages represent relatively aluminous compositions and the absence of garnet indicates that the metamorphism has not proceeded to the medium-grade conditions. They have typically gray and black colors.

The muscovite minerals can be distinguished by high interference colors and flaky shapes (Figs. 3-16, 3-17). The quartz crystals represent the relict or recrystallized crystals and display sutured boundaries (beginning of recrystallization) due to the

strong ductile deformation (Fig. 3-16). The biotite crystals have brownish color, mottled extinction and moderate interference colors (Figs. 3-17, 3-18).

Lastly, once again, the effect of strong deformation processes can be traced by presence of S1 and S2 cleavage planes. Here, S1 planes are intersected by S2 planes (Fig. 3-18).

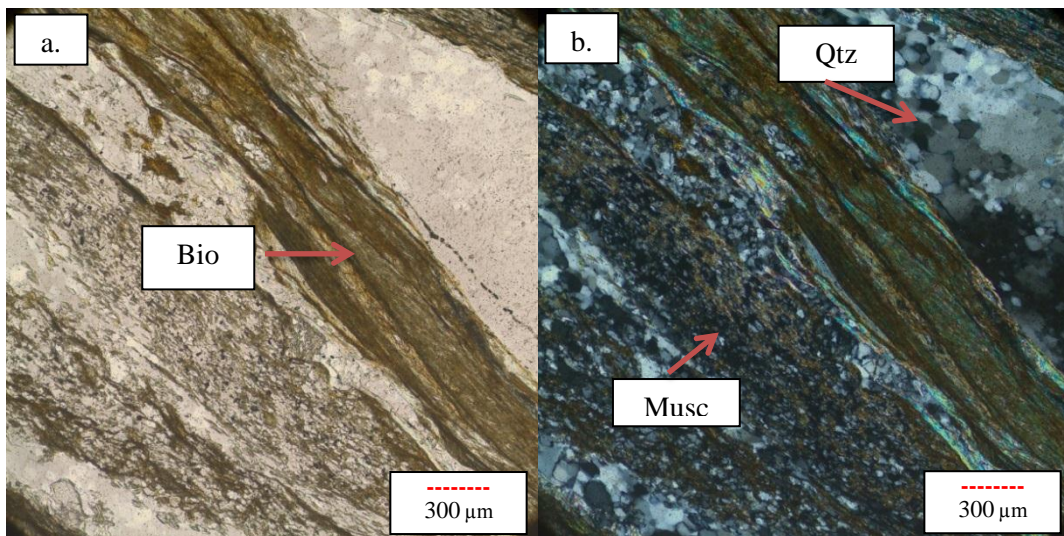


Figure 3-16: The quartz fragments and development of muscovite / biotite crystals within a foliated metapelite rock (Sample DRN-7, a. PPL b. XPL)

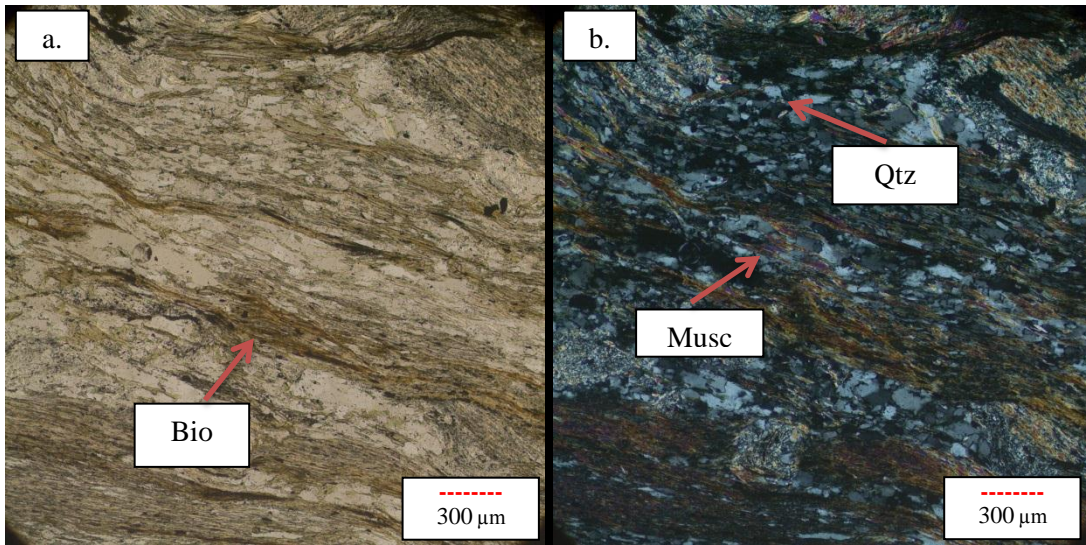


Figure 3-17: The quartz fragments and development of muscovite / biotite crystals within a foliated metapelite rock (Sample SCH-1, a. PPL b. XPL)

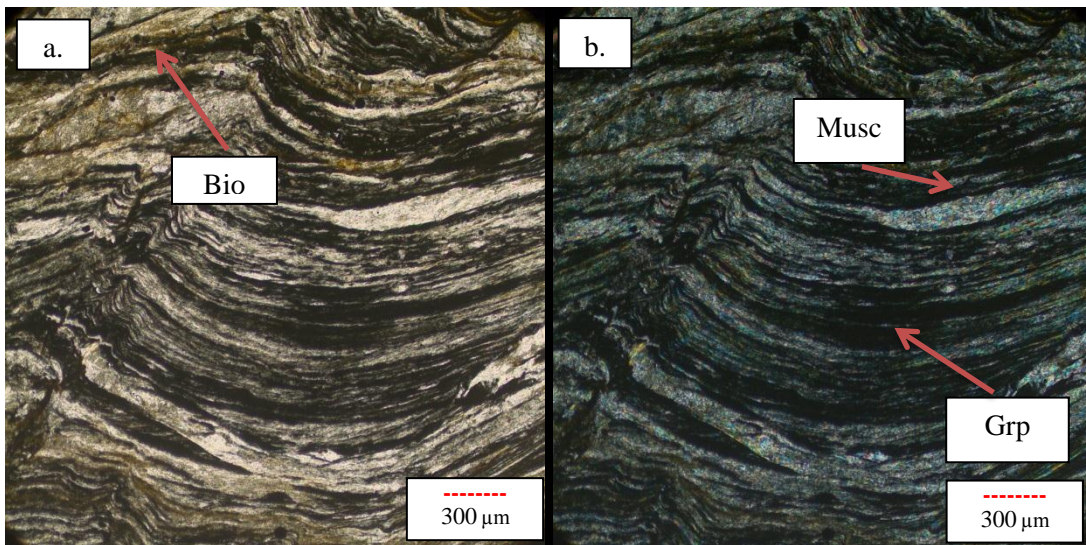


Figure 3-18: Development of muscovite / biotite / graphite crystals and S1 / S2 cleavage planes within a foliated metapelite rock (Sample 9, a. PPL b. XPL)

### **3.2. Çangaldağ Pluton (CP)**

As mentioned above, the Çandaldağ Pluton comprises diorites, dacite porphyries and granites which do not display any metamorphism signatures without only hydrothermal alteration products (e.g. sericitation in feldspars).

#### **3.2.1. Diorites**

The primary igneous mineral paragenesis of the dioritic rocks is made up clinopyroxene, plagioclase, biotite, amphibole and quartz (Figs. 3-19, 3-20, 3-21). They display holocrystalline / porphyritic texture. Hornblende crystals are one of the common phases in these rocks and they exhibit greenish to brownish colors with subhedral to euhedral shapes. (Figs. 3-19, 3-20).

The other essential phase is plagioclase crystals which have mostly anhedral and subhedral shapes (Figs. 3-20, 3-21). Some sericite crystals have been observed on these plagioclase crystals which reflect the effect of hydrothermal alteration or weathering. In some cases, the diorite samples can include coarse quartz phenocrysts which may be classified as quartz-diorite rather than typical diorite (Fig. 3-21). These quartz crystals are mainly anhedral and can be distinguished by fresher surface. Also, some opaque minerals are found in these samples. Overall petrographical characteristics of the diorites do not show any metamorphism effect without secondary alteration signatures.

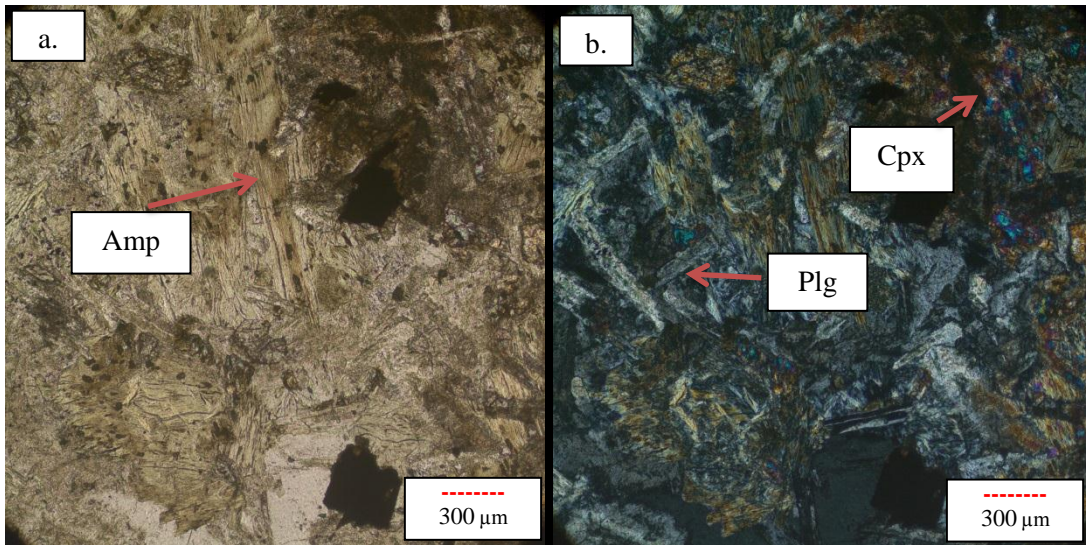


Figure 3-19: Clinopyroxene, Amphibole and plagioclase crystals in a diorite (Sample CN-1, a. PPL b. XPL)

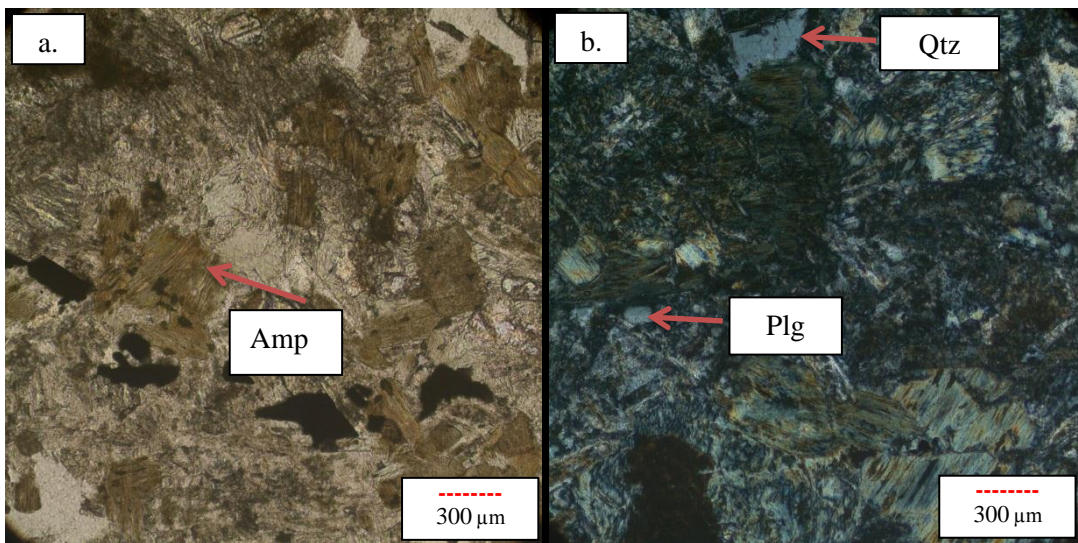


Figure 3-20: Amphibole, plagioclase and small quartz crystals in diorite (Sample CN-9, a. PPL b. XPL)

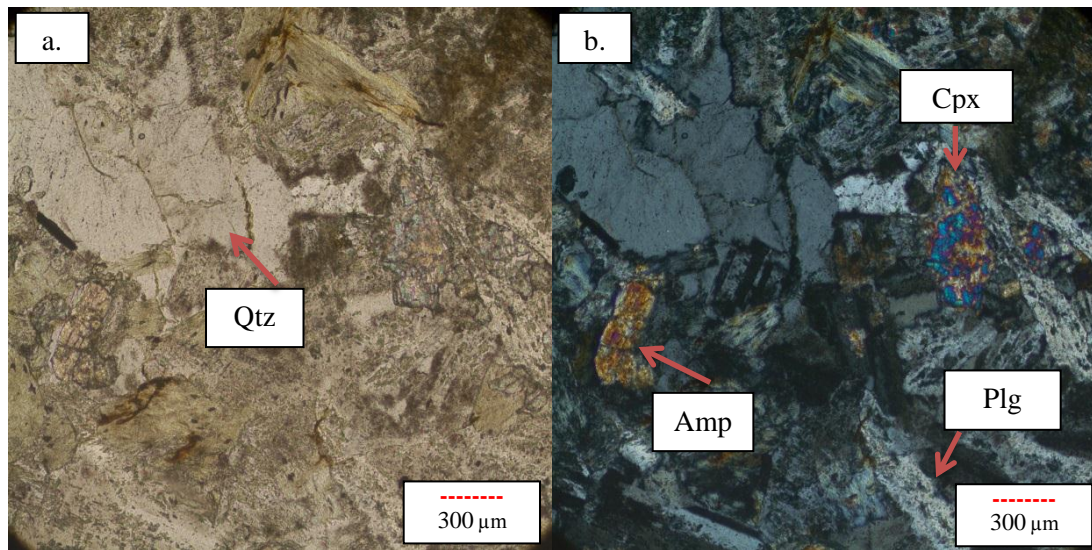


Figure 3-21: Amphibole, plagioclase, clinopyroxene and quartz crystals in a quartz-diorite (Sample CN11, a. PPL b. XPL)

### 3.2.2. Dacite Porphyries

The dacite porphyry represents the second common rock types within the CP. The phenocryst phases are composed of quartz, feldspar and biotite minerals and embedded in a fine-grained groundmass (Figs. 3-22, 3-23, 3-24). The quartz crystals have anhedral and subhedral shapes. They display typical wavy extinction and have quite fresh appearance. In some samples, the corroded quartz crystals (Figs. 3-23, 3-24) suggest the presence of interaction between these minerals and melt during the crystallization (magmatic corrosion).

The second common mineral is feldspar, and it is mostly altered to the sericite (Figs. 3-22, 3-24). In some samples, it has been also replaced by calcite. The calcite crystals can be identified by their high order interference colors under XPL. This process can be explained by effect of CO<sub>2</sub>-bearing late stage hydrothermal solutions. In addition to that, some biotite crystals have been slightly altered to the chlorite minerals (Fig. 3-24). These secondary chlorite crystals show pleochroism and

anomalous interference colors. All of these evidences confirm the presence of hydrothermal alteration process on these samples.

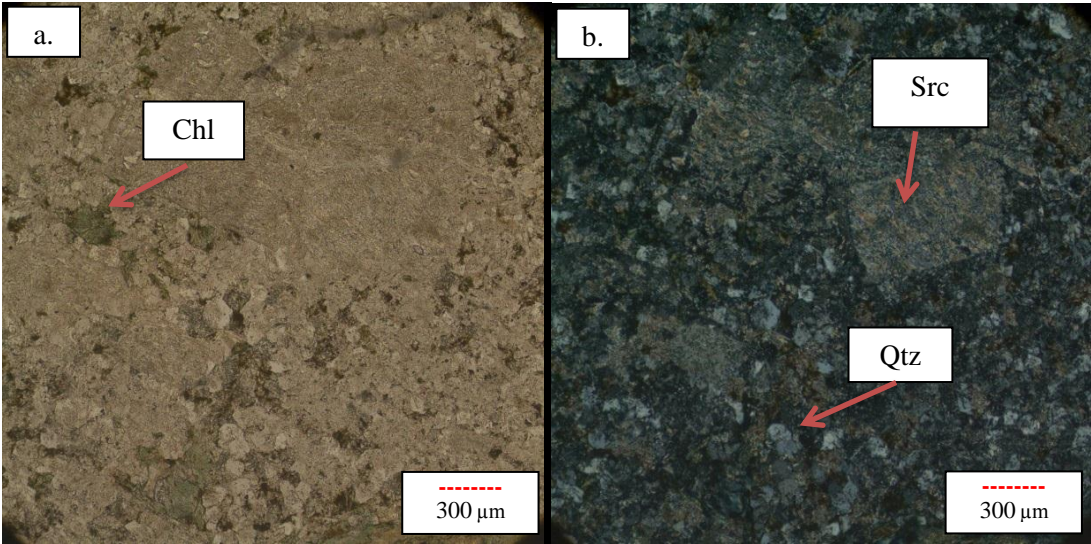


Figure 3-22: Development of chlorite and sericite crystals (on the plagioclase crystals) in a fine grained groundmass of dacite porphyry (Sample CN-3, a. PPL b. XPL)

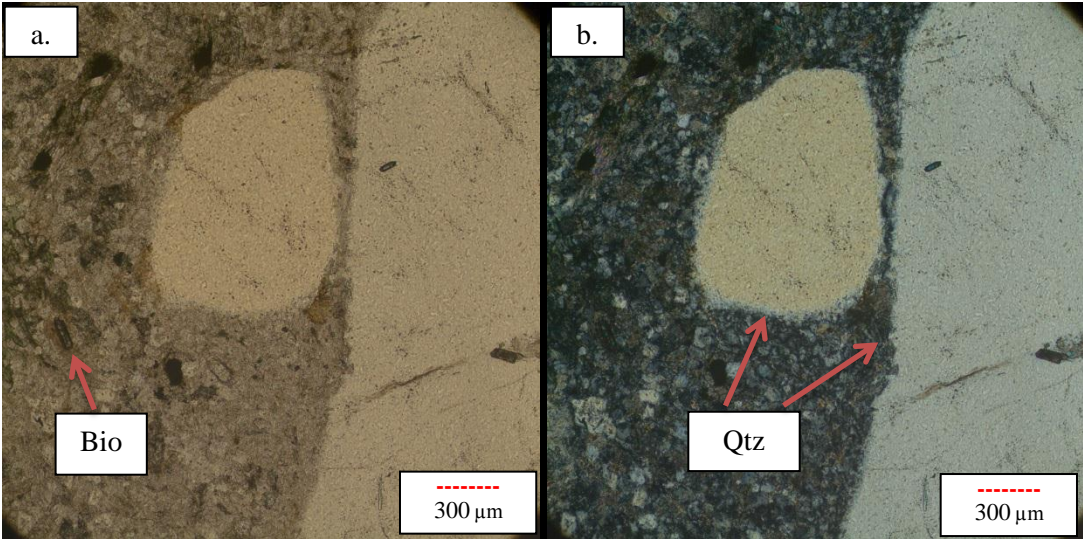


Figure 3-23: Quartz and biotite phenocrysts in a fine grained groundmass of dacite porphyry (Sample CN-5, a. PPL b. XPL)

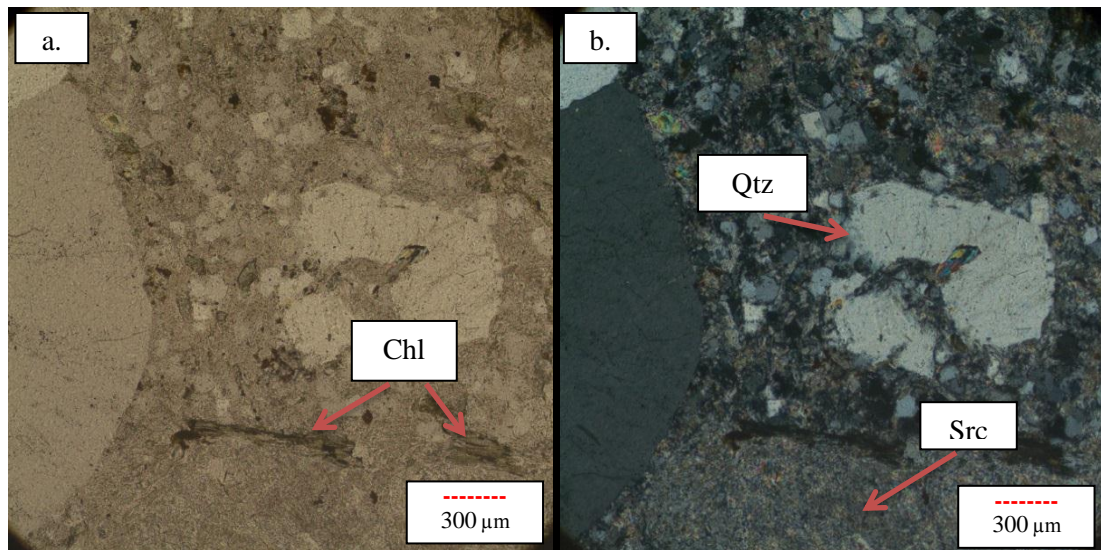


Figure 3-24: Quartz phenocrysts and development of chlorite and sericite crystals (on the feldspars) in a fine grained groundmass of dacite porphyry (Sample CN-8, a. PPL b. XPL)

### 3.2.3. Granites

The third rock type is granite within the CP. The granite samples are mainly composed of K-feldspar, plagioclase, quartz, hornblende and biotite. They display holocrystalline and porphyritic texture (Figs. 3-25, 3-26, 3-27). The K-feldspar crystals have slightly fresh surface and display parallel extinction. They are mainly anhedral and subhedral crystals. The plagioclase minerals display polysynthetic twinning and have mostly subhedral shapes. In some cases, the sericite minerals can be observed on the K- feldspar and plagioclase minerals. The quartz crystals display fresher appearances than K-feldspars and they show typical wavy extinction. Also, some quartz veins are found within these samples. Hornblende crystals show greenish to brownish colors with subhedral to euhedral shapes. Lastly, the biotite crystals can be distinguished by brownish color, mottled extinction and moderate interference colors.

Except for mylonitic deformation zones, there is no indication for the metamorphism on these rocks. The mylonitic zones are also characterized by intensive alteration.

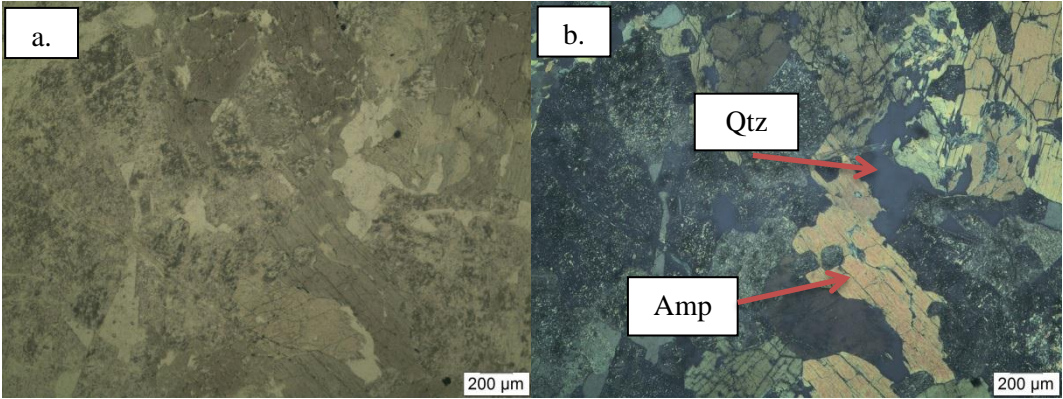


Figure 3-25: Quartz and amphibole crystals in a granite (Sample SL-2, a. PPL b. XPL)

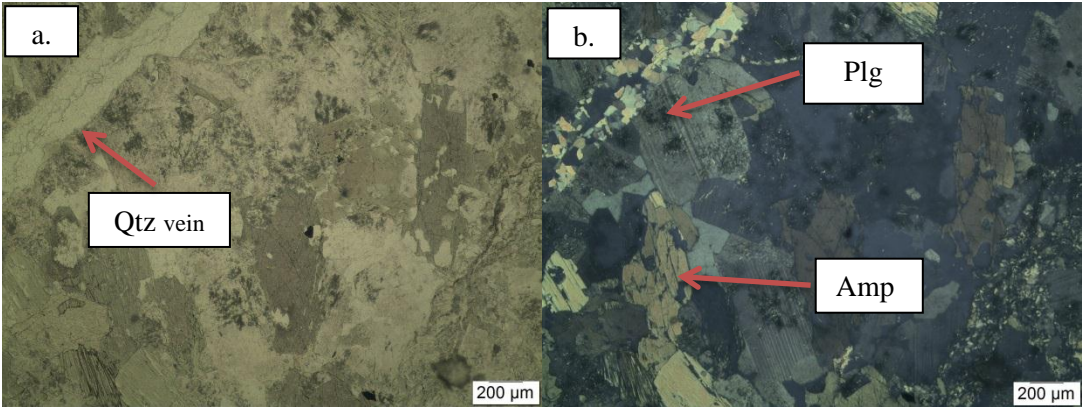


Figure 3-26: Secondary quartz vein, plagioclase and hornblende crystals in a granite (Sample SL-3, a. PPL b. XPL)

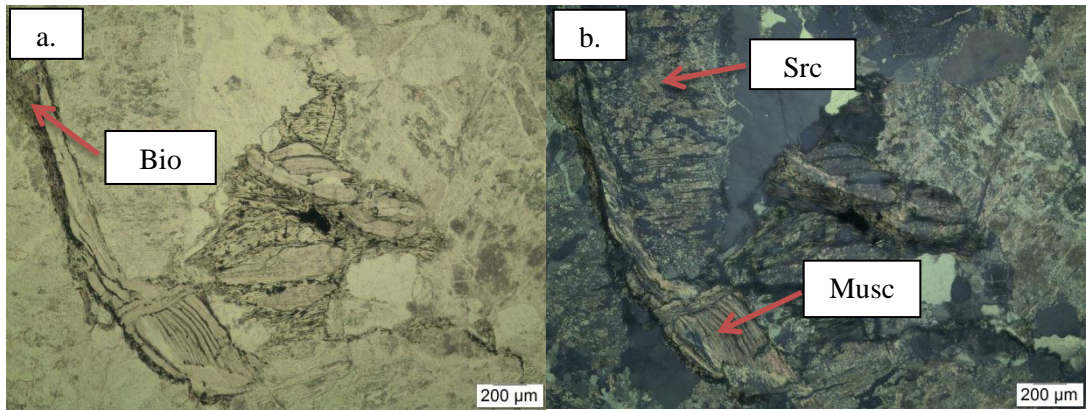


Figure 3-27: Biotite, muscovite and secondary sericite crystals (on the feldspars) in a granite (Sample SL-5, a. PPL b. XPL)



## CHAPTER 4

### GEOCHEMISTRY

#### 4.1. Introduction

The major and trace element data of the metavolcanic rocks within the Çangaldağ Metamorphic Complex (CMC) and the rocks of Çangaldağ Pluton (CP) will be evaluated in this chapter. The possible relationships of all of these magmatic rocks will be evaluated by regarding their whole rock geochemical characteristics.

The freshest samples were selected, and grouped for the geochemical analyses subsequent the petrographical observations on the collected samples along the three selected traverses in the study area (Fig. 2-4). Twenty four metavolcanic rocks for the CMC and eight samples for the CP were geochemically analyzed at the Acme Laboratories (Vancouver-Canada). For the results of analyses, please see Appendices A.

#### 4.2. Major and Trace Element Geochemistry of the Metavolcanic/subvolcanic Rocks within the Çangaldağ Metamorphic Complex

##### 4.2.1. Effects of the Post Magmatic Processes

Highly variable loss on ignition (LOI) values were observed in the metavolcanic rocks (1.4–6.0 wt.%; Appendices A). These values may indicate the effects of both low-grade metamorphism and hydrothermal alteration as also recognized by the petrographic observations. The mobility of large ion lithophile elements (LILE) due

to post-magmatic processes is evidenced when they are plotted against Zr as displayed by the scattering of data points (Fig. 4-1a). High Field Strength Elements (HFSE) and rare earth elements (REE), however, exhibit good correlations, indicating their immobile behavior under the secondary processes (Fig. 4-1b). Therefore, LILE will not be considered hereafter due to their mobile nature (Wood et al., 1976; Pearce, 1975; Floyd et al.; 2000). Instead, the trace elements (Ti, Zr, rare earth elements etc.) that are immobile under low-grade alteration / metamorphism conditions (e.g. Pearce and Cann, 1973; Floyd and Winchester, 1978) will be used for the geochemical evaluation of the studied rocks.

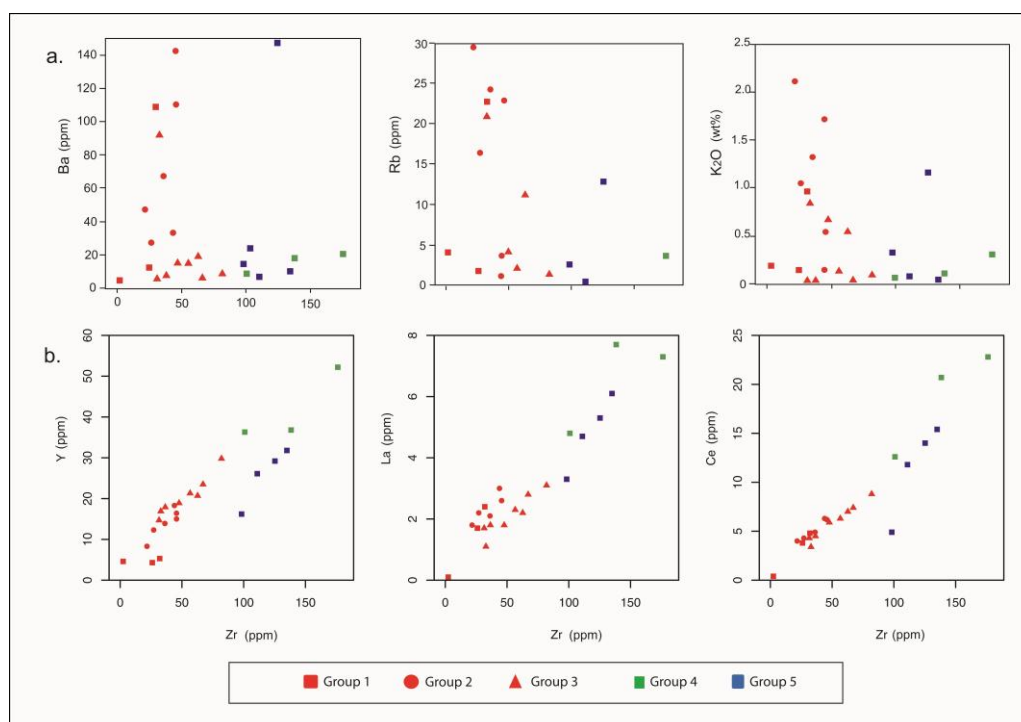


Figure 4-1: Plots of selected major and trace elements vs Zr. Group 1-2-3: Basalts and diabbases; Group 4: Metaandesites; Group 5: Metarhyodacites

#### 4.2.2. Geochemical Classification

All metavolcanic rocks within the CMC show sub-alkaline affinity ( $Nb/Y = 0.01-0.16$ ). Based upon the classification diagram (Pearce, 1996), the samples plot into the basalt, basaltic andesite, andesite and rhyo-dacite fields (Fig. 4-2). Additionally, these rocks were subdivided into several chemical groups based on their trace element systematics. Within these groups, both primitive and evolved members are present. While the groups 1, 2 and 3 include the primitive samples (basalts/diabases), the groups 4 (andesites) and 5 comprise evolved ones (rhyodacites).

Group 1 displays geochemical characteristics similar to boninitic rocks with high  $SiO_2$  (54.33-56.35 wt%) and  $MgO$  (10.35-10.68 wt%) concentrations (Fig. 4-2). Also, the members of this group have higher  $Zr/Ti$  (0.01-0.017) and  $Nb/Y$  (0.16-0.09) values than the other mafic samples. Group 2 and 3 mostly plot in the basalt field except for two samples (basaltic andesite), and largely overlap due to their similar  $Zr/Ti$  and  $Nb/Y$  ratios. Group 4 exhibits andesitic-basaltic andesitic composition (Fig. 4-2), whereas the samples plotting in the rhyolite/dacite field create the Group 5 with higher  $Zr/Ti$  ratios than the other groups.

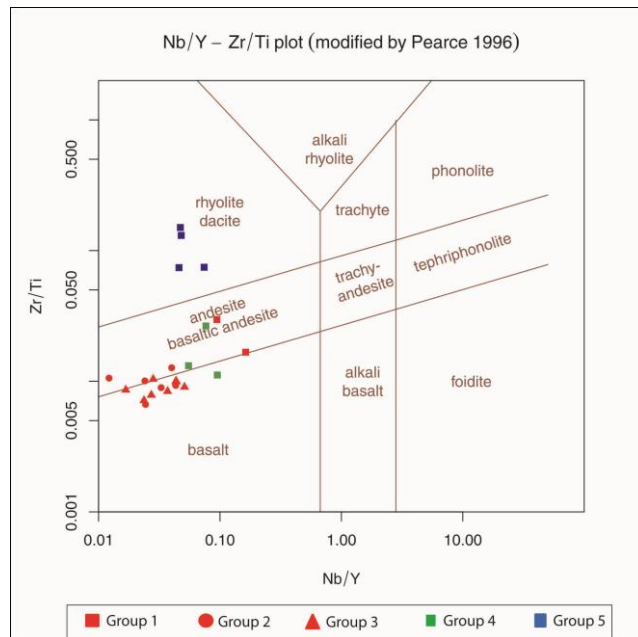


Figure 4-2: Zr–Ti v. Nb–Y (after Pearce 1996) diagram for the metavolcanic rocks of the Çangaldağ Metamorphic Complex. Group 1-2-3: Basalts and diabases; Group 4: Metaandesites; Group 5: Metarhyodacites

In the spider diagrams, Group 1 exhibits highly depleted HFSE contents relative to N-MORB (Nb=0.1-0.6 ppm; Zr=2.4-32 ppm; N-MORB Nb=2.33 ppm; Zr=74 ppm; Sun and McDonough, 1989). Furthermore, this group shows slightly concave REE patterns (except for DR-11) by enrichments ( $[La/Sm]_N = 1.48-3.32$ , where “N” denotes chondrite normalized (values from Sun and McDonough, 1989) of light rare earth elements (LREE) and heavy rare earth elements (HREE) relative to middle rare earth elements (MREE). Group 2 displays highly depleted Nb concentrations similar to Group 1, however it appears to be more enriched in terms of the other HFSE and HREE (Nb=0.2-0.7 ppm; Zr=27.1- 47.7 ppm). Group 1 is also characterized by relatively flat to LREE-depleted chondrite-normalized patterns ( $[La/Sm]_N = 0.68-1.26$ ; Figs. 4-3; 4-4). Group 3 displays HFSE (apart from Nb) and HREE concentrations similar to N-MORB (Nb=0.6-1.3 ppm; Zr=56.6-82 ppm) and it exhibits LREE-depleted patterns ( $[La/Sm]_N = 0.64-0.80$ ) (Figs. 4-3, 4-4). Among the

evolved groups, Group 4 is characterized by slight depletion in Ti and Eu and display more enriched patterns in terms of the other HFSEs (Nb=2-4 ppm; Zr=100.9-176.2 ppm) and REEs ( $[La/Sm]_N = 0.80-1.15$ ). However, the second evolved group (Group 5) displays significant anomalies in Ti and Eu and small enrichments (Figs. 4-3, 4-4) in the rest of the HFSEs (Nb= 1.2-3.5 ppm; Zr=98.3-135) and REEs ( $[La/Sm]_N = 1.11-2.69$ ).

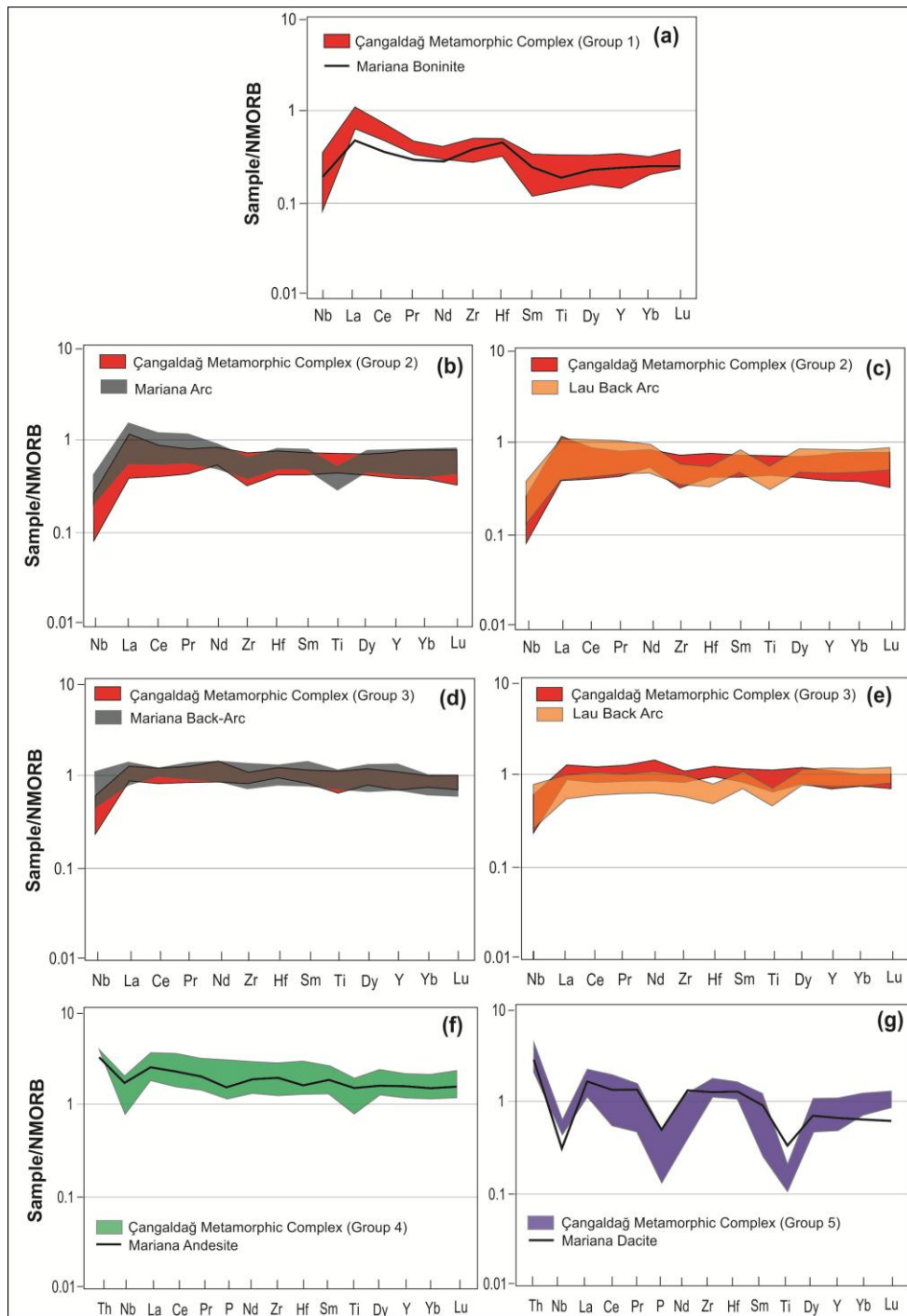


Figure 4-3: N-MORB normalized multi element spider diagrams (Sun and McDonough, 1989); the data of Mariana and Lau arc-back arc basin samples taken from Pearce et al. (1995, 2005). a. Group 1: Boninites; b-c. Group 2: Island arcs; d-e. Group 3: Back-arc basin basalts; f. Group 4: Metaandesites; g. Group 5: Metarhyodacites

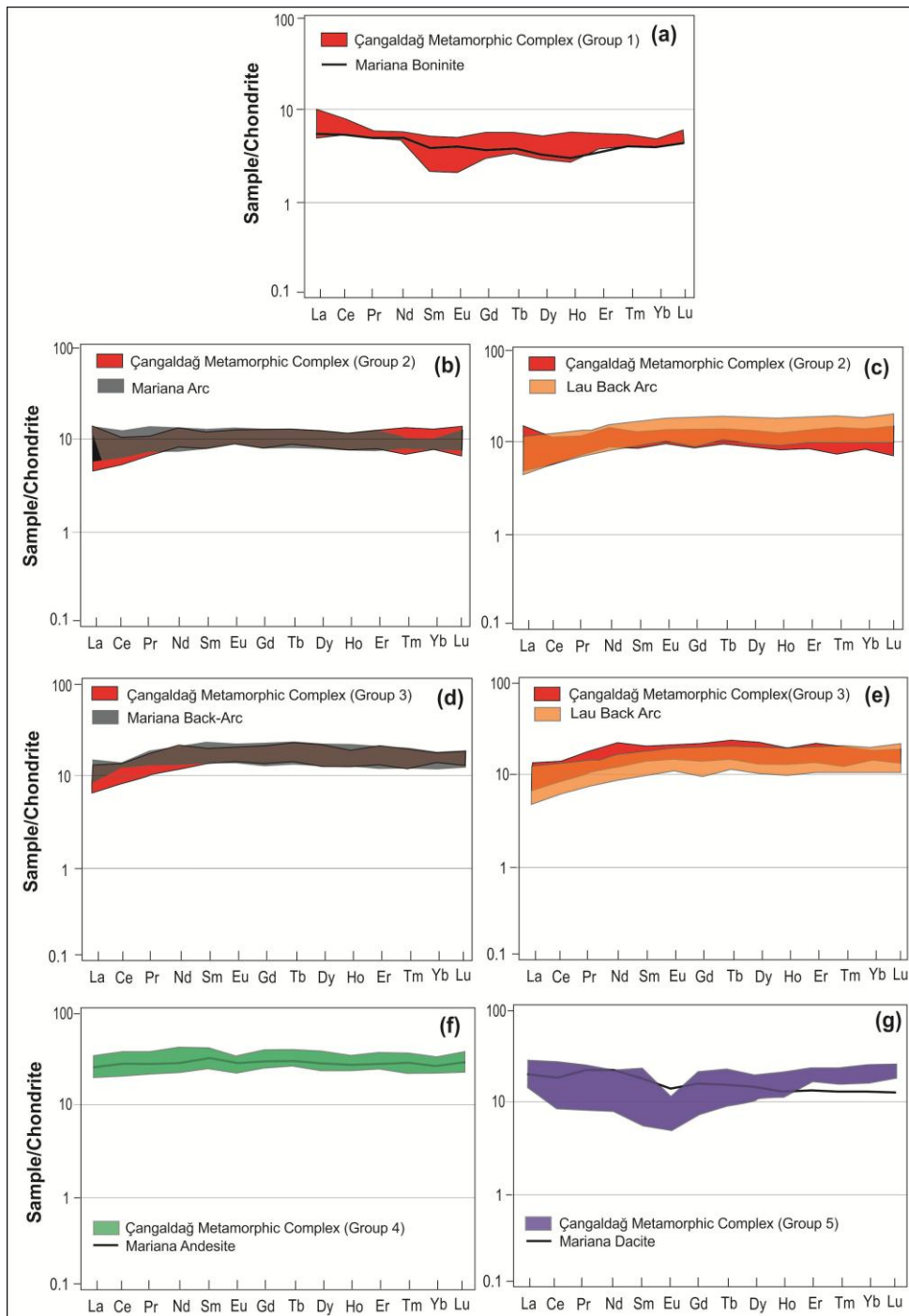


Figure 4-4: Chondrite normalized REE spider diagrams (Sun and McDonough, 1989); the data of Mariana and Lau arc-back arc basin samples taken from Pearce et al. (1995, 2005). a. Group 1: Boninites; b-c. Group 2: Island arcs; d-e. Group 3: Back-arc basin basalts; f. Group 4: Metaandesites; g. Group 5: Metarhyodacites.

### **4.2.3. Petrogenesis**

#### **4.2.3.1. Fractional Crystallization**

To define the possible effects of fractional crystallization, binary diagrams were used some trace elements including Ce, Y, La and Zr. When Ce, Y and La are plotted against Zr (Fig. 4-1b) an increasing trend can be traced from the basic groups towards the evolved ones. It must be noted, however, that Group 4 has overlapping or higher Zr, Ce, Y and La concentrations than Group 5 (Fig. 4-1b). The increasing concentrations of the incompatible elements in the evolved members may indicate the role of fractional crystallization during the evolution of the rocks. The decreasing concentrations of  $\text{Cr}_2\text{O}_3$  (Group 1-2-3= 0.06 wt %; Group 4= less than 0.002 wt %; Group 5= less than 0.002 wt %) and Ni (Group 1-2-3= 79.90 ppm; Group 4= 4.26 ppm; Group 5= 1.40 ppm) from the basic groups towards the evolved ones also back up the idea of fractionation during evolution (Appendices A). The effect of fractional crystallization is best observed on Group 5 that displays significant depletions in Ti and Eu, which may suggest fractionation of Ti-oxides and plagioclase. However, it must be noted that Group 5 does not seem to have been evolved from Group 4 due to the lower element enrichments levels (Figs. 4-3, 4-4).

#### **4.2.3.2. Mantle Source Characteristics**

The basic groups were taken into account to minimize the effects of fractional crystallization in order to characterize the mantle source(s) of the metavolcanic rocks within the CMC. The plots of Zr/Y vs Nb/Y and La/Yb vs Zr/Nb ratios can reveal important information related to the possible mantle sources (Fig. 4-5a; Sayit et al., 2016; Fig. 4-5b; Aldanmaz et al., 2000). The lower Zr/Y (0.52-6.04) and Nb/Y (0.02-0.16) values of the Çangaldağ samples may indicate derivation from a depleted mantle source (N-MORB Zr/Y= 2.64; Nb/Y= 0.08; Sun and McDonough, 1989). This idea is supported by the lower La/Yb (0.17-3.63) and higher Zr/Nb (37.14-228)

ratios, indicating involvement of a depleted mantle source in the petrogenesis of Çangaldağ metavolcanic rocks (N-MORB La/Yb= 0.81; Zr/Nb= 31.75). Such low ratios of Zr/Nb, Zr/Y and Nb/Y are also found in the basalts of the Mariana arc-back-arc system and Lau Basin in which depleted mantle sources are involved (Fig. 4-5), therefore further reinforcing the idea above.

As mentioned before, Group 1 shows boninite-like characteristics with highly depleted HFSE signatures. The boninitic nature is also confirmed by the similarity of the trace element patterns of Group 1 with the Mariana Arc boninite (Pearce et al., 1992). While such arc-like characteristics of Group 1 suggest the involvement of subduction component in their mantle source (e.g. Pearce and Peate, 1995), the depletions in HFSE may indicate different conditions in the mantle source such as stability of minor residual phases (e.g. zircon and titanite; Dixon and Batiza, 1979), re-melting of previously depleted mantle source (Green, 1973; Duncan and Green, 1987; Crawford et al., 1989) or high degree of partial melting (Pearce and Norry, 1979).

Like Group 1, Group 2 also shows subduction-related characteristics with enrichments in LREE over HFSE. This idea is supported by the fact that the Group 2 samples exhibit similar trace element systematics of the basalts from the Mariana Arc and Lau Basin (Pearce et al., 1995, 2005). This indicates that Group 2 has also derived from a subduction-modified mantle source. Group 3 also shares similar geochemical characteristics with the other primitive groups in that it reflects a subduction-related component in their mantle source. The difference, however, is that the overall characteristics of Group 3 samples are rather akin to those generated in back- arcs rather than island arcs. This group too reflects geochemical signatures indicating contribution of slab-derived components (Pearce et al., 1995, 2005; Figs. 4-4, 4-5).

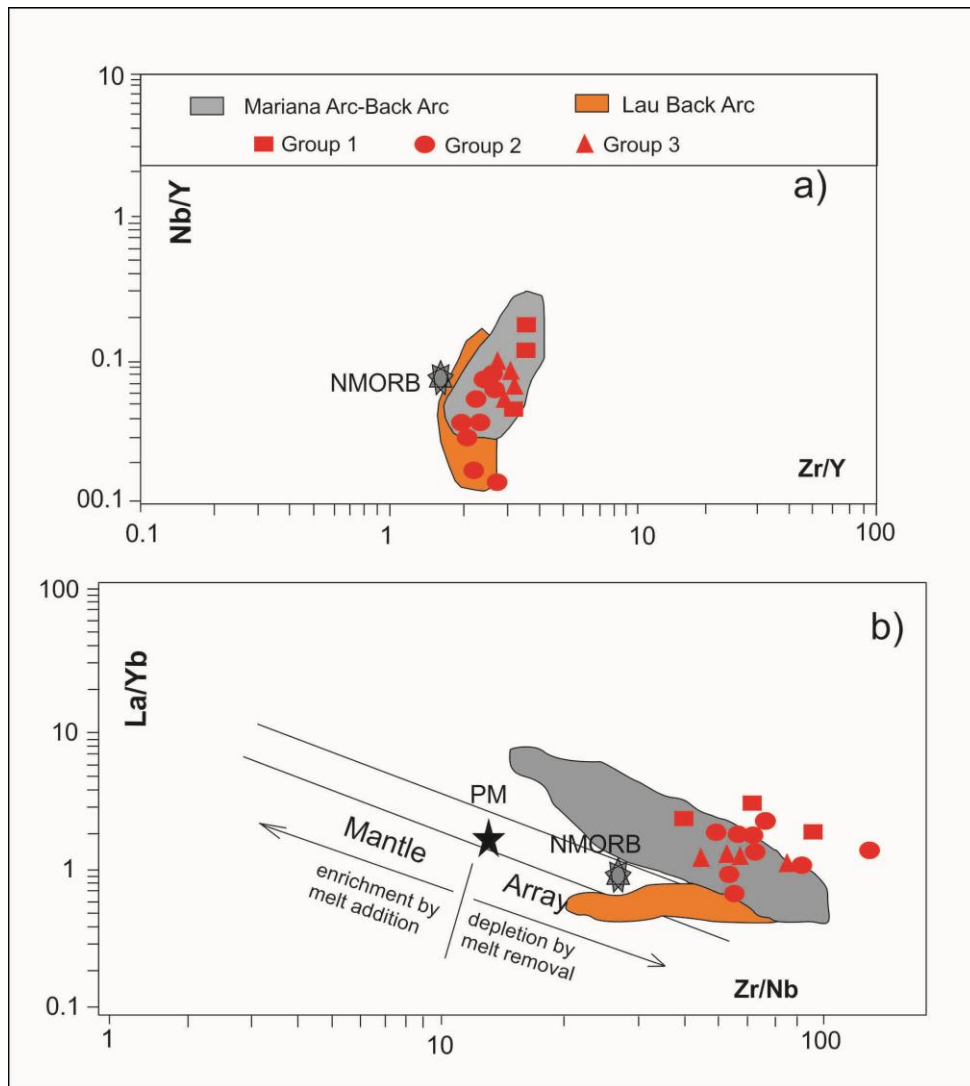


Figure 4-5: a. Nb/Y vs Zr/Y (Sayit et al., 2016) and b. La/Yb vs Zr/Nb (Aldanmaz et al., 2008) diagrams for the metavolcanic rocks of the CMC; the data of Mariana and Lau arc-back arc basin samples taken from Pearce et al. (1995, 2005). Group 1: Boninites; Group 2: Island arcs; Group 3: Back arc basalts

#### 4.2.3.3. Partial Melting

The  $\text{TiO}_2$ -Yb (Gribble et al., 1998) and Sm vs Sm/Yb (Sayit et al., 2016) diagrams (Fig. 4-6) were used in order to understand the melting systematics of the basic metavolcanic rocks from the CMC. In this regard, the samples with MgO

concentrations higher than 8 wt% were used in both diagrams to avoid the effects of fractional crystallization as much as possible. For the first diagram, the curve of “spinel lherzolite” is for non-modal batch melting and is labeled with degrees of  $F$  (estimate of degree of melting) for ‘primitive mantle’ (PM) source concentrations of 0.217%  $\text{TiO}_2$  and 0.493 ppm Yb (Sun and McDonough, 1989),  $D_0 = 0.117$  and 0.127 (modal bulk coefficient) for a lherzolite composition ol: opx: cpx of 54:30:16, and  $P = 0.325$  and 0.397 (non-modal bulk partition coefficient) for ol: opx: cpx melting proportions of 0:30:70. The curve of “garnet lherzolite” is for non-modal batch melting of a garnet lherzolite ‘primitive mantle’ source with ol: opx: cpx: gar composition and melt proportion of 52:29:16:3 and 0:45:45:10, respectively.  $D_0$  and  $P$  are 0.127 and 0.247 for  $\text{TiO}_2$ , and 0.288 and 0.684 for Yb. Both curves are labeled for from 5 to 40% melting (calculations taken from Gribble et al., 1998).

The modelling plots suggest that the members of Group 1 have been formed at the highest degree of partial melting (higher than 40%) from a spinel or garnet lherzolitic source. Group 2 follows Group 1 by lower degrees of partial melting with 20-30 %. Group 3, on the other hand, appears to have been formed at the lowest degrees of partial melting among three with 10-25 %. The extreme values observed in Group 1, however, are rather unrealistic. Instead, re-melting from a pre-depleted mantle source seems more plausible for the petrogenesis of this group (Green, 1973; Duncan and Green, 1987; Crawford et al., 1989). In order to confirm this idea, another diagram was used, which uses Sm-Yb systematics (Sayit et al., 2016) (Fig. 4-6b). Here, the mode of spinel peridotite source is 0.565 Ol + 0.220 Opx + 0.180 Cpx + 0.035 Spi. In constructing second curve, however, first 25% batch melt is extracted from the spinel peridotite source and the residue is modified by 1% garnet-facies melt. This metasomatized source is assumed to have a mode of 0.700 Ol + 0.220 Opx + 0.065 Cpx + 0.015 Spi, which melts in a fractional fashion with the proportions of 0.20 Ol + 0.15 Opx + 0.55 Cpx + 0.10 Spi (calculations taken from Sayit et al., 2016). This model shows that the Group 1 samples may indeed have been formed by re-melting of a pre-depleted source. In conclusion, while the trace element systematics of Group

2 and 3 metavolcanic rocks can be explained by different degrees of partial melting from a depleted spinel lherzolitic source (Fig. 4-6a), the highly depleted characteristics of Group 1 requires melting from a pre-depleted mantle source (Fig. 4-6b).

Based on the results above, the increasing degree of enrichments in HFSE and REE from Group 1 to Group 3, are more likely to be related to partial melting and previous melt extraction rather than fractional crystallization. In addition, H<sub>2</sub>O-rich fluids were reported to have an important role on the degree of melting of the mantle (Davies and Bickle, 1991; Stolper and Newman, 1994; Taylor and Martinez, 2003; Langmuir et al., 2006). Thus, the different degrees of partial melting observed in Group 2 and 3 may have been caused by the effect of water derived from the subduction processes (Keller et al., 1992).

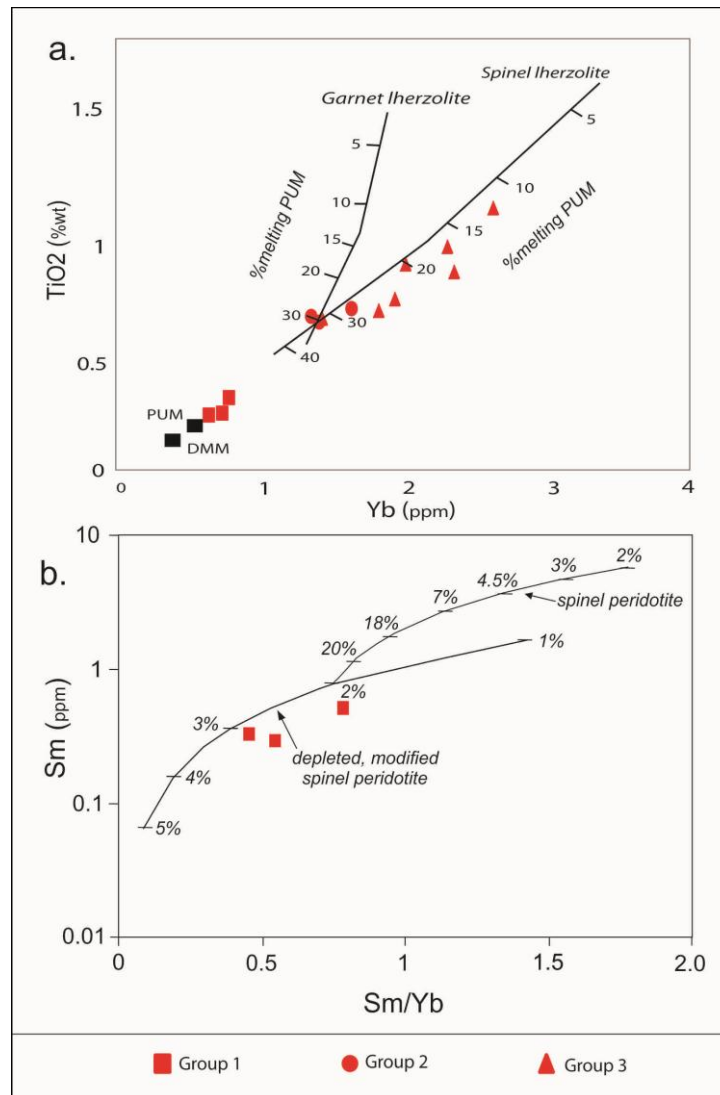


Figure 4-6: a.  $TiO_2$  – Yb (Gribble et al., 1998) and b. Sm vs Sm/Yb (Sayit et al., 2016) partial melting diagrams for the primitive metavolcanic rocks of the Çangaldağ Metamorphic Complex.

#### 4.2.3.4. Tectonomagmatic Discussion

When the samples from CMC with relatively high MgO (i.e. the basic groups 1, 2 and 3) are considered, they all exhibit the contributions from slab-derived component, which is typical in magmas generated in subduction-related settings

(Pearce and Peate, 1995). This idea is also supported by the diagrams constructed by Shervais (1982) and Meshede (1986), where the Çangaldağ samples plot in the arc-related regions (Fig. 4-7). Furthermore, all the primitive samples display depleted HFSE and HREE characteristics (N-MORB-like or even lower). When combined with the presence of subduction-related signatures, this may suggest that the Çangaldağ samples may have formed in an intra-oceanic subduction system (Peate et al., 1997; Pearce et al., 1995). Among three groups, however, Group 1 and 2 possess HFSE and HREE contents apparently lower than N-MORB, suggesting that they may have formed in the arc region of an oceanic arc-basin system. The boninitic Group 1 samples are especially indicative for generation at fore-arc region (Pearce et al., 1992). N-MORB-like features of Group 3, on the other hand, are more consistent with its generation in the back-arc region.

The idea that the Çangaldağ metavolcanic rocks represent the remnants of an intra-oceanic arc-basin system as proposed by this study is in general agreement with that of Ustaömer and Robertson (1999) who interpreted the same assemblage to have been generated in an oceanic arc. However, the idea that the CMC (similar with Nilüfer Unit from the Karakaya Complex) represents an oceanic plateau or oceanic islands as suggested by Okay et al. (2006) is not supported by the present findings. Here, it must be noted that this idea was revised as the presence of arc-related magmatism for the origin of the CMC in Okay et al. (2013, 2014) regarding the geochemical data that had been already reported in the study of Ustaömer and Robertson (1999). Therefore, overall geochemical data indicate that the metavolcanic rocks of the CMC were generated in an intra-oceanic fore-arc-arc-back arc basin environment.

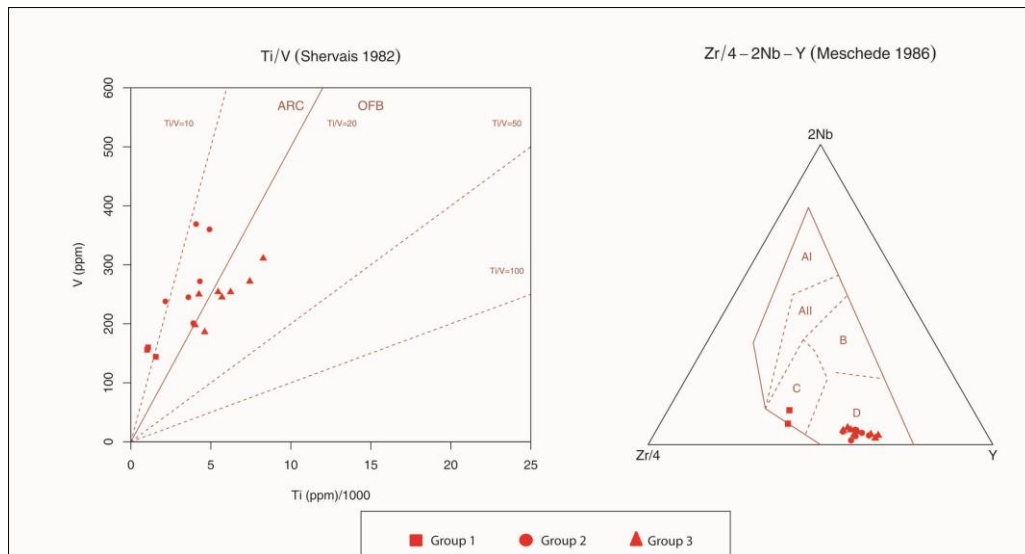


Figure 4-7: Geotectonic discrimination diagrams a) after Shervais (1982), b) after Meschede (1986)

### 4.3. Major and Trace Element Geochemistry of the Çangaldağ Pluton

#### 4.3.1. Geochemical Classification

The rocks of the CP plot into the gabbroic diorite, diorite, granodiorite (extrusive equivalent: dacite porphyry) and granite fields based upon the geochemical classification diagram (Fig. 4-8; Middlemost, 1985). The SiO<sub>2</sub> concentrations of the rock groups are as follows: diorites (between 52-55 wt%), dacite porphyry samples (between 66-68 wt%) and granite sample (73 wt%). All of these rocks have similar Na<sub>2</sub>O + K<sub>2</sub>O concentrations which change in a narrow range (4–6 wt%).

According to the several geochemical discrimination diagrams (Peccerillo and Taylor, 1976; Frost et al., 2001; Chappell and White, 2001), they plot into the subalkaline, calc-alkaline, magnesian and I-type fields, respectively (Fig. 4-9a, b, c, d). Of note, the granite sample is plotting near the S-type field (Fig. 4-9d). While all

of the types of these rocks display lower  $\text{Na}_2\text{O}$  and  $\text{K}_2\text{O}$  values compared to the alkaline rocks, they have higher concentrations compared to the tholeiitic and S-type granitoids.

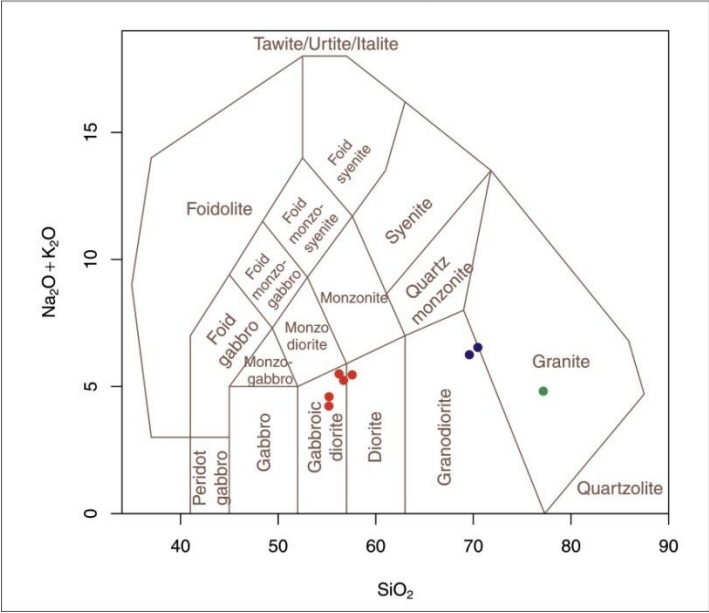


Figure 4-8: Geochemical classification of the Çangaldağ Pluton (Middlemost, 1985)

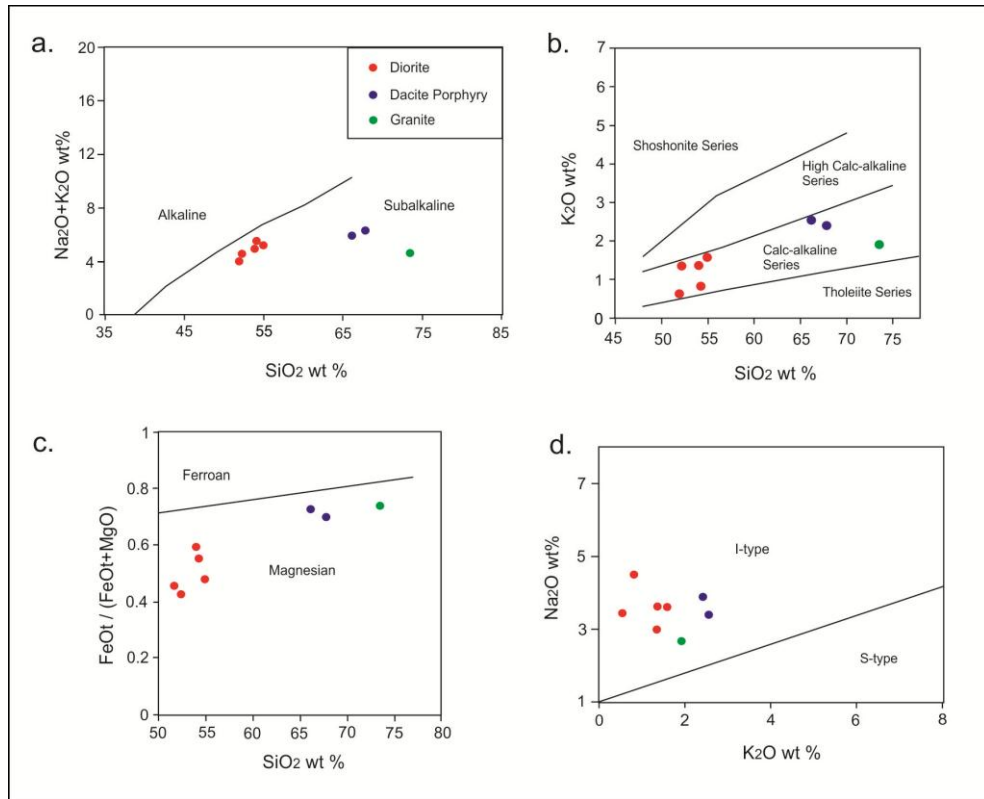


Figure 4-9: Geochemical discrimination diagram for the Çangaldağ Pluton a. Total alkali silica diagram b.  $K_2O$  vs  $SiO_2$  diagram (Peccerillo and Taylor, 1976) c.  $FeO_t / (FeO_t + MgO)$  vs  $SiO_2$  diagram (Frost et al., 2001) d.  $Na_2O$  vs  $K_2O$  diagram (Chappell and White, 2001).

The N-MORB and chondrite normalized multi element and rare earth element diagrams (Sun and McDonough, 1989) provide significant information in order to evaluate the characteristics of the magmatic rocks (Fig. 4-10a, b). All patterns show LILE / HFSE ( $[Th/Nb]_N = 18.53 - 31.96$ ; N:NMORB-normalized) and LREE / HREE ( $[La/Yb]_N = 3.60 - 11.78$ ; N: Chondrite-normalized) enrichments coupled with Nb (2.2-6.7 ppm) and Ti (0.09-0.63 wt%) anomalies in different levels, respectively (N-MORB Nb=2.33 ppm; Ti=0.76 wt%; Sun and McDonough, 1989). Only, the granite sample displays obviously different geochemical pattern, in particular, coupled with positive Eu anomaly (Fig 4-10a, b). All of these magmatic rocks show similar geochemical patterns with the volcanic arc granites (Pearce et al., 1984).

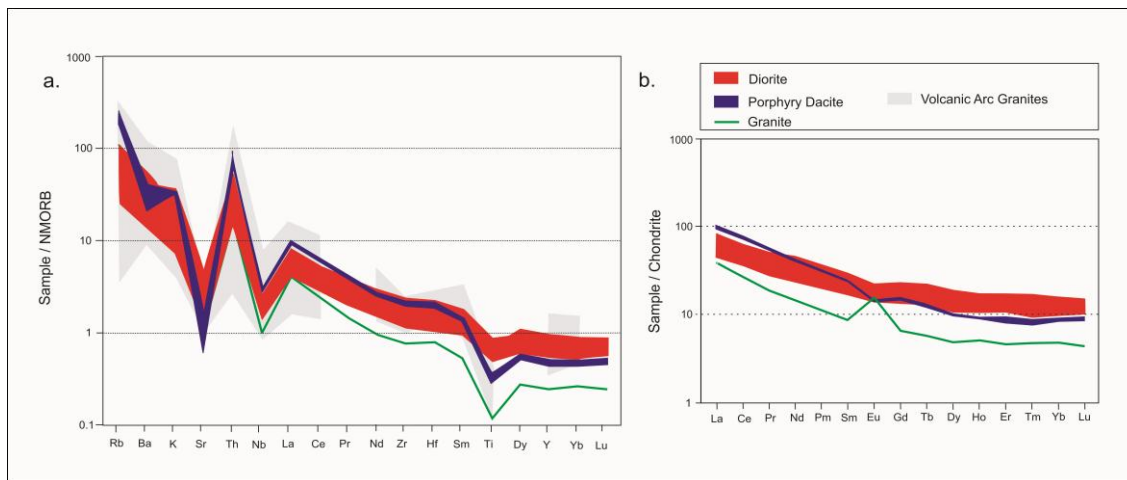


Figure 4-10: a. N-MORB normalized multi-element diagram b. Chondrite normalized rare earth element diagram. N-MORB and Chondrite normalization values are from Sun and McDonough (1989). Volcanic arc granites data from Pearce et al. (1984).

### 4.3.2. Petrogenesis

The variation diagrams were used by regarding the major ( $\text{MgO}$ ,  $\text{CaO}$ ,  $\text{K}_2\text{O}$ ,  $\text{TiO}_2$ ) and trace (Rb, La) elements vs  $\text{SiO}_2$  (Fig. 4-11) in order to identify the effects of fractional crystallization on the CP samples. All of these variation diagrams show the presence of the distinct fractional crystallization effect between diorite and dacite porphyry samples. While the incompatible elements (Rb, La,  $\text{K}_2\text{O}$ ) show positive trends with  $\text{SiO}_2$ ,  $\text{MgO}$ ,  $\text{TiO}_2$  and  $\text{CaO}$  display negative trends by increasing of  $\text{SiO}_2$  concentrations (Fig. 4-11). The  $\text{MgO}$  concentrations obviously decrease from diorite samples to the dacite porphyry samples (diorites = 4.35-8.22 wt%; dacite porphyries = 1.11 and 1.29 wt%) which indicate the presence of fractional crystallization (Appendices A). Moreover, the decreasing in  $\text{Cr}_2\text{O}_3$  (diorites = 0.015 – 0.072 wt %; Dacite porphyries = 0.004 and 0.006 wt%) and Ni (diorites = 22 - 150 ppm; dacite porphyries = 20 ppm) concentrations from the diorites to the dacite porphyry samples

also back up the idea of fractionation during evolution (Appendices A). In particular, these negative trends can be explained by crystallization of the more felsic minerals (i.e. feldspar). In other words, they indicate the fractionation of more mafic minerals such as clinopyroxene and Ca-rich plagioclase during the evolution of the rocks.

Among the magmatic rocks of the CP, the granite sample exhibits different behavior compared to the other samples (MgO = 0.50 wt%; Cr<sub>2</sub>O<sub>3</sub> = 0.010 wt%; Ni = 20 ppm; Fig. 4-11). This unlike behaviour may indicate the presence of different mantle source for the granite sample. In addition to that, this result is supported by different REE element pattern (positive Eu anomaly) for granite sample (Fig. 4-10a, b). On the other hand, the depletions in Ti and Eu (fractionation of clinopyroxene, Ti-oxide and plagioclase minerals) confirm the presence of effective fractional crystallization process for diorite and dacite porphyry samples (Fig. 4-10a, b). The fractionation of Ti-oxide and clinopyroxene minerals (Dixon and Batiza, 1979) can cause depletion in Ti concentrations.

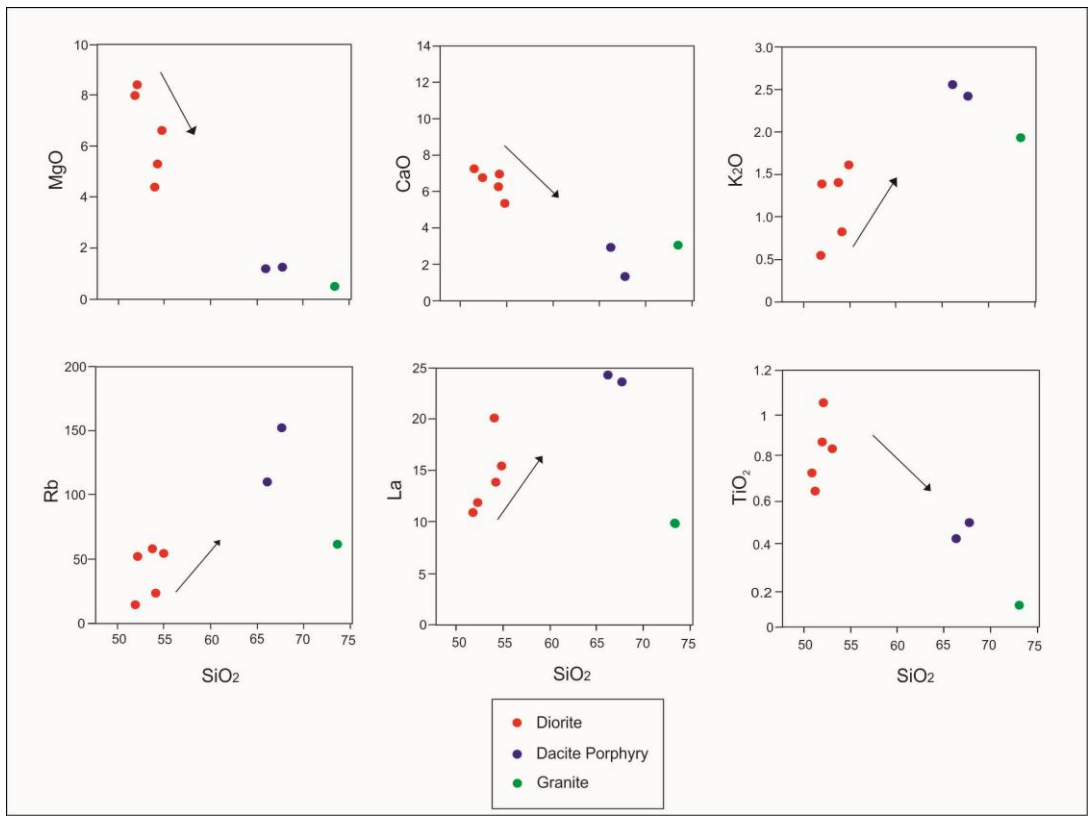


Figure 4-11: Harker variation diagrams for selected major (wt %) and trace (ppm) elements

The parental melts of the granitoids can be derived by the partial melting of mafic to felsic crustal rocks (Tepper et al., 1993; Roberts and Clemens, 1993). The major oxide ratios play an important role in order to determine possible source rocks for the granitoids (Patino Douce, 1999).

For instance, the partial melting mafic source such as amphibolites may cause the lower  $Al_2O_3 / (Fe_2O_3 + MgO + TiO_2)$  and  $Na_2O + K_2O / (Fe_2O_3 + MgO + TiO_2)$  ratios compared to the more felsic sources (greywacke, pelite). On the other hand, the lower values of  $Al_2O_3 + Fe_2O_3 + MgO + TiO_2$  and  $Na_2O + K_2O + Fe_2O_3 + MgO + TiO_2$  can indicate the deriving from more felsic sources (Patino Douce, 1999; Fig. 4-12).

The rocks of CP (except for granite sample) plot into the amphibolitic source field (Fig. 4-12). The geochemical characteristic of this sample, once again, indicates the presence of different mantle source compared to the diorite and dacite porphyry samples. While the diorites and dacite porphyries could be derived from an amphibolitic source, the granite can be product of the partial melting of a more felsic source such as greywake (Fig. 4-12). Sedimentary source for the granite sample is also confirmed by these results.

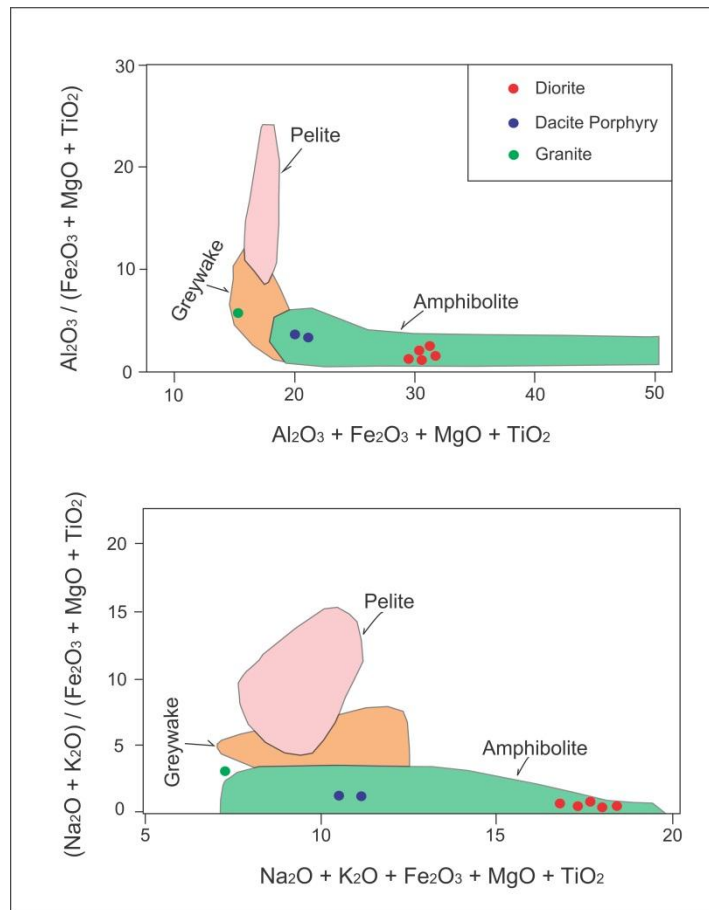


Figure 4-12: Plots showing compositional fields of experimental melts derived from partial melting of pelite, greywake and amphibolite. Data from Patino Douce (1999)

### 4.3.3. Tectonomagmatic Characteristics

The rocks of the CP display similar characteristics with volcanic arc granites (Fig. 4-13a; Pearce et al., 1984). The diorite samples have lower Rb values (14.6-57.1 ppm) compared to the granite (61.4 ppm) and dacite porphyries (109.2-151.1 ppm), respectively. Ta values are in 0.2-0.4 ppm for diorites, 0.6-0.7 ppm for dacite porphyries and 0.2 ppm for granite. Also, Y+Nb values change between 9-29.6 ppm. For instance, the lower Ta and Nb values suggest the effect of dehydrated slab component in the mantle source (Pearce et al., 2005). All of these values indicate arc magmatism for the CP. Additionally, the LILE and LREE enrichments (coupled with Nb anomalies) relative to HFSE and HREE represent subduction modified mantle source characteristics (Fig. 4-10a, b; Pearce et al., 1992; Pearce and Peate, 1995). In other words, they all exhibit the contribution of slab-derived component, which is typical in magmas generated in subduction-related settings (Pearce and Peate, 1995).

Th/Hf vs Ta/Hf and Th/Ta vs Yb discrimination diagrams were used in order to understand the type of arc magmatism (Schandl and Gorton, 2002; Fig. 4-13b). Particularly, Th is an useful element that gives important information about the source characteristics (Pearce and Peate, 1995). Both of these diagrams suggest a continental arc magmatism for the CP by higher Th/Hf (0.84-2.74) and lower Ta/Hf (0.05-0.17) ratios compared to the within plate volcanic zones and lower Th/Ta (9.75-16.5) compared to the oceanic arcs, respectively (Fig. 4-13b).

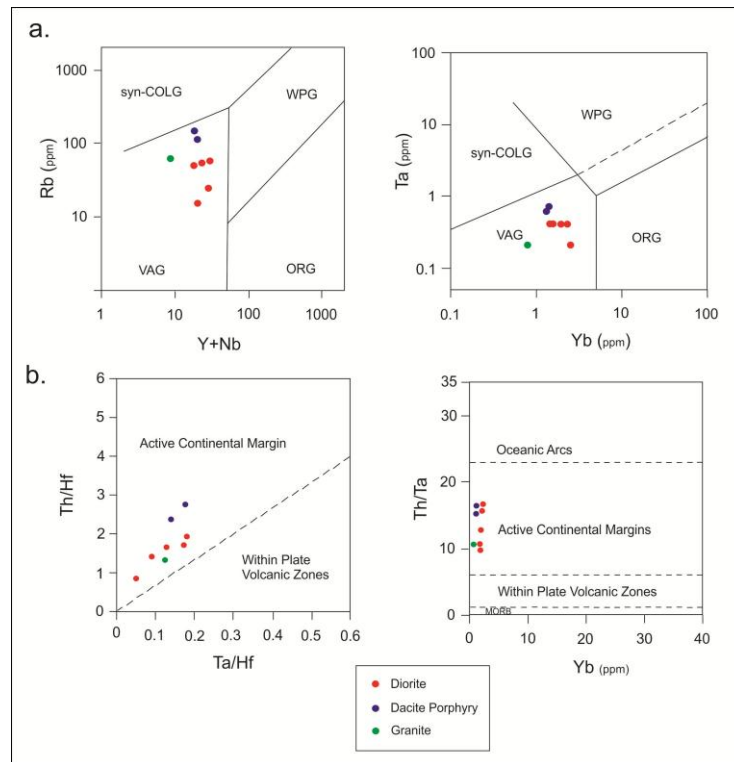


Figure 4-13: Geotectonic discrimination diagrams for the Çangaldağ Pluton a. Pearce et al., 1984 b. Schandl and Gorton (2002)

Additionally, this result is confirmed by Nb/Y vs Zr/Y and Th/Yb vs Nb/Yb ratio diagrams (Fig. 4-14) which also confirm the presence of continental arc magmatism. They display higher Nb/Y (0.13-0.54), Zr/Y (23.13-44.05), Th/Yb (1.26-7.27), Nb/Yb (1.30-4.96) ratios compared to oceanic arc magmatism (Condie and Kröner, 2013). All of these element ratios (Fig. 4-14) mostly display higher values than N-MORB and E-MORB (Sun and McDonough, 1989) sources which support the developing of continental arc magmatism.

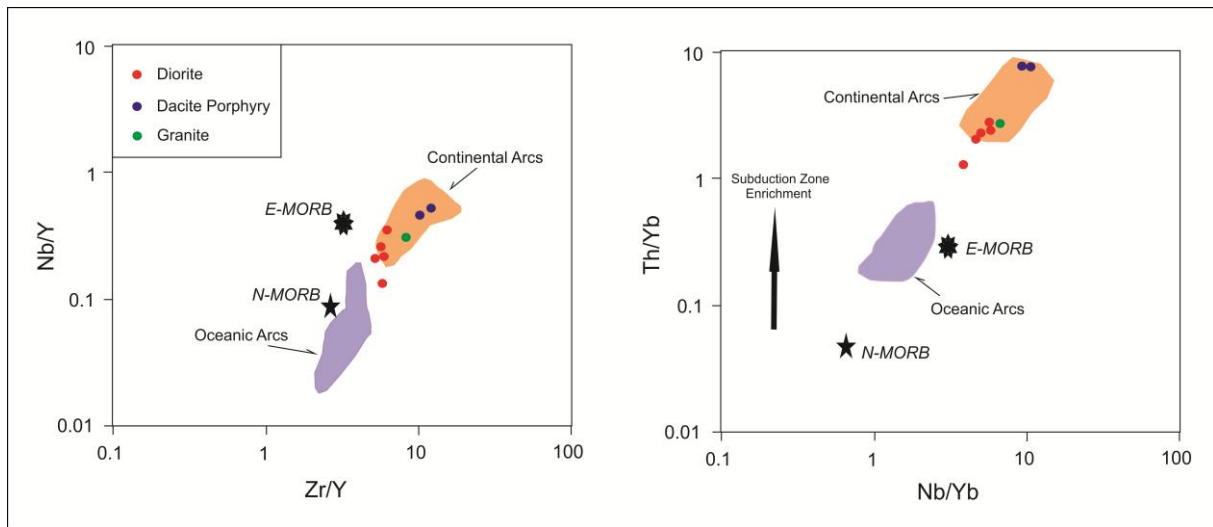


Figure 4-14: Nb/Y vs Zr/Y and Th/Yb vs Nb/Yb diagrams. Oceanic Arc and Continental Arcs values are from Condie and Kröner (2013). Average N-MORB and E-MORB values are from Sun and McDonough (1989)

In addition to the CP, 3 orthogneiss samples (Pre-Permian) from Devrekani Metamorphics were analyzed in order to understand the geochemical characteristics of their protoliths. As stated by Gücer and Arslan (2015), they show typical features of I-type calc-alkaline volcanic arc granitoids.

## CHAPTER 5

### U-Pb GEOCHRONOLOGY and Hf ISOTOPE SYSTEMATICS

#### 5.1. U-Pb Geochronology

The U-Pb geochronometers are amongst the most reliable radiometric methods for determining the age of igneous rocks. They are based on the decay of U to Pb isotopes ( $^{238}\text{U}$ - $^{206}\text{Pb}$  and  $^{235}\text{U}$ - $^{207}\text{Pb}$ ). These chronometers have been successfully applied to date magmatic rocks, which formed from a few million years ago to more than billion years of years in the past (e.g., Schmidberger et al., 2005; Simonetti and Neal, 2010; Isozaki et al., 2015; Köksal et al., 2013).

Zircon is a very useful mineral for U-Pb radiometric dating because it is a robust mineral and resistant to various secondary processes such as metamorphism, hydrothermal and surface alterations. Zircon can easily accommodate U but not Pb into its crystal structure at the time of crystallization. Thus, any Pb which accumulates within zircon is deemed radiogenic in origin, and hence forms the basis for the geochronometer since the decay constants for both  $^{235}\text{U}$  and  $^{238}\text{U}$  are well characterized. Additionally, zircon has a very high closure temperature (>900°C), which provides reliable results for dating (Flowers et al., 2005). Also, several other important U-bearing accessory minerals (apatite, nicolite, titanite, perovskite, baddeleyite) have been employed for in-situ U-Pb dating purposes (e.g., Bizzarro et al., 2002; Chen and Simonetti, 2014; Chen et al., 2013; Gumsley et al., 2015; Rasmussen et al., 2013; Köksal et al., 2004).

Recently, in-situ U-Pb dating of accessory minerals has become a more widely practiced technique instead of conventional single grain evaporation method, which

yields much more reliable data (e.g. Simonetti et al., 2005; Bianca et al., 2015; Zhu et al., 2015; Hu et al., 2014). One reason is that distinct magmatic events can be dated from core vs. rims of single mineral grains by using small laser spot sizes (e.g.,  $\leq 20$  microns). Moreover, it is cheaper and is characterized by rapid analysis duration with a simple sample preparation process compared to Isotope Dilution Thermal Ionization Mass Spectrometry (ID-TIMS), and Secondary Ion Mass Spectrometry (SIMS) techniques. In contrast, bulk zircon analysis will result in the masking of different magmatic and possibly metamorphic information present at the micron-scale.

In total, 8 samples (3 from Çangaldağ Metamorphic Complex (CMC), 2 from Çangaldağ Pluton (CP), 1 from orthogneiss (it cuts the Devrekani Metamorphics), 1 from Devrekani metadiorite (it cuts the Devrekani Metaophiolite), and 1 from diorite (Devrekani Granitoid) were investigated for geochronological purposes. Following the sample preparation process that included heavy mineral separation and careful hand-picking of crystals by using a stereo microscope, ~120 zircon grains were available for in-situ U-Pb analysis. However, 104 zircon grains could be analyzed due to the losing of some zircons during mounting process.

Table 2: Number of Zircon Grains

Unit	Rock Type	Sample Number	Number of Zircon Grains	Number of Spots
CMC	Metarhyodacite	AK-7	4	4
CMC	Metarhyodacite	AK-14	8	9
CMC	Metarhyodacite	AK-22	6	6
CP	Dacite Porphyry	CN-3	11	15
CP	Granite	SL-3	37	48
Devrekani Metamorphics	Orthogneiss	DVK-4A	18	18
Devrekani Metaophiolite	Metadiorite	DV-11	11	11
Devrekani Granitoid	Diorite	DVK-13	9	9

Additionally, three well established and recognized zircon standards, Plesovice, 91500, and GJ-1 were analyzed throughout the analytical sessions in order to validate and ensure the accuracy of the in-situ U-Pb results reported here. Subsequent to the analyses and data reduction, which included the using of Iolite software (v.3.1) and the excel-based macro IsoPlot (v.4.1), concordant, lower intercept, and/or weighted average ages were calculated and reported here.

### 5.1.1. Instrumentation and Data Acquisition

The Laser Ablation-Multicollector Inductively Coupled Plasma Mass Spectrometer (LA-MC-ICP-MS) instrument configuration which includes a NuPlasma II MC-ICP-MS instrument (Nu Instruments, UK) coupled to a NWR193 nm excimer laser ablation system (ESI-NWR). The samples and standards (Plesovice, 91500, GJ-1) were placed together simultaneously in the large volume ablation cell equipped with

a low-volume sampling ring. The laser ablation conditions and standards are given in Appendices E.

### 5.1.2. Çangaldağ Metamorphic Complex (CMC)

The morphology of the analysed zircons ranges from rounded to euhedral in shape, and internal structures may be diffused, oscillatory, laminated and unzoned (Appendices D). Zircon grains from three meta-rhyodacite samples (AK-7, AK-14 and AK-22) within the CMC were analyzed and the results are shown on Concordia ( $^{206}\text{Pb}/^{238}\text{U}$  vs  $^{207}\text{Pb}/^{235}\text{U}$ ) diagrams (Figs. 5-1, 5-2, 5-3). Three similar Middle Jurassic ages of  $176.4 \pm 5.9$  Ma for AK-7 (concordia age),  $156.2 \pm 2.9$  Ma for AK-14 (lower intercept age), and  $161 \pm 12$  Ma for AK-22 (weighted mean  $^{206}\text{Pb}/^{238}\text{U}$  age) were determined (Fig. 5-4).

It must be noted that the effects of low-grade metamorphism (greenschist facies) and hydrothermal alteration may cause Pb-loss within zircon, and leads to discordant results, i.e., data points plotting below the concordia curve (Figs. 5-1, 5-2). However, the reliable age data for samples investigated here were obtained on concordant data (e.g., Fig. 5-1), lower intercept and weighted mean ages, respectively. The combined geochronological results indicate the occurrence of Middle Jurassic magmatism for the CMC. The detailed U-Pb data and position of the laser ablation spots are given in Appendices B and D.

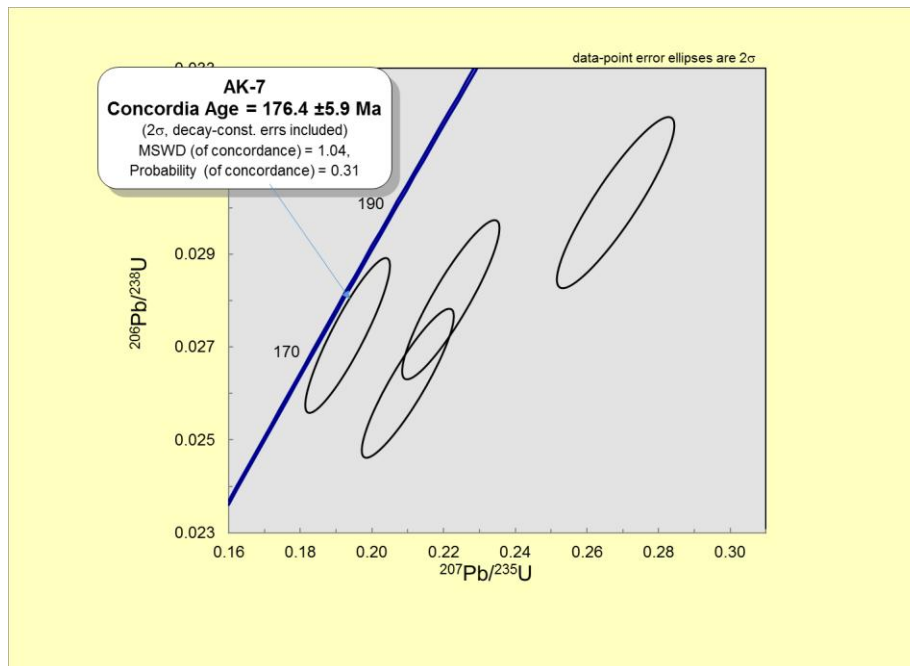


Figure 5-1:  $^{206}\text{Pb} / ^{238}\text{U}$  vs  $^{207}\text{Pb} / ^{235}\text{U}$  diagram and concordia age for AK-7 (metarhyodacite)

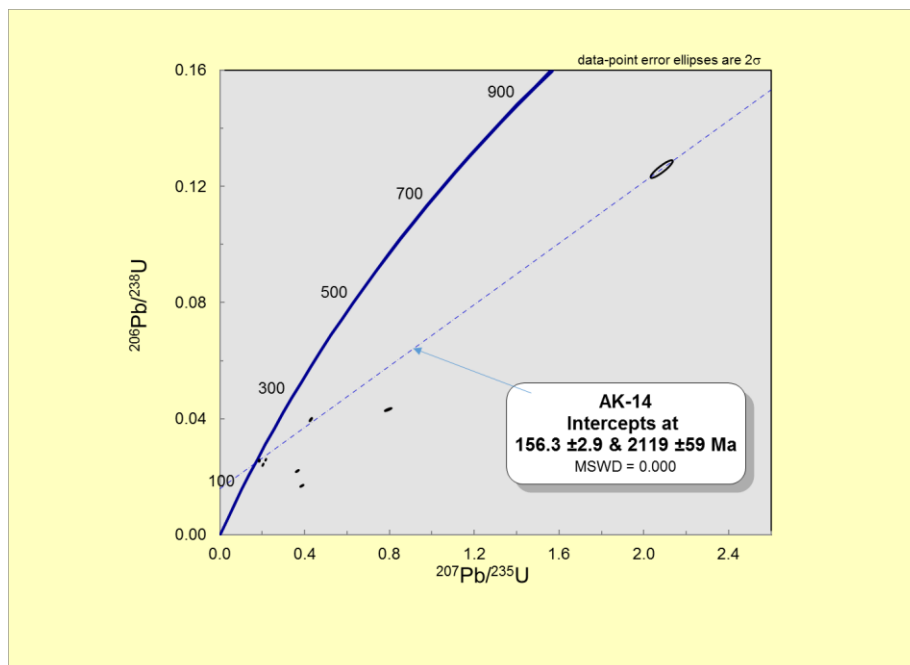


Figure 5-2:  $^{206}\text{Pb} / ^{238}\text{U}$  vs  $^{207}\text{Pb} / ^{235}\text{U}$  diagram and lower intercept age for AK-14 (metarhyodacite)

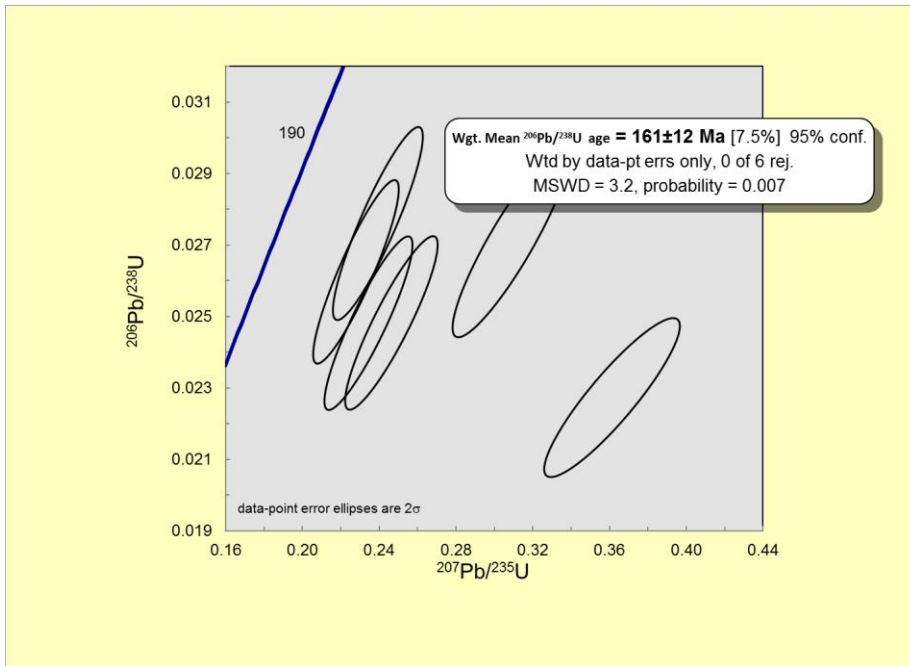


Figure 5-3:  $^{206}\text{Pb}/^{238}\text{U}$  vs  $^{207}\text{Pb}/^{235}\text{U}$  diagram and weighted mean age for AK-22 (metarhydacite)

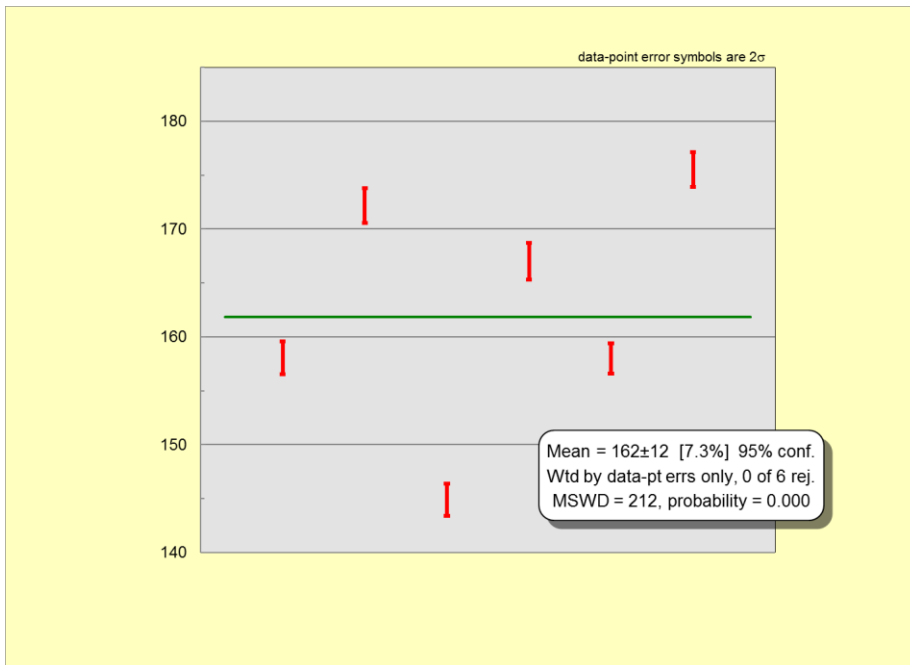


Figure 5-4:  $^{206}\text{Pb}/^{238}\text{U}$  (weighted mean age) data for AK-22 (metarhydacite)

### 5.1.3. Çangaldağ Pluton (CP)

The morphology of the analysed zircons ranges from rounded to euhedral in shape, and internal structures may be diffused, oscillatory, laminated and unzoned (Appendices D). Zircon grains obtained from dacite porphyry (CN-3) and granite (SL-3) samples within the CP were analyzed and the results are shown on concordia ( $^{206}\text{Pb} / ^{238}\text{U}$  vs  $^{207}\text{Pb} / ^{235}\text{U}$ ) diagrams (Figs. 5-5, 5-6, 5-7, 5-8). For both samples, Middle Jurassic ages of  $161.4 \pm 5.3$  Ma for CN-3 (concordia age),  $168.3 \pm 2.1$  Ma (lower intercept age), and  $169.9 \pm 1.7$  Ma (concordia age) for SL-3 were determined.

The age results for the samples from the CP suggest the occurrence of Middle Jurassic granitic magmatism, as is the case for the CMC. The detailed U-Pb data and laser ablation spots are given in Appendices B and D.

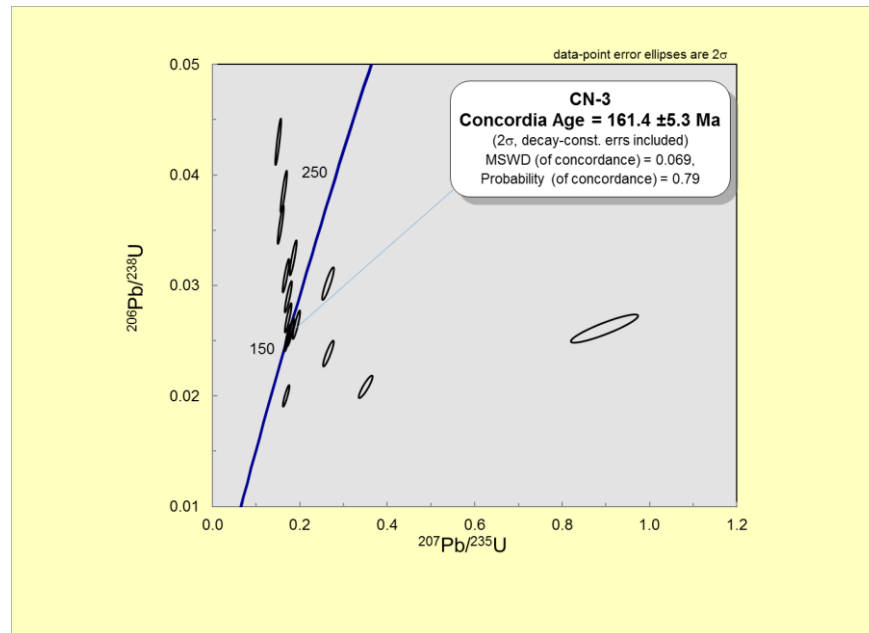


Figure 5-5:  $^{206}\text{Pb} / ^{238}\text{U}$  vs  $^{207}\text{Pb} / ^{235}\text{U}$  diagram and concordia age for CN-3 (daciteporphyry)

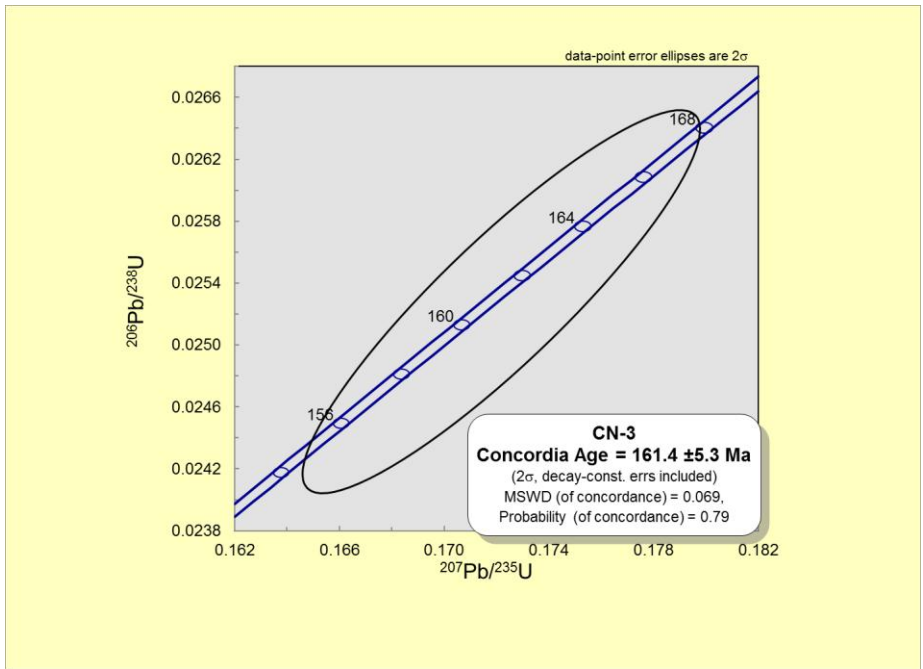


Figure 5-6:  $^{206}\text{Pb}/^{238}\text{U}$  vs  $^{207}\text{Pb}/^{235}\text{U}$  diagram and concordia age for CN-3 (dacite porphyry)

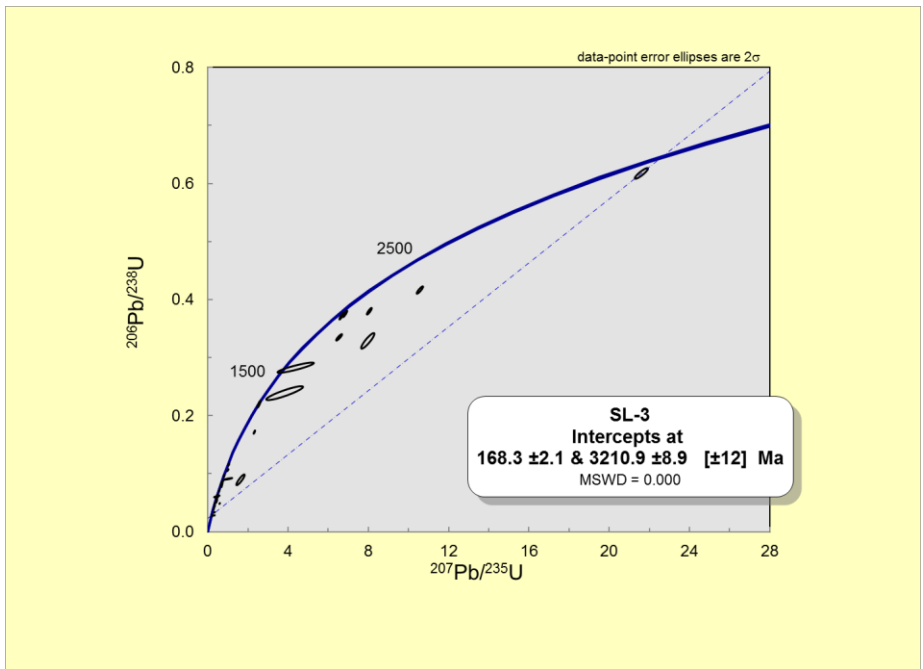


Figure 5-7:  $^{206}\text{Pb}/^{238}\text{U}$  vs  $^{207}\text{Pb}/^{235}\text{U}$  diagram and lower intercept age for SL-3 (S-type granite)

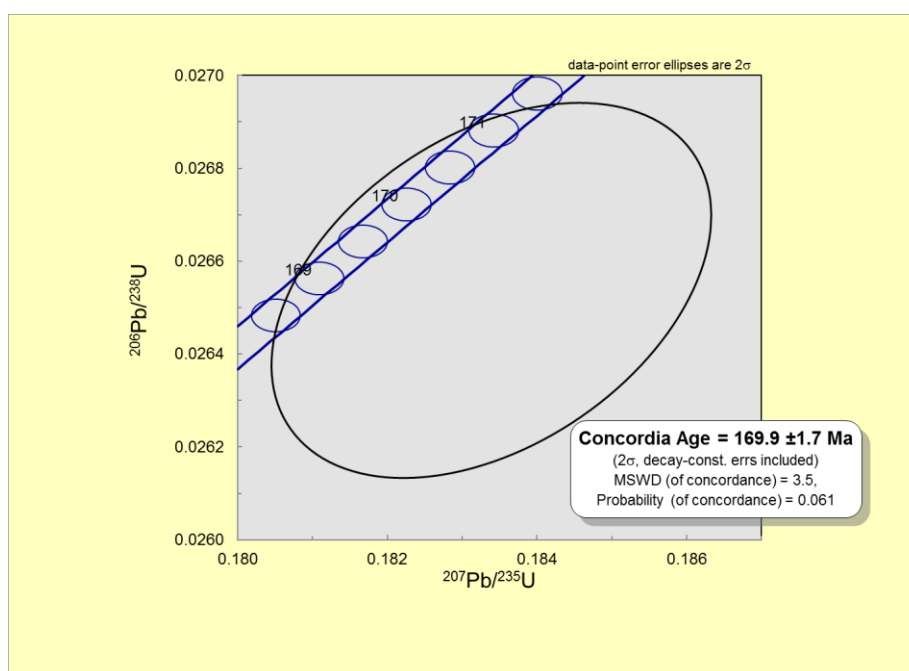


Figure 5-8:  $^{206}\text{Pb} / ^{238}\text{U}$  vs  $^{207}\text{Pb} / ^{235}\text{U}$  diagram and concordia age for SL-3 (S-type granite)

#### 5.1.4. Devrekani Orthogneiss

Based on field relations, several orthogneiss bodies intruding the Devrekani Metamorphics (mostly composed of amphibolites, gneiss, and metacarbonates) are affected by mylonitic deformation. Dating these orthogneisses can provide a relative age for the Devrekani Metamorphics. The morphology of the analysed zircons ranges from rounded to euhedral in shape, and internal structures may be diffused, oscillatory and unzoned (Appendices D). The zircon grains obtained from mylonitic granite (DVK-4A) were analyzed and the results are shown on concordia ( $^{206}\text{Pb}/^{238}\text{U}$  vs  $^{207}\text{Pb}/^{235}\text{U}$ ) diagrams (Figs. 5-9, 5-10). A Permian age of  $264 \pm 90$  Ma (lower intercept age) associated with a higher uncertainty was determined.

As seen in Figure 5-9, the zircon grains are characterized by excessive Pb loss. The latter may be attributed to the mylonitisation of these granitic bodies. Therefore, a

pre-Permian age can be estimated for the Devrekani Metamorphics based upon the combination of radiometric age data and field relations. The detailed U-Pb data and laser ablation spots are given in Appendices B and D.

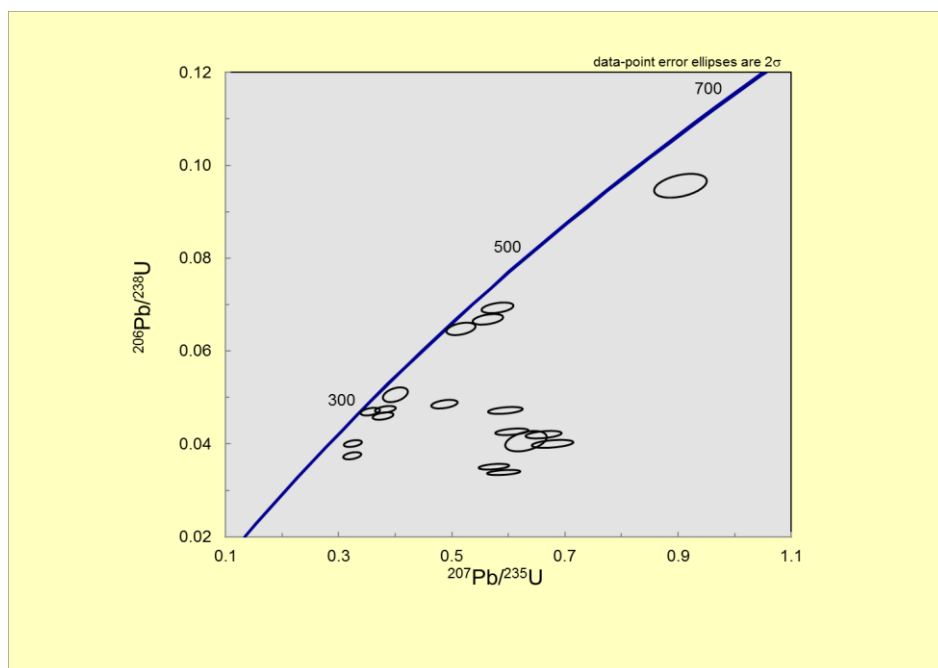


Figure 5-9:  $^{206}\text{Pb} / ^{238}\text{U}$  vs  $^{207}\text{Pb} / ^{235}\text{U}$  diagram and Pb-loss for DVK-4A (orthogneiss)

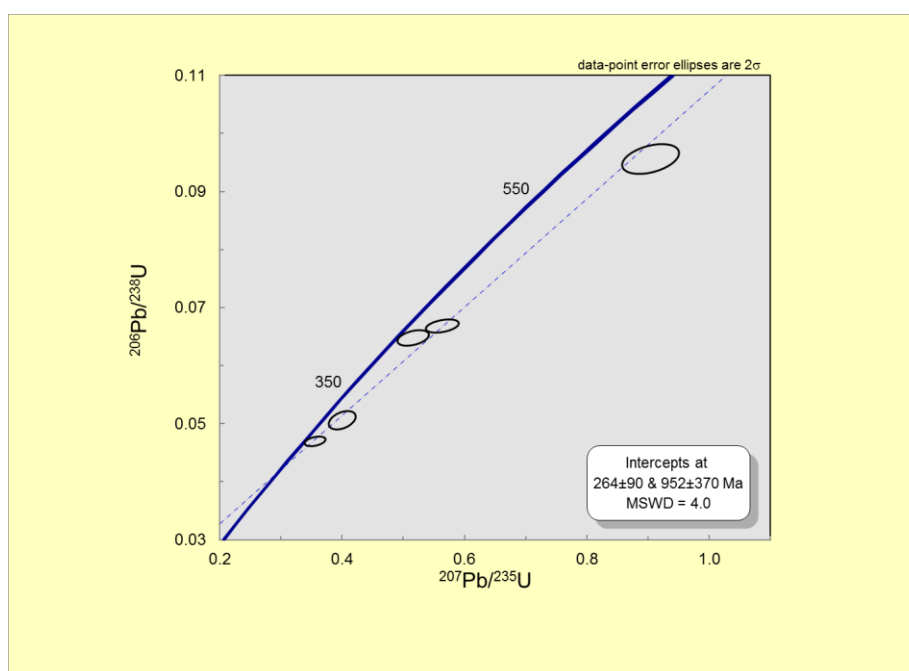


Figure 5-10:  $^{206}\text{Pb} / ^{238}\text{U}$  vs  $^{207}\text{Pb} / ^{235}\text{U}$  diagram and lower intercept age for DVK-4A (orthogneiss)

### 5.1.5. Metadiorite intruding Devrekani Metaophiolite

On the basis of field relations, two metadiorite bodies cut the Devrekani Metaophiolite, and hence provide a relative age for the Devrekani Metaophiolite. The morphology of the analysed zircons ranges from rounded to euhedral and internal in shape, structures may be diffused, oscillatory, laminated or unzoned (Appendices D). The zircon grains which were obtained from metadiorite (DV-11) were analyzed and the results are shown on the concordia ( $^{206}\text{Pb}/^{238}\text{U}$  vs  $^{207}\text{Pb}/^{235}\text{U}$ ) diagram (Fig. 5-11). A Middle Jurassic age of  $163.3 \pm 8.8$  Ma (lower intercept age) was determined.

This age of metadiorite also provides a pre-Middle Jurassic relative age for the Devrekani Metaophiolite. The other important result is the presence of post-Middle Jurassic age of metamorphism since both units are metamorphosed. The detailed U-Pb data and laser ablation spots are given in Appendices B and D.

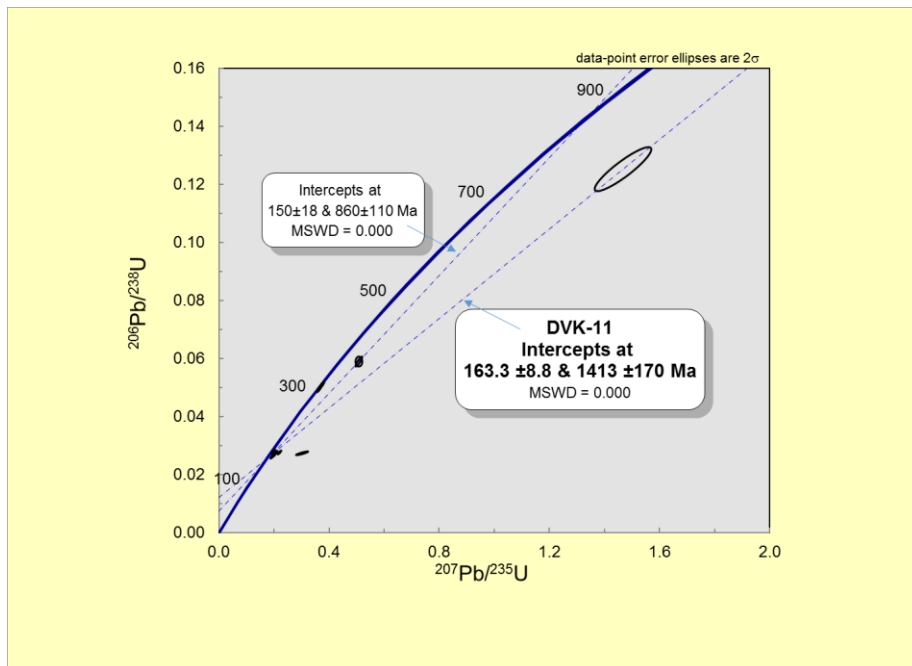


Figure 5-11:  $^{206}\text{Pb} / ^{238}\text{U}$  vs  $^{207}\text{Pb} / ^{235}\text{U}$  diagram and lower intercept age for DV-11 (metadiorite)

### 5.1.6. Devrekani Granitoid

This granitoid is different than Çangaldağ Pluton and located in the Devrekani town. It is mostly composed of diorites and granites. The morphology of the analysed zircons ranges from rounded to euhedral and internal structures may be diffuse, oscillatory, laminated or unzoned (Appendices D). The zircon grains extracted from granite (DVK-13) sample within the Devrakani Granitoid were analyzed and the results are shown on concordia diagrams ( $^{206}\text{Pb}/^{238}\text{U}$  vs  $^{207}\text{Pb}/^{235}\text{U}$ ) (Figs. 5-12, 5-13). A Middle Jurassic age of  $164.9 \pm 2.9$  Ma (weighted mean  $^{206}\text{Pb}/^{238}\text{U}$  age) was determined.

These results also suggest the occurrence of Middle Jurassic magmatism for the Devrekani Granitoid. The detailed U-Pb data and laser ablation spots in Appendices B and D.

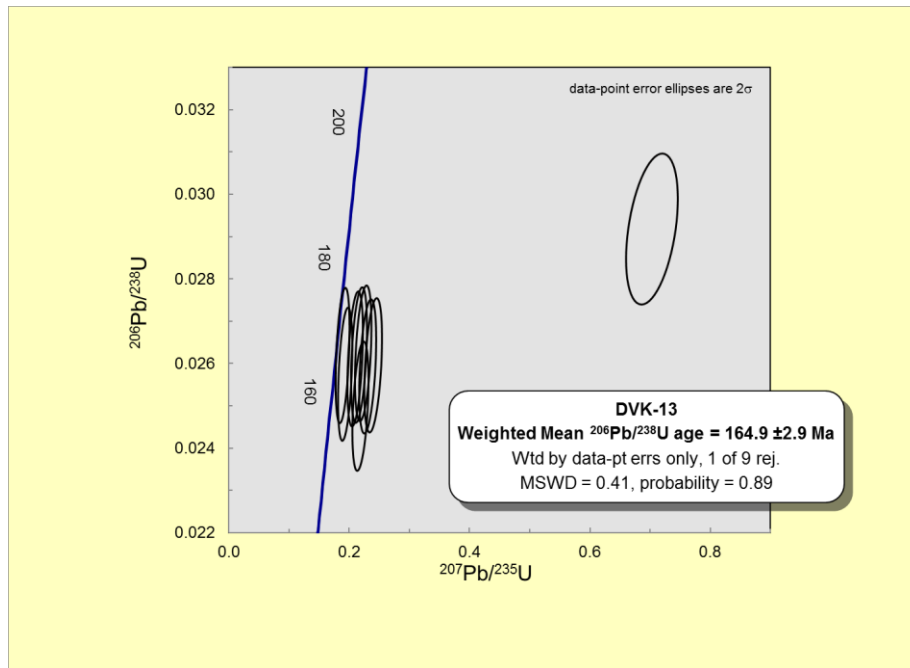


Figure 5-12:  $^{206}\text{Pb} / ^{238}\text{U}$  vs  $^{207}\text{Pb} / ^{235}\text{U}$  diagram and weighted age for DVK-13 (granite)

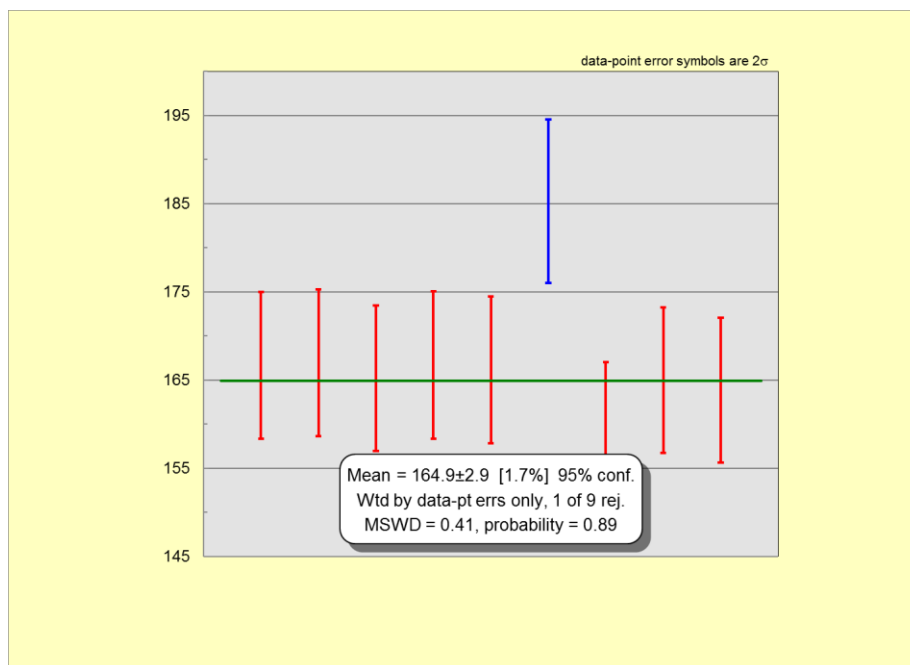


Figure 5-13:  $^{206}\text{Pb}/^{238}\text{U}$  (weighted mean age) data for DVK-13 (granite)

## 5.2. Lu-Hf isotope Systematics

Lu-Hf isotope method on zircon is one of the useful systems in order to evaluate mantle source(s) and determine depleted mantle ( $T_{DM}$ ) model age(s). This method is based on the  $\beta$ -decay of  $^{176}\text{Lu}$  to  $^{176}\text{Hf}$  isotope over time. The decay constant and half-life of  $^{176}\text{Lu}$  are  $1.983 \times 10^{-11} \text{ yr}^{-1}$  and 35.0 Ga (Bizarro et al., 2003), respectively. Recently, Hf isotope investigations of igneous samples have been successfully employed in many studies (e.g., Schmidberger et al., 2005; Zhao et al., 2015; Renjith et al., 2016).

Zircon is a very pertinent mineral for the Lu-Hf isotope method due to its resistant / robust nature under different secondary processes such as metamorphism, hydrothermal, and surface alteration. It has a very high closure temperature ( $>900^\circ\text{C}$ ), which provides reliable results for isotopic studies (e.g., Flowers et al., 2005).

Recently, in-situ Hf isotope investigations of zircon have become more widely adopted and performed instead of the conventional whole rock method, which yields much more reliable data (e.g., Simonetti and Neal, 2010). Moreover, distinct magmatic events can be determined from core-to-edge investigations on minerals by using small laser spot sizes (e.g.,  $\leq 50$  microns). In addition, it is cheaper and is characterized by a rapid analysis time compared to the whole rock method; moreover, the latter can mask different magmatic and metamorphic information present at the micron-scale.

Here, a total of 7 samples (3 from CMC, 2 from CP, 1 from Devrekani Metadiorite, and 1 from Devrekani Granitoid) were analyzed for in situ Hf isotope analyses; in particular the same zircon grains that were used investigated for the U-Pb ages. Lastly, three well established and recognized zircon standards, Plesovice, 91500, and BR266 were analyzed before the analytical sessions in order to validate and ensure the accuracy of the in-situ Hf results reported here.

### 5.2.1. Instrumentation and Data Acquisition

A Laser Ablation-Multicollector Inductively Coupled Plasma Mass Spectrometer (LA-MC-ICP-MS) combined instrument configuration (NuPlasma II from Nu Instruments, UK) was operated for the in-situ Hf analyses. Ablations were performed using a NWR193 nm laser ablation system (ESI-NWR). The samples and standards (Plesovice, 91500, BR266) were placed together in the large volume ablation cell equipped with a low-volume sampling ring. For the laser ablation conditions and standards please see Appendices E.

### 5.2.2. Çangaldağ Metamorphic Complex

Zircon grains from three meta-rhyodacite samples (AK-7, AK-14, and AK-22) within the CMC were analyzed and the results are shown on  $^{176}\text{Hf}/^{177}\text{Hf}$  vs time and  $\epsilon\text{Hf}$  diagrams (Figs. 5-15, 5-16, 5-17, 5-18, 5-19). In-situ  $^{176}\text{Hf}/^{177}\text{Hf}$  initial ratios range between  $0.28276 \pm 0.00003$  and  $0.28281 \pm 0.00003$  on the same zircons, and correspond to  $T_{\text{DM}}$  model ages between 538 and 678 Ma.

The calculated  $\epsilon\text{Hf}$  values for the Middle Jurassic magmatism are between 2.7 and -0.1 for the meta-rhyodacite samples (AK-7-concordant age, AK-14,-lower intercept age and AK-22-weighted mean age). Lastly, the effect of low-grade metamorphism (greenschist facies) and hydrothermal alteration may cause Pb-loss within zircon, and leads to plotting out of the DM and CHUR evolution lines (Figs. 5-14, 5-15). The detailed  $^{176}\text{Hf}/^{177}\text{Hf}$  initial ratios,  $T_{\text{DM}}$  model ages,  $\epsilon\text{Hf}$  values and laser ablation spots are given in Appendices C and D.

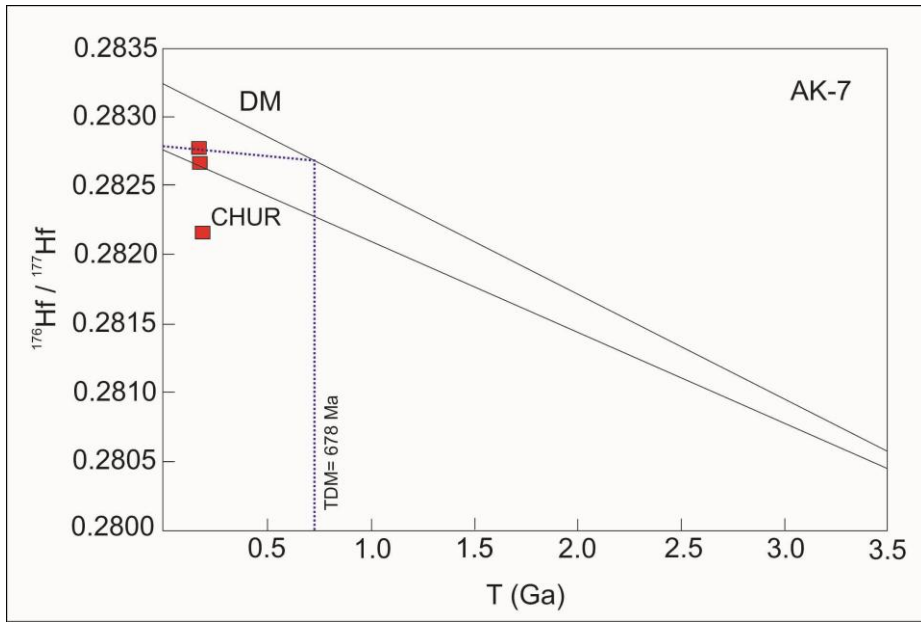


Figure 5-14:  $^{176}\text{Hf}/^{177}\text{Hf}$  vs Time for AK-7 (metarhyodacite)

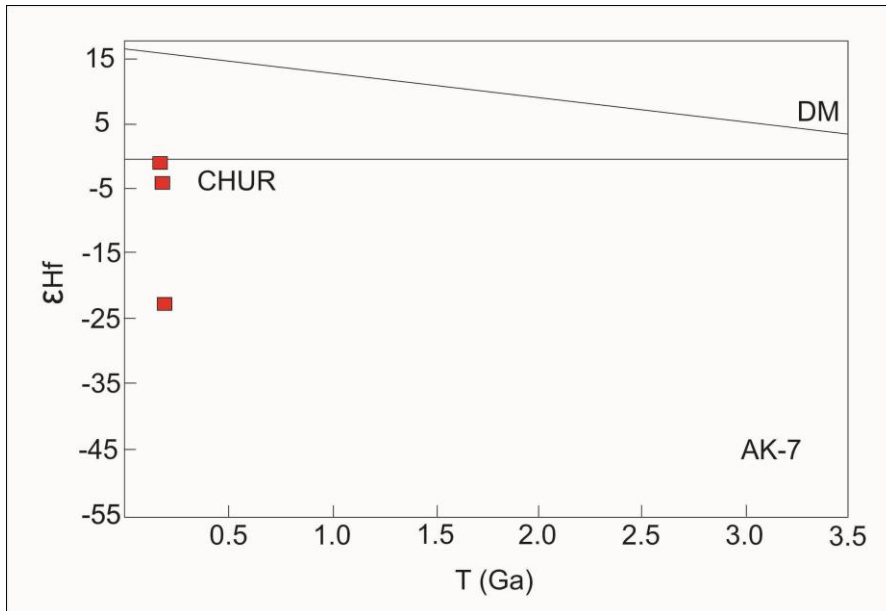


Figure 5-15:  $\epsilon\text{Hf}$  vs Time for AK-7 (metarhyodacite)

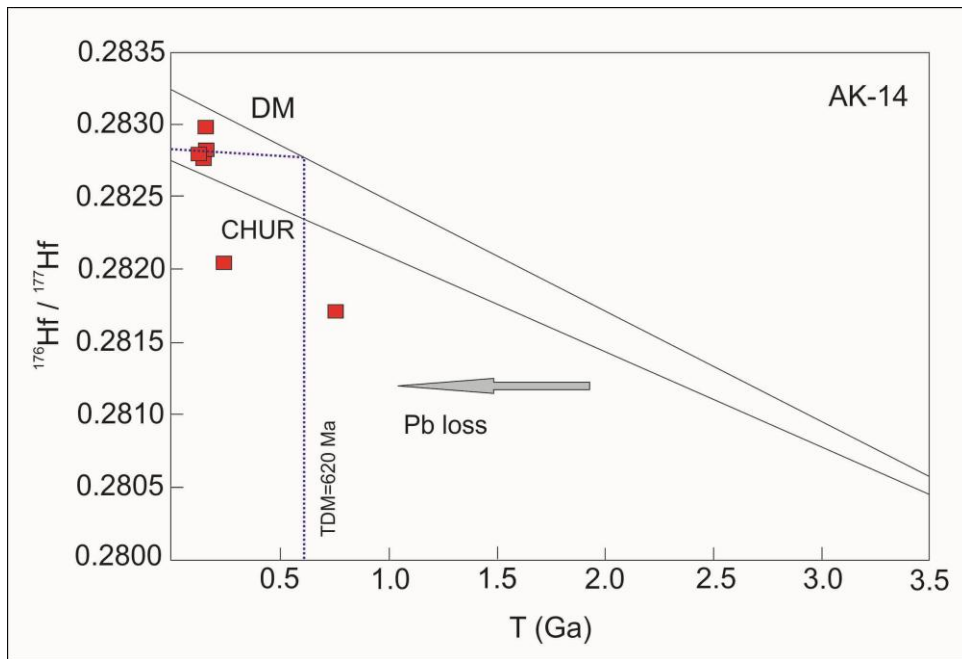


Figure 5-16:  $^{176}\text{Hf}/^{177}\text{Hf}$  vs Time for AK-14 (metarhyodacite)

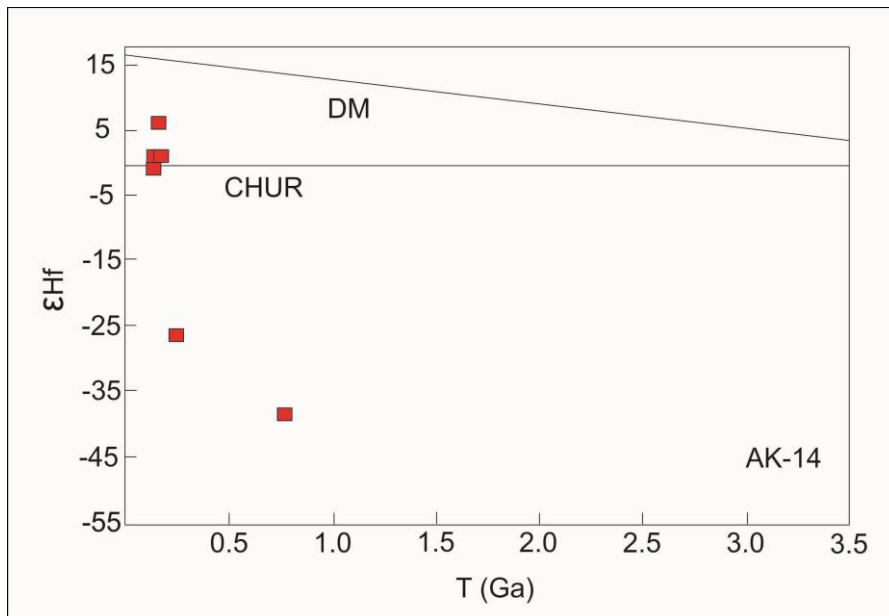


Figure 5-17:  $\epsilon_{\text{Hf}}$  vs Time for AK-14 (metarhyodacite)

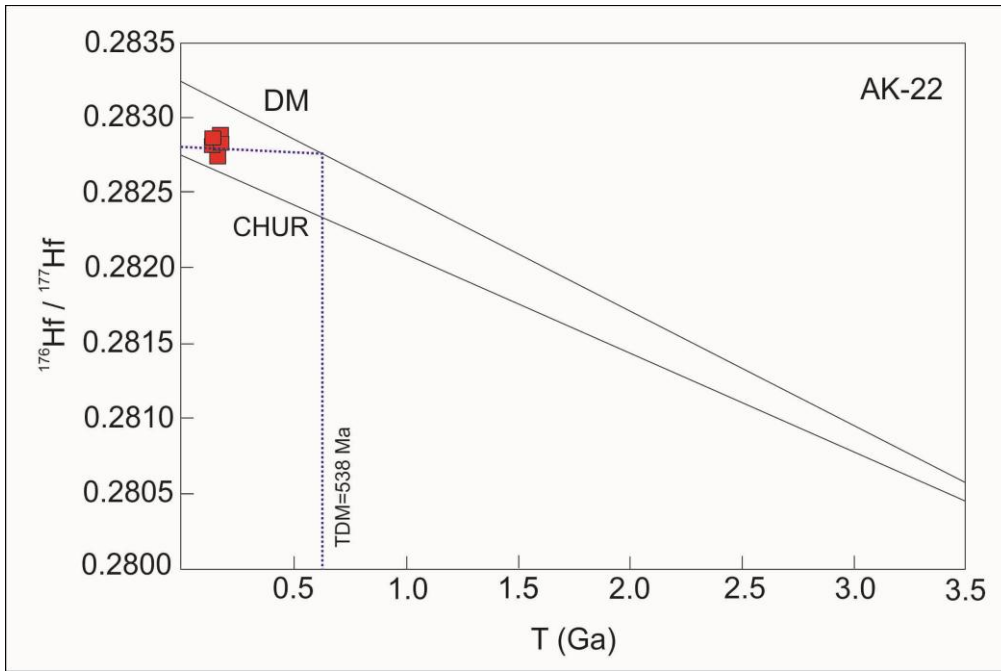


Figure 5-18:  $^{176}\text{Hf}/^{177}\text{Hf}$  vs Time for AK-22 (metarhyodacite)

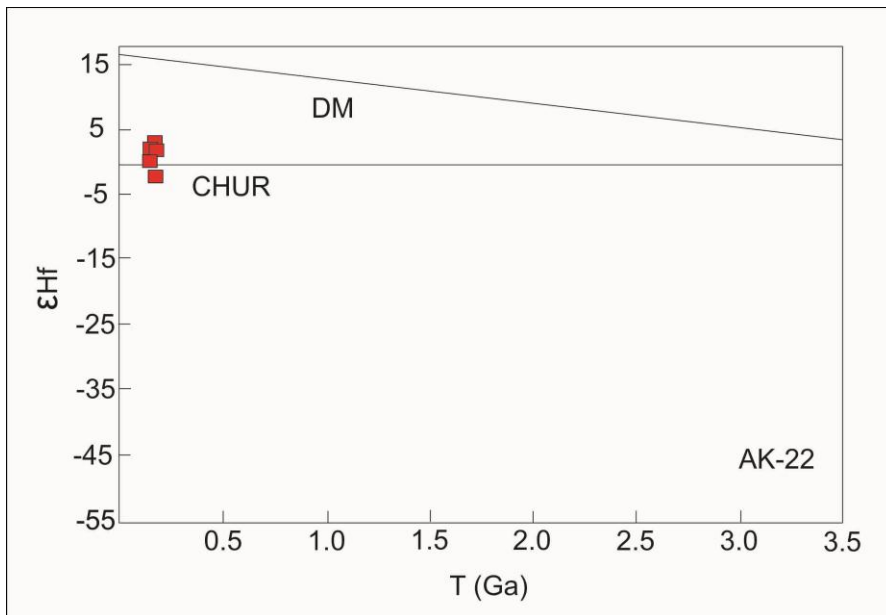


Figure 5-19:  $\epsilon\text{Hf}$  vs Time for AK-22 (metarhyodacite)

### 5.2.3. Çangaldağ Pluton

Zircon grains obtained from dacite porphyry (CN-3) and granite (SL-3) samples within the CP were analyzed, and the results are shown on  $^{176}\text{Hf}/^{177}\text{Hf}$  vs Time and  $\epsilon\text{Hf}$  diagrams (Figs. 5-20, 5-21, 5-22, 5-23). In-situ  $^{176}\text{Hf}/^{177}\text{Hf}$  initial ratios are  $0.28276 \pm 0.00003$  and  $0.28213 \pm 0.00002$  for the dacite porphyry (concordant age) and granite samples, respectively. These results correspond to the  $T_{\text{DM}}$  model ages which are 674 and 1512 Ma ages.  $\epsilon\text{Hf}$  values are -0.7 and -23.1, respectively. The detailed  $^{176}\text{Hf}/^{177}\text{Hf}$  initial ratios,  $T_{\text{DM}}$  model ages,  $\epsilon\text{Hf}$  values and laser ablation spots are given in Appendices C and D.

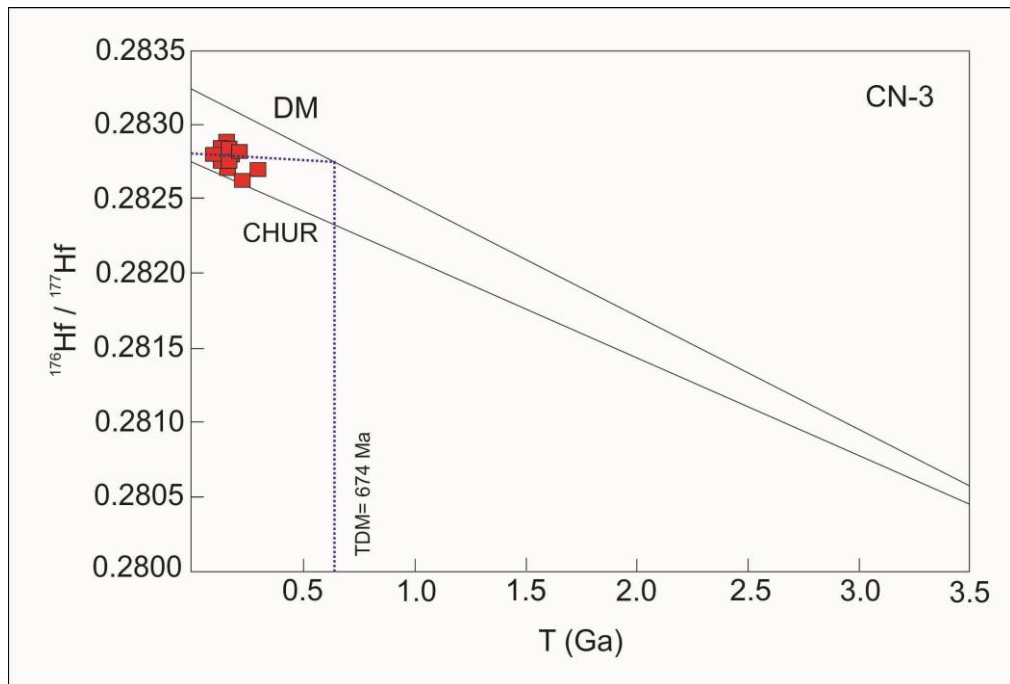


Figure 5-20:  $^{176}\text{Hf}/^{177}\text{Hf}$  vs Time for CN-3 (dacite porphyry)

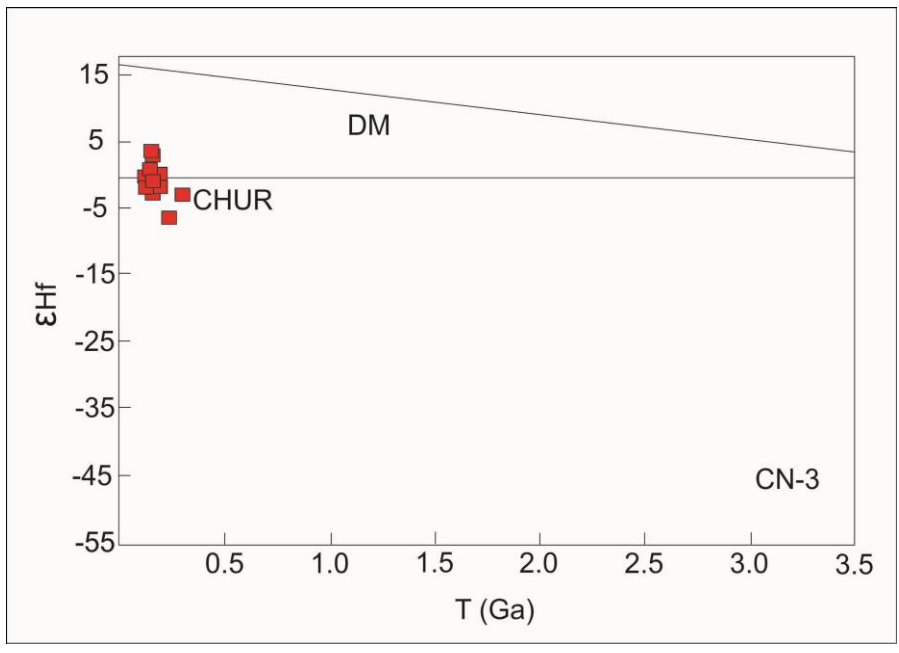


Figure 5-21:  $\epsilon_{\text{Hf}}$  vs Time for CN-3 (dacite porphyry)

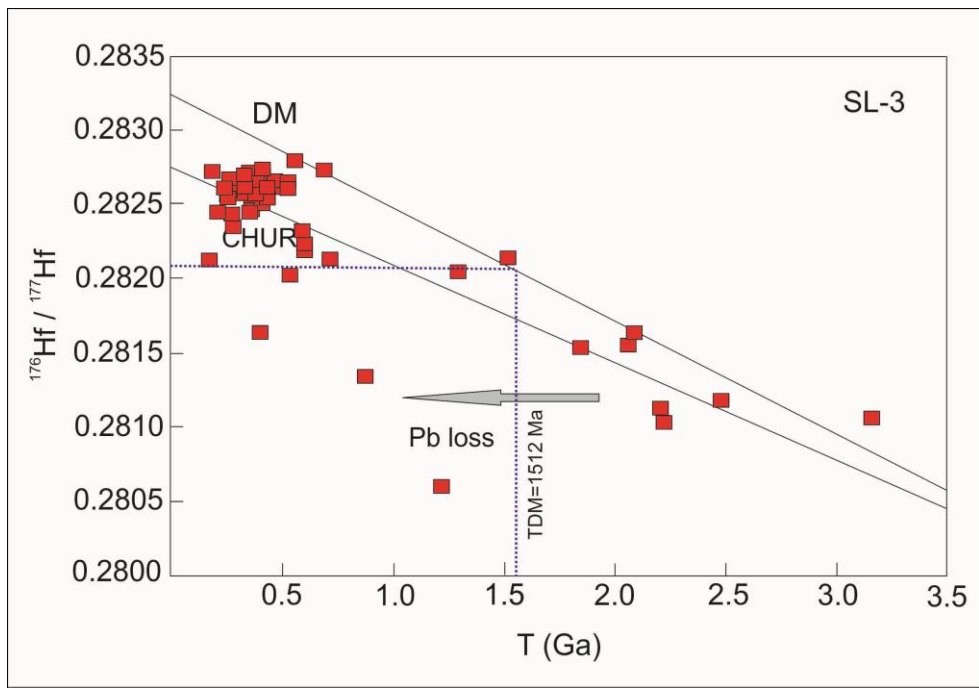


Figure 5-22:  $^{176}\text{Hf}/^{177}\text{Hf}$  vs Time for SL-3 (S-type granite)

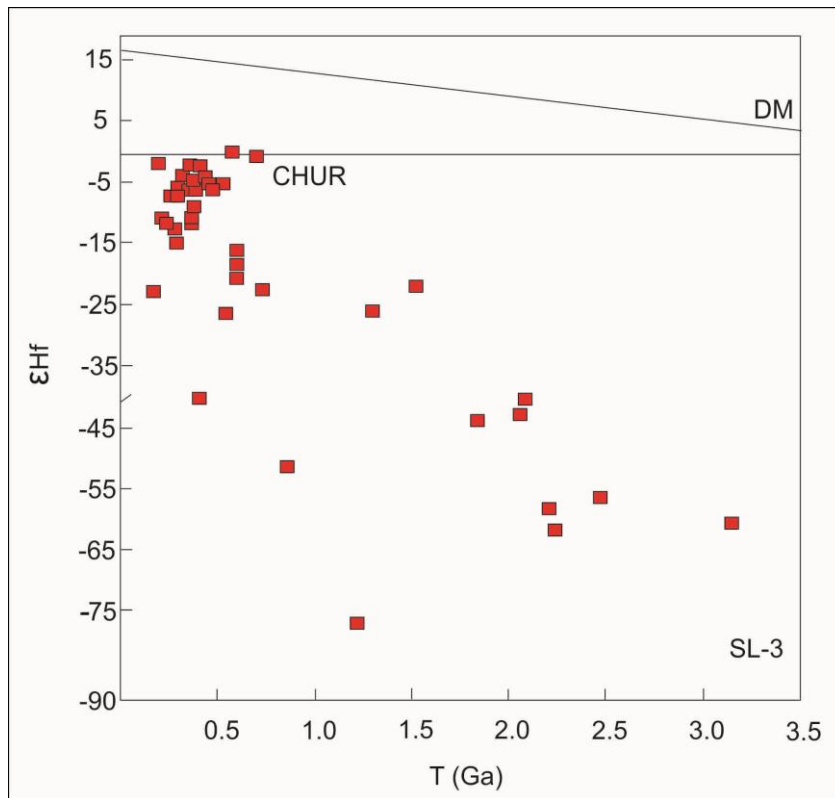


Figure 5-23:  $\epsilon_{\text{Hf}}$  vs Time for SL-3 (S-type granite)

#### 5.2.4. Metadiorite intruding Devrekani Metaophiolite

The zircon grains which were obtained from this metadiorite (DV-11) were analyzed and the results are shown on  $^{176}\text{Hf}/^{177}\text{Hf}$  vs Time and  $\epsilon_{\text{Hf}}$  diagrams (Figs. 5-24, 5-25). In-situ  $^{176}\text{Hf}/^{177}\text{Hf}$  initial ratio is  $0.28289 \pm 0.00003$  for the metadiorite sample that corresponds to 517 Ma  $T_{\text{DM}}$  model age.  $\epsilon_{\text{Hf}}$  value is about +4 for this zircon grain (lower intercept age). The detailed  $^{176}\text{Hf}/^{177}\text{Hf}$  initial ratios,  $T_{\text{DM}}$  model ages,  $\epsilon_{\text{Hf}}$  values and laser ablation spots are given in Appendices C and D.

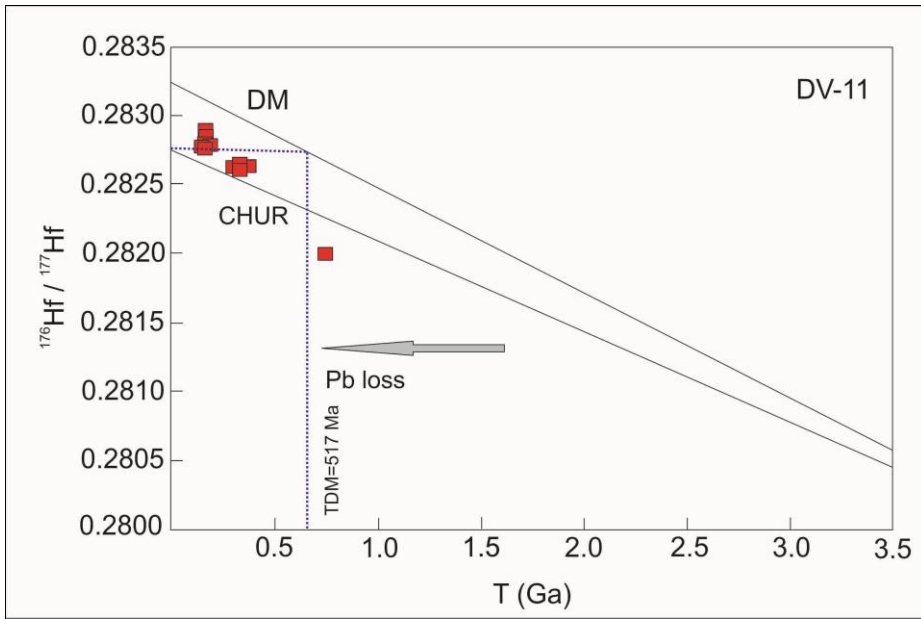


Figure 5-24:  $^{176}\text{Hf}/^{177}\text{Hf}$  vs Time for DV-11 (metadiorite)

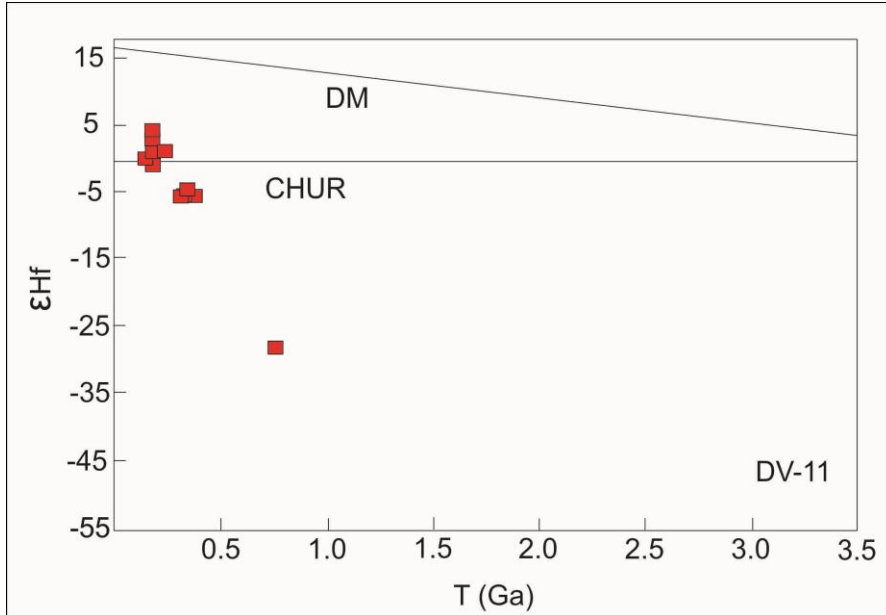


Figure 5-25:  $\epsilon\text{Hf}$  vs Time for DV-11 (metadiorite)

### 5.2.5. Devrekani Granitoid

The zircon grains extracted from granite (DVK-13) sample within the Devrekani Granitoid were analyzed and the results are shown on  $^{176}\text{Hf}/^{177}\text{Hf}$  vs Time and  $\epsilon\text{Hf}$  diagrams (Figs. 5-26, 5-27). In-situ  $^{176}\text{Hf}/^{177}\text{Hf}$  initial ratio is  $0.28289 \pm 0.00006$  for the granite sample, which corresponds to 513 Ma  $T_{\text{DM}}$  model age. Lastly, the calculated  $\epsilon\text{Hf}$  value is +4 for this zircon grain (weighted mean age). The detailed  $^{176}\text{Hf}/^{177}\text{Hf}$  initial ratios,  $T_{\text{DM}}$  model ages,  $\epsilon\text{Hf}$  values and laser ablation spots are given in Appendices C and D.

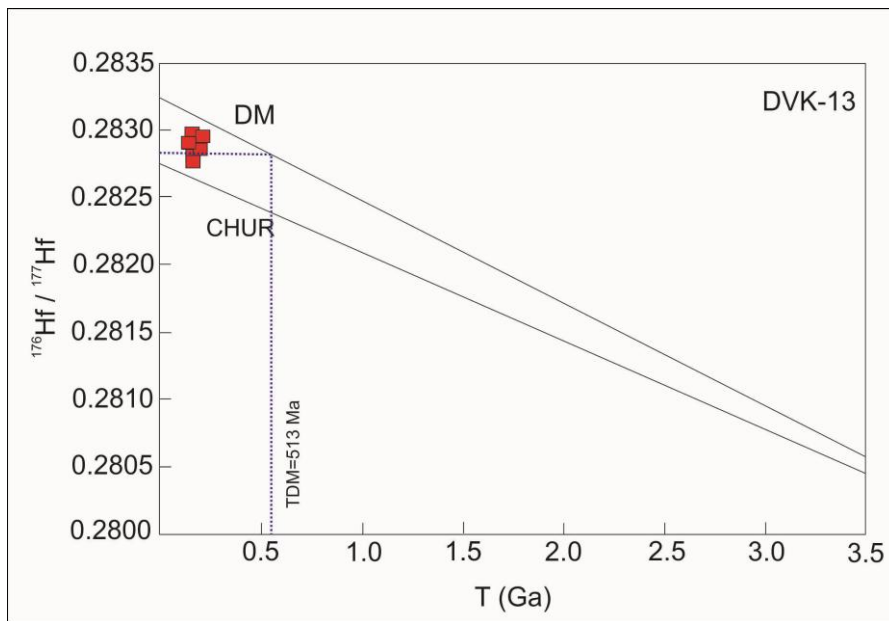


Figure 5-26:  $^{176}\text{Hf}/^{177}\text{Hf}$  vs Time for DVK-13 (granite)

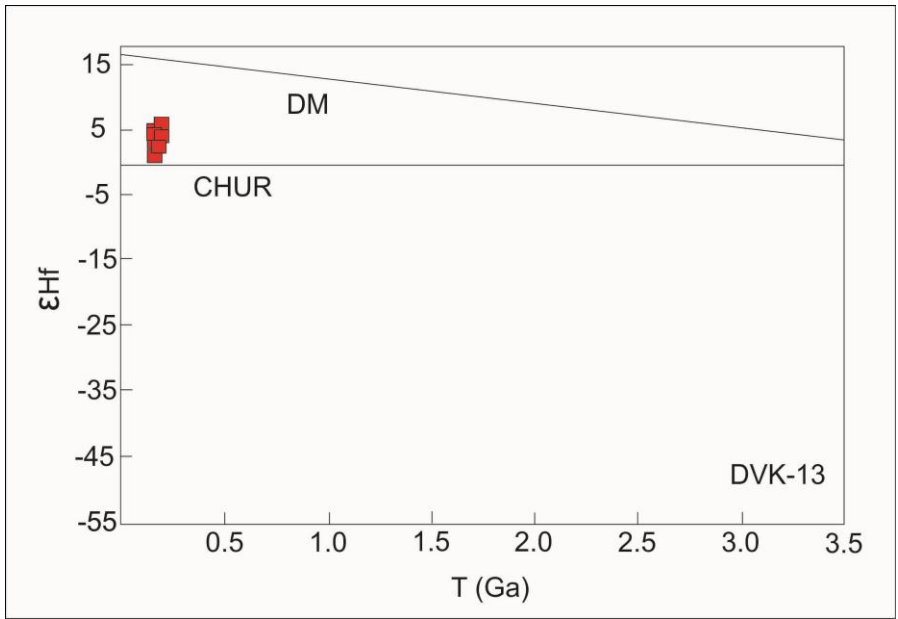


Figure 5-27:  $\epsilon_{\text{Hf}}$  vs Time for DVK-13 (granite)

## CHAPTER 6

### DISCUSSION

#### **6.1. New Insights into the Geological Evolution of the Çangaldağ Metamorphic Complex (CMC)**

##### **6.1.1. Geochemical Characteristics**

As mentioned in the geochemistry chapter (4), several representative samples were analyzed from the different metavolcanic rocks (metabasalts, metaandesites, metarhyodacites and metadiabases) within the CMC.

In the previous studies (Yılmaz, 1980, 1983; Yılmaz and Tüysüz, 1984; Şengün et al., 1988; Tüysüz, 1985, 1990; Boztuğ and Yılmaz, 1995; Uğuz and Sevin, 2007) The Çangaldağ unit was considered together with the Elekdağ and Domuzdağ units of the CPSC as part of the Paleotethyan ophiolite. Ustaömer and Robertson (1999) proposed that the metavolcanic rocks of the CMC represent the remnants of an island arc system. They actually used the term “oceanic arc above forearc basement” or “near continental margin oceanic arc” or “supra-subduction setting”, which is in very general terms confirmed by our findings. In addition to this, overall “arc-setting”, the characteristics of the back-arc magmatism have been determined here for the CMC.

On the other hand, the initial suggestion that the CMC (similar with Nilüfer Unit from the Karakaya Complex) represents an oceanic plateau or oceanic islands as suggested by Okay et al. (2006) is not consistent with our results in this study. It must be noted that this suggestion was revised by new age findings (Okay et al.,

2013, 2014) as “arc-related magmatism” considering the geochemical data from Ustaömer and Robertson (1999).

Overall our geochemical evaluation of these metavolcanic rocks indicates the presence of three different basic groups. The defined boninitic rocks (first group) are represented by highly depletions in HFSE and REE compared to N-MORB and Chondrite values, respectively (Figs. 4-3, 4-4). The second basic group (island arcs) displays lower depletions in HFSE and higher enrichments in REE patterns compared to the boninitic samples. The last primitive group (back arc basin) has higher enrichments in HFSE and REE values than the other two groups. In addition to that, the evolved volcanic rocks display the characteristics of the typical arc-back arc basin environments (Figs. 4-3, 4-4).

All of the basic metavolcanic rocks could have been derived from the spinel lherzolite by different degree of partial meltings. The fractional crystallization process has caused the derivation of andesitic rocks from the basic volcanic rocks. The geochemical characteristics of the most evolved rhyodacitic rocks reveals the presence of different mantle source compared to the other volcanic rocks within the CMC. To sum up, this complex proves, geochemically, the presence of a fore-arc-arc-back arc magmatism, shortly arc-basin system in the Central Pontides during the Middle Jurassic.

When correlated with other Middle Jurassic magmatism in the Central Pontides, these general geochemical characteristics of the CMC display intra-ocenic arc-backarc characteristics. However, the plutons and granitoids (e.g. Devrakani and Çangaldağ) show typical characteristics of the continental magmatism (will be explained in the next part; Nzegge, 2008; Çimen et al., 2016b).

### 6.1.2. U-Pb Geochronology

Regarding the in-situ U-Pb radiometric studies, metarhyodacite samples taken from the different locations within the CMC were dated using 18 zircons. The zircon grains from three meta-rhyodacite samples (AK-7, AK-14, and AK-22) provide similar Middle Jurassic ages of  $176 \pm 6$  Ma for AK-7 (concordia age),  $156 \pm 3$  Ma for AK-14 (lower intercept age), and  $161 \pm 12$  Ma for AK-22 (weighted mean  $^{206}\text{Pb}/^{238}\text{U}$  age). However, some of the zircons display loss of radiogenic Pb as the result of element diffusion (Schmidberger et al., 2005) due to the metamorphic overprint.

Recently, a Middle Jurassic age was also assigned to the metafelsic rocks by Okay et al. (2014) based upon the U-Pb dating from a single zircon grain within the CMC. As mentioned above, this result is supported by our preliminary U-Pb data from a number of measured zircon grains. In other words, there is yet little doubt about the intrusion age of the felsic volcanic protoliths of CMC which suggests the presence of an arc-basin during the Middle Jurassic in the Central Pontides.

### 6.1.3. Hf Isotope Systematics

The first data, based on the Hf isotopes from zircon grains, is given in this thesis. The Lu-Hf isotope systematic can provide significant data in relation to mantle source(s) and depleted mantle ( $T_{\text{DM}}$ ) model age(s). In-situ  $^{176}\text{Hf}/^{177}\text{Hf}$  initial ratios range between  $0.28281 \pm 0.00003$  and  $0.28276 \pm 0.00003$  on the same zircons, corresponding to  $T_{\text{DM}}$  model ages between 538 and 678 Ma. Moreover, the calculated  $\epsilon\text{Hf}$  values for the Middle Jurassic magmatism are between 2.7 and -1 from the metarhyodacite samples (AK-7, AK-14 and AK-22) which could be explained by mixing of depleted mantle and oceanic crustal sources for the magma generation (Vervoort et al., 1999; Kröner et al., 2014).

These results suggest that the magmatism associated with the CMC may have involved partial melting of a depleted mantle, affected by the Cadomian arc magmatism (Gürsu and Göncüoğlu, 2005). This Cadomian signature is common in Gondwana-derived terranes (Göncüoğlu, 2010; Nutman et al., 2013; Rapela et al., 2016). These zircon grains exhibit relatively homogenous initial  $^{176}\text{Hf}/^{177}\text{Hf}$  ratios close to CHUR values (0.282785; Bouvier et al., 2008).

## **6.2. New Insights into the Geological Evolution of the Çangaldağ Pluton (CP)**

### **6.2.1. Geochemical Characteristics**

There is not any published geochemical data for the CP in the literature. The geochemical evaluation of the CP supports the presence of the extensive arc related magmatism in the study area. This pluton has subalkaline, calc-alkaline, magnesian and I-type characteristics. It displays similar geochemical features with volcanic arc granites including LILE/HFSE enrichments coupled with Nb depletions. The various geochemical discrimination diagrams show the signatures of continental arc magmatism rather than oceanic arc. The significant fractional crystallization effects have played an important role during evolution of the dacite porphyries from the dioritic rocks. Moreover, they have been mostly derived by partial melting of a mafic amphibolitic source. Only, the granite displays different geochemical properties than the other magmatic rocks within the CP. To sum up, this pluton proves, geochemically, the presence of the continental arc magmatism in the Central Pontides.

### **6.2.2. U-Pb Geochronology**

In the literature, there is no published radiometric age data for the CP. In this study, first-time, the zircon grains obtained from dacite porphyry (CN-3) and granite (SL-3)

samples indicate the presence of Middle Jurassic ages of  $161 \pm 6$  Ma for CN-3 (concordia age),  $168 \pm 2$  Ma (lower intercept age) and  $170 \pm 2$  Ma (concordia age) for SL-3. The age results for the samples from this pluton suggest the occurrence of Middle Jurassic magmatism. Here, some zircon minerals display loss of radiogenic Pb as the result of element diffusion (Schmidberger et al., 2005) for the granite sample which can be reason of plotting out of the concordia line. Also, these radiometric age results can be also confirmed by the field relations. The CP cuts the Triassic units and overlain by the Upper Jurassic limestone.

Additionally, the wide range of the U-Pb age data (between 3165 and 170 Ma) which were analyzed from the zircons of granite sample support the deriving from a sedimentary source. In other words, the non-uniform distributions of the zircon ages indicate that all zircons do not have a common origin and formational process. In detail, this rock contains 1 (including individual and growth parts; Fig. 6-1) Archean zircon (2%), 7 Paleoproterozoic zircon (15%), 3 Mesoproterozoic zircons (6%), 7 Neoproterozoic zircons (15%), 3 Cambrian zircons (6%), 2 Ordovician zircons, 1 Silurian zircon (2%), 10 Devonian zircons (21%), 7 Carboniferous zircons (15%), 4 Permian zircons (8%), 1 Triassic zircon (2%) and 2 Jurassic zircons (4%). As obviously seen from these distributions, the magmatism associated with this granite sample has involved the different zircon populations from Archean to Triassic which may be found in a sedimentary source. These results show multiple periods of zircon growth (Schmidberger et al., 2005). For this magmatism, the known oldest source is the Devrekani Metamorphics in the study area which contains mostly paragneiss (including zircon minerals from 293 to 668 Ma), amphibolite, orthogneiss (age is between 316-252 Ma) and metacarbonate (Gücer and Arslan, 2015; Gücer et al., 2016).

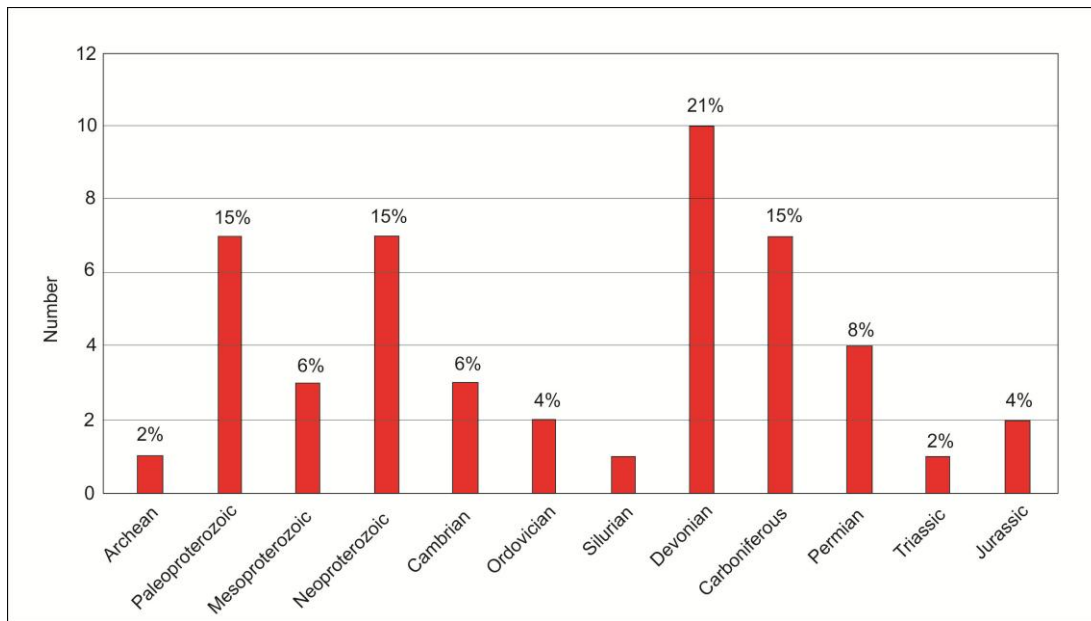


Figure 6-1: Distributions of the different ages from SL-3 (granite sample)

On the other hand, the zircons from dacite porphyry sample exhibit more consistent age data distribution (between 142 and 304 Ma) compared to the granite sample which should be related to the derivation from an igneous source.

### 6.2.3. Hf Isotope Systematics

Hf isotopes in zircons (known U-Pb ages) may provide significant information about source of the magma. Since zircon crystals are very refractory and major reservoir of Hf in most rocks, they can be easily used in order to understand evolution of the crust (Batumike et al., 2007). Here, the same zircon grains obtained from dacite porphyry (CN-3) and granite (SL-3) samples within the CP were analyzed during these studies. In-situ  $^{176}\text{Hf}/^{177}\text{Hf}$  initial ratios of two concordant Mid-Jurassic zircon grains are  $0.28276 \pm 0.00003$  and  $0.28213 \pm 0.00002$  for the dacite porphyry (concordant age) and granite (concordant age) samples, respectively. In the diagram which shows the relation between the age and initial Hf-isotope composition, the zircons are plotting mostly between Depleted Mantle (DM) and Chondritic Uniform Reservoir (CHUR)

lines. These results may indicate deriving from relatively juvenile magmas, whereas those that plot below the CHUR line suggest recycling of pre-existing crustal material (Batumike et al., 2007). The zircon grain from the dacite porphyry sample exhibits relatively homogenous initial  $^{176}\text{Hf}/^{177}\text{Hf}$  ratio close to CHUR values (0.282785; Bouvier et al., 2008). The other concordant zircon grain displays lower values than CHUR which could be related to contribution of crustal rocks for the magma generation.

These results correspond to the  $T_{\text{DM}}$  model ages which are 674 and 1512 Ma ages for Middle Jurassic magmatism from the dacite porphyry ( $161 \pm 6$  Ma) and granite ( $170 \pm 2$  Ma) samples, respectively. The model ages for these rocks suggest that the magmatism associated with the CP may have involved partial melting of the Neoproterozoic/Mesoproterozoic crustal rocks (such as Devrekani Metamorphics in the study area), which are common in Gondwana-derived terranes (Göncüoğlu, 2010; Nutman et al., 2013; Rapela et al., 2016). For the Middle Jurassic magmatism, the  $\epsilon\text{Hf}$  values of these zircon grains are -0.7 and -23.1 for the dacite porphyry and granite samples, respectively, which could be explained by mixing of depleted mantle and crustal sources for the magma generation (Vervoort et al., 1999; Kröner et al., 2014).

Also, once again, the wide range of the  $\epsilon\text{Hf}$  values from the granite sample (0 to -77.7) confirm the deriving from sedimentary source whereas the narrow range of  $\epsilon\text{Hf}$  data (3.1 to -2.5) from the dacite porphyry sample may be related to the derivation from an igneous source. In detail, according to the time, the  $\epsilon\text{Hf}$  values of the granite sample are as follows; Archean zircon (-60.6;  $T_{\text{DM}} = 2969$  Ma), Paleoproterozoic zircons (-41 to -61.2;  $T_{\text{DM}} = 2170\text{-}2940$  Ma), Mesoproterozoic (-22.7 to -77.7;  $T_{\text{DM}}=1478\text{-}3464$  Ma), Neoproterozoic (0 to -51.4;  $T_{\text{DM}}=639\text{-}2546$  Ma), Cambrian (-5.1 and -26.5;  $T_{\text{DM}}=845$  and  $1645$  Ma), Ordovician (-5.1;  $T_{\text{DM}}=843$  Ma), Devonian (-2.5 to -40.4;  $T_{\text{DM}}= 733\text{-}2179$  Ma), Carboniferous (-2.8 to -6.5;  $T_{\text{DM}}= 762\text{-}865$  Ma), Permian (-7.3 to 14.5;  $T_{\text{DM}}= 908\text{-}1176$  Ma), Triassic (-11.2;  $T_{\text{DM}}=1080$  Ma), Jurassic

(-1.7 and -23.1;  $T_{DM}$ = 709 and 1512 Ma). They display mostly negative values and plot below the CHUR line that could be related to involving of crustal rocks for generation of these zircon minerals. Some of these older zircon minerals lie on the near of CHUR line which may indicate a little production of juvenile magma for their formation (Batumike et al., 2007). The  $T_{DM}$  ages (from Neoproterozoic to Archean) obtained from the zircon minerals also exhibit the presence of recycled crustal materials during the main geological events. As in the U-Pb studies, the non-uniform distributions of the Hf data for the zircon minerals from the granite sample support that they do not share a common origin and formational process. This sample could have been derived a sedimentary source. However, the uniform distribution of the  $\epsilon_{Hf}$  values (3.1 to -2.5;  $T_{DM}$ =556-749 Ma) from dacite-porphry sample (CN-3) indicate a common igneous origin and formation process.

### **6.3. Overall Geodynamic Evolution**

The new petrological data (including whole rock geochemistry, U-Pb geochronology and Lu-Hf systematics) reported in this thesis about the CMC and CP plays a critical role to understand the geodynamic evolution of the Central Pontides. The CMC is cropping out between the Alpine Sakarya Composite Terrane and Istanbul-Zonguldak Terrane. The presence of two distinct oceanic domains, namely the Paleotethys and the Intra-Pontide branch of Neotethys between these two terranes during the Mid to Late Mesozoic is commonly accepted (Şengör and Yılmaz, 1981, Yılmaz et al., 1995; Tüysüz, 1999; Elmas and Yiğitbaş, 2001, Robertson and Ustaömer, 2004; Okay et al., 2006, 2008; Kaya, 1977, Kaya and Kozur, 1987; Göncüoğlu et al., 2008, 2012, 2014; Akbayram et al., 2013; Marroni et al., 2014). However, the paleogeographic and geodynamic settings of these oceans, as well as the lifespans of their oceanic lithosphere, subduction complexes, arcs etc. are a matter of debate.

In the previous studies, there is consensus that the Küre Complex represents the remnants of Paleotethyan Küre Basin (sensu Şengör and Yılmaz, 1981). The turbiditic sediments of the complex include Carnian-Norian fossils (Kozur et al., 2000; Okay et al., 2015) indicating that this basin was still open. On the other hand, recent data (Tekin et al., 2012; Göncüoğlu et al., 2012) shows that contemporaneous with the closure of the Küre basin another oceanic branch, the Intra-Pontide Ocean existed to the south of it. The remains of this ocean cover a vast area in Central Pontides (Fig. 2-4) and are included in the CPSC (Tekin et al., 2012).

In general terms, CPSC is an imbricated stack (e.g. Marroni et al., 2014; Aygül et al., 2016) of accretionary mélanges, dominated by variably deformed and metamorphosed volcanic rocks. Regarding the age; radiolarian data (Göncüoğlu et al., 2010, 2014) from basalt-chert associations indicate that this ocean was partly open until the early Late Cretaceous. Sayit et al. (2016) demonstrated recently that the volcanic rocks within the structurally lower units (Arkot Dağ, Domuz Dağ, Aylı Dağ units) were mainly derived from an intra-oceanic subduction system. Our new and detailed evaluation of geochemical data together with additional zircon ages clearly suggests that the CMC is a part of this system, as the petrogenetic characteristics of these rocks clearly indicate a fore arc-arc-back arc basin environment.

The Intra Pontide Ocean basin was obviously larger and older than the intra-oceanic subduction event producing the CMC volcanism during the Middle Jurassic time (Okay et al., 2014; Çimen et al., 2016a). That it existed prior to Middle Jurassic is proven by the Middle to Late Triassic oceanic volcanics found in the Arkot Dağ Melangé (Tekin et al., 2012). Moreover, it has not been completely eliminated by the Çangaldağ Mid-Jurassic subduction. This interpretation is supported by the presence of the Late Jurassic MORB-type volcanism in eastern Bolu area (Göncüoğlu et al., 2008). Additional evidence gives the Late Jurassic to early Late Cretaceous radiolarian ages from numerous outcrops within the IPOB (Göncüoğlu et al., 2012,

2014; Tekin et al., 2012). Considering that this complex tectonically overlies the Late Jurassic-Cretaceous mélanges with an emplacement direction from N to S we speculate that the Elekdağ, Domuz Dağ, Arkot Dağ and Aylı Dağ mélanges were originally located to the S of the Çangaldağ subduction (Fig. 6-2).

Previously, in relation to the origin of the CMC, two different models, a part of Karakaya Complex (conjugate of Nilüfer oceanic plateau) and island arc magmatism of the Paleotethyan Ocean, have been proposed by Okay et al. (2006) and Ustaömer and Robertson (1994, 1999), respectively. If this complex is a remnant of the Paleotethyan Ocean, the construction age must be older than Middle Jurassic that has been recently assigned by Okay et al. (2014). These models (magmatic products of the Paleotethyan Ocean) have been suggested by Ustaömer and Robertson (1999) and Okay et al. (2006) mainly based upon the pre-Mid Jurassic relative age (Yılmaz, 1980; Yılmaz and Boztuğ, 1986; Aydın et al., 1995). This relative age was given regarding the cutting relation between the CMC and CP. The Mid-Jurassic relative age was thought for the CP (there is no radiometric age data) based on the field relations as well. It cuts the Triassic Küre Complex and overlain by Upper Jurassic İnaltı limestone. However, the Middle Jurassic ages, reported in this study, obviously eliminate these Paleotethyan models for the generation of the CMC.

The modern analogues of the CMC can be found in several places in the world, such as intra-oceanic Mariana arc-basin system, where fore-arc, arc and back-arc components can be found all together (Pearce et al., 2005).

Another product of Middle Jurassic subduction-related magmatism in Central North Anatolia is represented by the CP. In contrast to the fore arc-arc-back arc character of the CMC, the Çangaldağ Pluton is a continental arc that intrudes the Küre Complex (Çimen et al., 2016b). To complete the geodynamic model proposed for CMC in the previous chapter and check its reliability the geological evaluation of the northerly located tectonic units such as the CP, the Devrekani Metamorphics were taken into

consideration for the Middle Jurassic period. For this, it is mainly emphasized the tectono-magmatic features and age of the CP. Therefore, we present the first whole rock geochemistry, zircon U-Pb age and Hf isotope data about the CP to reassess the geodynamic evolution of the Central Pontides. The region includes several granitoid complexes, which are predominantly Permo-Carboniferous (Deliktaş and Sivrikaya) and Middle Jurassic (e.g. Devrekani) in age (Bohomne and Yılmaz, 1984; Boztuğ and Yılmaz, 1995; Nzegge, 2008; Okay et al., 2014). These granitoid complexes were firstly recognized as Kastamonu Granitoid Belt (KGB; Yılmaz and Boztuğ, 1986) and interpreted as the magmatic products of orogenic collisional tectonics and crustal thickening during northward subduction of the Paleotethyan Ocean or southward subduction of the Küre marginal basin (e.g. Yılmaz and Boztuğ, 1986; Boztuğ et al., 1995; Ustaömer and Robertson, 1997; Nzegge, 2006; 2008). The CP (Çimen et al., 2016b), largest igneous body, is located in the northern part of the Central Pontide Structural Complex (CPSC) by Tekin et al. (2012) or Central Pontide Supercomplex by Okay et al. (2013).

In relation to the granitoid magmatism in the Central Pontides, Nzegge (2008) suggested that Sivrikaya Granitoid formed as a result of lithospheric slab break-off and/or lithospheric delamination/collapse processes during collision between Sakarya continent and Laurasia. Then, the uprising of hot asthenosphere caused the emplacement of purely crustal-derived peraluminous S-type Deliktaş Granitoid until Early Permian. The Jurassic magmatism (Devrekani and Asarcık Granitoids) was thought as a product of the southward subduction of the Küre Basin which was still open during Carnian-Norian (Kozur et al., 2000).

In addition to this widespread intra-oceanic arc back arc magmatism (e.g. CMC, Arkot Dağ, Domuz Dağ, Aylı Dağ units); the Middle Jurassic (from the U-Pb zircon ages) subduction-related continental arc magmatism is also represented by the Devrekani Granitoid (Nzegge, 2008) and Çangaldag Pluton (in this study) in the Central Pontides. It must be noted that, the Hf isotope systematics indicate the

mixing of depleted mantle and Neoproterozoic/Mesoproterozoic crustal rocks for the magma generation which may be existed in the Devrekani Metamorphics. Based upon all these evidences; the CP may have been formed by northward subduction (one of the multiple subductions) of the IPO during the Middle Jurassic (Fig. 6-2). In the suggested model, the prism 1 may represent the Aylı Dağ ophiolite and Arkot Dağ melange (including arc-back-arc volcanics; Göncüoğlu et al., 2012); the prism 2 may represent the Domuzdağ, Saka and Daday units (including again arc-back-arc volcanics; Sayit et al., 2016); the last subduction zone may have caused the generation of the Çangaldağ Pluton which displays, as mentioned above, the characteristics of continental arc magmatism (Çimen et al., 2016b; Fig. 6-2). The ages of these plutons (Çangaldağ and Devrekani) suggest the presence of different tectonic environment compared to the Sivrikaya and Deliktaş Granitoids (in the north) which are accepted the products of the Paleotethyan Ocean (Nzegge, 2008).

Finally, the IPO has been presumably consumed during the Late Cretaceous-Early Tertiary and its remnants have been tectonically moved to the south onto the Sakarya Composite Terrane (e.g. Göncüoğlu et al., 2000; Catanzariti et al., 2013, Ellero et al., 2015). The imbrication of the volcanic assemblages from the fore-arc, the island arc and the back-arc and their low grade metamorphism realized during the Early Cretaceous (Valanginian-Barremian) as evidenced by Ar-Ar white mica ages (Okay et al., 2013).

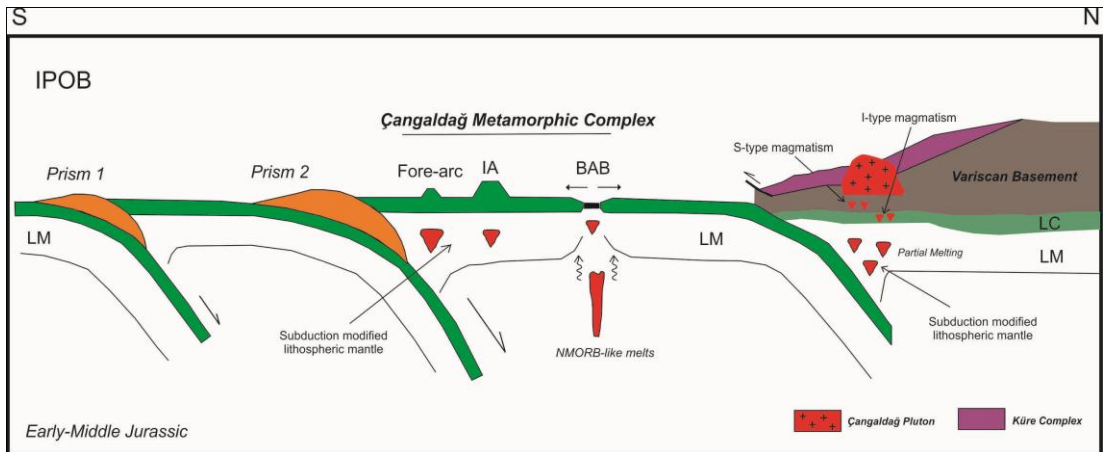


Figure 6-2: Possible geodynamic model for the Çangaldağ Metamorphic Complex and Çangaldağ Pluton (Prism 1: Aylı Dağ Ophiolite and Arkot Dağ Melange; Prism 2: Domuzdağ, Daday and Saka Units; Variscan Basement: Devrekani Units, Geme Complex, Sivrikaya and Deliktaş Granitoids; LM: Lithospheric Mantle; IA: Island Arcs; BAB: Back-arc Basalts; LC: Lower Crust)



## CHAPTER 7

### CONCLUSIONS

#### 7.1. Concluding remarks for the Çangaldağ Metamorphic Complex

The CMC in Central Pontides is an imbricated and low-grade metamorphic unit comprising metabasalts, metaandesites/basaltic andesites and metarhyodacites with volcanoclastic and clastic/carbonate rocks. The complex rests with a steep reverse fault on the Tertiary deposits of the Kastamonu-Boyabat Basin and is bounded by an oblique reverse fault or an overthrust with strike slip component by the CP.

The metavolcanic rocks from CMC include both basic and evolved members. Trace element systematics of the basic members suggests that these rocks were derived from a depleted mantle source modified by a subduction-component. While the presence of highly depleted signatures, such as the boninitic ones, indicates an intra-oceanic arc origin, the N-MORB-like characteristics are rather consistent with a back-arc origin. Thus, overall characteristics suggest that CMC represent remnants of an intra-oceanic arc-basin system, including melt generation both in arc and back-arc regions. The single zircon U-Pb data from the rhyodacites suggest a Middle Jurassic (156 -176Ma; in this study) age for the volcanism. The overall Hf data for the volcanic rocks from the CMC indicate that it could have been formed by mixing of depleted mantle and crustal sources (oceanic) for the magma generation.

The geochemical data strongly suggest to an intra-oceanic arc system with elements from the fore-arc, arc and back-arc components that were accreted during the closure of a northern segment of the Neotethyan Intra-Pontide Ocean.

## 7.2. Concluding remarks for the Çangaldağ Pluton

On the other hand, the CP, located in the northeast of the CMC, is composed of diorites, dacite porphyries and granites. Regionally, this huge igneous body intrudes Triassic Küre Complex. It is also overlain by Upper Jurassic İnaltı Limestone. These field relations provide Early-Middle Jurassic age as supported by Middle Jurassic radiometric ages (161-169 Ma; in this study).

This pluton exhibits calc-alkaline, magnesian and I-type characteristics. It has similar geochemical features to volcanic arc granites and the geochemical discrimination diagrams indicate the characteristics of continental arc magmatism. The dacite porphyries have been generated by significant fractional crystallization of the dioritic rocks. Moreover, they have been mostly derived from melts of a mafic amphibolitic source. The non-uniform distributions of the U-Pb and Hf data for granite samples indicate that this magmatism could have been derived from a sedimentary source. The age of these crustal rocks could be Neoproterozoic / Mesoproterozoic, which are common in Gondwana-derived terranes, based upon the calculated Hf  $T_{DM}$  model ages.

To conclude, the evaluation of the petrogenetic features and ages of the variably metamorphic oceanic volcanisms in the Central Pontide Structural Complex imply that the Intra-Pontide Ocean was consumed by stepwise intra-oceanic subductions giving way to a huge subduction-accretion prism to the N of the Cimmerian Sakarya Composite Terrane. The CMC forms a backarc basin system above the subducting Intra-Pontide oceanic crust close to a Sakarya-type continental crust, whereas the CP represents the marginal (continental) arc above another subducting slab within the Sakarya Composite terrane.

## REFERENCES

- Akbayram, K., Okay, A.I., and Satır, M., 2013. Early Cretaceous closure of the Intra-Pontide Ocean in western Pontides (northwestern Turkey). *Journal of Geodynamics*, 65, 38–55.
- Aldanmaz, E., Yalınız, M.K., Güçtekin, A., and Göncüoğlu, M.C., 2008. Geochemical characteristics of mafic lavas from the Tethyan ophiolites in western Turkey: implications for heterogeneous source contribution during variable stages of ocean crust generation, *Geological Magazine*, 145, 37-54.
- Altiner, D., and Kocyigit, A., 1993. Third remark on the geology of the Karakaya basin. An Anisian megablock in northern central Anatolia: micropaleontologic, stratigraphic and tectonic implications for the rifting stage of Karakaya basin, Turkey. *Revue de Palaeobiologie*, 12, 1-17.
- Aydın, M., Şahintürk, Ö., Serdar, H.S., Özçelik, Y., Akarsu, İ., Üngör, A., Çokuğraş, R., ve Kasar, S. 1986. Ballıdağ-Çangaldağı (Kastamonu) arasındaki bölgenin jeolojisi, *TJK Bülteni*, 29, 1-16.
- Aydın, M., Demir, O., Özçelik, Y., Terzioğlu, N., and Satır, M., 1995a. A geological revision of İnebolu, Devrekani, Ağlı and Küre areas: New observations in Paleotethys - Neo-Tethys sedimentary successions. In: *Geology of the Black Sea region* (eds. Erler, A., Ercan, T., Bingöl, E. and Örçen, S.), MTA/JMO, 33-38.
- Aydın, M., Demir, O., Serdar, H.S., Özyayın, S., and Harput, B., 1995b. Tectono-sedimentary evolution and hydrocarbon potential of Sinop-Boyabat basin, north Türkiye. In: *Geology of the Black Sea region* (eds. Erler, A., Ercan, T., Bingöl, E. and Örçen, S.), MTA/JMO, 254-263.
- Aygül M, Okay AI, Oberhänsli R, Sudo M (2016). Pre-collisional accretionary growth of the southern Laurasian active margin, Central Pontides, Turkey. *Tectonophysics* 671: 218-234.
- Batumike, J.M., O'Reilly, S.Y., Griffin, W.L., and Belousova, E.A., 2007. U–Pb and Hf-isotope analyses of zircon from the Kundelungu Kimberlites, D.R. Congo: Implications for crustal evolution. *Precambrian Research*, 156 (3-4), 195-225.
- Bizzarro, M., Simonetti, A., Stevenson, R.K., and David, J., 2002. Hf isotope evidence for a hidden mantle reservoir. *Geology*, 30, 771-774.

Bizzarro, M., J. A. Baker, H. Haack, D. Ulfbeck, and M. Rosing (2003), Early history of Earth's crust-mantle system inferred from hafnium isotopes in chondrites, *Nature*, 421, 931–933.

Bouvier, A., Vervoot, J.D., and Patchett, P.J., 2008. The Lu–Hf and Sm–Nd isotopic composition of CHUR: Constraints from unequilibrated chondrites and implications for the bulk composition of terrestrial planets. *Earth and Planetary Science Letters*. 273(1-2), 48-57.

Boynton, W.V., 1984. Cosmochemistry of the rare earth elements, meteorite studies, In: *Rare earth element geochemistry*. Henderson, P. (Editors), Elsevier Science Publication Company, Amsterdam, 63-114.

Boztuğ, D., 1983. Daday-Devrakani masifikuzeyindeki Büyükçay-Elşmalıçay granitik sokulumu. Yüksek Müh. Tezi, Hacettepe Üniversitesi, 149 s.

Boztuğ, D., and Yılmaz, O. 1983. Büyükçay-Elmalıçay granitoyidi (Kastamonu) ve çevre kayalarının mineralojik-petrografik ve jeokimyasal incelemesi. *Yerbilimleri*, 10, 71-88.

Boztuğ, D., 1988. Daday-Devrakani masifi güneybatı kesiminin mineralojik-petrografik ve jeokimyasal incelenmesi. Doktora Tezi, Hacettepe Üniversitesi.

Boztuğ, D., 1992a. Lithostratigraphic units and tectonics of the southwestern part of Daday-Devrekani massif, western Pontides, Turkey. *MTA Bulletin*, 114, 1-22.

Boztuğ, D., 1992b. Orta-Batı Pontidlerdeki Küre yöresi (K Kastamonu) magmatiti-metamorfitlerinin petrografisi ve magmatitlerin ana element jeokimyası. *Cumhuriyet Üniversitesi Müh. Fak. Dergisi, Seri-A, Yerbilimleri*, 9 (1), 75-106.

Boztuğ, D., Debon, F., Le Fort, P., and Yılmaz, O., 1995. High compositional diversity of the Middle Jurassic Kastamonu Plutonic Belt, northern Anatolia, Turkey. *Turkish Journal of Earth Sciences*, 4, 67-86.

Boztuğ, D., and Yılmaz, O., 1995. Daday-Devrekani masifi metamorfizması ve jeolojik evrimi, Kastamonu bölgesi, Batı Pontidler, Türkiye. *TJK Bülteni*, 38 (1), 33-52. (in Turkish).

Catanzariti, R., Ellero, A., Göncüoğlu, M.C., Marroni, M., Ottria, G., and Pandolfi L., 2013. The Taraklı Flysch in the Boyalı area (Sakarya Terrane, northern Turkey): Implications for the tectonic history of the Intra-Pontide suture zone. *Comptes Rendus Geoscience* 345, 454–461.

Chappell, B.W., and White, J.R., 2001. Two contrasting granite types: 25 years later. *Australian Journal of Earth Sciences*, 48, 489-499.

Chen, W., and Simonetti, A., 2014. Evidence for the multi-stage petrogenetic history of the Oka carbonatite complex (Quebec, Canada) as recorded by perovskite and apatite. *Minerals*, 4, 437-476.

Chen, W., Simonetti, A., and Burns, P.C., 2013. A combined geochemical and geochronological investigation of niocalite from the Oka carbonatite complex, Canada. *The Canadian Mineralogist*, 51, 785-800.

Cocks, L.R.M., and Torsvik, T.H., 2006. European geography in a global context from the Vendian to the end of the Palaeozoic. in Gee, D.G., and Stephenson, R.A., eds., *European Lithosphere Dynamics*: London, Geological Society, 83–95. *Memoirs* 32.

Condie, K.C. and Kroner, A., 2013. The building blocks of continental crust: Evidence for a major change in the tectonic setting of continental growth at the end of the Archean. *Gondwana Research*, 23, 394–402.

Çelik, Ö.F., Marzoli, A., Marschik, R., Chiaradia, M., Neubauer, F., and Öz, İ. 2011. Early-Middle Jurassic intra-oceanic subduction in the İzmir-Ankara-Erzincan Ocean, Northern Turkey: *Tectonophysics*. 509, 120-134.

Çimen, O., Sayıt, K., and Göncüoğlu, M.C., 2015. Preliminary Geological and Geochemical Data from the Çangaldağ Complex (Kastamonu-Turkey): Implications for the Geodynamic Evolution of the Central Pontides. *EGU General Assembly 2015*, April 12-17, Vienna, Austria.

Çimen, O., Göncüoğlu, M.C., Simonetti, A., and Sayıt, K., 2016a. Zircon U-Pb Geochronology, Hf isotopes and whole rock geochemistry of the metavolcanic rocks from the Çangaldağ Complex (Central Pontides, Turkey). *69th Geological Congress of Turkey. Abstracts and Programme*, 269-270.

Çimen, O., Göncüoğlu, M.C., Sayıt, K., and Simonetti, A., 2016b. Whole rock geochemistry, U-Pb geochronology and Lu-Hf isotope systematics of the Çangaldağ Pluton (Central Pontides, Turkey). *69th Geological Congress of Turkey. Abstracts and Programme*, 148-149.

Crawford, A.J., Falloon, T.J., and Green, D.H., 1989. Classification, petrogenesis and tectonic setting of boninites. In: Crawford AJ (ed) *Boninites*. Unwin Hyman, London, 1-49.

Davies, J.H., and Bickle, M.J., 1991. A physical model for the volume and composition of melt produced by hydrous fluxing above subduction zones. *Philosophical Transaction of the Royal Society*, 335, 355-364.

Derman, S., 1990. Batı Karadeniz Bölgesinin Geç Jura-Erken Kretase evrimi. 8. Petrol Kongresi Proceedings, 328-339.

Dixon, T.H., and Batiza, R., 1979. Petrology and chemistry of recent lavas in the Northern Marianas: Implications for the origin of island arc basalts. *Contributions to Mineralogy and Petrology*, 70, 167-181.

Duncan, R.A., and Green, D.H., 1987. The genesis of refractory melts in the formation of oceanic crust. *Contributions to Mineralogy and Petrology*, 96, 326-342.

Ellero, A., Ottria, G., Sayit, K., Catanzariti, R., Frassi, C., Göncüoğlu, M.C., Marroni, M., and Pandolfi, L., 2015. Geological and geochemical evidence for a Late Cretaceous continental arc in the central Pontides, northern Turkey. *Ofioliti* 40, 73-90.

Elmas, A., and Yiğitbaş, E., 2001. Ophiolite emplacement by strike-slip tectonics between the Pontide Zone and the Sakarya Zone in northwestern Anatolia, Turkey. *International Journal of Earth Sciences*, 90, 257–269.

Flowers, R.M., Bowring, S.A., Tulloch, A.J., and Klepeis, K.A., 2005. Tempo of burial and exhumation within the deep roots of a magmatic arc, Fiordland, New Zealand: *Geology*, 33, 17-20.

Floyd, P.A., and Winchester, J.A., 1978. Identification and discrimination of altered and metamorphosed volcanic rocks using immobile elements. *Chemical Geology*, 21, 291-306.

Floyd, P.A., Winchester, J.A., Seston, R., Kryza, R., and Crowley, Q.G., 2000. Review of geochemical variation in Lower Palaeozoic metabasites from the NE Bohemian Massif; intracratonic rifting and plume ridge interaction. In: W. Franke, V. Haak, O. Oncken and D. Tanner (Eds.), *Orogenic processes: Quantifications and modeling in the Variscan Belt*. Geological Society of London Special Publication, 179, 155-174.

Frassi, C., Göncüoğlu, M.C., Marroni, M., Pandolfi, L., Ruffini, L., Ellero, A., Ottria, G & Sayit, K. (2016). The Intra-Pontide suture zone in the Tosya-Kastamonu area, Northern Turkey, *Journal of Maps*, DOI: 10.1080/17445647.2016.1192330.

Frost, B. R., Barnes, C. G., Collins, W. J., Arculus, R. J., Ellis, D. J. & Frost, C. D. (2001). A geochemical classification for granitic rocks. *Journal of Petrology* 42, 2033–2048.

Galoyan, G., 2008. Etude pétrologique, géochimique et géochronologique des ophiolites du Petit Caucase (Arménie). PhD thesis, Université de Nice-Sophia Antipolis.

Galoyan, G., Rolland, Y., Sosson, M., Corsini, M., Billo, S., Verati, C., and Melkonian, R., 2009. Geology, geochemistry and  $^{40}\text{Ar}/^{39}\text{Ar}$  dating of Sevan ophiolites (Lesser Caucasus, Armenia): evidence for Jurassic Back-arc opening and hot spot event between the South Armenian Block and Eurasia. *Journal of Asian Earth Science*, 34, 135–153.

Goolaerts, A., Mattielli, N., de Jong, J., Weis, D. and Scoates, J. S., 2004. Hf and Lu reference values for the zircon standard 91500 by MCICP-MS. *Chemical Geology*, 206, 1-9.

Göncüoğlu, M. C., Kozlu, H., and Dirik, K., 1997. Pre-Alpine and Alpine terranes in Turkey: explanatory notes to the terrane map of Turkey. *Annales Géologiques des Pays Helleniques*, 37, 515-536.

Göncüoğlu, M. C., and Kozur, H., 1998. Remarks on the pre-Variscan development in Turkey. In: Linnemann, U., Heuse, T., Fatka, O., Kraft, P. Brocke, R. and Erdtmann, B.T. (eds), *Pre-variscan Terrane Analyses of "Gondwanean Europa"*, Proceedings, Schriften des Staatlichen Museum, Mineralogie Geologie, Dresden, 9, 137- 138.

Göncüoğlu, M. C., Turhan, N., Sentürk, K., Özcan, A., and Uysal, S., 2000. A geotraverse across NW Turkey: tectonic units of the Central Sakarya region and their tectonic evolution. In: Bozkurt, E., Winchester, J. A. & Piper, J. D. (eds) *Tectonics and Magmatism in Turkey and the Surrounding Area*, Geological Society of London, Special Publications, 173, 139–162.

Göncüoğlu, M.C., Yalınız, K., and Tekin, U.K., 2006. Geochemistry, tectono-magmatic discrimination and radiolarian ages of basic extrusives within the Izmir-Ankara Suture Belt (NW Turkey): Time Constraints for the Neotethyan Evolution. *Ofioliti* 31, 25-38.

Göncüoğlu, M.C., Çapkinoğlu, S., Gürsu, S., Noble, P., Turhan, N., Tekin, U.K., Okuyucu, C. and Göncüoğlu, Y., 2007. The Mississippian in the Central and Eastern Taurides (Turkey): constraints on the tectonic setting of the Tauride-Anatolide Platform. *Geologica Carpathica*, 58, 427-442.

Göncüoğlu, M.C., Gürsu, S., Tekin, U.K., and Köksal, S., 2008. New data on the evolution of the Neotethyan Oceanic Branches in Turkey: Late Jurassic ridge spreading in the Intra-Pontide Branch. *Ofioliti*, 33, 153-164.

Göncüoğlu, M.C., 2010. Introduction to the Geology of Turkey: Geodynamic evolution of the pre-Alpine and Alpine Terranes. MTA, 1-69.

Göncüoğlu, M.C., Sayit, K., and Tekin, U.K., 2010. Oceanization of the northern Neotethys: geochemical evidence from ophiolitic melange basalts within the Izmir–Ankara suture belt, NW Turkey. *Lithos*, 116 (1), 175-187.

Göncüoğlu, M.C., Marroni, M., Sayit, K., Tekin, U.K., Ottria, G., Pandolfi, L., and Ellero, A., 2012. The Aylı Dağ ophiolite sequence (Central-Northern Turkey): A fragment of Middle Jurassic Oceanic Lithosphere within the Intra-Pontide suture zone. *Ofioliti*, 37 (2), 77-92.

Göncüoğlu, M.C., Marroni, M., Pandolfi, L., Ellero, A., Ottria, G., Catanzariti, R., Tekin, U.K., and Sayit, K., 2014. The Arkot Dağ Melange in Araç area, central Turkey: Evidence of its origin within the geodynamic evolution of the Intra-Pontide suture zone. *Journal of Asian Earth Science*, 85, 117-139.

Görür, N., 1988. Timing of opening of the Black Sea basin. *Tectonophysics*, 47, 247-262.

Görür, N., Monod, O., Okay, A. I., Şengör, A. M. C., Tüysüz, O., Yiğitbaş, E., Sakıncı, M., and Akkök, R., 1997. Palaeogeographic and tectonic position of the Carboniferous rocks of the western Pontides (Turkey) in the frame of the Variscan belt. *Bulletin de la Société Géologique de France* 168, 197–205.

Green, D.H., 1973. Experimental melting studies on a model upper mantle composition at high pressure under water-saturated and water-unsaturated conditions. *Earth Planetary Science Letter*, 19, 37-53.

Gribble, R.F., Stern, R.J., Newman, S., Bloomer, S.H., and O’Hearn, T. 1998. Chemical and isotopic composition of lavas from the northern Mariana Trough; implications for magma genesis in back-arc basins. *Journal of Petrology*, 39, 125-154.

Griffin, W.L., Wang, X., Jackson, S.E., Pearson, N.J., O’Reilly, S.Y., Xu, X., and Zhou, X., 2002. Zircon chemistry and magma mixing, SE China: In situ analysis of Hf isotopes, Tonglu and Pingtan igneous complexes. *Lithos*, 61, 237-269.

Gumsley, A., Olsson, J., Söderlund, U., Kock, M., Hofmann, A., and Klausen, M., 2015. Precise U-Pb baddeleyite age dating of the Usushwana Complex, southern Africa - Implications for the Mesoarchean magmatic and sedimentological evolution of the Pongola Supergroup, Kaapvaal Craton. *Precambrian Research*, 267, 17-185.

Gücer, M.A., and Arslan, M., 2015. Petrochemistry, petrology, geochronology and P-T estimation of the Devrekani (Kastamonu, N Turkey) Massif. *Goldschmidt, Abstracts*. p. 1113.

Gücer, M.A., Arslan, M., Sherlock, S., and Heaman, L.M., 2016. Permo-Carboniferous granitoids with Jurassic high temperature metamorphism in Central Pontides, Northern Turkey. *Mineralogy and Petrology*, 1-22.

Gürsu, S., and Göncüoğlu, M.C., 2005. Early Cambrian back-arc volcanism in the western Taurides, Turkey: implications for rifting along the northern Gondwanan margin. *Geological Magazine* 142 (5): 617-631.

Hässig, M., Rolland, Y., Sosson, M., Galoyan, G., Müller, C., Avagyan, A., and Sahakyan, L., 2013. New structural and petrological data on the Amasia ophiolites (NW Sevan-Akera suture zone, Lesser Caucasus): insights for a large-scale obduction in Armenia and NE Turkey. *Tectonophysics* 588, 135–153.

Hipplyte, J.J., Espurt, N., Kaymakci, N., Sangu, E., and Müller, C., 2016. Cross-sectional anatomy and geodynamic evolution of the Central Pontide orogenic belt (northern Turkey). *International Journal of Earth Sciences*, 105 (1), 81-106.

Horn, I., Rudnick, R.L., McDonough, W.F., 2000, Precise elemental and isotope ratio determination by simultaneous solution nebulization and laser ablation–ICP–MS: application to U–Pb geochronology: *Chemical Geology*, 164(3–4), 281–201.

Hu, J., Gong, W., Wu, S., Liu, Y., and Liu, S., 2014. LA-ICP-MS zircon U–Pb dating of the Langshan Group in the northeast margin of the Alxa block, with tectonic implications. *Precambrian Research*, 255, 756-770.

Izosaki, Y., Ehiro, M., Nakahata, H., Aoki, K., Sakata, S., and Hirata, T., 2015. Cambrian plutonism in Northeast Japan and its significance for the earliest arc-trench system of proto-Japan: New U–Pb zircon ages of the oldest granitoids in the Kitakami and Ou Mountains. *Journal of Asian Earth Sciences*, 108, 136-149.

Jackson, S.E., Pearson, N.J., Griffin, W.L., and Belousova, E.A., 2004. The application of laser ablation-inductively coupled plasma-mass spectrometry to in situ U–Pb zircon geochronology. *Chemical Geology*, 211, 47-69.

Kaya, O., 1977. Gemlik Orhangazı alanının Paleozoyik temel yapısına yaklaşım. *Yerbilimleri*, 3: 115-128 (in Turkish with English abstract).

Kaya, O., and Kozur, H., 1987. A new and different Jurassic to Early Cretaceous sedimentary assemblage in northwestern Turkey (Gemlik, Bursa): implications for the pre-Jurassic to Early Cretaceous tectonic evolution. *Yerbilimleri*, 14: 253-268.

Kaya, M.Y., and Altner, D., 2014. *Terebella lapilloides* Münster, 1833 from the Upper Jurassic-Lower Cretaceous İntalti carbonates, northern Turkey: Its taxonomic position and paleoenvironmental/paleoecological significance. *Turkish Journal of Earth Science*, 23, 166-183.

Keller, R.A., Fisk, M.R., White, W.M., and Birkenmajer, K., 1992. Isotope and trace element constraints on mixing and melting models of marginal basin volcanism, Barnfield Strait, Antarctica. *Earth Planetary Science Letter*, 111, 287-303.

Ketin, İ., and Gümüş, Ö., 1963. Sinop-Ayancık arasında III. Bölgeye dahil sınırların jeolojisi. TPAO Rapor No: 288, Ankara.

Konya, S., Pehlivanoglu, H., and Teşrekli, M., 1988. Kastamonu, Taşköprü, Devrekani yöresi jeokimya raporu. MTA.

Kozur, H., Aydın, M., Demir, O., Yakar, H., Göncüoğlu, M.C., and Kuru F., 2000. New stratigraphic results from the Paleozoic and Early Mesozoic of the Middle Pontides (Northern Turkey). *Geologia Croatia*, 53, 209-268.

Köksal, S., Toksoy-Köksal, F., Göncüoğlu, M.C., Möller, A., Gerdes, A., and Frei, D., 2013. Crustal source of the Late Cretaceous Satansarı monzonite stock (central Anatolia – Turkey) and its significance for the Alpine geodynamic evolution. *Journal of Geodynamics*. 65, 82-93.

Köksal, S., Romer, R. L., Göncüoğlu, M. C., Toksoy-Köksal, F., 2004. Timing of post-collisional H-type to A-type granitic magmatism: U-Pb titanite ages from Alpine central Anatolian Granitoids (Turkey). *International Journal of Earth Science*, 93, 974-989.

Kröner, A., Hoffmann, J.E., Xie, H., Münker, C., Hegner, E., Wan, Y., Hofmann, A., Liu, D., and Yang, J., 2014. Generation of early Archaean grey gneisses through melting of older crust in the eastern Kaapvaal craton, southern Africa. *Precambrian Research*, 255, 823-846.

Langmuir, C.H., Bézous, A., Escrig, S., and Parman, S.W., 2006. Chemical systematics and hydrous melting of the mantle in back-arc basins. In: Christie DM, et al. (Ed.), *Back-arc spreading systems: geological, biological, chemical and physical interactions*. *Geophysical Monograph Series*, 166, 87-146.

Ludwig, K.R., 2008. *Manual for Isoplot 3.7*: Berkeley Geochronology Center, Special Publication, 4, 77.

Marroni, M., Frassi, C., Göncüoğlu, M.C., Dİ Vincenzo, G., Pandolfi, L., Rebay, G., Ellero, A., and Ottaria, G., 2014. Late Jurassic amphibolite-facies metamorphism in

the Intra-Pontide Suture Zone (Turkey): an eastward extension of the Vardar Ocean from the Balkans into Anatolia?. *Journal of Geological Society*, 171, 605-608.

Meschede, M., 1986. A method of discriminating between different types of midocean ridge basalts and continental tholeiites with the Nb-Zr-Y diagram. *Chemical Geology*, 56, 207-218.

Middlemost, E.A.K., 1985. *Magmas and magmatic rocks. An introduction to igneous petrology*. London, New York, Longman, 266.

Nutman, A.P., Buckman, S., Hidaka, H., Kamiichi, T., Belousova, E., and Aitchison, J., 2013. Middle Carboniferous-Early Triassic eclogite–blueschist blocks within a serpentinite mélangé at Port Macquarie, eastern Australia: Implications for the evolution of Gondwana's eastern margin. *Gondwana Research*, 24(3-4), 1038-1050.

Nzegge, O. M., Satir, M., Siebel, W., and Taubald., H., 2006. Geochemical and isotopic constraints on the genesis of the Late Palaeozoic Deliktaş, and Sivrikaya granites from the Kastamonu granitoid belt (Central Pontides, Turkey). *Neues Jahrbuch für Mineralogie*, 183, 27-40.

Nzegge, O., 2008. Petrogenesis and geochronology of the Deliktaş, Sivrikaya and Devrekani granitoids and basement, Kastamonu Belt-Central Pontides (NW Turkey): Evidence for Late Paleozoic-Mesozoic plutonism, and geodynamic interpretation. PhD Thesis, 177 p.

Okay, A.I., Siyako, M., and Bürkan, K.A., 1990. Biga Yarımadasının jeolojisi ve tektonik evrimi. *Türkiye Petrol Jeologları Derneği Bülteni*, 2, 121-183.

Okay, A.I., Şengör, A. M. C., and Görür, N. 1994. Kinematic history of the opening of the Black Sea and its effects on the surrounding regions. *Geology*, 22, 267-270.

Okay, A.I., and Şahintürk, O., 1997. Geology of the Eastern Pontides. *American Association of Petroleum Geologists, Memoir*, 68, 291-313.

Okay, A.I., and Tuysuz, O., 1999. Tethyan sutures of northern Turkey. In: *The Mediterranean Basins: Tertiary Extension within the Alpine Orogen* (eds Durand, B., Jolivet, L., Horvath, F. & Seranne, M.). Geological Society of London, Special Publication, 156, 475–515.

Okay, A.I., 2000. Was the Late Triassic orogeny in Turkey caused by the collision of an oceanic plateau? in Bozkurt, E., Winchester, J.A., and Piper, J.A.D., eds., *Tectonics and magmatism in Turkey and surrounding area*. Geological Society of London, Special Publication, 173, 25-41.

Okay, A.I., Tüysüz, O., Satır, M., Özkan-Altıner, S., Altıner, D., Sherlock, S., and Eren, R.H., 2006. Cretaceous and Triassic subduction-accretion, high-pressure-low-temperature metamorphism, and continental growth in the Central Pontides, Turkey. *GSA Bulletin*, 118, 1247-1269.

Okay, A.I., Bozkurt, E., Satır, M., Yiğitbaş, E., Crowley, Q.G., and Shang, C.K., 2008. Defining the southern margin of Avalonia in the Pontides: Geochronological data from the Late Proterozoic and Ordovician granitoids from NW Turkey. *Tectonophysics*, 461, p. 252-264.

Okay, A.I., Gürsel, S., Sherlock, S., Altıner, D., Tüysüz, O., Kylander-Clark, A.R.C., and Aygül, M., 2013. Early Cretaceous sedimentation and orogeny on the active margin of Eurasia: Southern Central Pontides, Turkey. *Tectonics*, 32, 1247-1271.

Okay, A.I., Gürsel, S., Tüysüz, O., Sherlock, S., Keskin, M., and Kylander-Clark, A.R.C., 2014. Low-pressure - high-temperature metamorphism during extension in a Jurassic magmatic arc, Central Pontides, Turkey. *Journal of Metamorphic Geology*, 32, 49-69.

Okay, A.I., Altıner, D., and Kılıç, A., 2015. Triassic limestone, turbidites and serpentinite—the Cimmeride orogeny in the Central Pontides. *Geological Magazine*, 152, 460-479.

Okay, A.I., and Nikishin, M.A., 2015. Tectonic evolution of the southern margin of Laurasia in the Black Sea region. *International Geology Review*, 1-26.

Özcan, A., Göncüoğlu M.C., Turhan, N., Uysal, Ş., and Şentürk, K., 1990. Late Paleozoic evolution of the Kütahya-Bolkardağ Belt. *METU Journal of Pure and Applied Science*, 21, 211-220.

Parlak, O., Çolakoğlu A., Dönmez, C., Sayak, H., Yıldırım, N., Türkel, A., and Odabaşı, İ., 2013. Geochemistry and tectonic significance of ophiolites along the İzmir-Ankara-Erzincan Suture Zone in northeastern Anatolia. *Geological Society, London*, 372, 75-105.

Patiño Douce, A. E., 1999. What do experiments tell us about the relative contributions of crust and mantle to the origin of granitic magmas? In: Castro, A., Fernandez, C. & Vigneresse, J. (eds) *Understanding Granites: Integrating New and Classical Techniques*. Geological Society, London, Special Publications 168, 55-75.

Paton, C., Woodhead, J.D., Hellstrom, J.C., Hergt, J.M., Greig, A., Maas, R., 2010. Improved laser ablation U–Pb zircon geochronology through robust downhole fractionation correction: *Geochemistry Geophysics Geosystems* ( $G^3$ ), 11 (3).

Pearce, J.A., and Cann, J.R., 1973. Tectonic setting of basic volcanic rocks determined using trace element analyses. *Earth Planetary Science Letter*, 19, 290-300.

Pearce, J.A., 1975. Basalt geochemistry used to investigate past tectonic environments on Cyprus. *Tectonophysics*, 25, 41-67.

Pearce, J.A., and Norry, M., 1979. Petrogenetic implications of Ti, Zr, Y and Nb variations in volcanic rocks. *Contribution Mineralogy and Petrology*, 69, 33-47.

Pearce, J. A., Harris, N. W., and Tindle, A. G., 1984. Trace element discrimination diagrams for the tectonic interpretation of granitic rocks. *Journal of Petrology* 25, 956-983.

Pearce, J.A., van der Laan, S.R., Arculus, R.J., Murton, B.J., Ishii, T., Peate, D.W., and Parkinson, I.J., 1992. Boninite and harzburgite from Leg 125 (Bonin-Mariana forearc): a case study of magma genesis during the initial stages of subduction. *Proceedings of the Ocean Drilling Programme, Science Research*, 125, 623-659.

Pearce, J.A., and Peate, D.W., 1995. Tectonic implications of the composition of volcanic arc magmas. *Annual Review of Earth and Planetary Science*, 23, 251- 286.

Pearce, J.A., Ernewein, M., Bloomer, S.H., Parson, L.M., Murton, B.J., and Johnson, L.E., 1995. Geochemistry of Lau Basin volcanic rocks: influence of ridge segmentation and arc proximity. In: Smellie J.L., (ed.), *Volcanism Associated with Extension at Consuming Plate Margins*. Geological Society, London, Special Publication, 81, 53-75.

Pearce, J.A., 1996. A user's guide to basalt discrimination diagrams. In: Wyman DA (ed). *Trace element geochemistry of volcanic rocks: applications for massive sulphide exploration*. Short course notes 12. Geological Association of Canada, 79-113.

Pearce, J.A., Stern, R.J., Bloomer, S.H., and Fryer, P., 2005. Geochemical mapping of the Mariana arc-basin system: Implications for the nature and distribution of subduction components. *Geochemical Geophysical Geosystems*, 6(7), Q07006.

Pearson, N.J., Griffin, W.L., and O'Reilly, S.Y., 2008. Mass fractionation correction in laser ablation multiple-collector ICP-MS: precise and accurate in situ isotope ratio measurement. In: Sylvester P, editor. *Laser Ablation-ICP-MS in the Earth Sciences*. Mineralogical Association of Canada Short Course Series, 40, 93-116.

Peate, D.W., Pearce, J.A., Hawkesworth, C.J., Collie, H., Edwards, C.H.M., and Hirose, K., 1997. Geochemical variations in Vanuatu arc lavas: the role of subducted material and a variable mantle wedge composition. *Journal of Petrology*, 38, 1331-1358.

Peccerillo, A., and Taylor, S.R., 1976. Geochemistry of Eocene calc-alkaline volcanic rocks of the Kastamonu area. Northern Turkey. *Contribution to Mineralogy and Petrology*, 58, 63-81.

Perfit, M.R., and Fornari, D.J., 1983. Geochemical studies of abyssal lavas recovered by DSRV ALVIN from the eastern Galapagos Rift - Inca Transform - Ecuador Rift: II. Phase chemistry and crystallization history. *Journal of Geophysical Research*, 88, 530-550.

Rapela, C.W., Verdecchia, S.O., Casquet, C., Pankhurst, R.J., Baldo, E.G., Galindo, C., Murra, J.A., Dalhquist, J.A., and Fanning, C.M., 2016. Identifying Laurentian and SW Gondwana sources in the Neoproterozoic to Early Paleozoic metasedimentary rocks of the Sierras Pampeanas: Paleogeographic and tectonic implications. *Gondwana Research*, 32, 193-212.

Rasmussen, B., Fletcher, I.R., and Muhling, J.R., 2013. Dating deposition and low-grade metamorphism by in situ U-Pb geochronology of titanite in the Paleoproterozoic Timeball Hill Formation, southern Africa. *Chemical Geology*, 351, 29-39.

Renjith, M.L., Santosh, M., Li, T., Satyanarayanan, M., Korakoppa, M.M., Tsunogae, T., Subba Rao, D.V., Krishna, A.K., and Charan, S.N., 2016. Zircon U-Pb age, Lu-Hf isotope, mineral chemistry and geochemistry of Sundamalai peralkaline pluton from the Salem Block, southern India: Implications for Cryogenian adakite-like magmatism in an aborted rift. *Journal of Asian Earth Sciences*, 115, 321-344.

Roberts, M.P., and Clemens, J.D., 1993. Origin of high-potassium, calc-alkaline, I-type granitoids. *Geology*, 21, 825-828.

Robertson, A.H.F., Parlak, O., and Ustaömer, T., 2012. Overview of the Paleozoic-Neogene evolution of Neotethys in the Eastern Mediterranean region (Southern Turkey, Cyprus, Syria). *Petroleum Geoscience*, 18, 381-404.

Robertson, A.H.F., and Ustaömer, T., 2004. Tectonic evolution of the Intra-Pontide suture zone in the Armutlu Peninsula, NW Turkey. *Tectonophysics*, 381, 175-209.

Robertson, A., Parlak, O., Ustaömer, T., Taslı, K., İnan, N., Dumitrica, P., and Karaoğlan, F., 2014. Subduction, ophiolite genesis and collision history of Tethys adjacent to the Eurasian continental margin: new evidence from the Eastern Pontides, Turkey. *Geodinamica Acta*, 1-64.

- Rolland, Y., Galoyan, G., Sosson, M., Melkonian, R., and Avagyan, A., 2010. The Armenian ophiolite: Insights for Jurassic back-arc formation, lower Cretaceous hot spot magmatism and upper Cretaceous obduction over the South Armenian block. *Geological Society, London*, 340, 353-382.
- Sayit, K., Göncüoğlu, M.C., and Furman, T., 2010. Petrological reconstruction of Triassic seamounts/oceanic islands within the Palaeotethys: Geochemical implications from the Karakaya subduction/accretion Complex, Northern Turkey. *Lithos*, 119, 501–511.
- Sayit, K., and Göncüoğlu, M.C., 2013. Geodynamic evolution of the Karakaya Mélange Complex, Turkey: a review of geological and petrological constraints. *Journal of Geodynamics*, 65, 56–65.
- Sayit, K., Marroni, M., Göncüoğlu, M.C., Pandolfi, L., Ellero, A., Ottria, G., Frassi, C., 2016. Geological setting and geochemical signatures of the mafic rocks from the Intra-Pontide Suture Zone: implications for the geodynamic reconstruction of the Mesozoic Neotethys. *International Journal of Earth Science*, 105, 39-64.
- Schandl, E. S., and Gorton, M. P., 2002. Application of high field strength elements to discriminate tectonic settings in VMS environments. *Economic Geology* 97, 629-642.
- Scherer, E. E., Münker, C., and Mezger, K., 2001. Calibration of the Lu-Hf clock. *Science*, 293, 683-687.
- Schmidberger, S.S., Heaman, L.M., Simonetti, A., Creaser, R.A., and Cookenboo, H.O., 2005. Formation of Paleoproterozoic eclogitic mantle, Slave province (Canada): insights from in-situ Hf and U-Pb isotope analyses of mantle zircons. *Earth Planetary Science Letters*, 240, 621-633.
- Shervais, J.W., 1982. Ti–V plots and the petrogenesis of modern ophiolitic lavas. *Earth Planetary Science Letter*, 59, 101–118.
- Slama, J., Kosler, J., Condon, D.J., Crowley, J.L., Gerdes, A., Hanchar, J.M., Horstwood, M.S.A., Morris, G.A., Nasdala, L., Norberg, N., Schaltegger, U., Schoene, N., Tubrett, M.N., and Whitehouse, M.J., 2008. Plesovice zircon - a new natural reference material for U-Pb and Hf isotopic microanalysis. *Chemical Geology*, 249, 1-2, 1-35.
- Simonetti, A., Heaman, L.R., Hartlaub, R., Creaser, T., MacHattie, T.G., and Böhm, C., 2005. U-Pb zircon dating by laser ablation-MC-ICP-MS using a new multiple ion counting Faraday collector array. *Journal of Analytical Atomic Spectrometry*, 20, 677–686.

Simonetti, A., and Neal, C.R., 2010. In-situ chemical U-Pb dating, and Hf isotope investigation of megacrystic zircons, Malaita (Solomon Islands): Evidence for multiple stage alkaline magmatic activity beneath the Ontong Java Plateau. *Earth Planet Science Letters*, 295, 251–261.

Şahin, S. Y., Güngör, Y., Aysal, N., and Öngen, S., 2009. Geochemistry and SHRIMP zircon U-Pb dating of granitoids within the Strandja and Istanbul Zones (NW Turkey). Abstracts, 62nd Geological Congress of Turkey, Ankara, 598–9.

Stampfli, G.M., and Borel, G.D., 2002. A plate tectonic model for the Palaeozoic and Mesozoic constrained by dynamic plate boundaries and restored synthetic oceanic isochrones. *Earth Planetary Science Letters*, 169, 17–33.

Stolper, E., and Newman, S., 1994. The role of water in the petrogenesis of Mariana trough magmas. *Earth Planet Science Letter*, 121, 293-325.

Sun, S.S., and McDonough, W.F., 1989. Chemical and isotopic systematics of oceanic basalts: implications for mantle composition and processes. Geological Society, London, Special Publication, 42, 313-345.

Şen, Ş., 2013. New evidences for the formation of and for petroleum exploration in the fold-thrust zones of the central Black Sea Basin of Turkey. *American Association of Petroleum Geologists Bulletin*, 97, 465-485.

Şengör, A.M.C., and Yılmaz, Y., 1981. Tethyan evolution of Turkey: A plate tectonic approach. *Tectonophysics*, 75, 181–241.

Şengör, A.M.C., 1984. The Cimmeride Orogenic System and the Tectonics of Eurasia. Geological Society of America, Special paper, 195, 82.

Şengün, M., Akçaöre, F., Keskin, H., Akat, U., Altun, İ.E., Deveciler, E., Sevin, M., Armağan, F., Erdoğan, K., Acar, Ş., and Gündüz, H., 1988. Daday-Kastamonu-İnebolu yöresinin jeolojisi. MTA Raporu, No: 8994 (yayımlanmamış).

Taylor, B., and Martinez, F. 2003. Back-arc basin basalt systematics. *Earth Planetary Science Letter*, 210, 481-497.

Tekin, U.K., Göncüoğlu, M.C., Pandolfi, L., and Marroni, M., 2012. Middle Late Triassic radiolarian cherts from the Arkotdağ melange in northern Turkey: implications for the life span of the northern Neotethyan branch. *Geodinamica Acta*, 25, 3-4, 305-319.

Tepper, J.H., Nelson, B.K., Bergantz, G.W., and Irving, A.J., 1993. Petrology of the Chilliwack batholith, North Cascades, Washington: Generation of calc-alkaline

granitoids by melting of mafic lower crust with variable water fugacity: Contributions to Mineralogy and Petrology, 113, 333–351.

Tera, F., and Wasserburg, G.J., 1972. U–Th–Pb systematics in lunar highland samples from the Luna 20 and Apollo 16 missions. Earth and Planetary Science Letters, 17, 36–51.

Topuz, G., Göçmengil, G., Rolland, Y., Çelik, Ö.F., Zack, T., and Schmitt, A.K., 2013. Jurassic accretionary complex and ophiolite from northeast Turkey: No evidence for the Cimmerian continental ribbon. Geology, 41, 255–258.

Tüysüz, O., 1985. Kargı Masifi ve dolayındaki tektonik birliklerin ayırıcı ve araştırılması (petrolojik inceleme). Doktora tezi, İstanbul Üniversitesi, Fen Bilimleri Enstitüsü, 431 s.

Tüysüz, O., Yiğitbaş, E., and Serdar, H.S., 1989. Orta Pontidlerin güney kesiminin jeolojisi. TPAO Arama Grubu, Rapor No. 2596, 291.

Tüysüz, O., 1990. Tectonic evolution of a part of the Tethyside orogenic collage: The Kargı Massif, northern Turkey. Tectonics, 9, 141-160.

Tüysüz, O., 1993. Karadeniz'den Orta Anadolu'ya bir jeotravers: kuzey Neo-Tetisin tektonik evrimi (A geotraverse from the Black Sea to the Central Anatolia: Tectonic evolution of the northern Neo-Tethys). TPJD Bülteni, Turkish Association of Petroleum Geologists Bulletin, 5, 1-33.

Tüysüz, O., 1999. Geology of the Cretaceous sedimentary basins of the Western Pontides. Geological Journal, 34, 75-93.

Uğuz, M.F., and Sevin, M., 2007. Türkiye Jeoloji Haritaları, Kastamonu-E32 Paftası. Jeoloji Etütleri Dairesi, 32 s.

Ustaömer, T., and Robertson, A.H.F., 1993. A late Palaeozoic-Early Mesozoic marginal basin along the active southern continental margin of Eurasia: evidence from the Central Pontides (Turkey) and adjacent regions. Geological Journal, 28, 219-238.

Ustaömer, T., and Robertson, A.H.F., 1994. Late Palaeozoic marginal basin and subduction-accretion: the Palaeotethyan Küre Complex, Central Pontides, northern Turkey. Geological Society, London, 151, 291-305.

Ustaömer, T., and Robertson, A.H.F., 1999. Geochemical evidence used to test alternative plate tectonic models for pre-Upper Jurassic (Palaeotethyan) units in the Central Pontides, N Turkey. Geological Journal, 34, 25-53.

Ustaömer, P. A., and Rogers, G., 1999. The Bolu Massif: remnant of a pre-Early Ordovician active margin in the west Pontides, northern Turkey. *Geological Magazine*, 136, 579-592.

Ustaömer, P.A., Mundil, R., and Renne, P.R., 2005. U/Pb and Pb/ Pb zircon ages for arc-related intrusions of the Bolu Massif (W Pontides, NW Turkey): Evidence for Late Precambrian (Cadomian) age. *Terra Nova*, 17, 215–223.

Vervoort, J.D., Patchett, P.J., Blichert-Toft, J., and Albarede, F., 1999. Relationship between Lu-Hf and Sm-Nd systems in the global sedimentary system. *Earth Planetary Science Letters*, 168, 79-99.

Wiedenbeck, M., Alle, P., Corfu, F., Griffin, W.L., Meier, M., Oberli, F., von Quadt, A., Roddick, J.C., and Spiegel, W., 1995. Three natural zircon standards for U–Th–Pb, Lu–Hf, trace element and REE analyses. *Geostandards Newsletter*, 19, 1-23

Wood, D.A., Gibson, I.L., and Thompson, R.N., 1976. Elemental mobility during zeolite facies metamorphism of the Tertiary basalts of eastern Iceland. *Contributions to Mineralogy and Petrology*, 55, 241-254.

Woodhead, J., Hergt, J. M., Schelley, M., Eggins, S., and Kemp, R., 2004. Zircon Hf-isotope analysis with an excimer laser, depth profiling, ablation of complex geometries, and concomitant age estimation. *Chemical Geology*, 209 (1), 121-135.

Yanev, S., Göncüoğlu, MC, Boncheva, I., Gedik I., Lakova, I, Maliakov, Y., Özgül, N. Sachanski, V., Sağlam, G., and Timur, E., 2004. Correlation of the Paleozoic terranes in Bulgaria and NW Turkey: preliminary results. In: Chatzipetros, A. A. and Pavlidis, S. B. (eds) *Proceed. 5. Int. Symp. Eastern Meditt. Geol., Thessaloniki*, 215-218.

Yılmaz, O., 1980. Daday-Devrakani masifi kuzeydoğu kesimi litostratigrafi birimleri ve tektoniği. *Yerbilimleri*, 5-6, 101-135.

Yılmaz, O., 1981. Daday-Devrakani masifi Ebrek metamorfizminin petrografisi ve tüm kayaç kimyası. *Yerbilimleri*, 8, 71-82.

Yılmaz, O., 1983. Çangal metaofiyolitinin mineralojik-petrografik incelenmesi ve metamorfizma koşulları. *Yerbilimleri*, 10, 45-58.

Yılmaz, O., and Boztuğ, D., 1986. Kastamonu granitoid belt of northern Turkey: First arc plutonism product related to the subduction of the Paleo-Tethys. *Geology*, 14, 179-183.

Yılmaz, O., and Boztuğ, D., 1987. Petrography, petrochemistry and solidification sequences of the Ağlı pluton from the Kastamonu granitoid belt, northern Turkey, *Yerbilimleri*, 14, 91-107.

Yılmaz, O., 1988. L'ensemble ophiolitique de Çangal (Turquie du Nord): Mise en évidence d'un métamorphisme océanique et d'un rétro-métamorphisme cataclastique tardif. *Geologie Alpine*, 64, 113–132.

Yılmaz, Y., and Tüysüz, O., 1984. Kastamonu-Boyabat-Vezirköprü-Tosya arasındaki bölgenin jeolojisi (Ilgaz-Kargı masiflerinin etüdü). MTA rapor No. 7838.

Yılmaz, Y., and Şengör, A.M.C., 1985. Palaeo-Tethyan ophiolites in northern Turkey: Petrology and tectonic setting. *Ofioliti*, 10, 485-504.

Yılmaz, O., and Bonhomme, M.G., 1991. K-Ar isotopic age evidence for a Lower to Middle Jurassic low-pressure and a Lower Cretaceous high-pressure metamorphic events in north-central Turkey. *Terra Abstracts*, 3(1), 501.

Yılmaz, Y., and Tüysüz, O., 1991. Anatomy of an imbricated zone: geology of the Kargı Massif, central Pontides. *Bulletin of the Technical University of Istanbul*, 44, 279-299.

Yılmaz, Y., Serdar, H.S., Genç, C., Yiğitbaş, E., Gürer, Ö.F., Elmas, A., Yıldırım, M., Bozcu, M., and Gürpınar, O., 1997. The geology and evolution of the Tokat Massif, south-central Pontides, Turkey. *International Geological Review*, 39, 365-382.

Zhao, L., Tiesheng, L., Peng, P., Guo, J., Wang, W., Wang, H., Santosh, M., and Zhai M., 2015. Anatomy of zircon growth in high pressure granulites: SIMS U-Pb geochronology and Lu-Hf isotopes from the Jiaobei Terrane, eastern North China Craton. *Gondwana Research*, 28(4), 1373-1390.

Zhu, M.T., Zhang, L.C., Dai, Y.P., and Whang, C.L., 2015. In situ zircon U–Pb dating and O isotopes of the Neoproterozoic Hongtoushan VMS Cu–Zn deposit in the North China Craton: Implication for the ore genesis. *Ore Geology Reviews*, 67, 354-367.



# APPENDICES A

Major and trace element concentrations of the Çangaldağ Metavolcanic Rocks

Sample	Group 1										Group 2										Group 3										Group 4					Group 5				
	DR-11	BLV-6	53	AK-5	48	KPZ-9b	12	AK-1	KPZ-3	32	32	BLV-20	18	DR-4	KPZ-7	8a	KPZ-1	KPZ-6	DRN-15	DRN-17	DVK-10	BLV-23	AK-7	AK-14	19															
SiO <sub>2</sub> %	46.38	54.33	56.55	48.50	51.58	46.64	45.28	48.44	50.11	44.15	44.15	48.74	46.93	57.90	47.96	47.56	47.51	48.91	59.48	63.27	51.03	76.94	77.13	78.03	75.82															
Al <sub>2</sub> O <sub>3</sub>	15.99	13.29	12.54	15.55	17.08	18.23	13.24	17.87	15.11	18.26	16.46	16.88	14.87	14.87	15.24	16.13	15.51	15.52	14.22	14.20	15.18	12.09	11.69	11.88	12.40															
Fe <sub>2</sub> O <sub>3</sub>	5.54	6.51	6.87	9.27	8.86	8.80	9.43	9.46	9.63	13.68	6.14	9.04	11.80	11.80	11.05	10.46	9.94	9.51	10.44	7.90	13.16	2.05	2.65	1.85	2.70															
MgO	16.00	7.08	6.20	10.56	6.81	7.94	14.94	8.98	8.13	7.86	8.56	8.60	4.72	6.56	6.56	8.48	8.86	8.58	4.43	2.96	4.61	1.16	0.52	0.42	0.83															
Na <sub>2</sub> O	0.79	3.56	2.39	2.45	5.67	2.57	1.46	4.04	3.57	2.35	2.28	2.16	5.40	3.00	4.54	1.87	3.16	5.06	1.26	1.46	6.00	0.10	3.15	0.13	0.38															
K <sub>2</sub> O	0.18	0.14	0.96	2.11	0.55	0.84	0.02	1.72	0.01	1.05	1.32	0.66	0.14	0.14	0.09	0.01	0.55	0.12	0.05	0.31	0.10	0.03	1.16	0.31	0.06															
TiO <sub>2</sub>	0.17	0.26	0.18	0.36	0.60	0.77	0.67	0.72	0.71	0.68	0.65	0.95	0.82	1.38	1.24	1.04	0.91	1.28	1.11	1.28	0.27	0.15	0.16	0.22	0.25															
P <sub>2</sub> O <sub>5</sub>	0.02	0.03	0.03	0.06	0.06	0.05	0.07	0.08	0.06	0.08	0.05	0.08	0.07	0.17	0.17	0.20	0.15	0.15	0.16	0.33	0.27	0.03	0.02	0.02	0.06															
MnO	0.11	0.12	0.09	0.18	0.15	0.18	0.16	0.24	0.19	0.28	0.12	0.14	0.13	0.17	0.20	0.15	0.15	0.15	0.18	0.14	0.18	0.06	0.06	<0.01	0.05															
Cr <sub>2</sub> O <sub>3</sub>	0.151	0.087	0.091	0.067	<0.002	0.061	0.160	0.052	0.024	0.003	0.066	0.016	<0.002	0.045	0.045	0.019	0.027	0.045	<0.002	<0.002	<0.002	<0.002	<0.002	<0.002	<0.002															
LOI	3.3	3.8	3.6	3.9	4.0	3.5	5.7	4.7	3.7	4.9	3.5	4.0	2.3	2.5	6.1	3.3	3.4	3.4	3.3	2.0	1.9	1.4	1.5	2.8	1.5															
Sum	99.88	99.89	99.85	99.85	99.87	99.81	99.85	99.87	99.84	99.83	99.90	99.83	99.80	99.80	99.86	99.80	99.88	99.88	99.86	99.86	99.87	99.92	99.88	99.89	99.88															
Sc ppm	50	37	29	42	37	31	37	41	47	44	44	42	40	40	40	41	46	47	26	22	33	11	11	10	12															
Ba	4	12	109	47	142	93	6	110	6	27	67	15	33	8	6	19	15	15	9	20	18	10	169	14	6															
Cs	0.3	<0.1	0.6	0.5	0.1	1.6	0.2	0.5	<0.1	0.3	0.6	0.4	<0.1	0.1	<0.1	1.3	0.3	0.3	<0.1	<0.1	<0.1	<0.1	0.2	<0.1	<0.1															
Rb	0.1	0.8	0.9	0.7	1.3	1.1	1.0	1.4	0.2	0.9	1.2	1.5	1.3	2.5	1.9	1.4	1.7	1.7	2.9	5.2	3.7	3.7	3.1	2.6	3.2															
Nb	<0.1	0.7	0.7	0.6	0.8	0.4	0.4	0.3	0.3	0.6	0.4	0.6	0.6	1.3	1.2	1.1	1.1	0.6	2.0	4.9	3.5	3.5	3.1	2.2	3.2															
Sr	170.1	36.4	125.9	110.7	111.1	335.7	23.4	132.6	235.6	114.3	174.4	138.2	135.8	132.3	210.3	168.4	202.1	33.1	35.5	67.9	20.1	108.1	108.1	27.1	53.8															
Th	<0.1	<0.1	<0.1	<0.1	<0.1	<0.1	<0.1	<0.1	<0.1	<0.1	<0.1	<0.1	<0.1	<0.1	<0.1	<0.1	<0.1	<0.1	0.2	0.4	<0.2	0.1	0.1	<0.1	<0.1															
U	<0.1	<0.1	<0.1	<0.1	<0.1	<0.1	<0.1	<0.1	<0.1	<0.1	<0.1	<0.1	<0.1	<0.1	<0.1	<0.1	<0.1	<0.1	0.2	0.4	<0.2	0.1	0.1	<0.1	<0.1															
V	156	144	160	238	245	186	198	272	250	369	201	245	360	311	272	254	254	56.5	100.9	176.2	138.4	135.0	125.3	98.3	111.0															
Zr	2.4	26.0	32.0	21.7	45.6	32.9	31.5	45.6	36.5	27.1	36.2	47.7	43.9	82.0	67.1	62.7	56.5	62.7	36.3	52.2	36.8	31.8	29.2	16.2	26.1															
Y	4.6	4.3	5.3	8.3	15.0	16.9	14.7	16.4	17.9	12.3	13.9	18.9	18.3	29.8	23.5	20.7	21.3	36.3	0.3	0.6	0.3	0.3	0.7	0.6	0.2															
Pb	0.4	0.4	0.7	0.5	0.7	0.7	0.2	0.6	0.4	0.5	0.3	0.1	0.2	0.2	0.5	0.2	0.1	0.1	1.3	0.6	0.6	50	55	17	75															
Zn	9	35	31	48	59	43	42	62	41	103	33	16	78	56	75	35	38	38	136	100	56	50	55	17	75															
Ni	48.5	119.2	163.4	73.2	19.0	163.6	224.2	98.2	36.9	23.1	62.8	32.7	4.6	68.0	148.1	35.1	37.6	1.4	3.8	7.6	6.6	0.6	3.4	0.5	1.1															
La	0.1	1.7	2.4	1.8	2.6	1.1	1.7	2.6	1.8	2.2	2.1	1.8	3.0	3.1	2.8	2.2	2.3	4.8	7.3	7.7	6.1	6.1	5.3	3.3	4.7															
Ce	0.4	3.8	4.8	4.0	6.2	3.4	6.2	4.5	4.3	4.9	5.9	6.3	6.3	8.8	7.4	7.0	6.3	12.6	22.8	20.7	15.4	14.0	14.0	4.9	11.8															
Pr	0.09	0.47	0.54	0.49	0.90	0.65	0.71	1.03	0.73	0.67	0.71	0.95	0.93	1.58	1.27	1.18	1.13	2.05	3.55	2.96	2.06	1.96	0.74	1.71																
Nd	0.8	2.3	2.6	2.3	4.4	4.0	4.1	4.0	4.0	4.1	5.8	5.3	5.3	9.8	7.0	6.9	6.4	10.5	18.3	14.3	9.7	9.4	3.5	8.3																
Sm	0.30	0.33	0.53	0.78	1.62	1.71	1.44	1.73	1.50	1.27	1.45	1.53	1.53	2.98	2.25	2.21	2.32	3.74	5.89	4.29	2.80	3.07	0.79	2.36																
Eu	0.23	0.12	0.23	0.29	0.53	0.68	0.64	0.66	0.54	0.54	0.55	0.74	0.55	1.13	1.04	0.88	0.92	1.30	1.76	1.76	0.61	0.70	0.28	0.54																
Gd	0.64	0.62	0.74	1.16	2.27	2.39	2.05	2.28	2.18	1.71	2.20	2.76	2.51	4.34	3.50	3.25	3.21	5.42	7.80	6.05	4.29	3.49	1.44	3.26																
Tb	0.13	0.13	0.14	0.21	0.43	0.44	0.37	0.41	0.43	0.33	0.38	0.53	0.48	0.79	0.66	0.57	0.61	1.01	1.45	1.11	0.69	0.77	0.33	0.61																
Dy	0.85	0.76	0.91	1.31	2.73	3.03	2.64	2.68	2.97	2.18	2.31	3.25	3.21	5.11	4.55	3.72	3.84	6.90	9.32	6.31	4.55	4.68	2.55	4.04																
Ho	0.18	0.16	0.20	0.33	0.54	0.64	0.53	0.51	0.56	0.44	0.51	0.73	0.67	1.05	0.91	0.76	0.77	1.47	1.88	1.40	1.10	1.06	0.64	0.96																
Er	0.08	0.06	0.62	0.90	1.75	1.87	1.79	1.72	2.12	1.32	1.49	1.88	2.16	3.43	2.80	2.15	2.48	4.37	5.77	4.27	3.51	3.42	2.45	3.27																
Tm	0.05	0.11	0.10	0.14	0.26	0.30	0.24	0.27	0.27	0.18	0.24	0.30	0.31	0.49	0.44	0.32	0.37	0.65	0.87	0.59	0.55	0.55	0.49	0.36	0.48															
Yb	0.56	0.71	0.66	0.85	1.77	1.94	1.40	1.62	1.82	1.32	1.58	2.02	2.09	3.09	2.67	2.33	2.38	4.00	5.55	5.77	4.27	3.93	3.54	2.55	3.15															
Lu	0.08	0.11	0.11	0.15	0.27	0.26	0.24	0.25	0.27	0.17	0.22	0.26	0.32	0.46	0.44	0.33	0.35	0.62	0.92	0.52	0.59	0.60	0.56	0.47	0.54															

## Major and trace element data for the Çangaldağ Pluton

Sample	SL-1	SL-2	CN-1	CN-9	CN-11	CN-8	CN-3	SL-3-gra
			Diorite			Dacite Porphyry		Granite
SiO <sub>2</sub> (wt%)	54.30	54.07	51.94	52.24	54.86	67.78	66.13	73.54
Al <sub>2</sub> O <sub>3</sub>	16.43	17.43	14.97	15.33	15.41	15.62	15.11	11.76
Fe <sub>2</sub> O <sub>3</sub>	7.25	6.82	7.17	6.83	6.73	3.28	3.22	1.55
MgO	5.30	4.35	8.13	8.22	6.62	1.29	1.11	0.50
CaO	6.87	6.32	6.99	6.82	5.36	1.29	2.95	3.03
Na <sub>2</sub> O	4.50	3.60	3.44	2.97	3.61	3.88	3.38	2.67
K <sub>2</sub> O	0.81	1.40	0.54	1.38	1.59	2.41	2.56	1.92
TiO <sub>2</sub>	0.85	1.05	0.69	0.63	0.84	0.44	0.37	0.15
P <sub>2</sub> O <sub>5</sub>	0.11	0.18	0.11	0.08	0.12	0.15	0.12	0.15
MnO	0.13	0.14	0.12	0.12	0.13	0.06	0.08	0.04
Cr <sub>2</sub> O <sub>3</sub>	0.028	0.015	0.062	0.072	0.045	0.006	0.004	0.010
LOI	3.2	4.4	5.6	5.1	4.5	3.7	4.9	4.6
Sum	99.80	99.79	99.80	99.77	99.82	99.92	99.91	99.95
Ba (ppm)	174	330	87	258	177	138	249	295
Ni	22	23	150	139	94	<20	<20	<20
Sc	25	19	22	21	22	7	6	4
Co	26.2	23.3	31.7	31.1	25.8	7.0	5.0	2.0
Cs	0.4	2.0	0.2	0.7	0.2	4.5	3.2	1.8
Ga	15.0	17.2	14.6	14.2	14.5	16.9	17.0	8.6
Hf	3.9	4.4	2.3	2.2	3.1	4.2	3.9	1.6
Nb	3.4	6.0	3.3	3.7	4.4	6.7	6.5	2.2
Rb	24.0	57.1	14.6	51.5	53.5	151.1	109.2	61.4
Sr	282.4	362.0	87.9	264.5	64.8	55.7	119.8	101.1
Ta	0.2	0.4	0.4	0.4	0.4	0.6	0.7	0.2
Th	3.3	6.2	3.9	4.2	5.1	9.8	10.7	2.1
U	1.1	2.4	1.4	1.7	2.1	3.0	3.8	0.8
V	166	152	142	136	148	45	38	21
W	0.8	0.6	<0.5	1.2	1.3	1.5	3.1	1.8
Zr	149.8	170.9	89.3	85.6	109.0	155.0	145.8	58.0
Y	25.8	23.6	17.7	15.5	18.6	12.4	13.7	6.8
La	13.9	20.1	10.8	11.6	15.2	23.6	24.4	9.9
Ce	32.0	39.6	23.3	22.6	28.8	47.4	46.4	18.1
Pr	4.33	4.95	2.83	2.69	3.57	5.15	5.23	1.89
Nd	18.4	21.1	11.7	11.1	15.2	19.2	18.8	7.2
Sm	4.46	4.23	2.89	2.57	3.31	3.59	3.66	1.40
Eu	1.25	1.31	0.86	0.80	0.84	0.81	0.76	0.91
Gd	4.78	4.52	3.12	2.79	3.55	2.93	3.13	1.38
Tb	0.83	0.73	0.52	0.48	0.58	0.44	0.48	0.22
Dy	4.74	4.17	3.19	2.70	3.58	2.39	2.51	1.25
Ho	0.98	0.96	0.68	0.60	0.76	0.49	0.51	0.29
Er	2.82	2.47	2.05	1.78	2.16	1.32	1.51	0.76
Tm	0.43	0.38	0.29	0.24	0.32	0.19	0.22	0.12
Yb	2.60	2.32	1.92	1.62	2.12	1.35	1.47	0.79
Lu	0.38	0.35	0.29	0.26	0.33	0.21	0.23	0.11

## APPENDICES B

Detailed Age Data for the AK-7 (Çangaldağ Metamorphic Complex; metarhyodacite)

Grain #	$^{238}\text{U}$ (volts)	$^{238}\text{U}$ (cps)	$^{206}\text{Pb}/^{238}\text{U}$	$2\sigma$	$^{207}\text{Pb}/^{235}\text{U}$	$2\sigma$	$^{207}\text{Pb}/^{206}\text{Pb}$	$2\sigma$	$^{206}\text{Pb}/^{238}\text{U}$ Age (Ma)	$^{207}\text{Pb}/^{235}\text{U}$ Age (Ma)	$^{207}\text{Pb}/^{206}\text{Pb}$ Age (Ma)
AK-7-1	0.5110	578125	0.0262	0.0013	0.2100	0.0105	0.0581	0.0029	166 ± 9	193 ± 10	533 ± 27
AK-7-2	0.4680	573125	0.0301	0.0015	0.2680	0.0134	0.0635	0.0032	191 ± 10	239 ± 12	683 ± 35
AK-7-3	0.4090	486250	0.0280	0.0014	0.2220	0.0111	0.0575	0.0029	178 ± 9	203 ± 11	506 ± 26
AK-7-4	0.2309	270313	0.0273	0.0014	0.1932	0.0097	0.0517	0.0026	173 ± 9	179 ± 9	270 ± 14

Detailed Age Data for the AK-14 (Çangaldağ Metamorphic Complex; metarhyodacite)

Grain #	$^{238}\text{U}$ (volts)	$^{238}\text{U}$ (cps)	$^{206}\text{Pb}/^{238}\text{U}$	$2\sigma$	$^{207}\text{Pb}/^{235}\text{U}$	$2\sigma$	$^{207}\text{Pb}/^{206}\text{Pb}$	$2\sigma$	$^{206}\text{Pb}/^{238}\text{U}$ Age (Ma)	$^{207}\text{Pb}/^{235}\text{U}$ Age (Ma)	$^{207}\text{Pb}/^{206}\text{Pb}$ Age (Ma)
AK-14-1-1	0.1510	113750	0.0169	0.0003	0.3867	0.0062	0.1692	0.0070	107 ± 2	331 ± 5	2544 ± 20
AK-14-1-2	0.1772	171250	0.0220	0.0003	0.3653	0.0057	0.1195	0.0009	140 ± 2	315 ± 5	1946 ± 13
AK-14-2	0.0718	80313	0.0241	0.0003	0.2030	0.0022	0.0527	0.0007	153 ± 2	187 ± 2	641 ± 23
AK-14-3	0.2821	316813	0.0256	0.0003	0.1854	0.0018	0.0527	0.0003	162 ± 2	172 ± 2	315 ± 13
AK-14-4	0.4100	461250	0.0258	0.0003	0.2164	0.0015	0.0607	0.0005	164 ± 2	198 ± 2	626 ± 16
AK-14-5	0.1097	220000	0.0431	0.0004	0.7940	0.0130	0.1340	0.0018	272 ± 3	592 ± 8	2145 ± 24
AK-14-6	0.0924	520625	0.1260	0.0025	2.0840	0.0430	0.1196	0.0006	767 ± 14	1144 ± 14	1949 ± 9
AK-14-7	0.2570	451875	0.0397	0.0005	0.4288	0.0047	0.0789	0.0007	250 ± 3	362 ± 4	1164 ± 18
AK-14-8	0.3559	398750	0.0256	0.0002	0.1870	0.0012	0.0530	0.0003	162 ± 2	174 ± 2	329 ± 11

Detailed Age Data for the AK-22 (Çangaldağ Metamorphic Complex; metarhyodacite)

Grain #	$^{238}\text{U}$ (volts)	$^{238}\text{U}$ (cps)	$^{206}\text{Pb}/^{238}\text{U}$	$2\sigma$	$^{207}\text{Pb}/^{235}\text{U}$	$2\sigma$	$^{207}\text{Pb}/^{206}\text{Pb}$	$2\sigma$	$^{206}\text{Pb}/^{238}\text{U}$ Age (Ma)	$^{207}\text{Pb}/^{235}\text{U}$ Age (Ma)	$^{207}\text{Pb}/^{206}\text{Pb}$ Age (Ma)
AK-22-1	0.4747	520000	0.0248	0.0020	0.2464	0.0197	0.0718	0.0057	158 ± 13	223 ± 18	977 ± 78
AK-22-2	0.5932	697500	0.0271	0.0022	0.3084	0.0247	0.0826	0.0066	172 ± 14	272 ± 22	1257 ± 100
AK-22-3	0.5880	585625	0.0227	0.0018	0.3613	0.0289	0.1151	0.0092	144 ± 12	313 ± 25	1879 ± 150
AK-22-4	0.3790	436250	0.0263	0.0021	0.2279	0.0182	0.0628	0.0050	167 ± 14	208 ± 17	686 ± 54
AK-22-5	0.4040	438125	0.0248	0.0020	0.2344	0.0188	0.0685	0.0055	158 ± 13	213 ± 18	878 ± 70
AK-22-6	0.1115	140188	0.0276	0.0022	0.2393	0.0191	0.0628	0.0050	175 ± 14	217 ± 18	680 ± 54

Detailed Age Data for the CN-3 (Çangaldag Pluton; dacite porphyry)

Grain #	<sup>238</sup> U [volts]	<sup>206</sup> Pb (cps)	<sup>206</sup> Pb / <sup>207</sup> Pb	<sup>206</sup> Pb / <sup>238</sup> U	2σ	<sup>207</sup> Pb / <sup>235</sup> U	2σ	<sup>207</sup> Pb / <sup>206</sup> Pb	2σ	<sup>206</sup> Pb / <sup>238</sup> U Age (Ma)	<sup>207</sup> Pb / <sup>235</sup> U Age (Ma)	<sup>207</sup> Pb / <sup>206</sup> Pb Age (Ma)
CN-3-1	0.0810	98563	1000	0.0200	0.0190	0.1684	0.0062	0.0384	0.0094	127 ± 120	158 ± 6	343 ± 420
CN-3-2	0.1194	153063	3000000	0.0271	0.0250	0.1731	0.0063	0.0322	0.0088	172 ± 160	162 ± 6	621 ± 390
CN-3-3-1	0.1140	153938	1000000	0.0325	0.0300	0.1845	0.0066	0.0294	0.0081	206 ± 190	172 ± 6	743 ± 360
CN-3-3-2	0.0682	90125	1000000	0.0309	0.0290	0.1679	0.0062	0.0255	0.0068	196 ± 180	157 ± 5	919 ± 300
CN-3-4	0.1296	162500	230000	0.0290	0.0270	0.1734	0.0067	0.0240	0.0052	184 ± 170	162 ± 6	986 ± 280
CN-3-5	0.1185	145625	200000	0.0355	0.0330	0.1559	0.0057	0.0210	0.0052	224 ± 210	147 ± 5	1121 ± 230
CN-3-6	0.1304	153875	340000	0.0385	0.0360	0.1680	0.0061	0.0209	0.0051	244 ± 230	153 ± 6	1126 ± 230
CN-3-7-1	0.0859	109750	700000	0.0430	0.0410	0.1503	0.0055	0.0178	0.0043	270 ± 250	142 ± 5	1266 ± 190
CN-3-7-2	0.2164	263625	6640	0.0261	0.0240	0.8970	0.0630	0.2610	0.0660	166 ± 150	646 ± 34	3174 ± 390
CN-3-8-1	0.1759	208000	25000	0.0253	0.0230	0.1722	0.0062	0.0513	0.0130	160 ± 150	161 ± 6	252 ± 580
CN-3-8-2	0.1711	202500	35000	0.0238	0.0220	0.0790	0.0100	0.0790	0.0200	151 ± 140	238 ± 9	1168 ± 510
CN-3-9	0.0869	110500	31000	0.0258	0.0240	0.1786	0.0065	0.0503	0.0130	164 ± 150	166 ± 6	208 ± 580
CN-3-10	0.2347	217688	8020	0.0208	0.0190	0.3504	0.0130	0.1311	0.0330	132 ± 120	304 ± 10	2102 ± 450
CN-3-11-1	0.1430	190313	28000	0.0265	0.0240	0.1918	0.0070	0.0514	0.0130	168 ± 150	178 ± 6	255 ± 570
CN-3-11-2	0.2355	353750	67000	0.0302	0.0280	0.2643	0.0110	0.0616	0.0150	191 ± 170	237 ± 9	650 ± 520
Standard												
91500-1	0.0022	68188	50000	0.1477	0.1400	1.8010	0.0660	0.0753	0.0190	890 ± 780	1044 ± 22	1073 ± 500
91500-2	0.0006	55950	60000	0.1648	0.1500	1.7930	0.0650	0.0748	0.0190	981 ± 840	1043 ± 23	1060 ± 500
91500-3	0.0006	55375	infinite	0.1605	0.1500	1.7910	0.0660	0.0751	0.0190	960 ± 830	1041 ± 24	1071 ± 490
91500-4	0.0008	57313	infinite	0.1605	0.1500	1.8060	0.0660	0.0747	0.0190	958 ± 820	1047 ± 24	1057 ± 500

### Detailed Age Data for the SL-3 (Çangaldag Pluton; S-type granite)

Grain #	$^{238}\text{U}$ (volts)	$^{206}\text{Pb}$ (cps)	$^{206}\text{Pb}/^{238}\text{U}$	$2\sigma$	$^{207}\text{Pb}/^{235}\text{U}$	$2\sigma$	$^{207}\text{Pb}/^{206}\text{Pb}$	$2\sigma$	$^{207}\text{Pb}/^{206}\text{Pb}$	$2\sigma$	$^{206}\text{Pb}/^{238}\text{U}$ (Ma)	$^{207}\text{Pb}/^{235}\text{U}$ (Ma)	$^{207}\text{Pb}/^{206}\text{Pb}$ Age (Ma)
SL-3-1	0.0080	241688	17000	0.1756	6.8410	0.0046	0.1320	0.0860	0.1320	0.0004	2056 ± 22	2091 ± 11	2123 ± 6
SL-3-2	0.0127	62125	8700	0.0811	0.7040	0.0034	0.0650	0.0098	0.0650	0.0005	501 ± 20	527 ± 16	641 ± 17
SL-3-3	0.0398	170375	16000	0.0824	0.6760	0.0012	0.0098	0.0080	0.0098	0.0003	510 ± 7	524 ± 6	600 ± 11
SL-3-4	0.0823	689375	134000	0.1718	2.3210	0.0023	0.0320	0.0110	0.0320	0.0003	1021 ± 12	1218 ± 9	1582 ± 5
SL-3-5	0.0247	135688	20000	0.0963	0.8145	0.0012	0.0110	0.00615	0.0110	0.0003	592 ± 7	605 ± 6	655 ± 9
SL-3-6	0.0510	185313	40000	0.0714	0.5700	0.0019	0.0170	0.0057	0.0170	0.0002	444 ± 12	456 ± 11	527 ± 10
SL-3-7-1	0.1082	315625	102000	0.0612	0.4500	0.0013	0.0057	0.0048	0.0057	0.0002	383 ± 5	386 ± 4	403 ± 8
SL-3-7-2	0.0679	189813	32000	0.0610	0.4500	0.0013	0.0100	0.0077	0.0100	0.0007	381 ± 8	435 ± 24	510 ± 27
SL-3-8	0.0254	321250	81000	0.2389	3.8300	0.0098	0.1800	0.0075	0.1800	0.0016	1378 ± 51	1521 ± 50	1731 ± 27
SL-3-9	0.0246	84625	16700	0.0600	0.5003	0.0008	0.0075	0.0058	0.0075	0.0004	375 ± 5	399 ± 5	593 ± 13
SL-3-10-1	0.0392	128813	infinite	0.0630	0.4822	0.0009	0.0072	0.0052	0.0072	0.0003	394 ± 5	418 ± 12	411 ± 5
SL-3-10-2	0.0128	52250	infinite	0.0603	0.4620	0.0008	0.0069	0.0054	0.0069	0.0004	377 ± 5	385 ± 5	424 ± 15
SL-3-11	0.0005	33063	infinite	0.1063	0.9960	0.0014	0.0631	0.0260	0.0631	0.0011	651 ± 8	699 ± 13	830 ± 32
SL-3-12	0.0175	103188	infinite	0.0962	0.7998	0.0014	0.0120	0.0060	0.0120	0.0003	591 ± 8	596 ± 7	601 ± 12
SL-3-13-1	0.0013	30888	infinite	0.0882	0.7690	0.0011	0.0210	0.00614	0.0210	0.0007	544 ± 7	571 ± 9	639 ± 23
SL-3-13-2	0.0074	53375	infinite	0.0844	0.6874	0.0013	0.0180	0.0090	0.0180	0.0004	522 ± 8	531 ± 6	563 ± 13
SL-3-14	0.0013	40900	infinite	0.1161	1.0520	0.0015	0.0180	0.0080	0.0180	0.0005	707 ± 9	725 ± 7	767 ± 15
SL-3-15	0.0328	61913	infinite	0.0336	0.3290	0.0005	0.0718	0.0031	0.0718	0.0031	212 ± 3	287 ± 11	918 ± 83
SL-3-16	0.0216	71875	300000	0.4165	10.6570	0.0052	0.1300	0.1837	0.1300	0.0005	2245 ± 24	2485 ± 12	2685 ± 4
SL-3-17	0.0286	69938	infinite	0.0531	0.4400	0.0025	0.0250	0.0097	0.0250	0.0007	333 ± 16	364 ± 18	571 ± 24
SL-3-18-1	0.1373	368875	22000	0.0993	0.4449	0.0007	0.0095	0.0046	0.0095	0.0002	371 ± 4	373 ± 4	395 ± 7
SL-3-18-2	0.1379	368875	34000	0.0960	0.4190	0.0007	0.0058	0.0045	0.0058	0.0002	350 ± 5	355 ± 4	388 ± 9
SL-3-19	0.0461	114813	7400	0.0484	0.3524	0.0006	0.0048	0.0029	0.0048	0.0002	304 ± 4	306 ± 4	324 ± 11
SL-3-20-1	0.0676	89313	11000	0.0265	0.1834	0.0003	0.0024	0.0050	0.0024	0.0003	168 ± 2	170 ± 2	197 ± 13
SL-3-20-2	0.0335	76375	11500	0.0441	0.3420	0.0011	0.0097	0.0062	0.0097	0.0004	278 ± 7	297 ± 7	457 ± 14
SL-3-21	0.0237	87375	80000	0.0635	0.4888	0.0009	0.0071	0.0052	0.0071	0.0006	396 ± 5	404 ± 5	460 ± 12
SL-3-22	0.0902	373750	80000	0.0896	1.6300	0.0072	0.1700	0.1076	0.1700	0.0059	545 ± 45	647 ± 76	847 ± 76
SL-3-23	0.0199	299375	110500	0.2828	4.3800	0.0072	0.4300	0.1271	0.4300	0.0072	1602 ± 36	1853 ± 23	2056 ± 10
SL-3-24	0.0861	110500	80000	0.0280	0.2620	0.0004	0.0710	0.0541	0.0710	0.0010	178 ± 3	218 ± 15	359 ± 36
SL-3-25	0.0049	100500	21000	0.2198	2.5500	0.0049	0.0680	0.0834	0.0680	0.0007	1279 ± 27	1279 ± 22	1276 ± 17
SL-3-26	0.0453	752500	640000	0.3290	7.9700	0.0110	0.2700	0.1758	0.2700	0.0006	1827 ± 52	2215 ± 31	2612 ± 5
SL-3-27-1	0.0056	203000	infinite	0.3714	6.6590	0.0046	0.0830	0.0630	0.0830	0.0004	2035 ± 22	2067 ± 11	2092 ± 5
SL-3-27-2	0.0463	118125	160000	0.4888	0.9390	0.0007	0.0110	0.0878	0.0110	0.0006	307 ± 4	472 ± 7	1379 ± 14
SL-3-28-1	0.0586	980000	7000000	0.3350	6.5420	0.0045	0.1200	0.1413	0.1200	0.0013	1862 ± 21	2049 ± 16	2240 ± 15
SL-3-28-2	0.0083	413125	infinite	0.6174	21.6020	0.0076	0.2700	0.2521	0.2700	0.0006	3099 ± 30	3165 ± 12	3197 ± 4
SL-3-29	0.0037	40875	infinite	0.0913	1.0200	0.0012	0.1600	0.0621	0.1600	0.0008	563 ± 7	607 ± 15	658 ± 21
SL-3-30-1	0.0789	217813	infinite	0.0562	0.4254	0.0007	0.0665	0.0546	0.0665	0.0002	352 ± 5	360 ± 4	396 ± 9
SL-3-30-2	0.0496	145375	200000	0.0573	0.4341	0.0007	0.0664	0.0546	0.0664	0.0002	359 ± 4	366 ± 4	400 ± 9
SL-3-31	0.0560	167250	infinite	0.0599	0.4635	0.0008	0.0664	0.0546	0.0599	0.0002	374 ± 5	379 ± 5	390 ± 9
SL-3-32	0.0293	616250	infinite	0.3800	8.0270	0.0047	0.1000	0.1535	0.3800	0.0004	2076 ± 22	2236 ± 11	2384 ± 5
SL-3-33-1	0.0911	22875	13000	0.0505	0.3799	0.0007	0.0651	0.0545	0.0651	0.0002	317 ± 4	326 ± 4	389 ± 8
SL-3-33-2	0.0545	106868	13100	0.0383	0.2862	0.0005	0.0041	0.0046	0.0383	0.0003	242 ± 3	256 ± 3	394 ± 12
SL-3-34	0.0878	122563	20000	0.0288	0.2095	0.0002	0.0028	0.0027	0.0288	0.0003	483 ± 3	193 ± 3	314 ± 13
SL-3-35-1	0.0967	239188	infinite	0.0499	0.3683	0.0006	0.0048	0.0056	0.0499	0.0002	314 ± 4	318 ± 4	353 ± 8
SL-3-35-2	0.0909	218625	13000	0.0499	0.3734	0.0007	0.0055	0.0043	0.0499	0.0002	314 ± 5	322 ± 4	381 ± 10
SL-3-36-1	0.0991	234375	58000	0.0496	0.3637	0.0006	0.0047	0.0050	0.0496	0.0002	312 ± 4	314 ± 4	328 ± 9
SL-3-36-2	0.0790	188938	29000	0.0491	0.3582	0.0006	0.0048	0.0052	0.0491	0.0002	308 ± 4	310 ± 4	318 ± 9
SL-3-37	0.0309	67188	7000	0.0400	0.3037	0.0006	0.0049	0.0044	0.0400	0.0003	252 ± 4	269 ± 4	387 ± 12
Standart													
91500-1	0.0059	97813	26000	0.1765	1.8270	0.0022	0.1765	0.0748	0.1765	0.0003	1047 ± 12	1064 ± 9	1063 ± 9
91500-2	0.0053	92625	25000	0.1753	1.8270	0.0022	0.1753	0.0750	0.1753	0.0003	1041 ± 12	1054 ± 9	1068 ± 9
91500-3	0.0059	95875	57000	0.1764	1.8300	0.0022	0.1764	0.0749	0.1764	0.0003	1047 ± 12	1056 ± 9	1065 ± 9
91500-4	0.0044	86313	infinite	0.1764	1.8310	0.0023	0.1764	0.0752	0.1764	0.0004	1047 ± 12	1056 ± 9	1071 ± 10
91500-5	0.0039	82938	104400	0.1801	1.8650	0.0023	0.1801	0.0748	0.1801	0.0004	1067 ± 13	1068 ± 9	1061 ± 10

Detailed Age Data for the DVK-4A (Devrekani orthogneiss)

Grain #	$^{238}\text{U}$ (volts)	$^{206}\text{Pb}$ (cps)	$^{206}\text{Pb} / ^{206}\text{Pb}$	$^{206}\text{Pb} / ^{238}\text{U}$	$2\sigma$	$^{207}\text{Pb} / ^{235}\text{U}$	$2\sigma$	$^{207}\text{Pb} / ^{206}\text{Pb}$	$2\sigma$	$^{206}\text{Pb} / ^{238}\text{U}$ Age (Ma)	$2\sigma$	$^{207}\text{Pb} / ^{235}\text{U}$ Age (Ma)	$2\sigma$	$^{207}\text{Pb} / ^{206}\text{Pb}$ Age (Ma)	$2\sigma$
DVK-4A-1	0.1161	349000	90000	0.0668	0.0009	0.5637	0.0220	0.0613	0.0017	417 ± 6	0.0017	453 ± 14	0.0017	648 ± 61	0.0017
DVK-4A-2	0.3570	632500	4730	0.0400	0.0007	0.6780	0.0300	0.1255	0.0054	252 ± 5	0.0054	523 ± 18	0.0054	2001 ± 76	0.0054
DVK-4A-3	0.1839	785625	60000	0.0956	0.0021	0.9040	0.0380	0.0682	0.0019	588 ± 12	0.0019	653 ± 20	0.0019	873 ± 58	0.0019
DVK-4A-4	0.6260	1008125	37600	0.0375	0.0006	0.3239	0.0130	0.0625	0.0018	237 ± 4	0.0018	285 ± 10	0.0018	690 ± 60	0.0018
DVK-4A-5	0.3150	643750	8140	0.0472	0.0006	0.5946	0.0250	0.0918	0.0029	297 ± 4	0.0029	473 ± 15	0.0029	1454 ± 54	0.0029
DVK-4A-6	0.4568	835625	5433	0.0420	0.0007	0.6621	0.0260	0.1145	0.0034	265 ± 5	0.0034	515 ± 16	0.0034	1869 ± 53	0.0034
DVK-4A-7	0.1830	533750	48000	0.0648	0.0011	0.5161	0.0210	0.0579	0.0016	404 ± 7	0.0016	422 ± 14	0.0016	525 ± 62	0.0016
DVK-4A-8	0.4230	906250	105000	0.0506	0.0013	0.4002	0.0180	0.0574	0.0016	317 ± 8	0.0016	341 ± 13	0.0016	506 ± 62	0.0016
DVK-4A-9	0.2230	330625	5510	0.0339	0.0005	0.5916	0.0240	0.1275	0.0040	214 ± 3	0.0040	471 ± 15	0.0040	2053 ± 55	0.0040
DVK-4A-10	0.2064	428750	42000	0.0474	0.0006	0.3825	0.0150	0.0586	0.0017	298 ± 4	0.0017	328 ± 11	0.0017	548 ± 64	0.0017
DVK-4A-11	0.1812	560000	68000	0.0693	0.0009	0.5807	0.0230	0.0606	0.0017	432 ± 6	0.0017	465 ± 15	0.0017	622 ± 61	0.0017
DVK-4A-12	0.3180	488750	4930	0.0406	0.0018	0.6310	0.0300	0.1170	0.0039	256 ± 11	0.0039	494 ± 19	0.0039	1892 ± 62	0.0039
DVK-4A-13	0.4054	615625	5113	0.0351	0.0005	0.5744	0.0220	0.1182	0.0034	222 ± 4	0.0034	460 ± 14	0.0034	1928 ± 51	0.0034
DVK-4A-14	0.4260	750625	38000	0.0401	0.0006	0.3251	0.0130	0.0587	0.0017	253 ± 4	0.0017	285 ± 10	0.0017	550 ± 63	0.0017
DVK-4A-15	0.1755	378750	16840	0.0486	0.0008	0.4869	0.0190	0.0721	0.0021	305 ± 5	0.0021	402 ± 13	0.0021	986 ± 57	0.0021
DVK-4A-16	0.3785	753125	43800	0.0460	0.0007	0.3783	0.0150	0.0596	0.0017	289 ± 4	0.0017	325 ± 11	0.0017	588 ± 61	0.0017
DVK-4A-17	0.6214	1240625	98000	0.0470	0.0007	0.3558	0.0140	0.0548	0.0015	295 ± 5	0.0015	309 ± 10	0.0015	402 ± 63	0.0015
DVK-4A-18	0.2699	502875	7550	0.0426	0.0006	0.6061	0.0240	0.1033	0.0030	269 ± 4	0.0030	481 ± 15	0.0030	1683 ± 53	0.0030

Detailed Age Data for the DV-11 (Metadiorite intruding Devrekani Metaophiolite)

Grain #	<sup>238</sup> U (volts)	<sup>206</sup> Pb (cps)	<sup>206</sup> Pb / <sup>204</sup> Pb	<sup>206</sup> Pb / <sup>238</sup> U	Z $\sigma$	<sup>207</sup> Pb / <sup>235</sup> U	Z $\sigma$	<sup>207</sup> Pb / <sup>206</sup> Pb	Z $\sigma$	<sup>206</sup> Pb / <sup>238</sup> U Age (Ma)	<sup>207</sup> Pb / <sup>235</sup> U Age (Ma)	<sup>207</sup> Pb / <sup>206</sup> Pb Age (Ma)
DV-11-1	0.0074	17188	2300	0.0274	0.0005	0.3020	0.0180	0.0799	0.0047	174 ± 4	264 ± 13	1086 ± 94
DV-11-2	0.0610	82813	60000	0.0275	0.0005	1.1979	0.0040	0.0522	0.0016	174 ± 4	183 ± 4	289 ± 69
DV-11-3	0.0302	44188	4400	0.0277	0.0005	0.2200	0.0054	0.0577	0.0020	176 ± 4	201 ± 5	499 ± 69
DV-11-4	0.0946	233750	36000	0.0510	0.0009	0.3743	0.0071	0.0536	0.0016	320 ± 6	322 ± 6	352 ± 68
DV-11-5	0.0626	83188	13000	0.0268	0.0005	0.2010	0.0049	0.0547	0.0019	170 ± 4	185 ± 5	378 ± 71
DV-11-6	0.0695	196875	11340	0.0590	0.0014	0.5083	0.0100	0.0636	0.0021	369 ± 9	417 ± 7	713 ± 71
DV-11-7	0.0813	109563	70000	0.0281	0.0005	0.1992	0.0039	0.0517	0.0016	178 ± 4	184 ± 4	269 ± 68
DV-11-8	0.1442	744375	60000	0.1253	0.0062	1.4670	0.0840	0.0836	0.0026	757 ± 35	893 ± 34	1277 ± 61
DV-11-9	0.2027	465000	12000	0.0496	0.0009	0.3641	0.0069	0.0531	0.0016	312 ± 6	315 ± 6	331 ± 68
DV-11-10	0.0225	35375	infinite	0.0276	0.0006	0.2065	0.0048	0.0540	0.0018	175 ± 4	190 ± 4	360 ± 74
DV-11-11	0.0449	59688	2000	0.0262	0.0005	0.1932	0.0050	0.0537	0.0018	166 ± 4	179 ± 5	348 ± 74
Standard												
91500-1	0.0040	82500	10000	0.1796	0.0033	1.8546	0.0360	0.0750	0.0023	1065 ± 18	1064 ± 13	1066 ± 61
91500-2	0.0051	90625	18000	0.1786	0.0033	1.8522	0.0350	0.0753	0.0023	1059 ± 18	1064 ± 13	1075 ± 61
91500-3	0.0054	94063	72000	0.1822	0.0033	1.8859	0.0360	0.0751	0.0023	1078 ± 18	1076 ± 13	1069 ± 61
91500-4	0.0050	89250	14000	0.1773	0.0032	1.8266	0.0350	0.0746	0.0023	1052 ± 18	1055 ± 13	1057 ± 61

Detailed Age Data for the DVK-13 (Devrekani Granitoid, granite)

Grain #	<sup>238</sup> U (volts)	<sup>206</sup> Pb (cps)	<sup>206</sup> Pb / <sup>204</sup> Pb	<sup>206</sup> Pb / <sup>238</sup> U	Z $\sigma$	<sup>207</sup> Pb / <sup>235</sup> U	Z $\sigma$	<sup>207</sup> Pb / <sup>206</sup> Pb	Z $\sigma$	<sup>206</sup> Pb / <sup>238</sup> U Age (Ma)	<sup>207</sup> Pb / <sup>235</sup> U Age (Ma)	<sup>207</sup> Pb / <sup>206</sup> Pb Age (Ma)
DVK-13-1	0.2753	318313	19000	0.0262	0.0002	0.1892	0.0024	0.0524	0.0005	166 ± 2	175 ± 2	295 ± 18
DVK-13-2	0.3698	431875	15000	0.0262	0.0002	0.2235	0.0080	0.0627	0.0021	166 ± 2	204 ± 7	641 ± 63
DVK-13-3	0.7870	906250	15530	0.0260	0.0002	0.2400	0.0042	0.0672	0.0013	165 ± 2	218 ± 4	822 ± 37
DVK-13-4	0.2640	300000	21700	0.0262	0.0002	0.2165	0.0043	0.0595	0.0006	166 ± 2	198 ± 4	578 ± 23
DVK-13-5	0.2740	316875	22700	0.0261	0.0002	0.2101	0.0019	0.0583	0.0004	166 ± 2	193 ± 2	541 ± 15
DVK-13-6	0.0740	99063	3000	0.0292	0.0010	0.7030	0.0790	0.1590	0.0120	185 ± 6	495 ± 43	2200 ± 140
DVK-13-7	0.3540	386250	16400	0.0250	0.0003	0.2189	0.0052	0.0638	0.0011	159 ± 2	201 ± 5	726 ± 36
DVK-13-8	0.5210	590625	23400	0.0259	0.0002	0.2309	0.0032	0.0644	0.0004	165 ± 2	210 ± 3	754 ± 14
DVK-13-9	0.3566	402125	25000	0.0257	0.0002	0.1935	0.0021	0.0545	0.0004	163 ± 1	179 ± 2	387 ± 17
Standard												
91500-1	0.0109	132813	21000	0.1780	0.0012	1.8473	0.0160	0.0754	0.0003	1055 ± 7	1062 ± 6	1078 ± 9
91500-2	0.0116	136125	27000	0.1761	0.0012	1.8378	0.0160	0.0757	0.0003	1045 ± 7	1059 ± 6	1085 ± 9
91500-3	0.0144	155750	6400	0.1748	0.0012	1.8324	0.0170	0.0757	0.0003	1038 ± 7	1056 ± 6	1084 ± 9
91500-4	0.0139	152063	5270	0.1754	0.0012	1.8480	0.0170	0.0765	0.0004	1041 ± 7	1061 ± 6	1106 ± 9

### Detailed Age Data for the Plesovice

Grain #	$^{238}\text{U}$ (volts)	$^{206}\text{Pb}$ (cps)	$^{206}\text{Pb} / ^{238}\text{U}$	$2\sigma$	$^{207}\text{Pb} / ^{235}\text{U}$	$2\sigma$	$^{207}\text{Pb} / ^{206}\text{Pb}$	$2\sigma$	$^{206}\text{Pb} / ^{238}\text{U}$ Age (Ma)	$^{207}\text{Pb} / ^{235}\text{U}$ Age (Ma)	$^{207}\text{Pb} / ^{206}\text{Pb}$ Age (Ma)
PLS-1	0.2441	570625	0.0544	0.0014	0.3886	0.0230	0.0516	0.0026	341 ± 9	333 ± 17	267 ± 110
PLS-2	0.2559	599375	0.0550	0.0014	0.3950	0.0240	0.0521	0.0026	345 ± 9	338 ± 17	289 ± 110
PLS-3	0.2519	586250	0.0545	0.0014	0.3931	0.0240	0.0522	0.0026	341 ± 9	336 ± 17	293 ± 110
PLS-4	0.2367	556875	0.0550	0.0014	0.3981	0.0240	0.0524	0.0026	345 ± 9	340 ± 17	302 ± 110
PLS-5	0.1817	430000	0.0550	0.0014	0.4009	0.0240	0.0528	0.0026	344 ± 9	342 ± 17	317 ± 110
PLS-6	0.2433	582500	0.0567	0.0015	0.4083	0.0240	0.0518	0.0026	355 ± 9	347 ± 18	276 ± 110
PLS-7	0.2464	588750	0.0566	0.0015	0.4070	0.0240	0.0518	0.0026	355 ± 9	346 ± 18	273 ± 110
PLS-8	0.2395	568750	0.0563	0.0015	0.4065	0.0240	0.0521	0.0026	352 ± 9	346 ± 18	290 ± 110
PLS-9	0.1979	473125	0.0562	0.0015	0.4062	0.0240	0.0520	0.0026	352 ± 9	346 ± 18	285 ± 110
PLS-10	0.2191	524375	0.0562	0.0015	0.4087	0.0240	0.0523	0.0026	352 ± 9	348 ± 17	295 ± 110
PLS-11	0.2507	598125	0.0563	0.0015	0.4104	0.0250	0.0525	0.0026	353 ± 9	349 ± 18	306 ± 110

### Detailed Age Data for the 91500

Grain #	$^{238}\text{U}$ (volts)	$^{206}\text{Pb}$ (cps)	$^{206}\text{Pb} / ^{238}\text{U}$	$2\sigma$	$^{207}\text{Pb} / ^{235}\text{U}$	$2\sigma$	$^{207}\text{Pb} / ^{206}\text{Pb}$	$2\sigma$	$^{206}\text{Pb} / ^{238}\text{U}$ Age (Ma)	$^{207}\text{Pb} / ^{235}\text{U}$ Age (Ma)	$^{207}\text{Pb} / ^{206}\text{Pb}$ Age (Ma)
91500-1	0.0123	135000	0.1734	0.0019	1.8005	0.0160	0.0753	0.0003	1030 ± 11	1045 ± 6	1074 ± 8
91500-2	0.0123	133813	0.1709	0.0019	1.7749	0.0150	0.0753	0.0003	1016 ± 10	1036 ± 6	1076 ± 7
91500-3	0.0121	133563	0.1736	0.0019	1.7946	0.0150	0.0751	0.0002	1031 ± 10	1043 ± 6	1069 ± 7
91500-4	0.0107	122875	0.1734	0.0019	1.7950	0.0150	0.0751	0.0003	1030 ± 10	1043 ± 6	1070 ± 7
91500-5	0.0118	131000	0.1725	0.0018	1.7904	0.0150	0.0752	0.0003	1025 ± 10	1041 ± 6	1073 ± 8
91500-6	0.0122	133625	0.1730	0.0019	1.7833	0.0150	0.0749	0.0003	1028 ± 10	1039 ± 6	1063 ± 7
91500-7	0.0112	125688	0.1742	0.0019	1.7912	0.0150	0.0747	0.0002	1034 ± 10	1042 ± 6	1059 ± 7
91500-8	0.0109	123188	0.1731	0.0018	1.7756	0.0150	0.0745	0.0002	1029 ± 10	1036 ± 6	1053 ± 7
91500-9	0.0098	117188	0.1753	0.0018	1.8026	0.0150	0.0749	0.0003	1041 ± 10	1046 ± 6	1064 ± 7
91500-10	0.0111	126625	0.1749	0.0019	1.8226	0.0160	0.0756	0.0003	1038 ± 10	1053 ± 6	1083 ± 7
91500-11	0.0108	123188	0.1738	0.0018	1.7846	0.0150	0.0745	0.0002	1032 ± 10	1039 ± 6	1055 ± 7
91500-12	0.0105	122063	0.1741	0.0018	1.8059	0.0150	0.0752	0.0003	1034 ± 10	1047 ± 6	1073 ± 7

### Detailed Age Data for the GJ-1

Grain #	$^{238}\text{U}$ (volts)	$^{206}\text{Pb}$ (cps)	$^{206}\text{Pb} / ^{204}\text{Pb}$	$^{206}\text{Pb} / ^{238}\text{U}$	$2\sigma$	$^{207}\text{Pb} / ^{235}\text{U}$	$2\sigma$	$^{207}\text{Pb} / ^{206}\text{Pb}$	$2\sigma$	$^{206}\text{Pb} / ^{238}\text{U}$ Age (Ma)	$^{207}\text{Pb} / ^{235}\text{U}$ Age (Ma)	$^{207}\text{Pb} / ^{206}\text{Pb}$ Age (Ma)
GJ-1-1	0.0702	315813	52000	0.0972	0.0013	0.8061	0.0072	0.0601	0.0002	597 ± 8	600 ± 5	605 ± 9
GJ-1-2	0.0704	318563	56000	0.0981	0.0013	0.8112	0.0074	0.0601	0.0002	603 ± 8	603 ± 5	605 ± 9
GJ-1-3	0.0736	328000	119000	0.0972	0.0013	0.8041	0.0073	0.0601	0.0002	598 ± 8	599 ± 5	604 ± 9
GJ-1-4	0.0717	321250	297000	0.0979	0.0013	0.8096	0.0073	0.0601	0.0002	601 ± 8	602 ± 5	604 ± 8
GJ-1-5	0.0713	320188	1100000	0.0975	0.0013	0.8063	0.0073	0.0600	0.0002	599 ± 8	600 ± 5	603 ± 9
GJ-1-6	0.0713	320938	250000	0.0979	0.0013	0.8102	0.0074	0.0600	0.0002	602 ± 8	602 ± 5	602 ± 9
GJ-1-7	0.0731	325000	8400	0.0968	0.0013	0.8019	0.0073	0.0600	0.0002	595 ± 8	597 ± 5	604 ± 8
GJ-1-8	0.0732	326313	9300	0.0971	0.0013	0.8024	0.0072	0.0599	0.0002	597 ± 8	598 ± 4	597 ± 9
GJ-1-9	0.0733	327375	infinite	0.0977	0.0013	0.8102	0.0073	0.0601	0.0002	600 ± 8	602 ± 5	605 ± 9
GJ-1-10	0.0735	331313	16000	0.0981	0.0013	0.8111	0.0073	0.0600	0.0002	603 ± 8	603 ± 5	601 ± 8
GJ-1-11	0.0737	330063	infinite	0.0975	0.0013	0.8086	0.0073	0.0601	0.0002	599 ± 8	601 ± 5	606 ± 9



## APPENDICES C

Detailed Hf Data for the **AK-7** (Çangaldağ Metamorphic Complex; metarhyodacite)

Grain #	$^{176}\text{Hf}/^{177}\text{Hf}$	SE	$T_{DM}$ (Ma)	$\epsilon\text{Hf}$	$^{176}\text{Lu}/^{177}\text{Hf}$	$^{173}\text{Yb}/^{177}\text{Hf}$	$^{178}\text{Hf}/^{177}\text{Hf}$	SE	Total Hf Int (V)
AK-7-2	0.28215	0.00002	1496	-22.5	0.00106	0.04997	1.46724	0.00003	3.67
AK-7-3	0.28267	0.00003	782	-4.0	0.00060	0.02676	1.46734	0.00005	2.86
AK-7-4	0.28276	0.00003	678	-1.0	0.00126	0.05913	1.46738	0.00004	3.56

Detailed Hf Data for the **AK-14** (Çangaldağ Metamorphic Complex; metarhyodacite)

Grain #	$^{176}\text{Hf}/^{177}\text{Hf}$	SE	$T_{DM}$ (Ma)	$\epsilon\text{Hf}$	$^{176}\text{Lu}/^{177}\text{Hf}$	$^{173}\text{Yb}/^{177}\text{Hf}$	$^{178}\text{Hf}/^{177}\text{Hf}$	SE	Total Hf Int (V)
AK-14-1	0.28277	0.00002	676	-0.6	0.00202	0.10426	1.46730	0.00004	4.05
AK-14-2	0.28280	0.00003	620	0.6	0.00135	0.05155	1.46725	0.00005	2.56
AK-14-3	0.28296	0.00003	413	6.2	0.00235	0.10601	1.46717	0.00006	2.77
AK-14-4	0.28281	0.00003	606	1.0	0.00149	0.06054	1.46729	0.00006	2.50
AK-14-5	0.28171	0.00004	2067	-38.1	0.00071	0.02710	1.46739	0.00005	2.71
AK-14-6	0.28204	0.00003	1623	-26.2	0.00071	0.03091	1.46736	0.00004	3.14

Detailed Hf Data for the **AK-22** (Çangaldağ Metamorphic Complex; metarhyodacite)

Grain #	$^{176}\text{Hf}/^{177}\text{Hf}$	SE	$T_{DM}$ (Ma)	$\epsilon_{Hf}$	$^{176}\text{Lu}/^{177}\text{Hf}$	$^{173}\text{Yb}/^{177}\text{Hf}$	$^{178}\text{Hf}/^{177}\text{Hf}$	SE	Total Hf Int (V)
AK-22-1	0.28284	0.00003	566	2.0	0.00144	0.05791	1.46742	0.00005	1.99
AK-22-2	0.28272	0.00003	724	-2.1	0.00128	0.05549	1.46718	0.00005	3.02
AK-22-3	0.28281	0.00003	608	0.9	0.00131	0.05699	1.46737	0.00007	2.86
AK-22-5	0.28281	0.00003	607	0.8	0.00109	0.04822	1.46747	0.00005	2.85
AK-22-6	0.28286	0.00004	538	2.7	0.00136	0.05842	1.46748	0.00006	2.19

Detailed Hf Data for the **CN-3** (Çangaldağ Pluton; dacite porphyry)

Grain#	$^{176}\text{Hf}/^{177}\text{Hf}$	SE	$T_{DM}$ (Ma)	$\epsilon_{Hf}$	$^{176}\text{Lu}/^{177}\text{Hf}$	$^{173}\text{Yb}/^{177}\text{Hf}$	$^{178}\text{Hf}/^{177}\text{Hf}$	SE	Total Hf Int (V)
CN-3-1	0.28277	0.00003	656	-0.4	0.00127	0.04792	1.46727	0.00005	2.00918
CN-3-2	0.28287	0.00003	556	3.1	0.00363	0.16577	1.46731	0.00004	2.06990
CN-3-3-1	0.28277	0.00002	669	-0.5	0.00181	0.07439	1.46727	0.00005	2.06109
CN-3-3-2	0.28277	0.00002	677	-0.6	0.00194	0.08069	1.46723	0.00004	1.92049
CN-3-4	0.28280	0.00002	624	0.6	0.00167	0.07284	1.46730	0.00004	2.35007
CN-3-5	0.28279	0.00003	673	0.1	0.00332	0.14576	1.46737	0.00005	1.96434
CN-3-6	0.28277	0.00002	693	-0.5	0.00312	0.16027	1.46719	0.00003	2.80073
CN-3-8	0.28276	0.00003	674	-0.7	0.00153	0.06839	1.46724	0.00004	2.15573
CN-3-9	0.28271	0.00002	749	-2.5	0.00180	0.07878	1.46719	0.00004	2.24974
CN-3-11	0.28272	0.00003	732	-2.3	0.00147	0.06700	1.46737	0.00004	2.60776

Detailed Hf Data for the SL-3 (Çangaldag Pluton; S-type granite)

Grain #	$^{176}\text{Hf}/^{177}\text{Hf}$	SE	$T_{DM}$ (Ma)	$\epsilon_{\text{Hf}}$	$^{176}\text{Lu}/^{177}\text{Hf}$	$^{173}\text{Yb}/^{177}\text{Hf}$	$^{176}\text{Hf}/^{177}\text{Hf}$	SE	Total Hf Int (V)
SL-3-1	0.28163	0.00002	2170	-41.0	0.00066	0.02672	1.46739	0.00003	2.93
SL-3-2	0.28204	0.00002	1645	-26.5	0.00095	0.03776	1.46720	0.00004	3.49
SL-3-3	0.28264	0.00002	855	-5.1	0.00194	0.07869	1.46736	0.00003	2.48
SL-3-4	0.28059	0.00002	3464	-77.7	0.00010	0.00448	1.46727	0.00003	3.26
SL-3-5	0.28221	0.00002	1427	-20.3	0.00140	0.05559	1.46729	0.00003	3.29
SL-3-6	0.28264	0.00002	843	-5.1	0.00146	0.05635	1.46725	0.00003	2.77
SL-3-7	0.28260	0.00002	875	-6.4	0.00066	0.02436	1.46739	0.00003	2.82
SL-3-8	0.28214	0.00002	1478	-22.7	0.00038	0.01144	1.46725	0.00003	3.14
SL-3-9	0.28164	0.00002	2179	-40.4	0.00116	0.04874	1.46734	0.00004	2.33
SL-3-10	0.28263	0.00002	836	-5.4	0.00060	0.02224	1.46733	0.00003	2.72
SL-3-11	0.28274	0.00002	688	-1.5	0.00075	0.02570	1.46737	0.00004	2.50
SL-3-12	0.28232	0.00002	1264	-16.6	0.00079	0.03214	1.46728	0.00003	2.33
SL-3-13	0.28279	0.00002	639	0.0	0.00119	0.04886	1.46734	0.00003	2.52
SL-3-14	0.28215	0.00002	1484	-22.6	0.00059	0.02443	1.46723	0.00003	2.54
SL-3-15	0.28238	0.00002	1176	-14.5	0.00053	0.02082	1.46724	0.00004	2.25
SL-3-16	0.28118	0.00002	2807	-56.7	0.00147	0.06248	1.46727	0.00004	2.85
SL-3-17	0.28246	0.00002	1077	-11.4	0.00107	0.03901	1.46727	0.00003	2.67
SL-3-18	0.28271	0.00002	762	-2.8	0.00188	0.07533	1.46733	0.00004	2.37
SL-3-19	0.28266	0.00002	808	-4.5	0.00094	0.03397	1.46715	0.00004	2.47
SL-3-20	0.28213	0.00002	1512	-23.1	0.00085	0.02862	1.46730	0.00003	2.75
SL-3-21	0.28271	0.00002	733	-2.5	0.00099	0.02856	1.46726	0.00004	2.04
SL-3-22	0.28133	0.00003	2546	-51.4	0.00051	0.02843	1.46734	0.00003	2.72
SL-3-23	0.28155	0.00002	2277	-43.5	0.00085	0.05487	1.46723	0.00004	2.65
SL-3-24	0.28247	0.00002	1080	-11.2	0.00144	0.01255	1.46717	0.00004	2.22
SL-3-25	0.28205	0.00003	1604	-26.2	0.00029	0.02583	1.46735	0.00004	2.31
SL-3-26	0.28113	0.00002	2816	-58.7	0.00057	0.03980	1.46725	0.00004	2.43
SL-3-27	0.28157	0.00002	2268	-43.1	0.00099	0.06208	1.46724	0.00003	2.54
SL-3-28	0.28107	0.00003	2969	-60.6	0.00165	0.01624	1.46735	0.00004	2.23
SL-3-29	0.28226	0.00002	1324	-18.5	0.00040	0.03244	1.46730	0.00004	2.21
SL-3-30	0.28260	0.00002	882	-6.5	0.00082	0.02833	1.46735	0.00004	2.34
SL-3-31	0.28253	0.00002	975	-9.0	0.00079	0.02868	1.46721	0.00004	2.24
SL-3-32	0.28105	0.00002	2940	-61.2	0.00099	0.04373	1.46740	0.00003	2.49
SL-3-33-1	0.28262	0.00003	856	-5.8	0.00093	0.03664	1.46720	0.00004	2.12
SL-3-33-2	0.28258	0.00002	908	-7.3	0.00063	0.02471	1.46729	0.00004	2.85
SL-3-34	0.28274	0.00003	709	-1.7	0.00130	0.05279	1.46731	0.00005	1.69
SL-3-35	0.28265	0.00002	817	-4.8	0.00086	0.03401	1.46727	0.00004	2.15
SL-3-36	0.28263	0.00002	849	-5.5	0.00097	0.04070	1.46725	0.00004	2.30
SL-3-37	0.28243	0.00002	1131	-12.7	0.00132	0.05971	1.46721	0.00004	1.87

Detailed Hf Data for the **DV-11** (Metadiorite intruding Devrekani Metaophiolite)

Grain #	$^{176}\text{Hf}/^{177}\text{Hf}$	SE	$T_{\text{DM}}$ (Ma)	$\epsilon\text{Hf}$	$^{176}\text{Lu}/^{177}\text{Hf}$	$^{173}\text{Yb}/^{177}\text{Hf}$	$^{178}\text{Hf}/^{177}\text{Hf}$	SE	Total Hf Int (V)
DV-11-1	0.28278	0.00003	671	-0.2	0.00257	0.09876	1.46723	0.00004	1.79
DV-11-3	0.28277	0.00003	660	-0.7	0.00084	0.03122	1.46732	0.00004	2.12
DV-11-4	0.28262	0.00002	864	-5.9	0.00111	0.04369	1.46726	0.00004	2.46
DV-11-5	0.28289	0.00003	517	3.8	0.00291	0.11981	1.46723	0.00004	2.01
DV-11-6	0.28263	0.00002	844	-5.5	0.00079	0.03274	1.46717	0.00004	3.12
DV-11-7	0.28281	0.00002	614	0.7	0.00141	0.05997	1.46725	0.00003	2.46
DV-11-8	0.28199	0.00002	1715	-28.1	0.00119	0.05208	1.46724	0.00003	3.06
DV-11-9	0.28262	0.00002	855	-5.7	0.00091	0.03548	1.46723	0.00003	2.64
DV-11-10	0.28279	0.00003	636	0.1	0.00126	0.04567	1.46730	0.00005	2.19
DV-11-11	0.28278	0.00002	658	-0.3	0.00167	0.06406	1.46725	0.00004	2.19

Detailed Hf Data for the **DVK-13** (Devrekani Granitoid, granite)

Grain #	$^{176}\text{Hf}/^{177}\text{Hf}$	SE	$T_{\text{DM}}$ (Ma)	$\epsilon\text{Hf}$	$^{176}\text{Lu}/^{177}\text{Hf}$	$^{173}\text{Yb}/^{177}\text{Hf}$	$^{178}\text{Hf}/^{177}\text{Hf}$	SE	Total Hf Int (V)
DVK-13-1	0.28292	0.00003	463	4.9	0.00226	0.10018	1.46733	0.00005	2.17
DVK-13-3	0.28289	0.00002	493	3.8	0.00125	0.05383	1.46732	0.00004	2.13
DVK-13-4	0.28289	0.00003	551	3.9	0.00531	0.24329	1.46729	0.00004	1.85
DVK-13-5	0.28282	0.00004	590	1.2	0.00101	0.04511	1.46735	0.00006	1.34
DVK-13-6	0.28294	0.00005	434	5.6	0.00206	0.09090	1.46736	0.00007	1.45
DVK-13-7	0.28292	0.00005	456	4.9	0.00180	0.07666	1.46732	0.00007	1.03
DVK-13-8	0.28289	0.00006	513	3.8	0.00272	0.13028	1.46725	0.00007	1.49

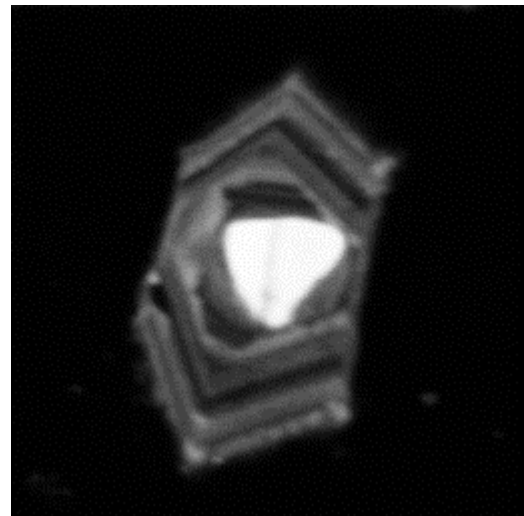
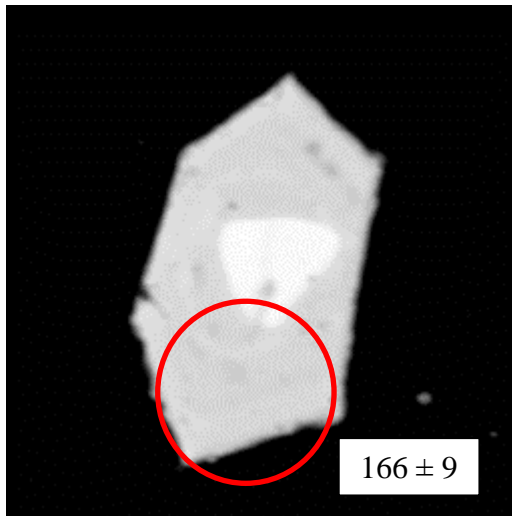
## APPENDICES D

BSE and CL images of the zircons from the AK-7 (Çangadal Metamorphic Complex, Metarhyodacite)

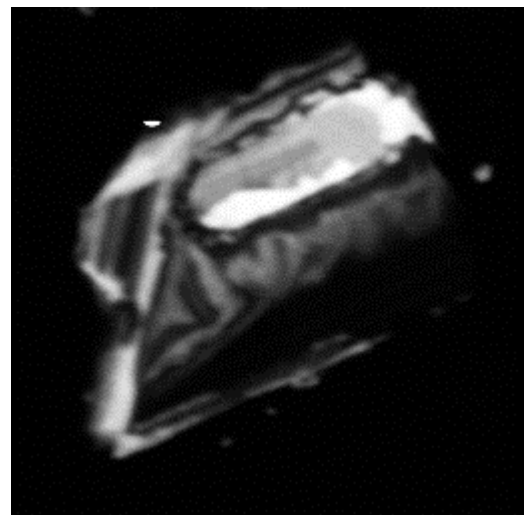
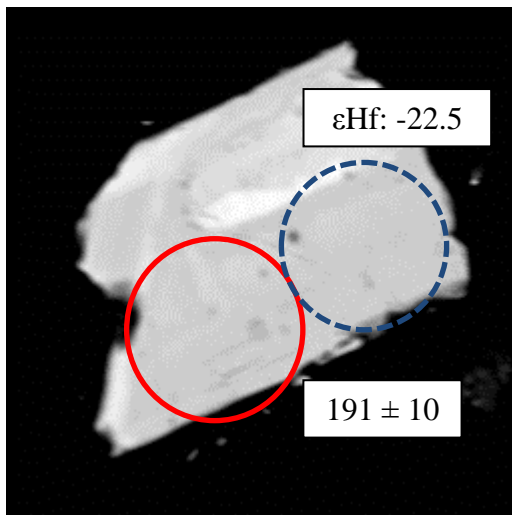
Circle: U-Pb age (Ma, laser spot size 35 micron), dash circle Hf isotope (laser spot size 35 micron)

**BSE**

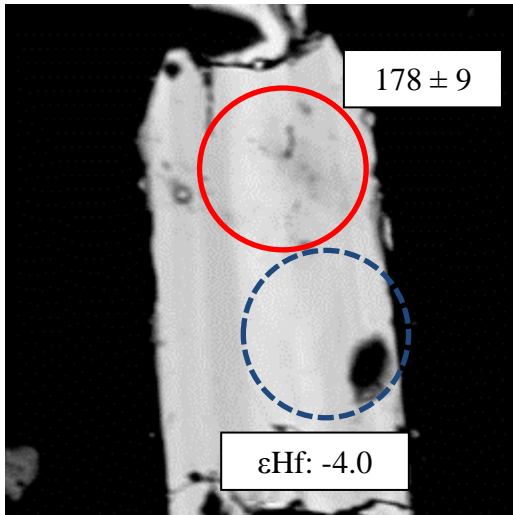
**CL**



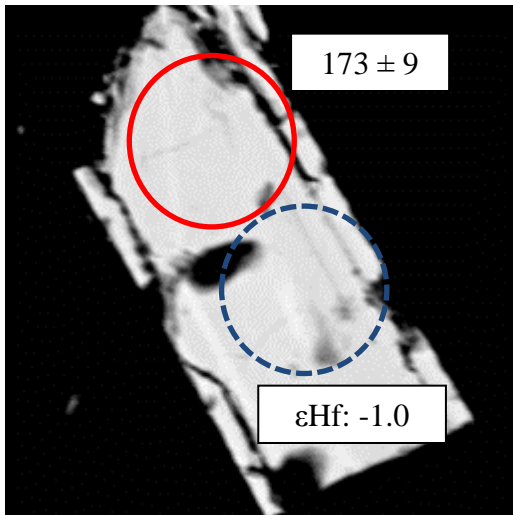
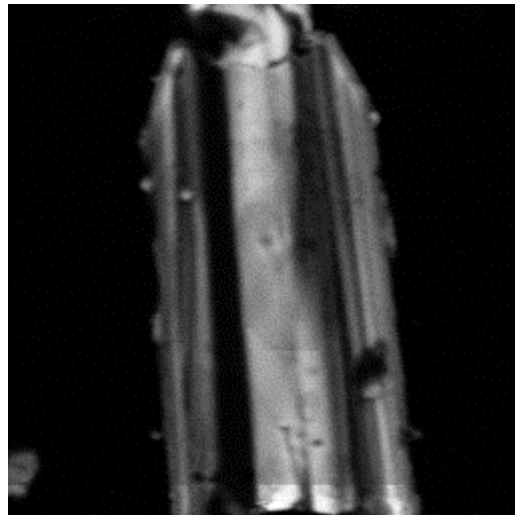
**AK-7-1**



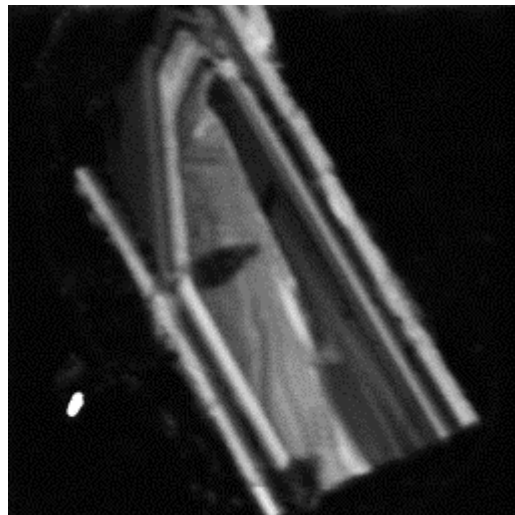
**AK-7-2**



**AK-7-3**



**AK-7-4**

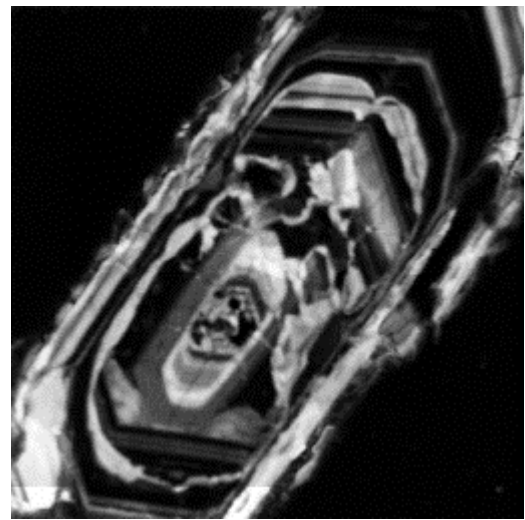
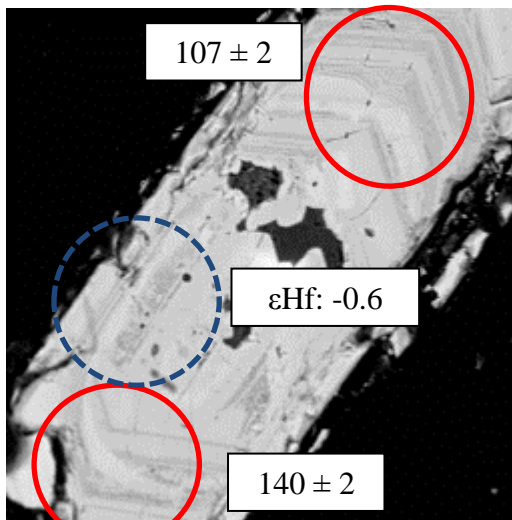


BSE and CL images of the zircons from the **AK-14** (Çangadal Metamorphic Complex, Metarhyodacite)

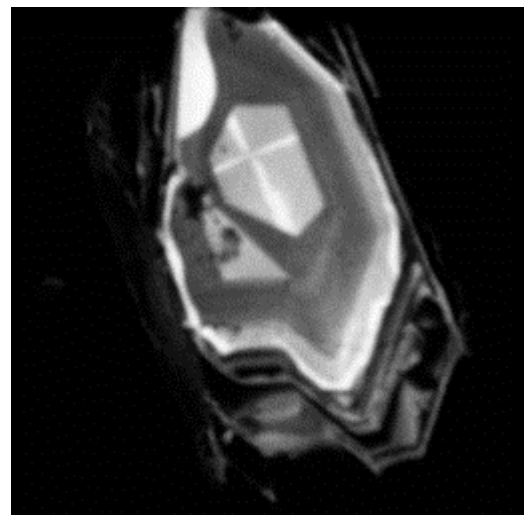
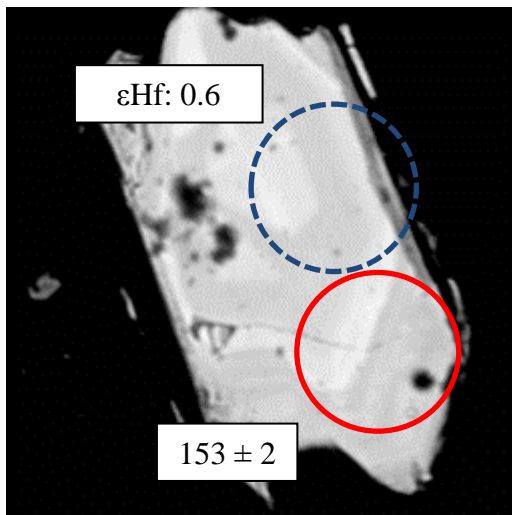
Circle: U-Pb age (Ma, laser spot size 35 micron), dash circle Hf isotope (laser spot size 35 micron)

**BSE**

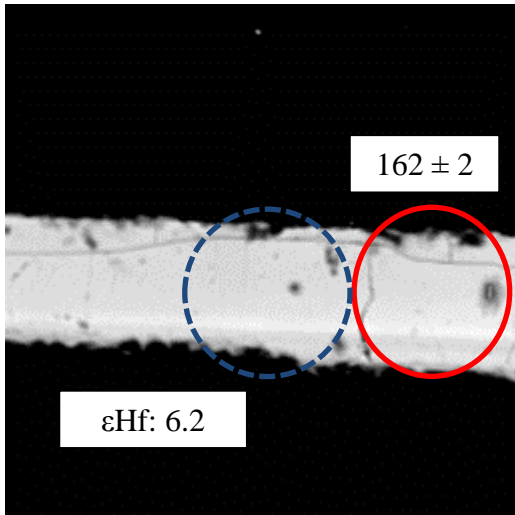
**CL**



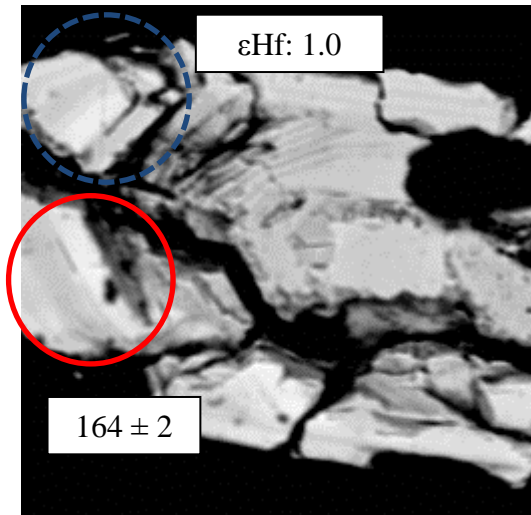
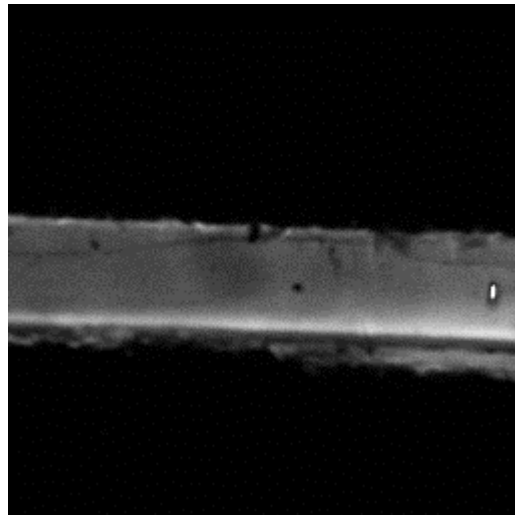
**AK-14-1**



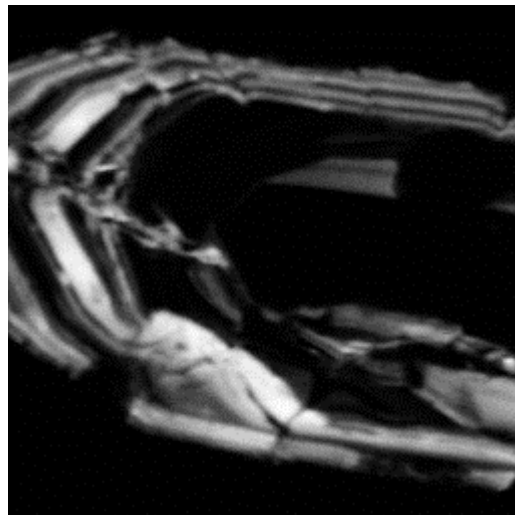
**AK-14-2**

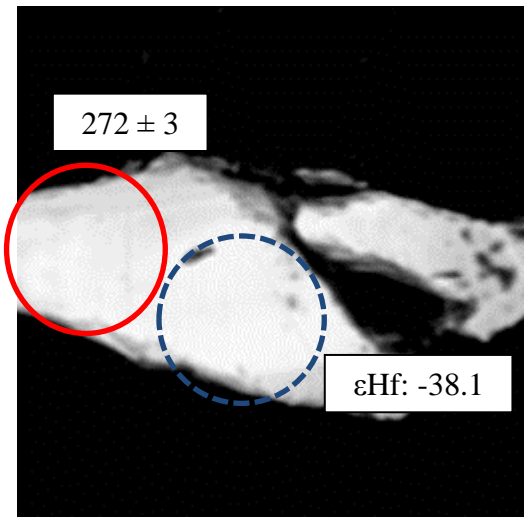


**AK-14-3**

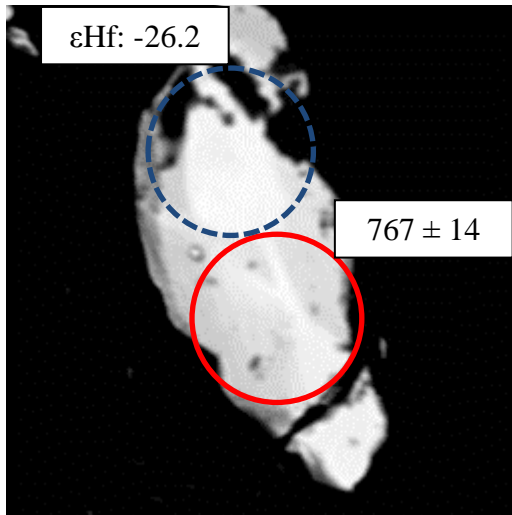
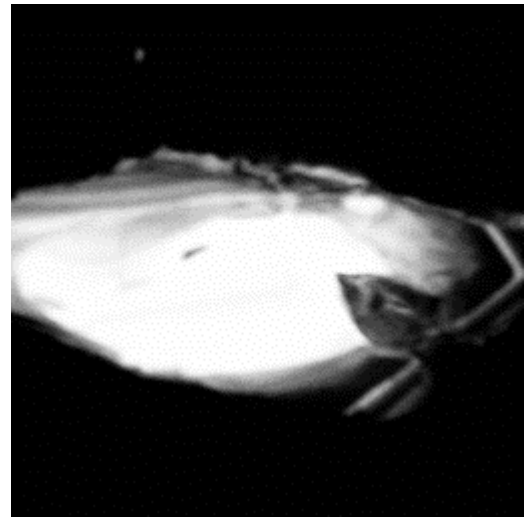


**AK-14-4**

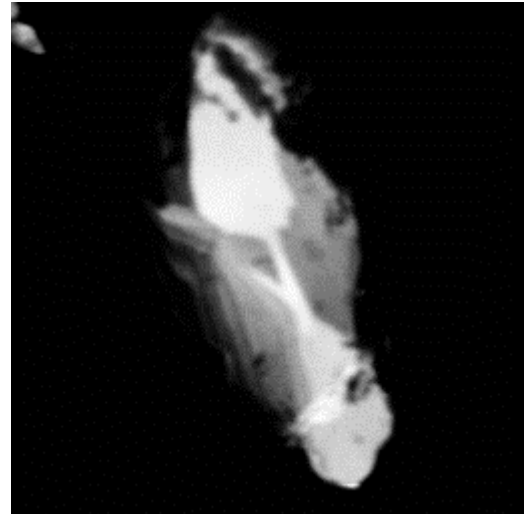


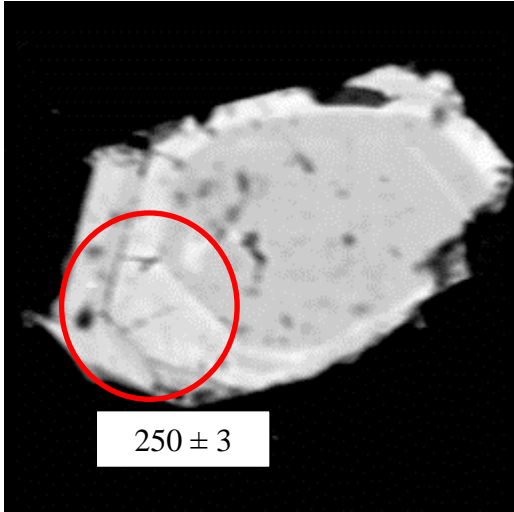


**AK-14-5**

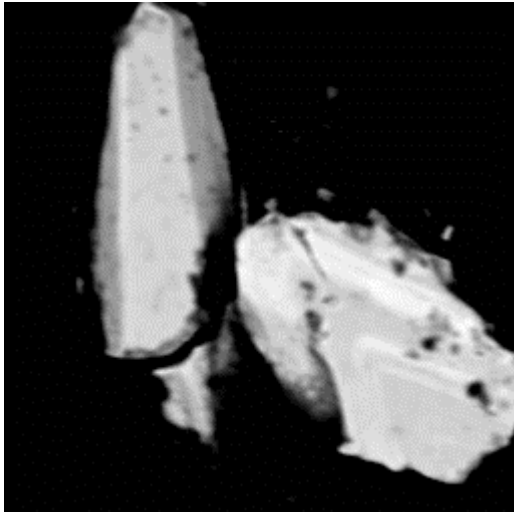
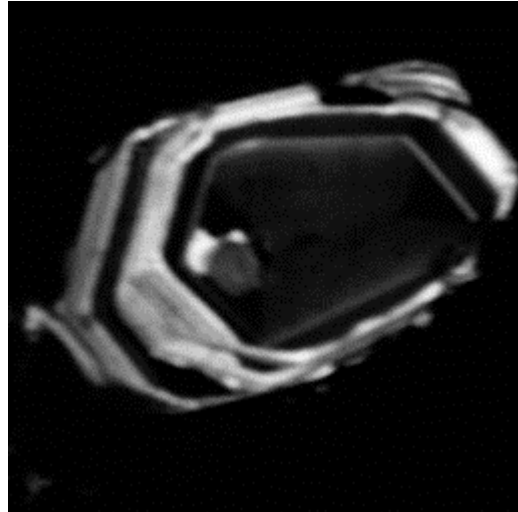


**AK-14-6**

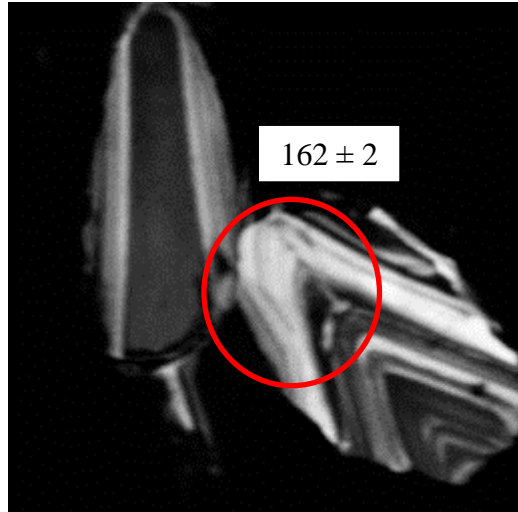




**AK-14-7**



**AK-14-8**

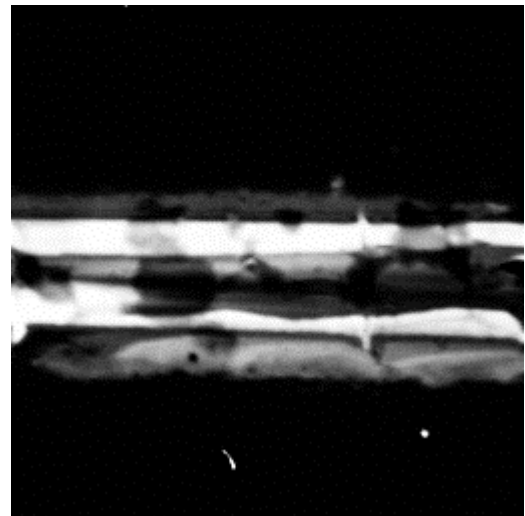
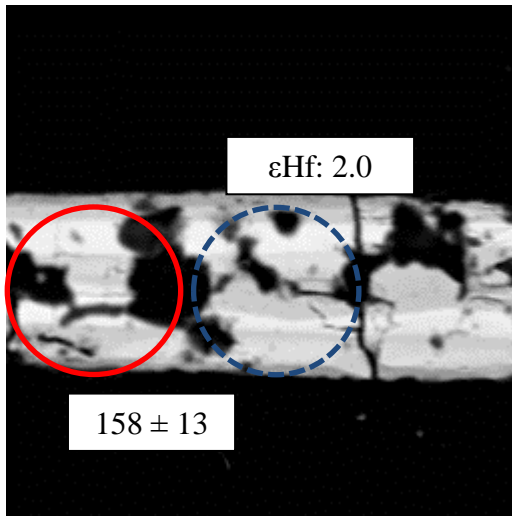


BSE and CL images of the zircons from the **AK-22** (Çangadal Metamorphic Complex, Metarhyodacite)

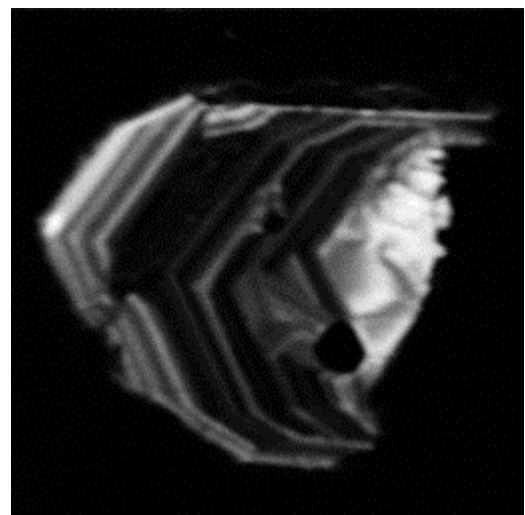
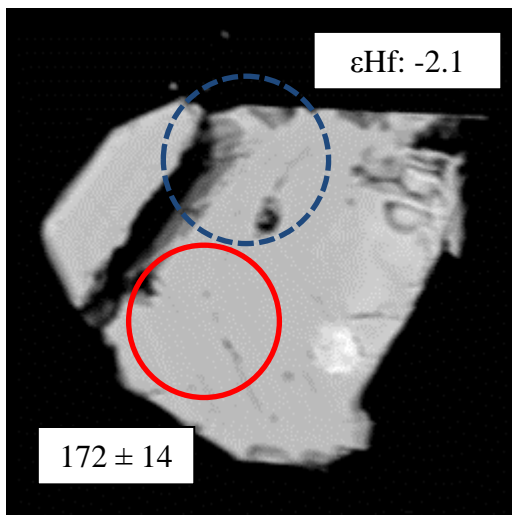
Circle: U-Pb age (Ma, laser spot size 35 micron), dash circle Hf isotope (laser spot size 35 micron)

**BSE**

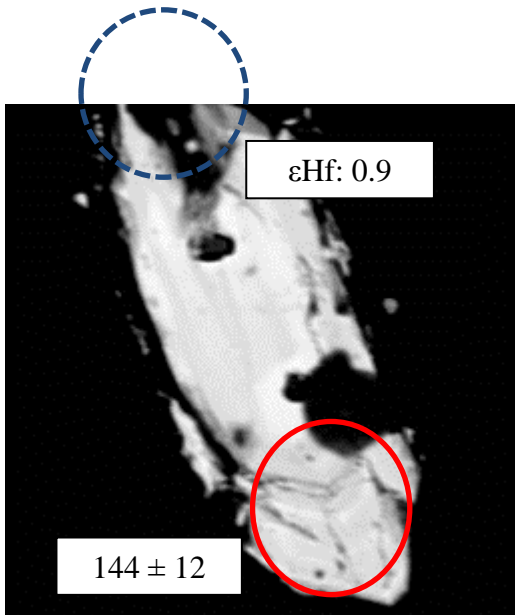
**CL**



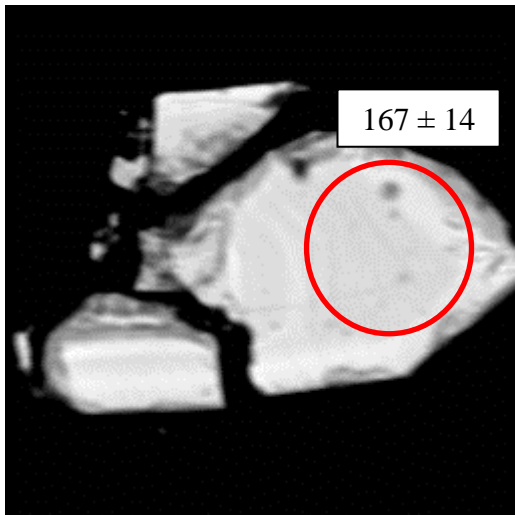
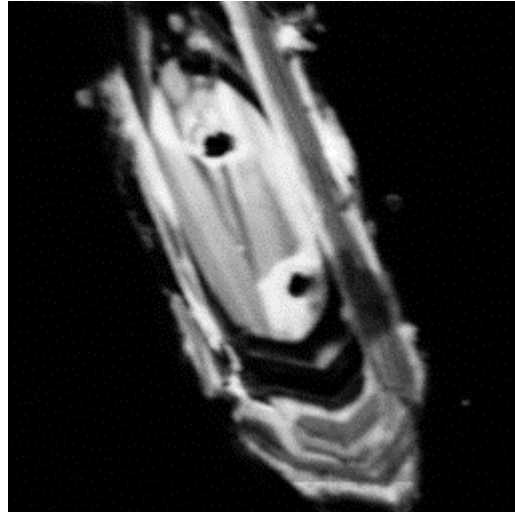
**AK-22-1**



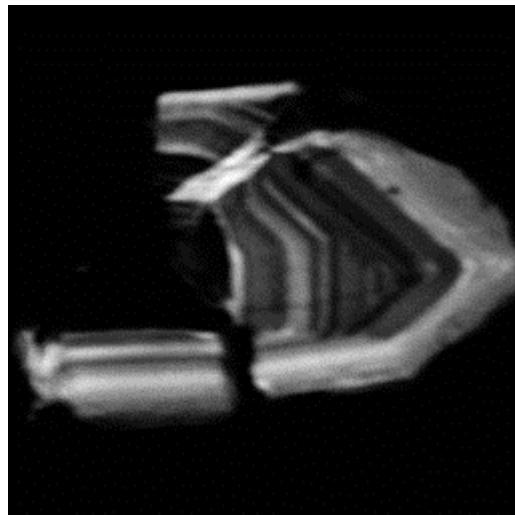
**AK-22-2**

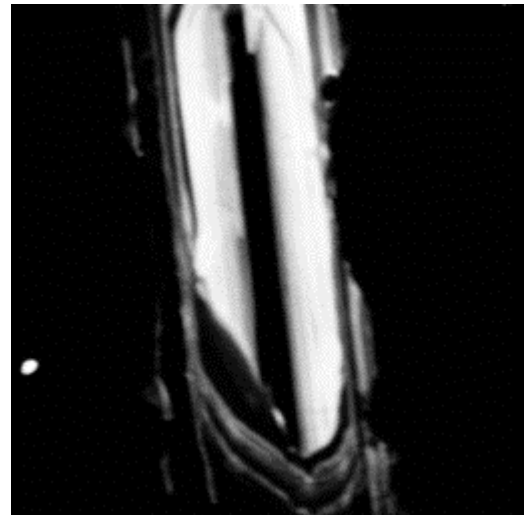
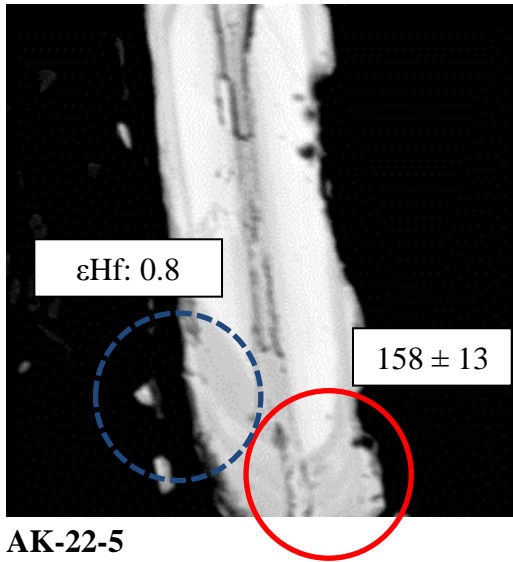


**AK-22-3**

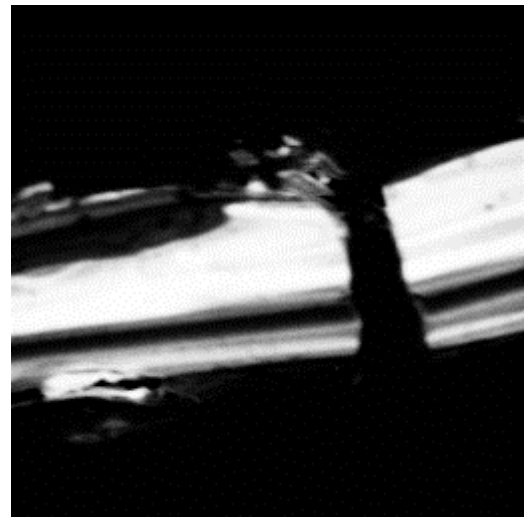
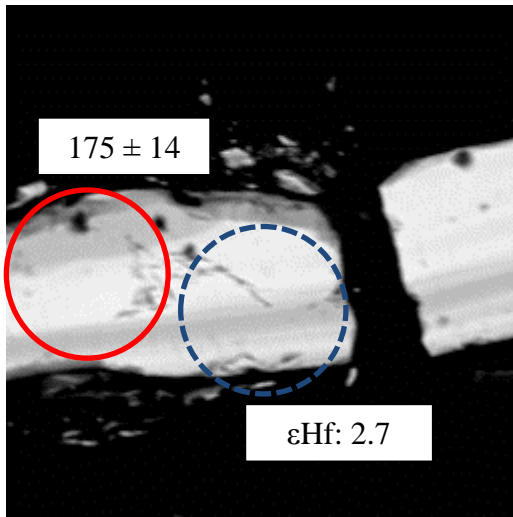


**AK-22-4**





AK-22-5



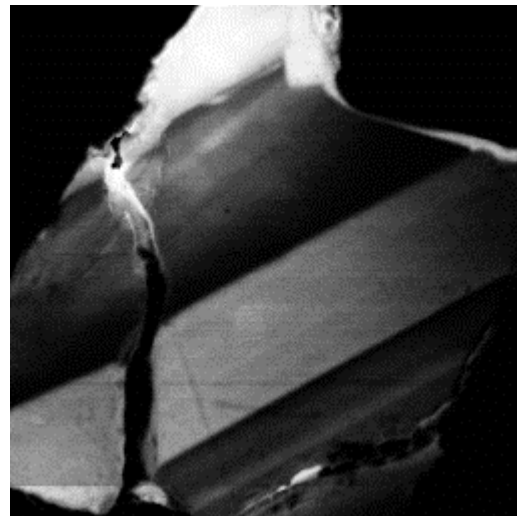
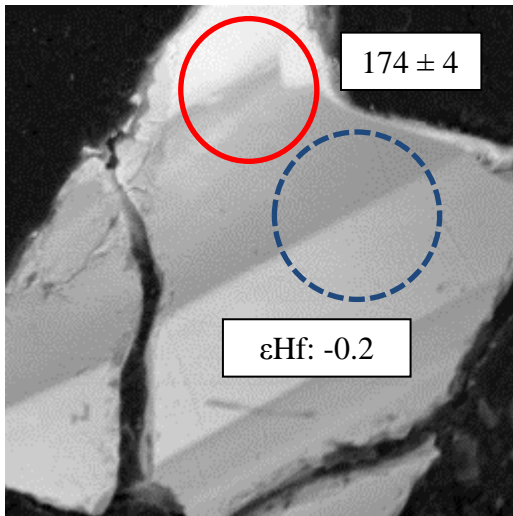
AK-22-6

BSE and CL images of the zircons from the **DV-11** (Metadiorite intruding Devrekani Metaophiolite)

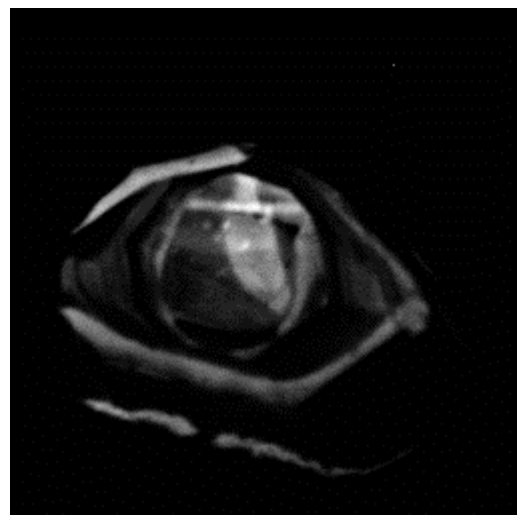
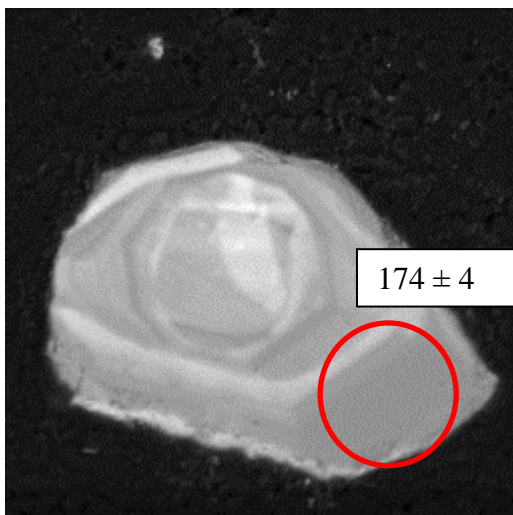
Circle: U-Pb age (Ma, laser spot size 25 micron), dash circle Hf isotope (laser spot size 35 micron)

**BSE**

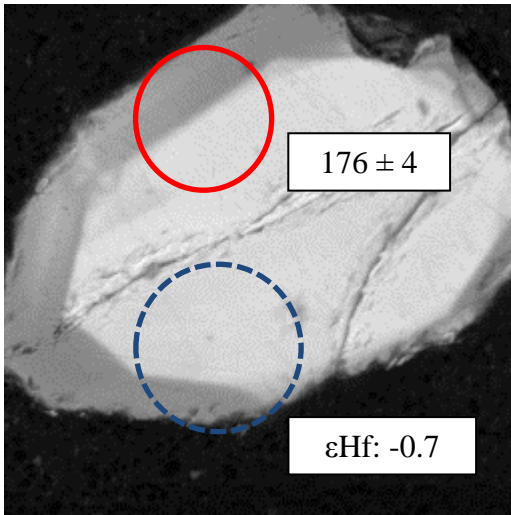
**CL**



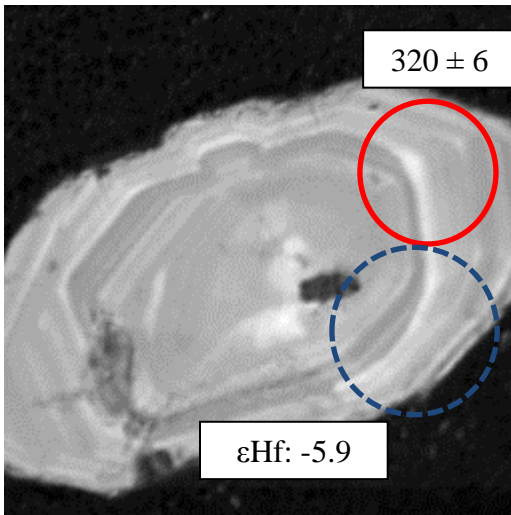
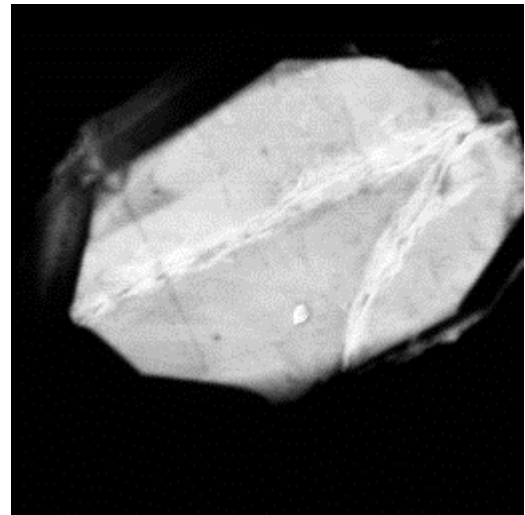
**DV-11-1**



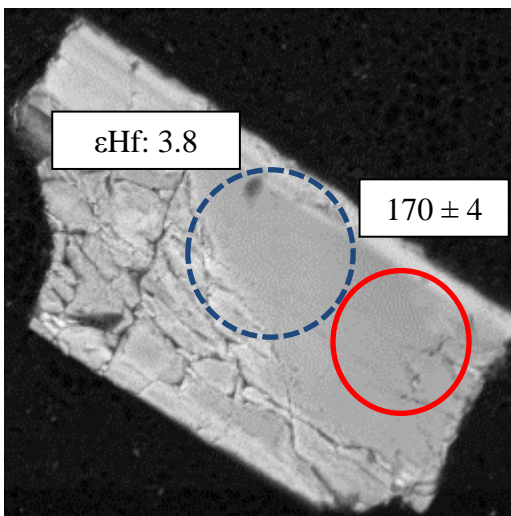
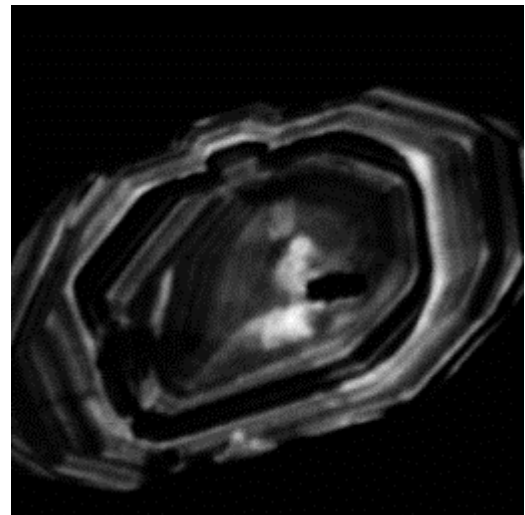
**DV-11-2**



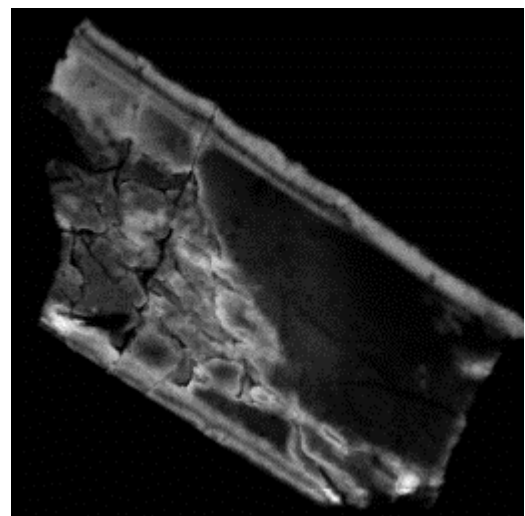
DV-11-3

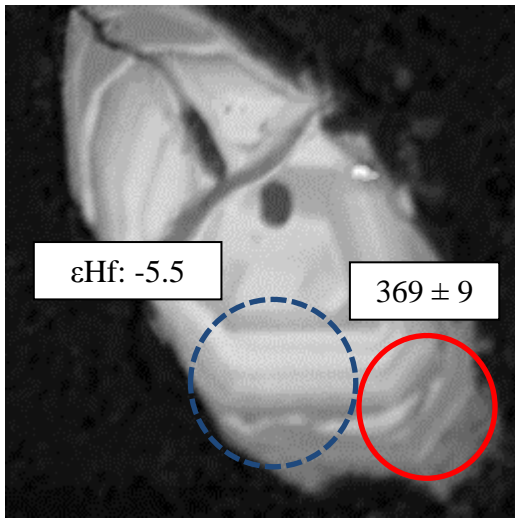


DV-11-4

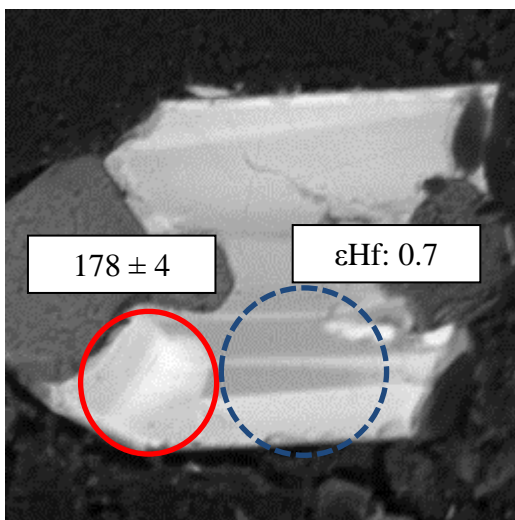
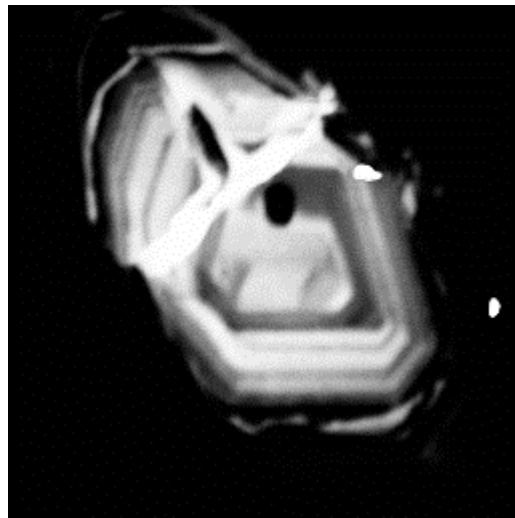


DV-11-5

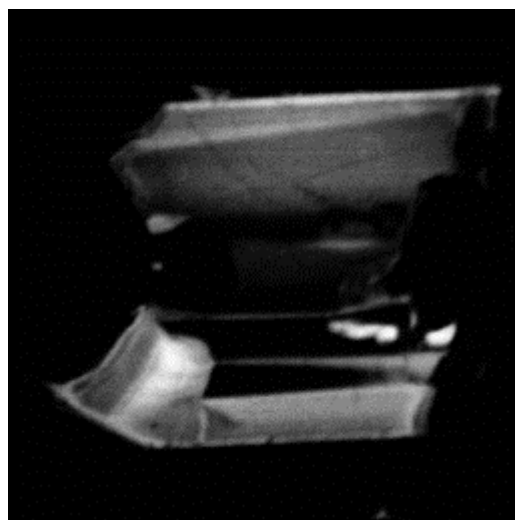


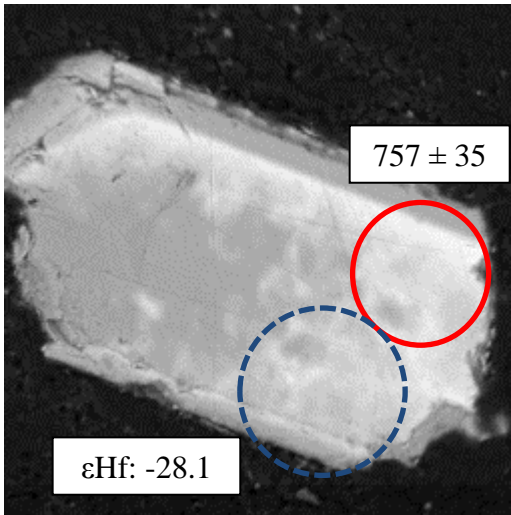


DV-11-6

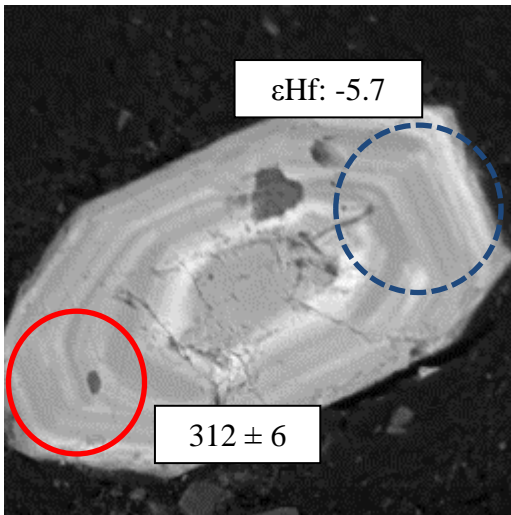
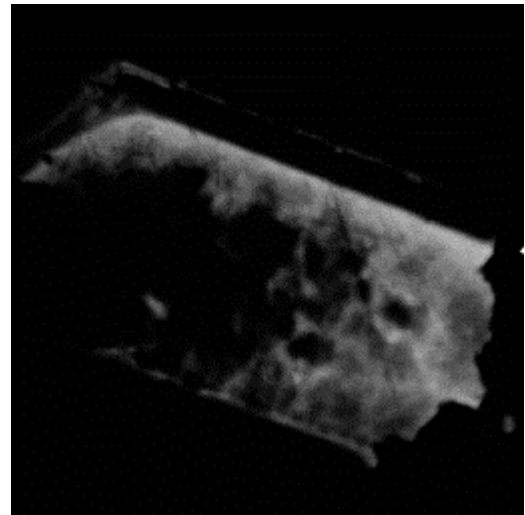


DV-11-7

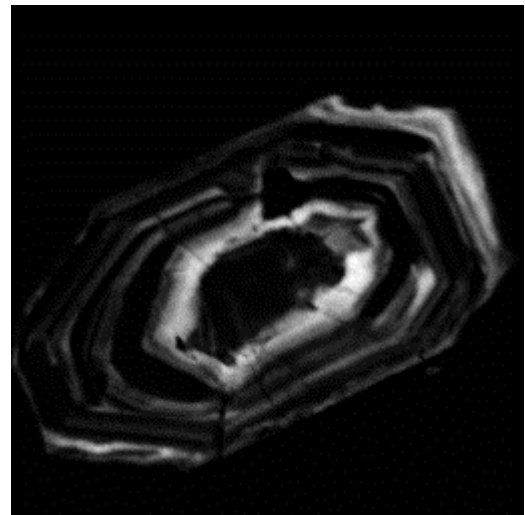


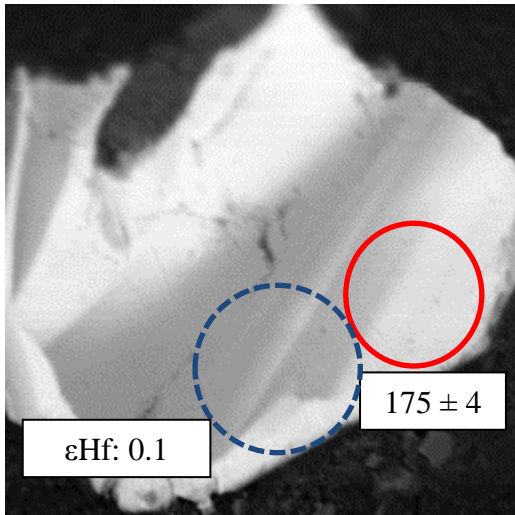


**DV-11-8**

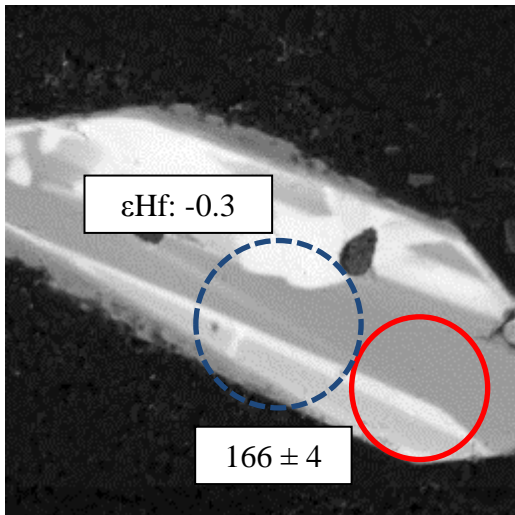
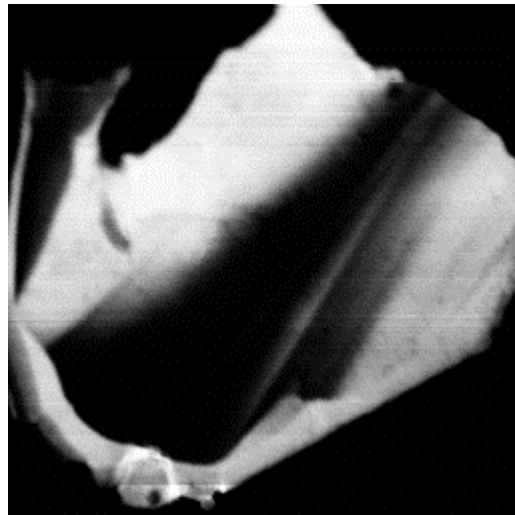


**DV-11-9**

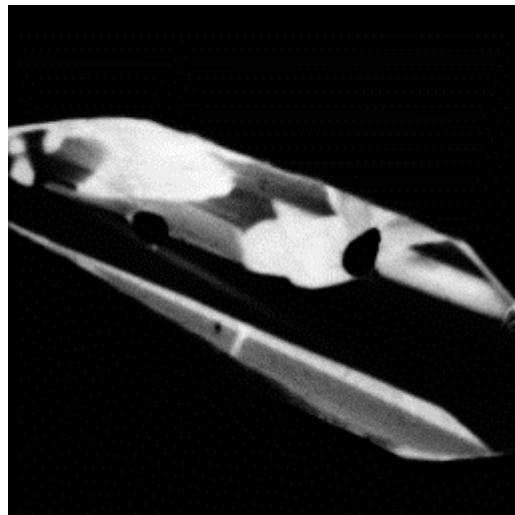




DV-11-10



DV-11-11

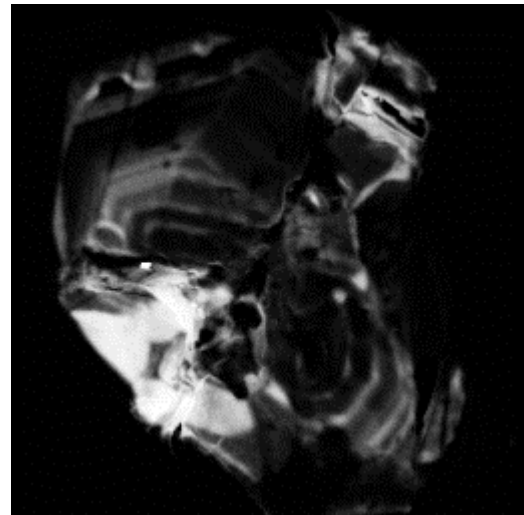
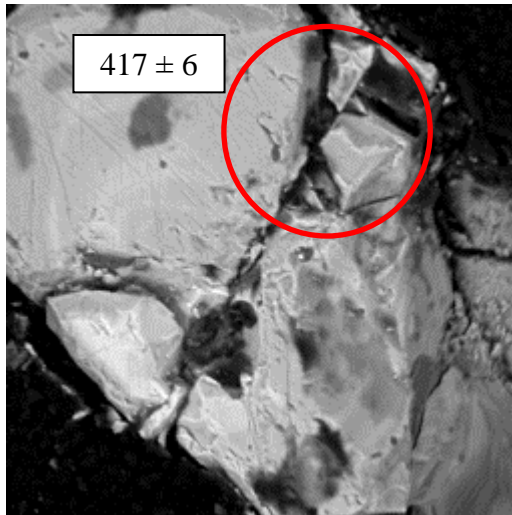


BSE and CL images of the zircons from the **DVK-4A** (Devrekani Orthogneiss)

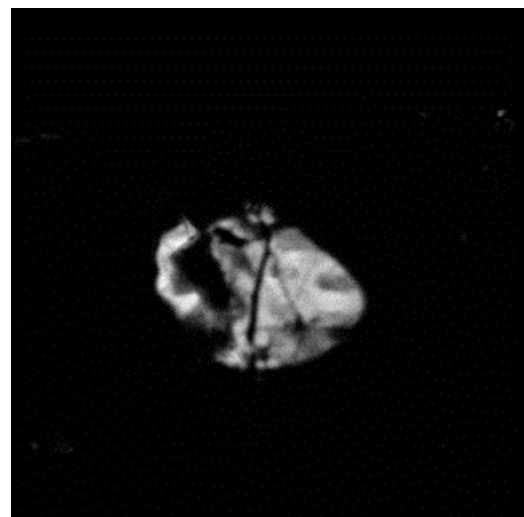
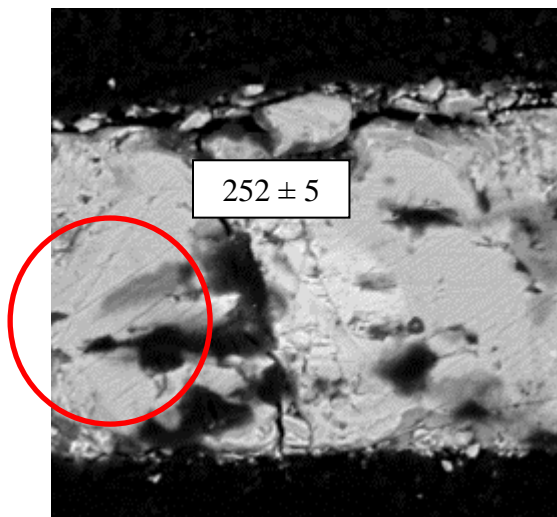
Circle: U-Pb age (Ma, laser spot size 35 micron)

**BSE**

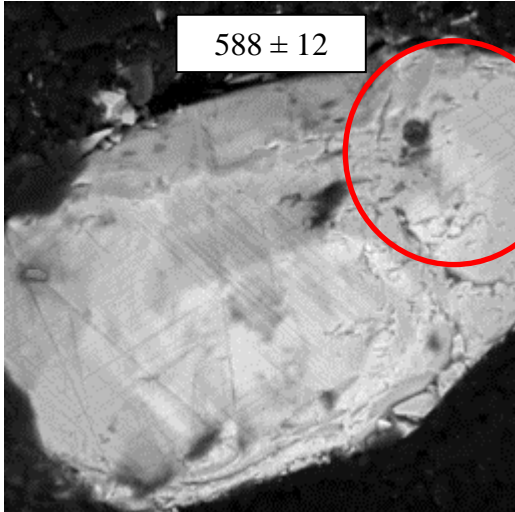
**CL**



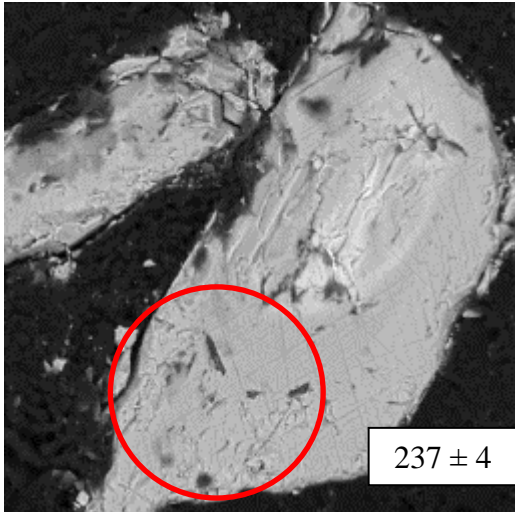
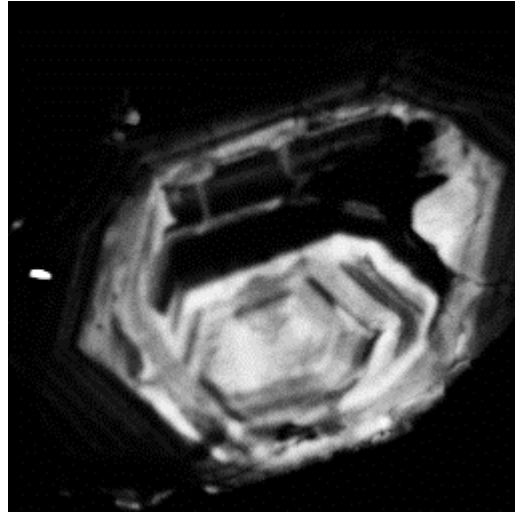
**DVK-4A-1**



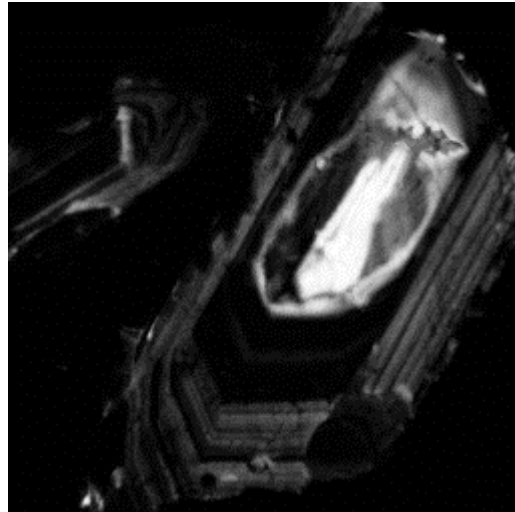
**DVK-4A-2**

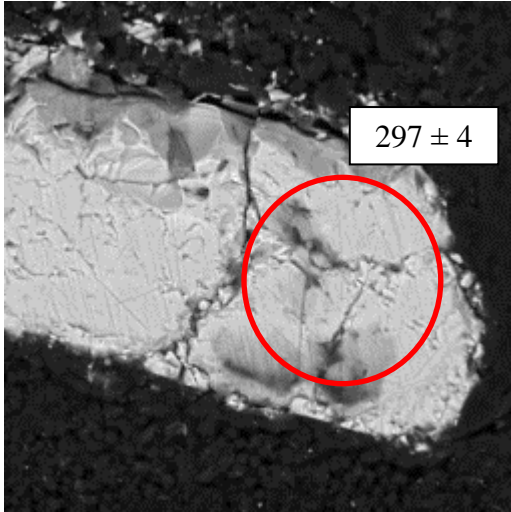


DVK-4A-3

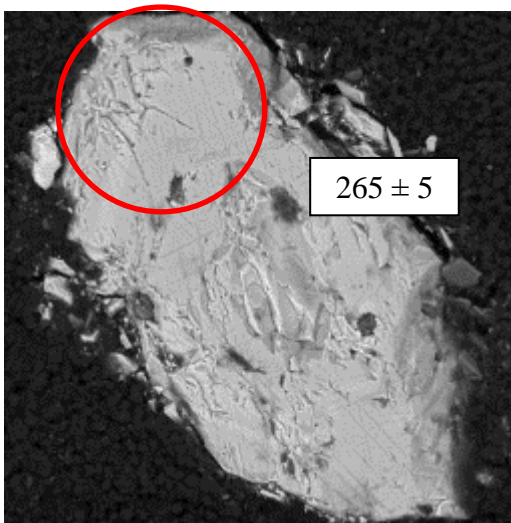
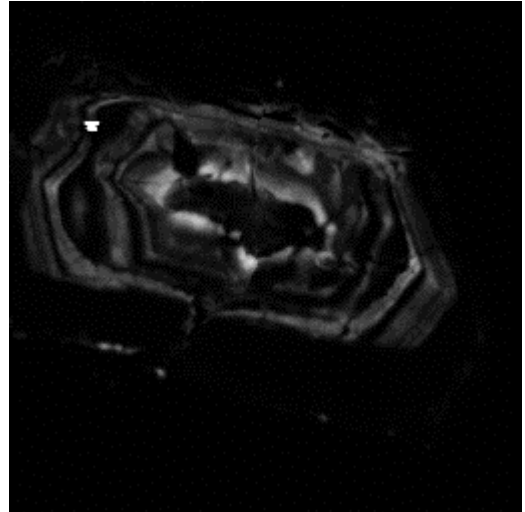


DVK-4A-4

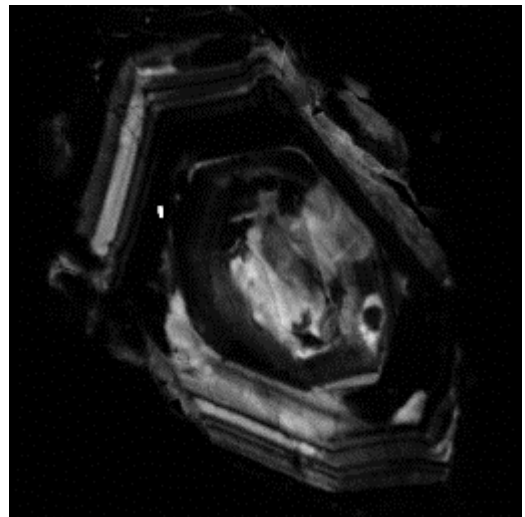


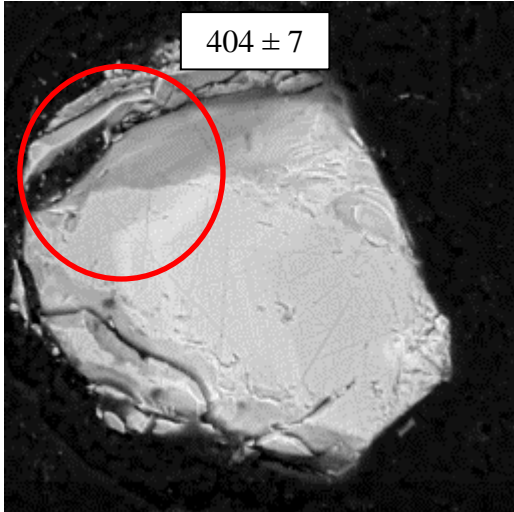


**DVK-4A-5**

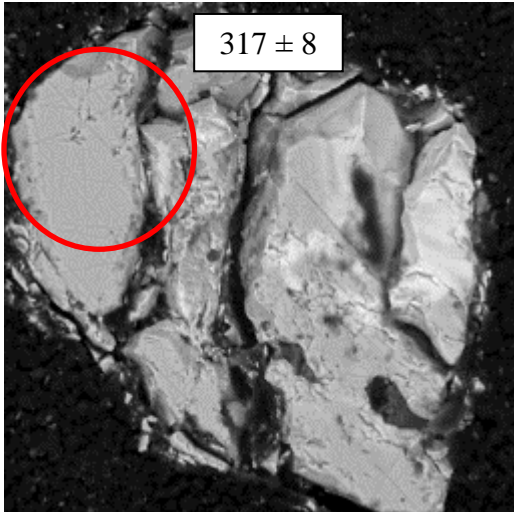
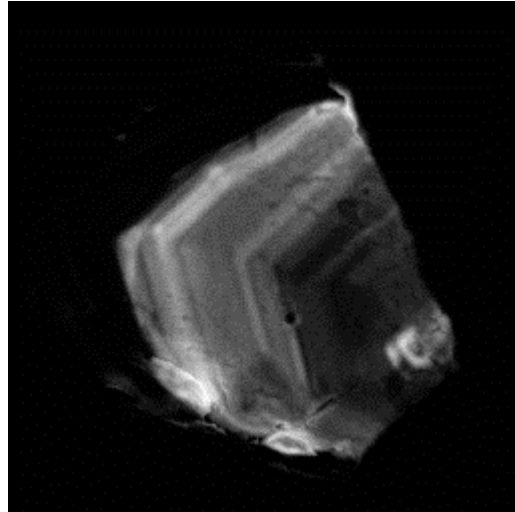


**DVK-4A-6**

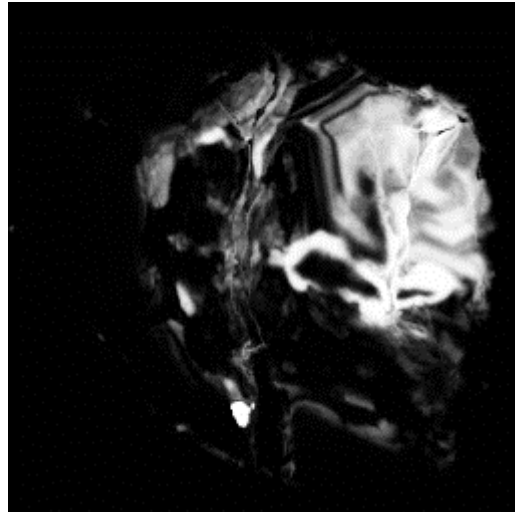


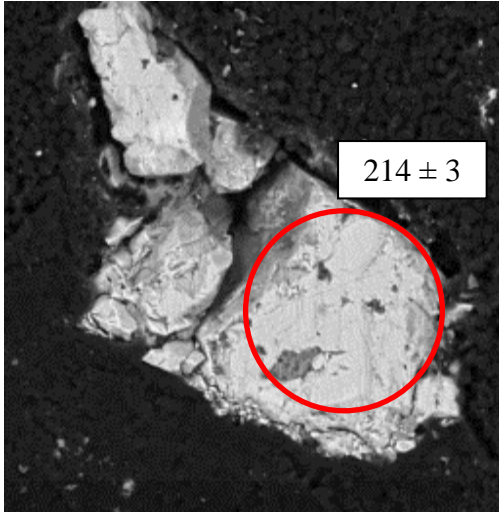


**DVK-4A-7**

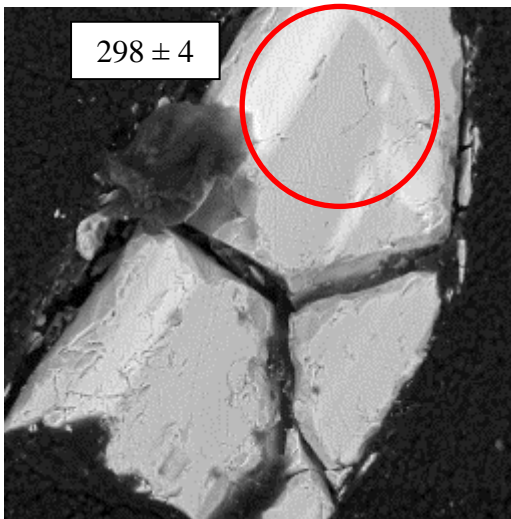
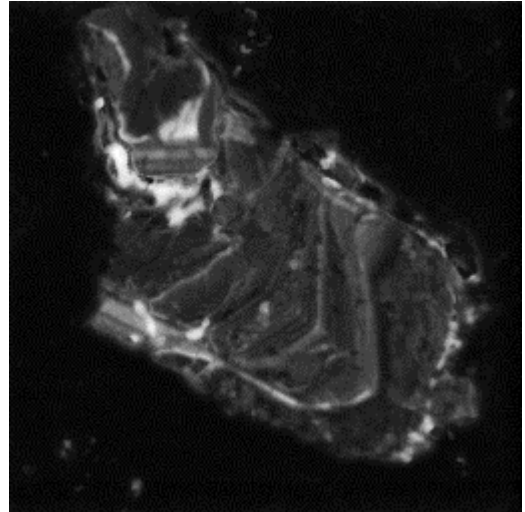


**DVK-4A-8**

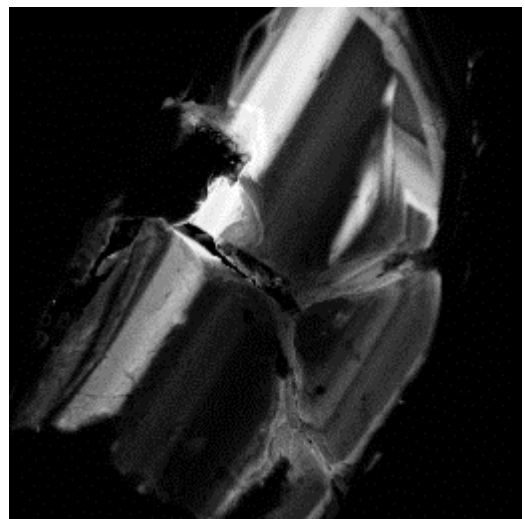


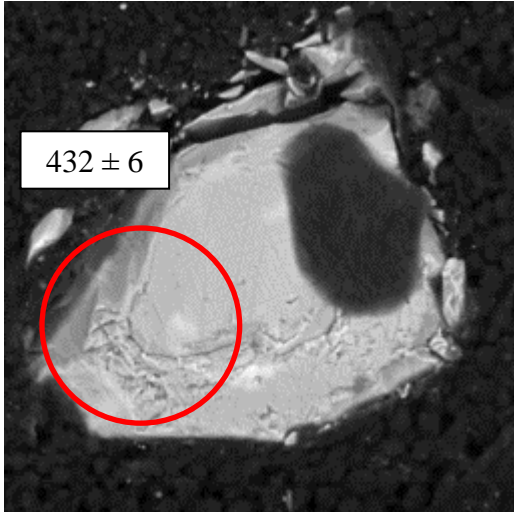


**DVK-4A-9**

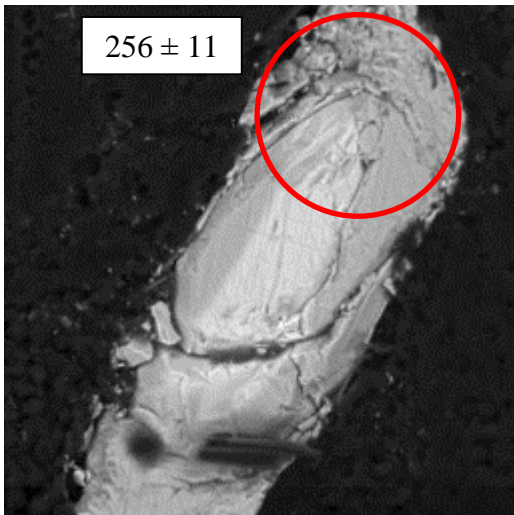
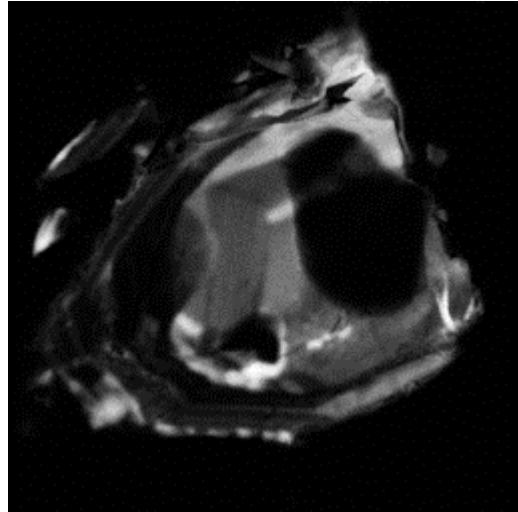


**DVK-4A-10**

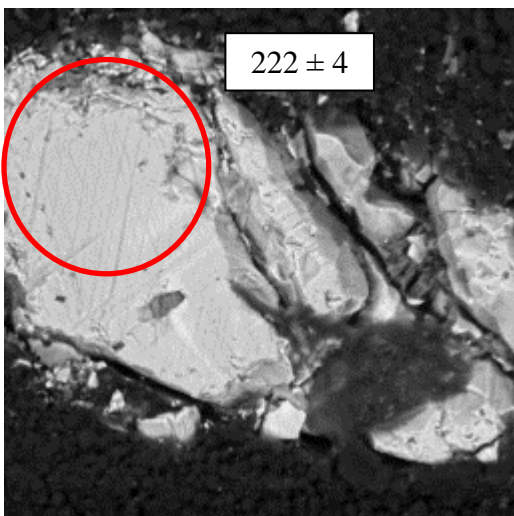
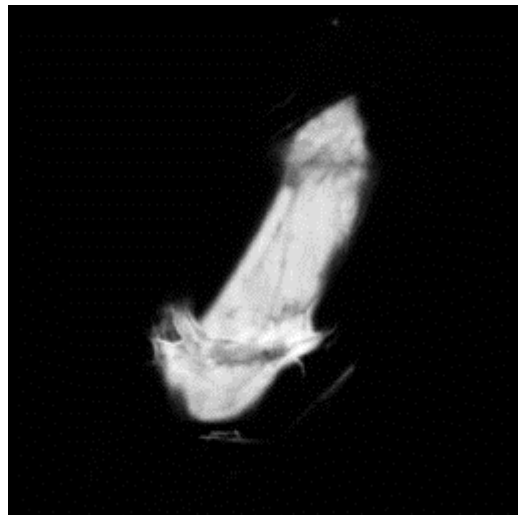




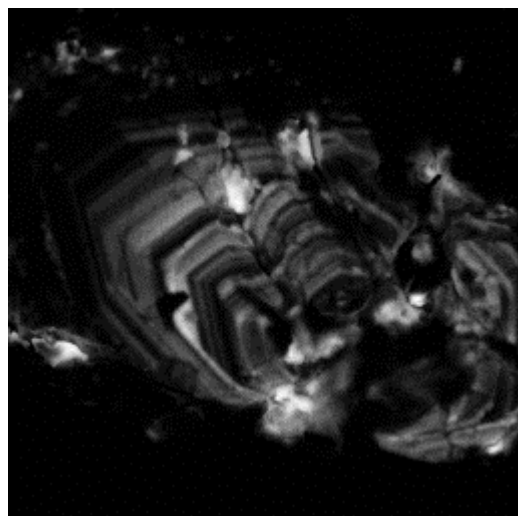
DVK-4A-11

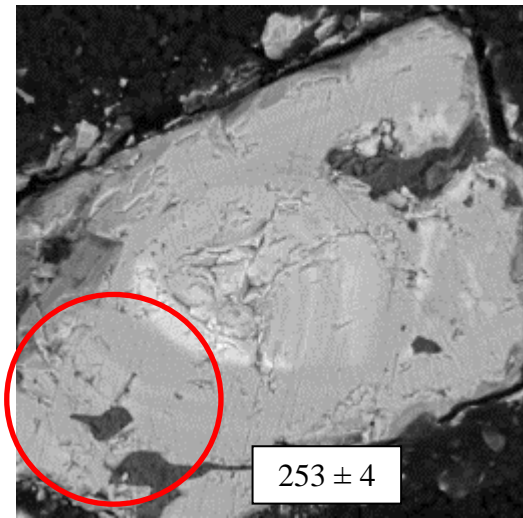


DVK-4A-12

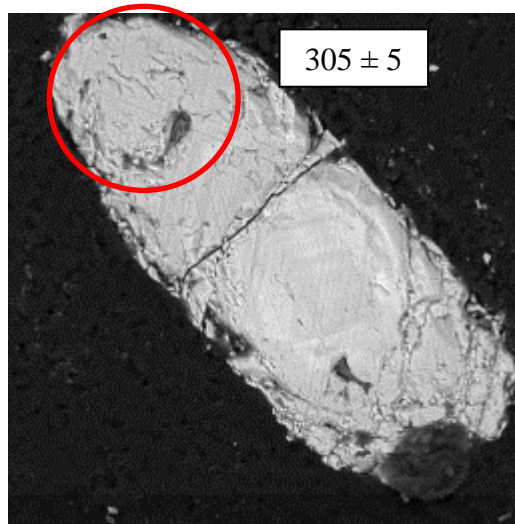
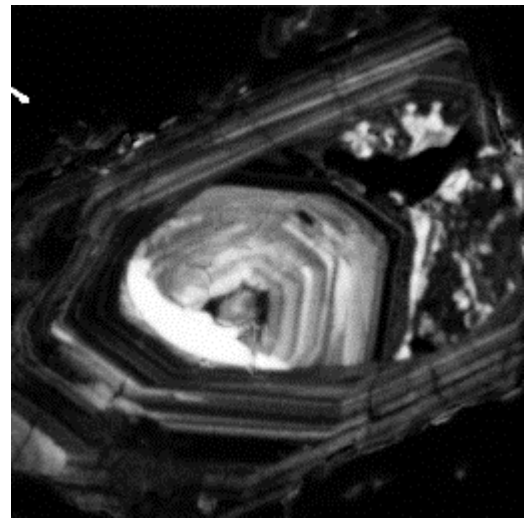


DVK-4A-13

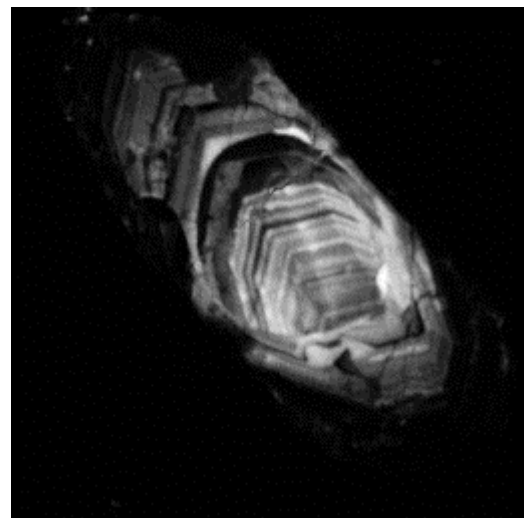


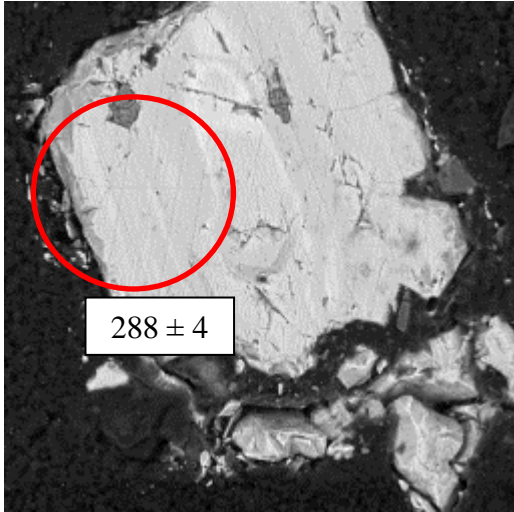


**DVK-4A-14**

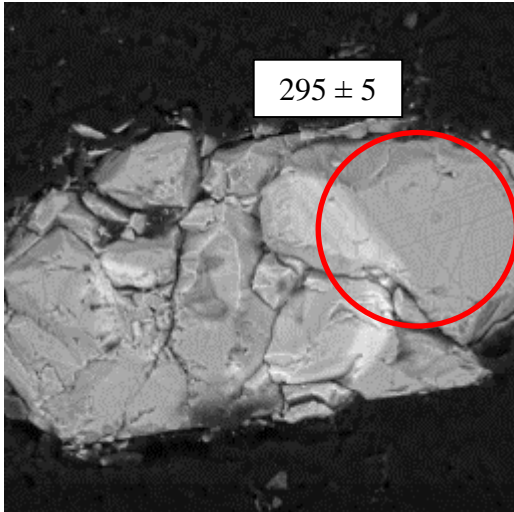
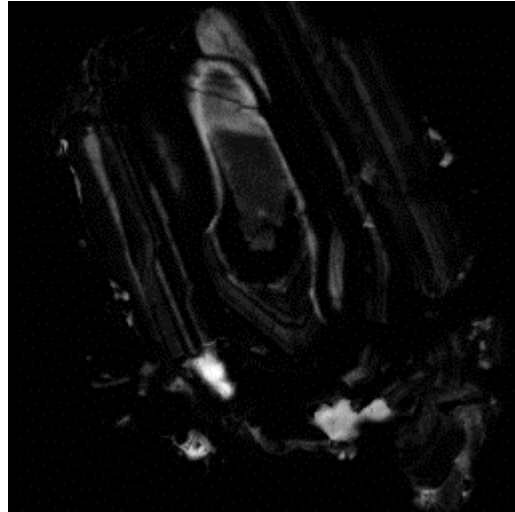


**DVK-4A-15**

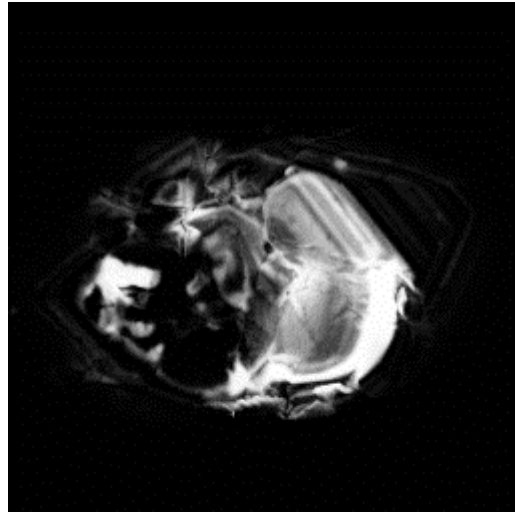


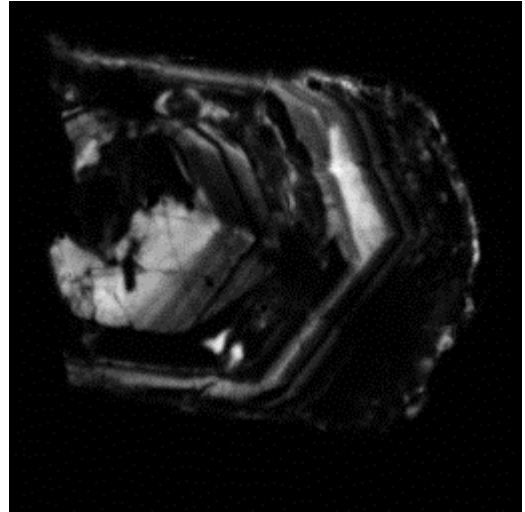
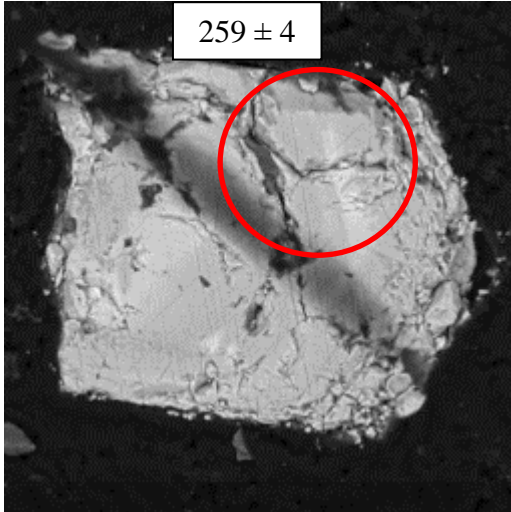


**DVK-4A-16**



**DVK-4A-17**





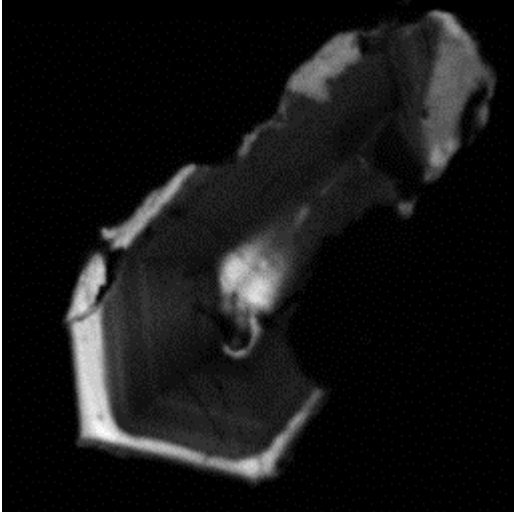
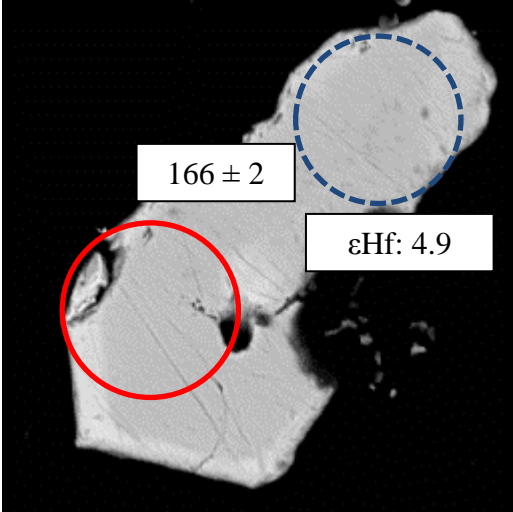
**DVK-4A-18**

BSE and CL images of the zircons from the DVK-13 (Devrekani Granitoid, Granite)

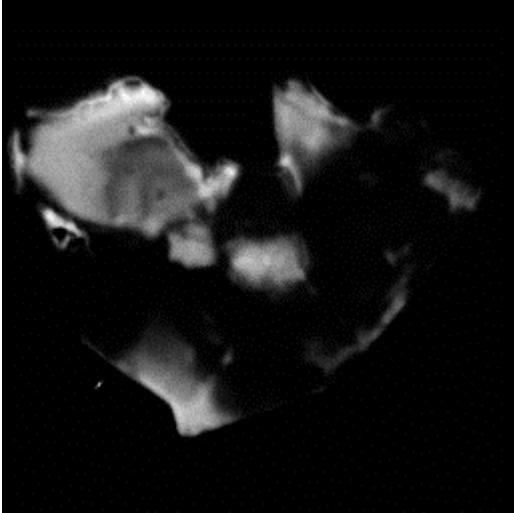
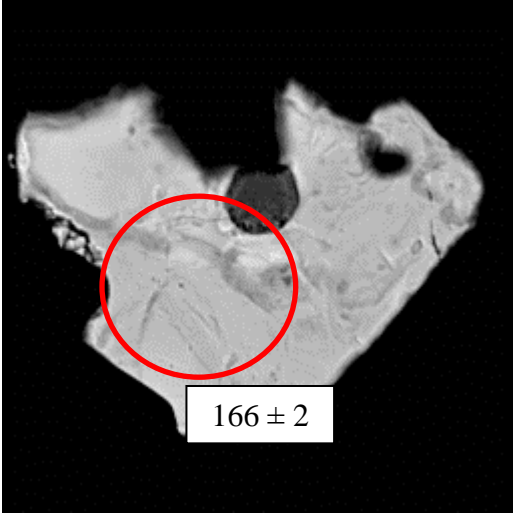
Circle: U-Pb age (Ma, laser spot size 35 micron), dash circle Hf isotope (laser spot size 35 micron)

BSE

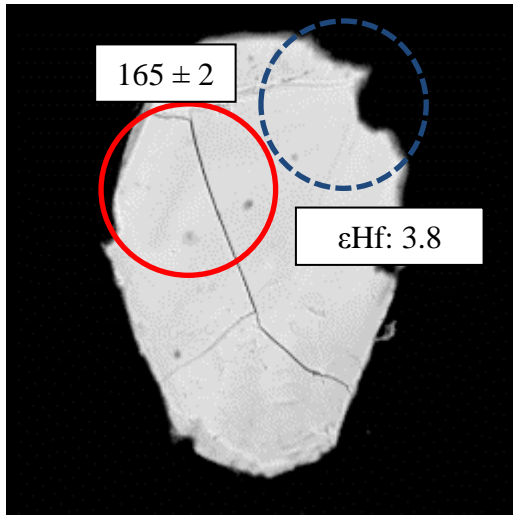
CL



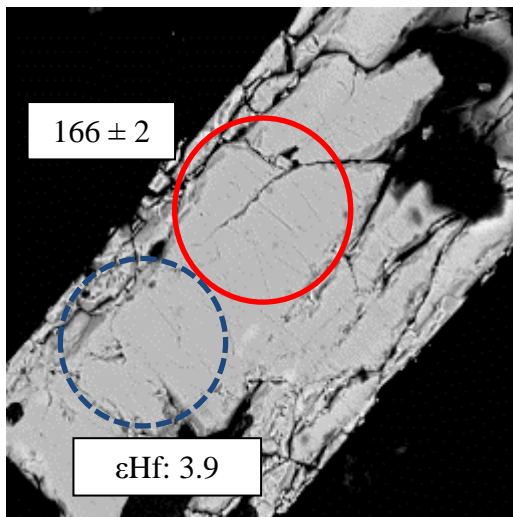
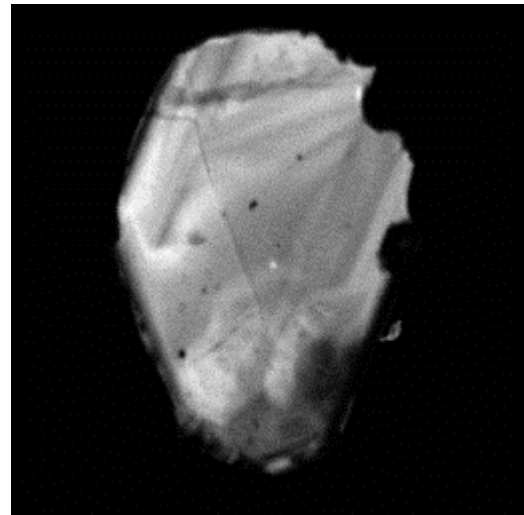
DVK-13-1



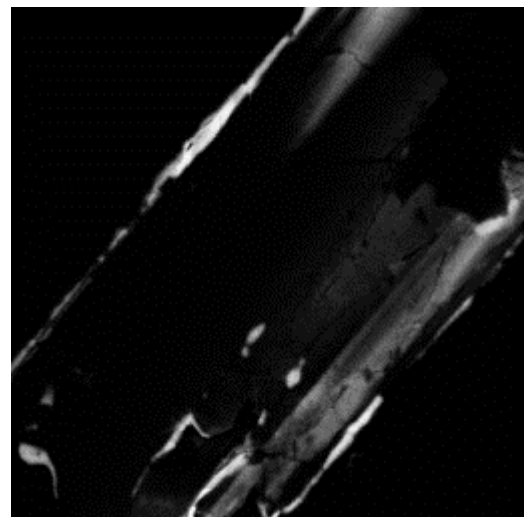
DVK-13-2

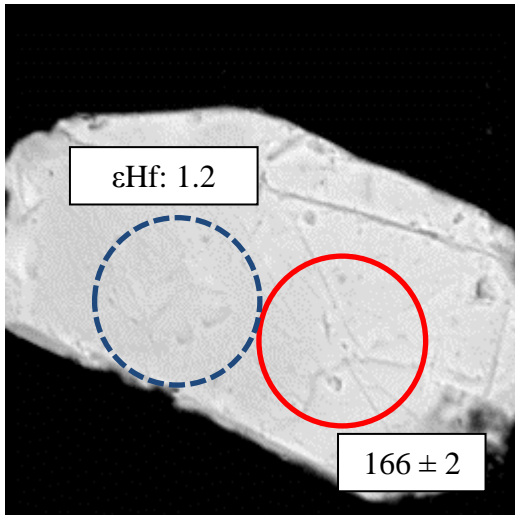


**DVK-13-3**

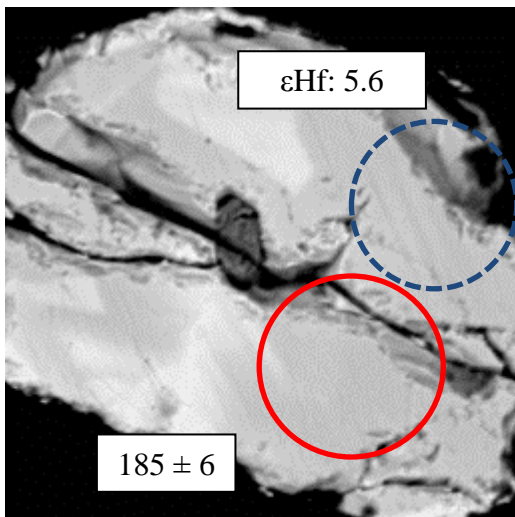
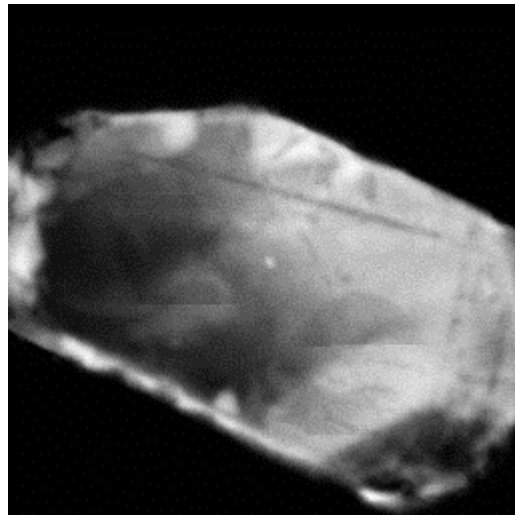


**DVK-13-4**

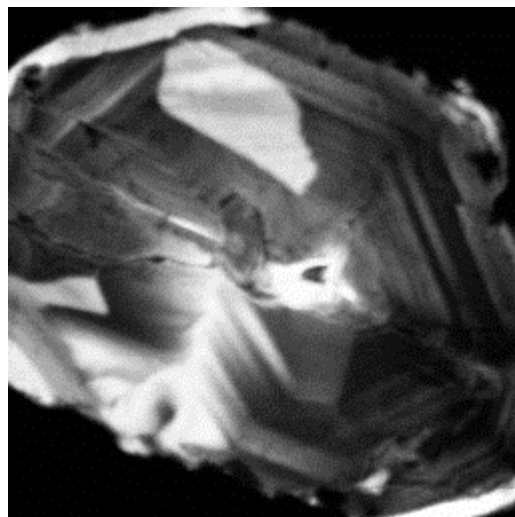


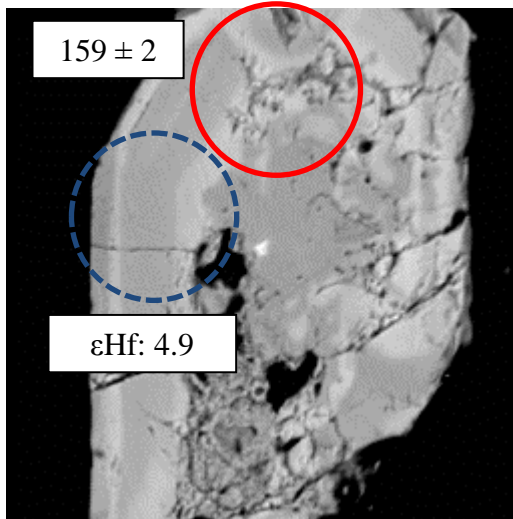


DVK-13-5

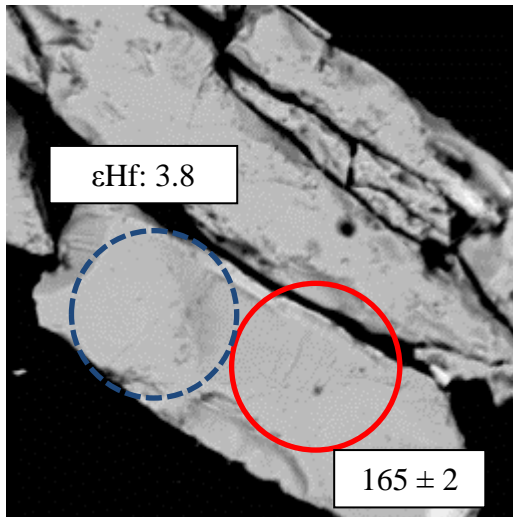
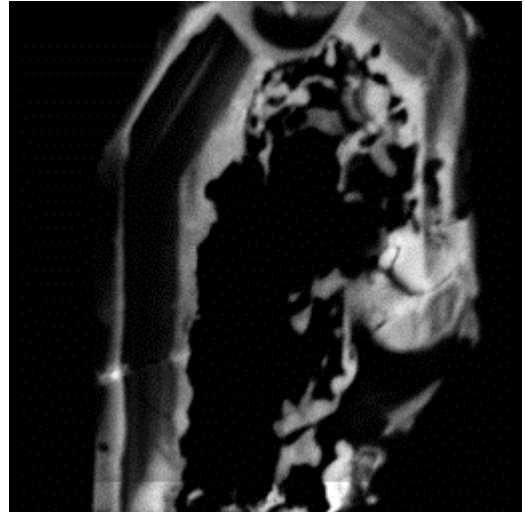


DVK-13-6

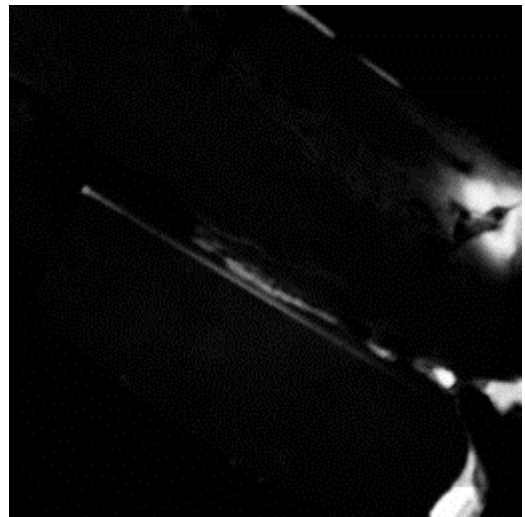


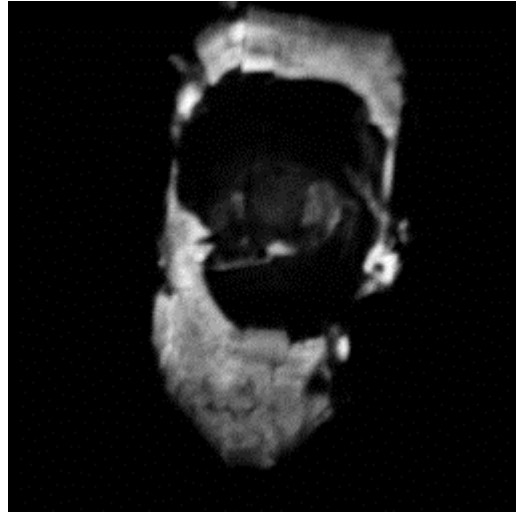
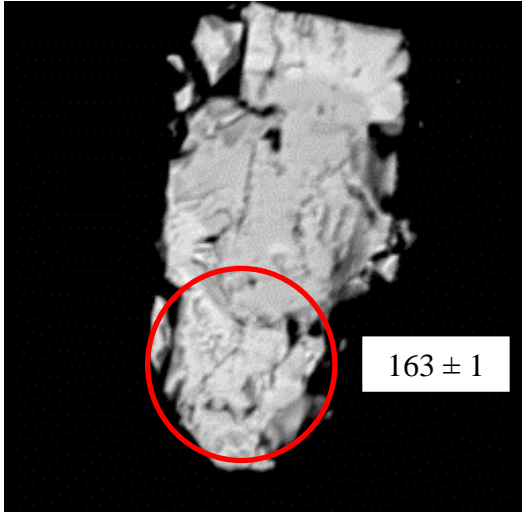


DVK-13-7



DVK-13-8





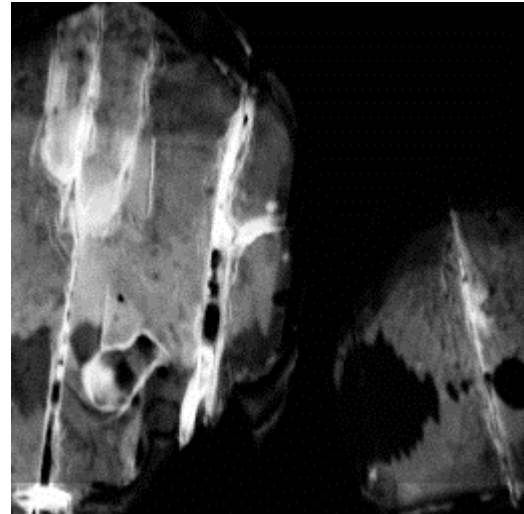
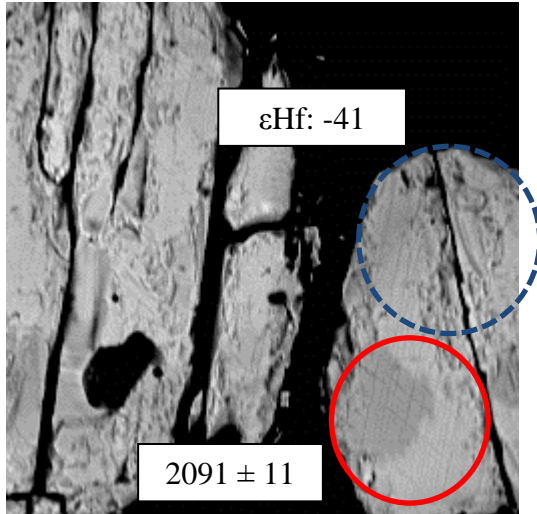
DVK-13-9

BSE and CL images of the zircons from the **SL-3** (Çangaldağ Pluton, S-type granite)

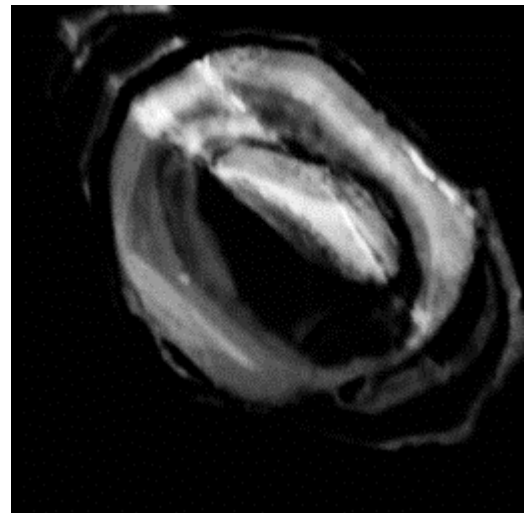
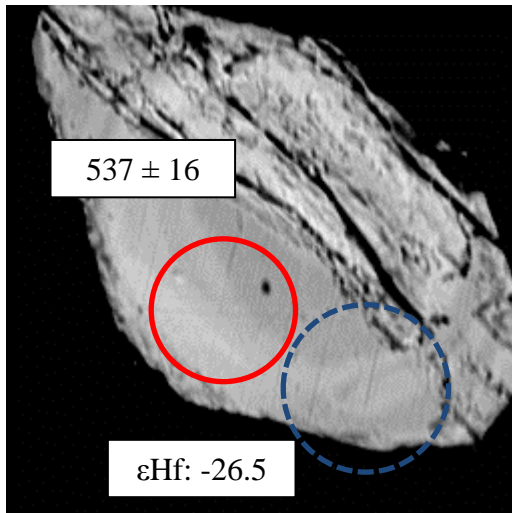
Circle: U-Pb age (Ma, laser spot size 25 micron), dash circle Hf isotope (laser spot size 35 micron)

**BSE**

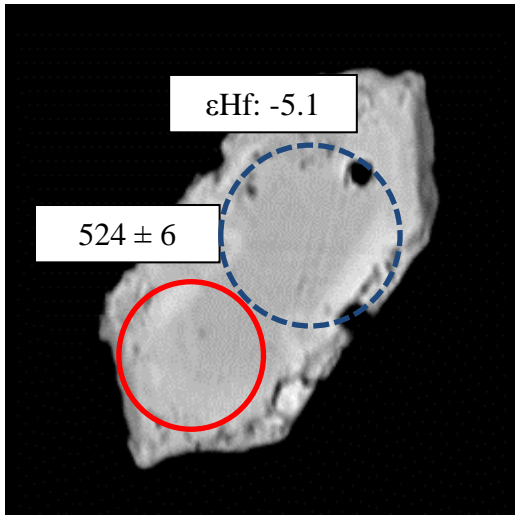
**CL**



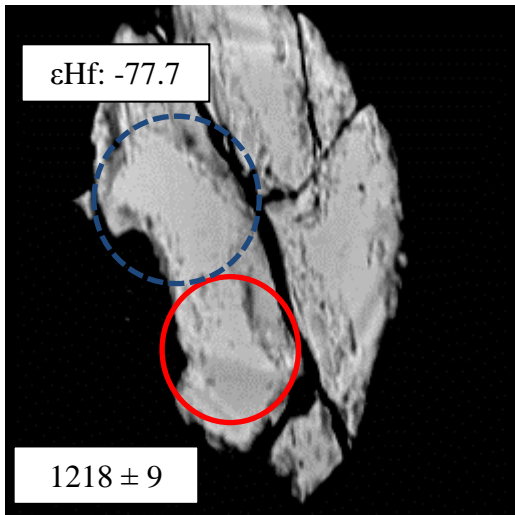
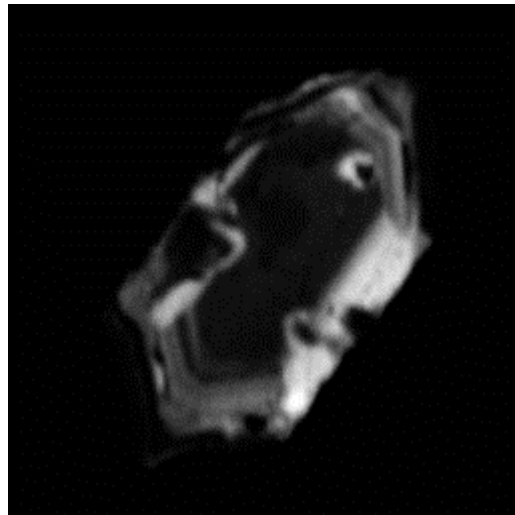
**SL-3-1**



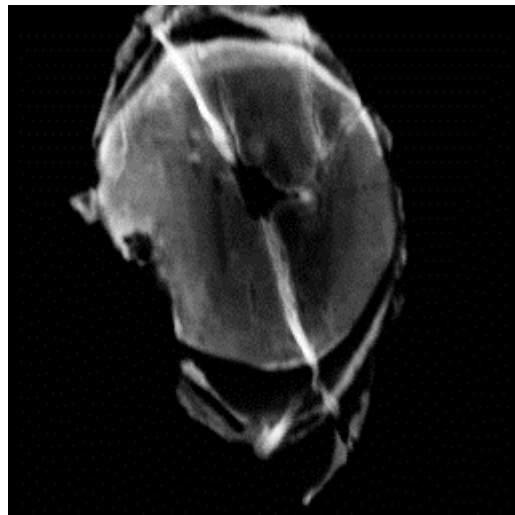
**SL-3-2**

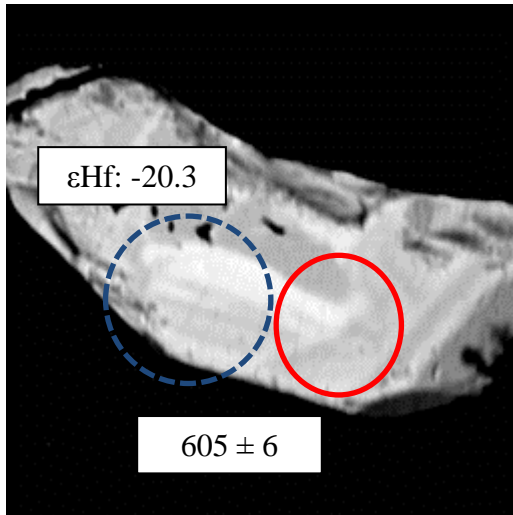


SL-3-3

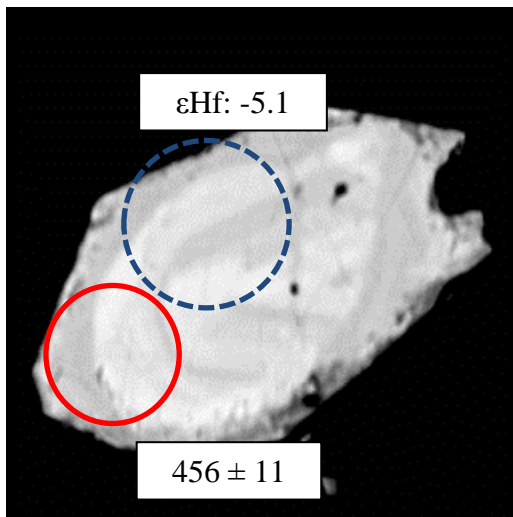
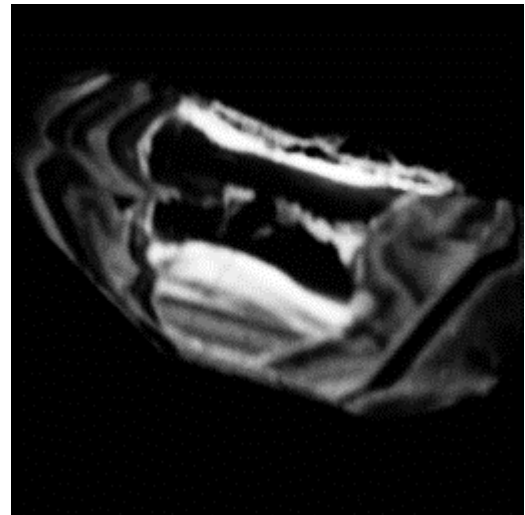


SL-3-4

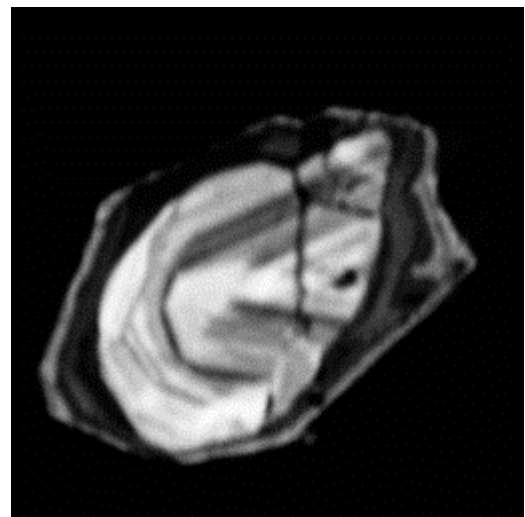


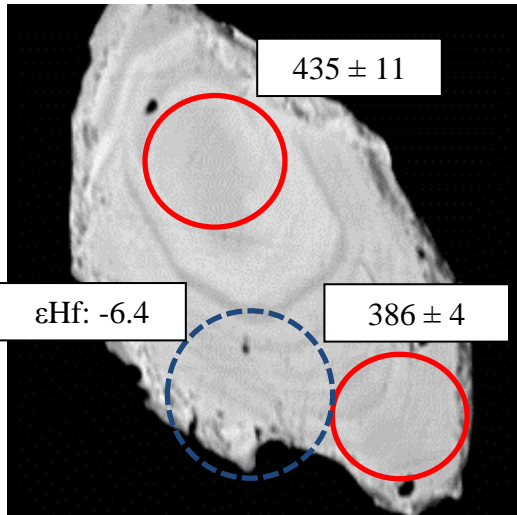


**SL-3-5**

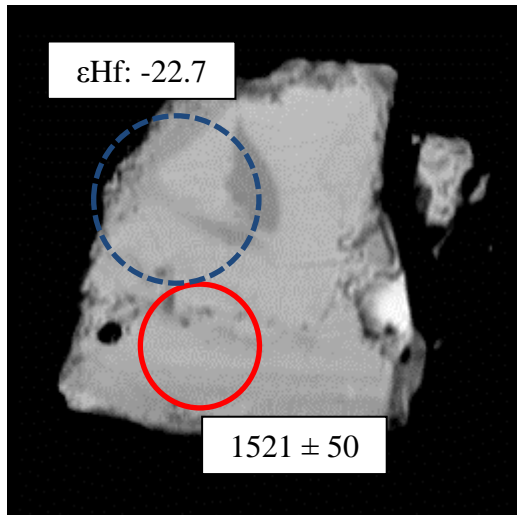
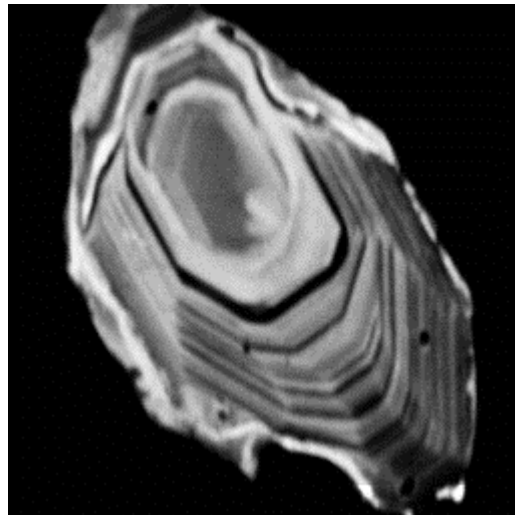


**SL-3-6**

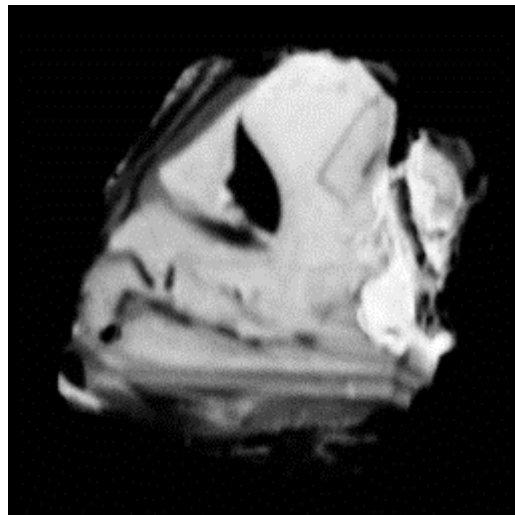


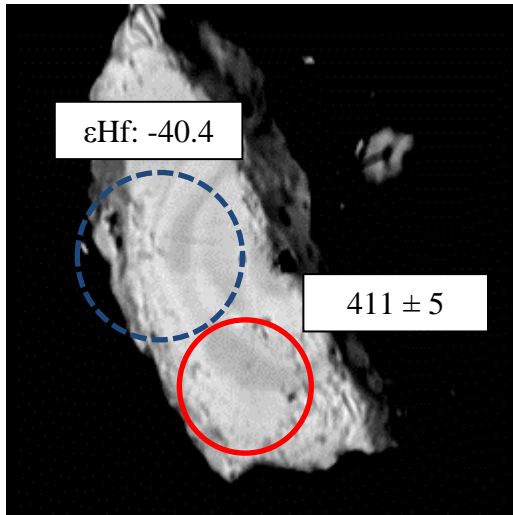


SL-3-7

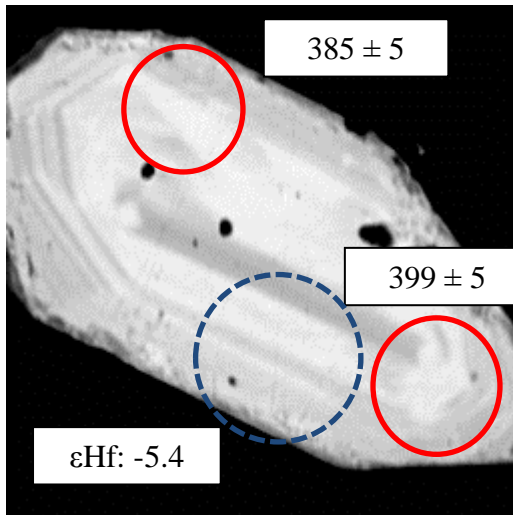
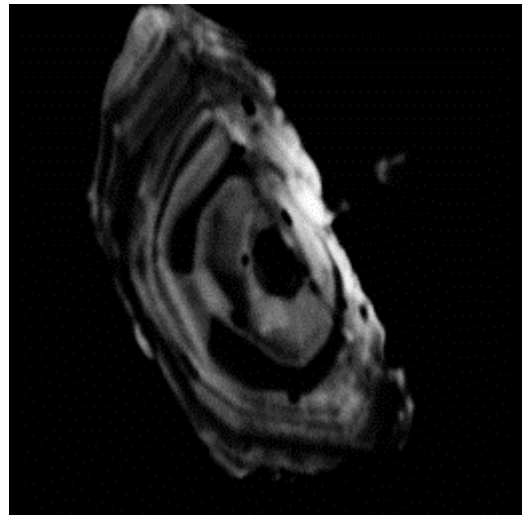


SL-3-8

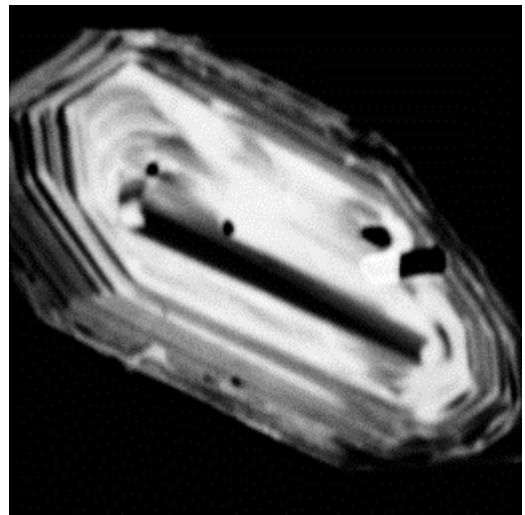


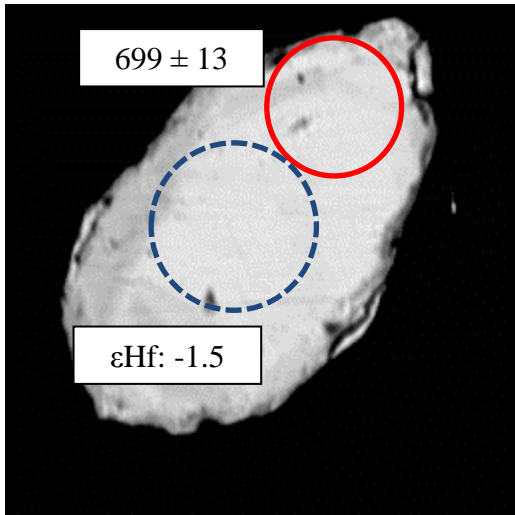


**SL-3-9**

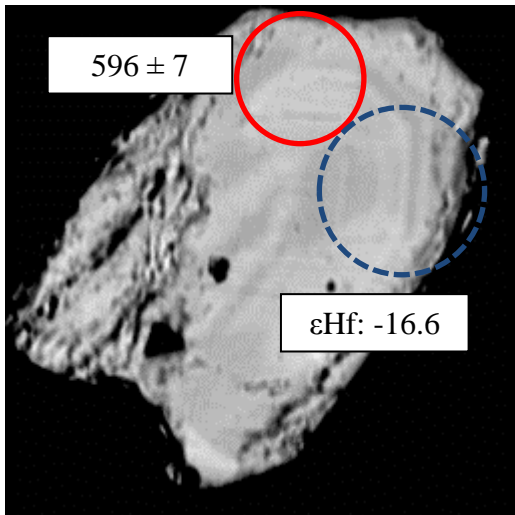
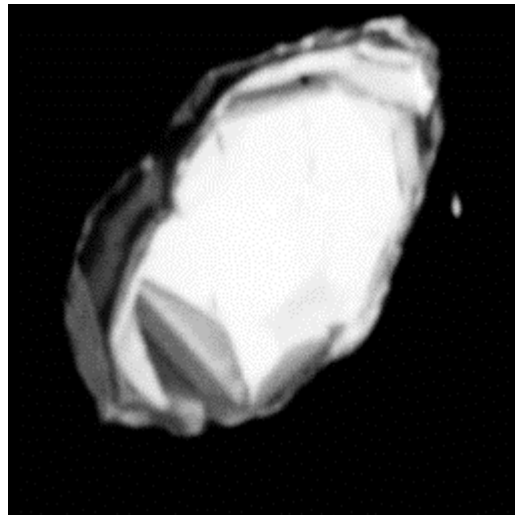


**SL-3-10**

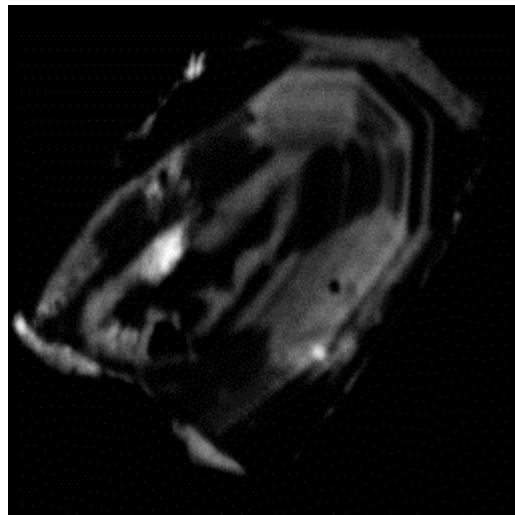


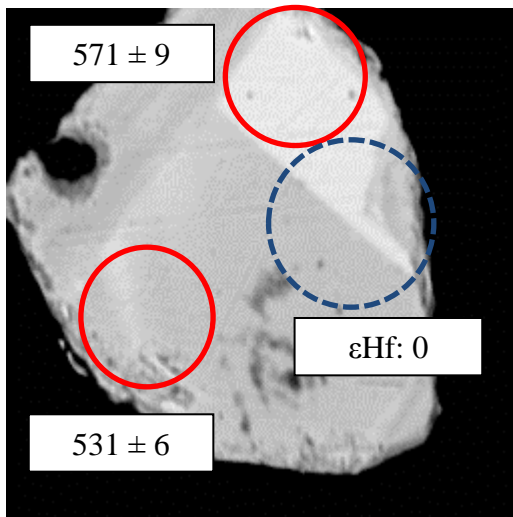


SL-3-11

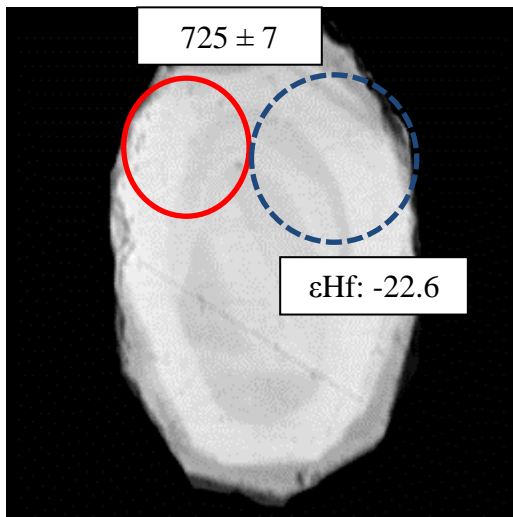
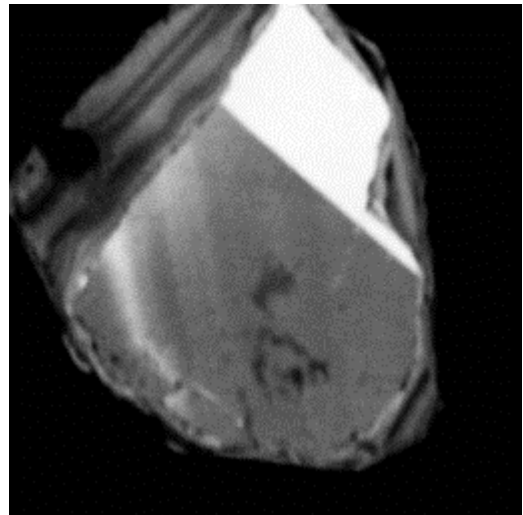


SL-3-12

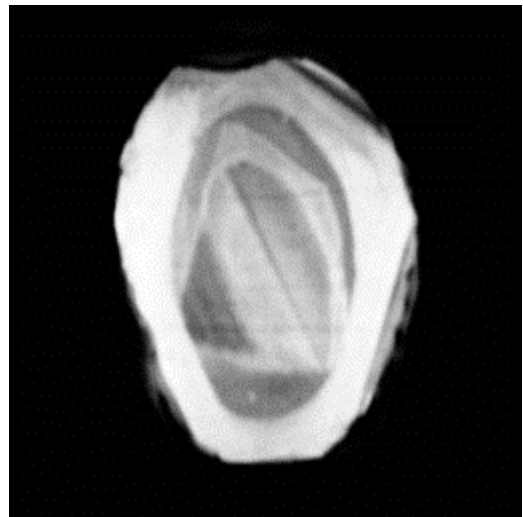


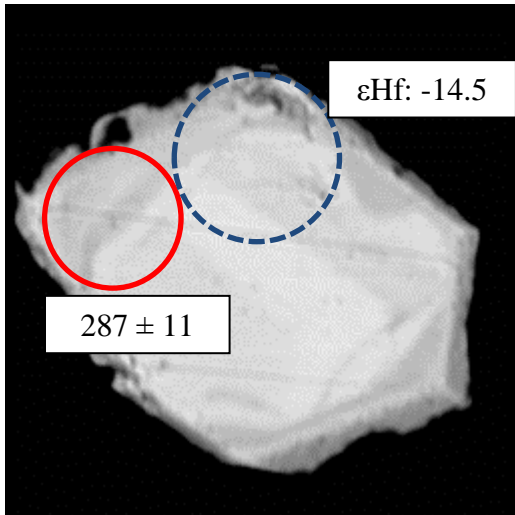


SL-3-13

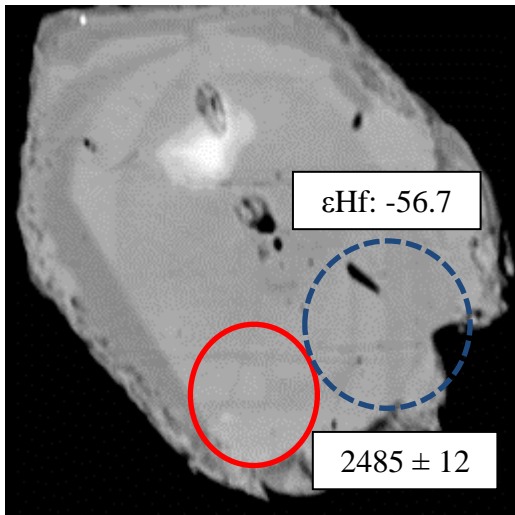
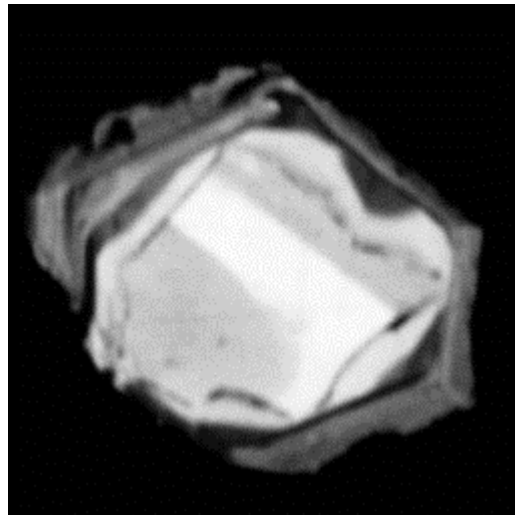


SL-3-14

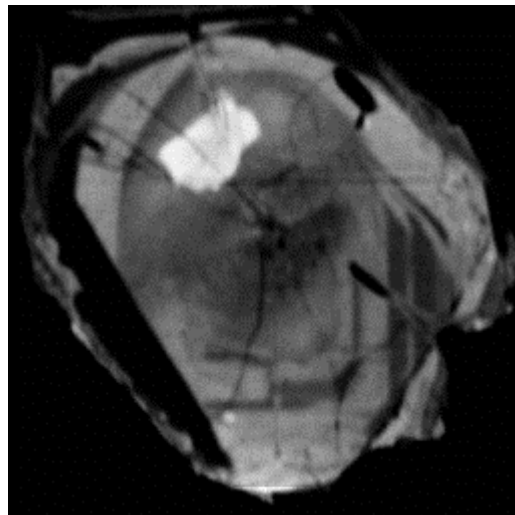


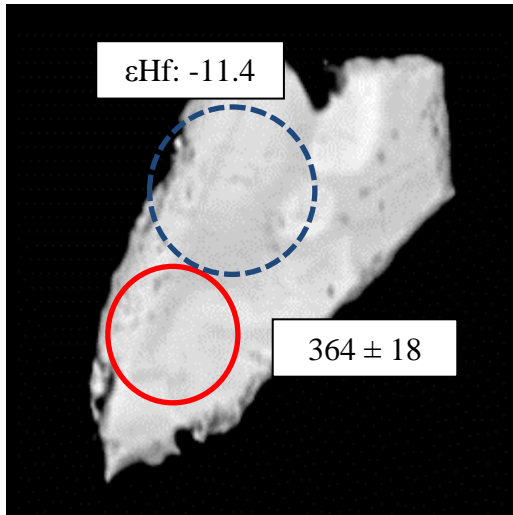


SL-3-15

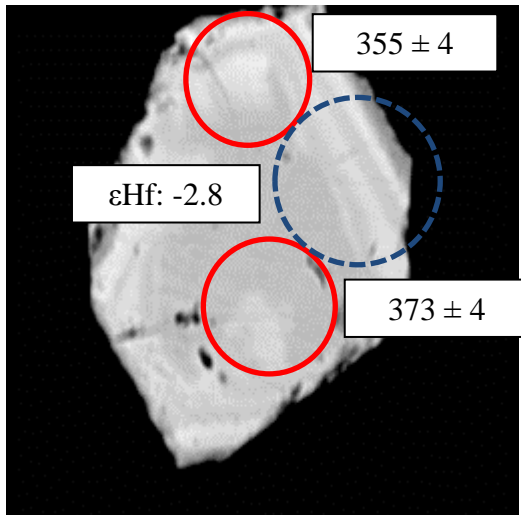
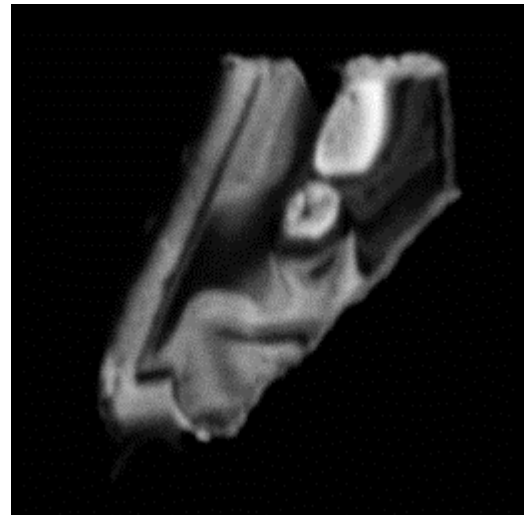


SL-3-16

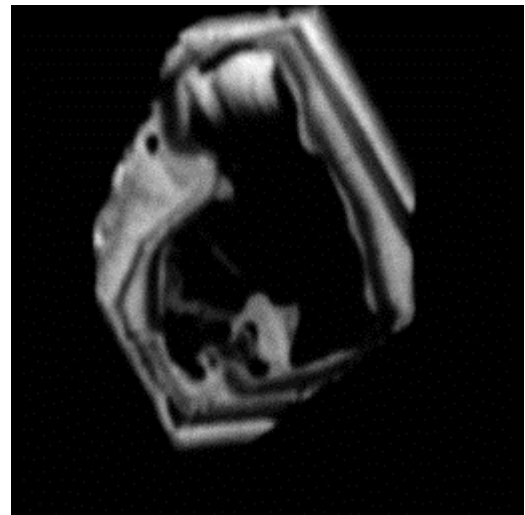


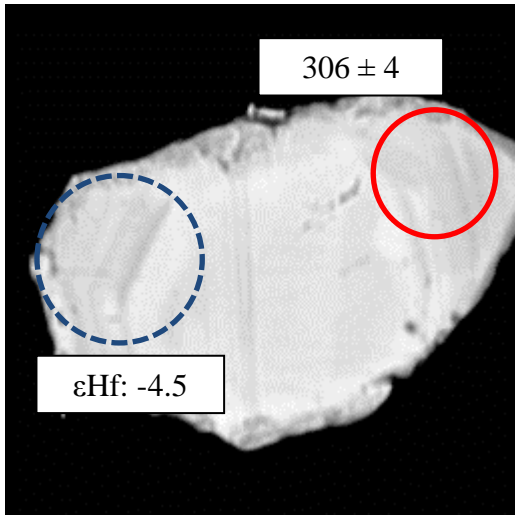


SL-3-17

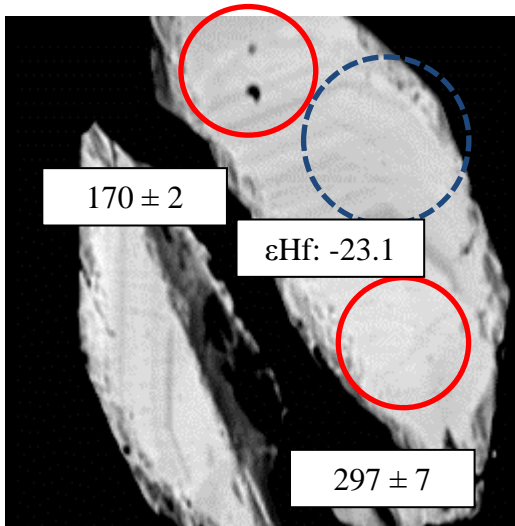
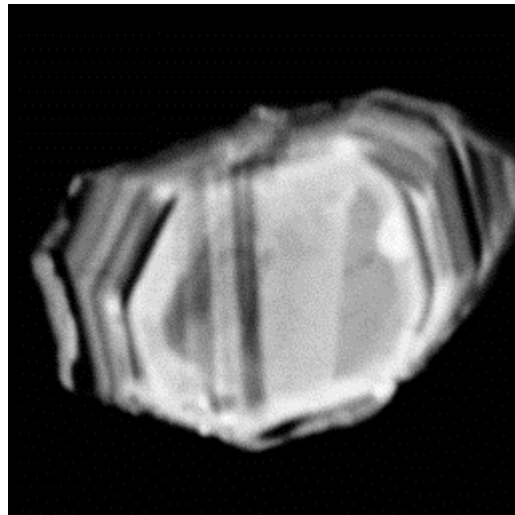


SL-3-18

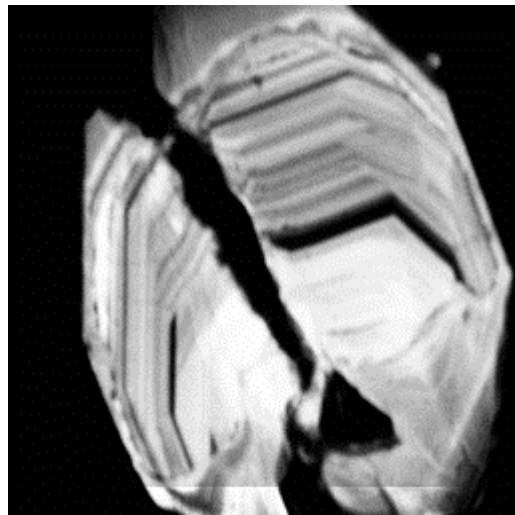


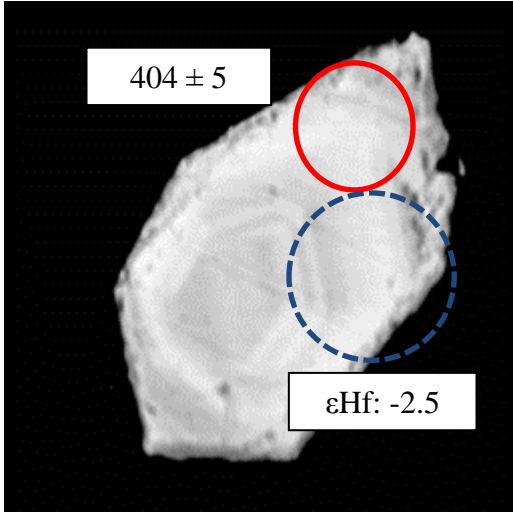


SL-3-19

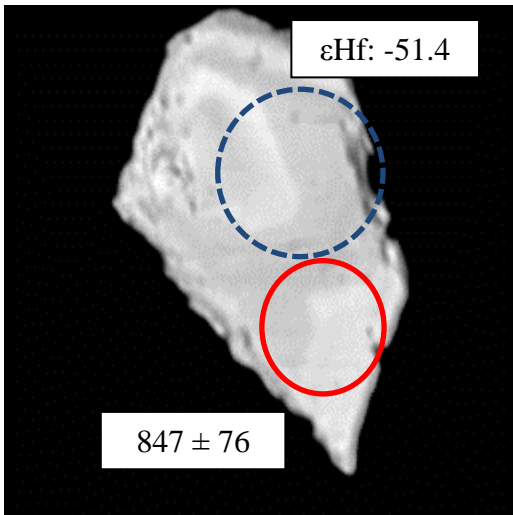
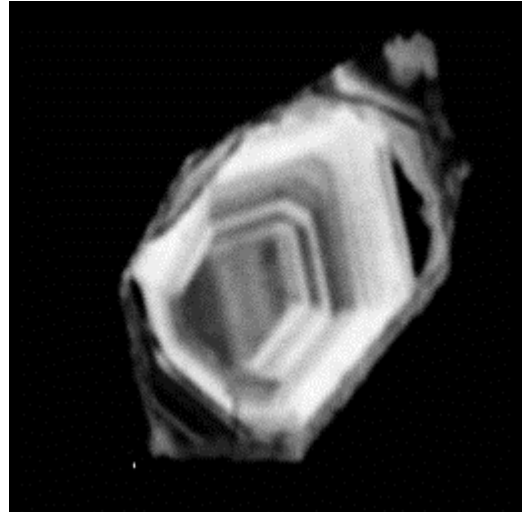


SL-3-20

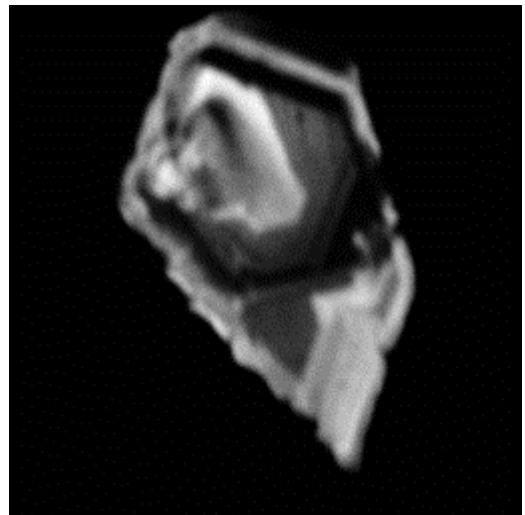


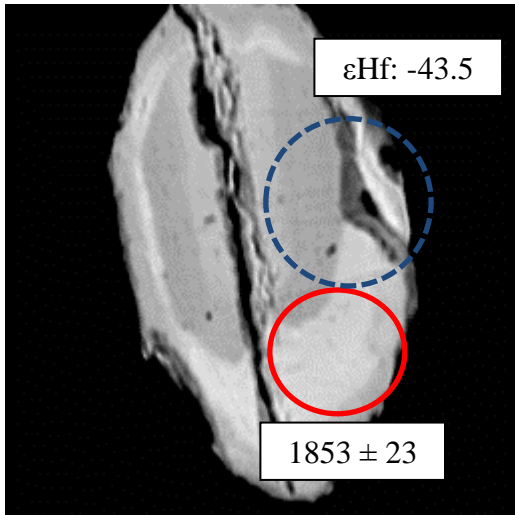


SL-3-21

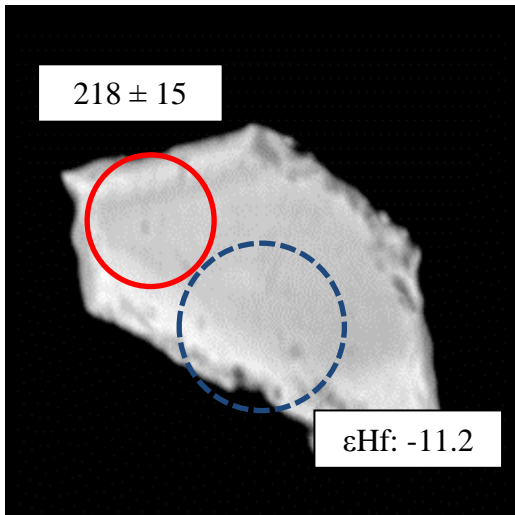
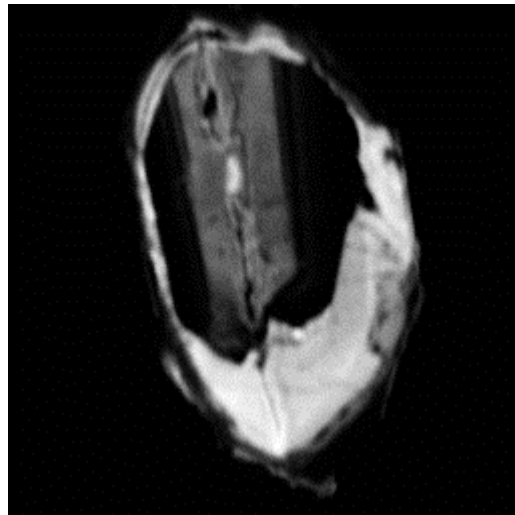


SL-3-22

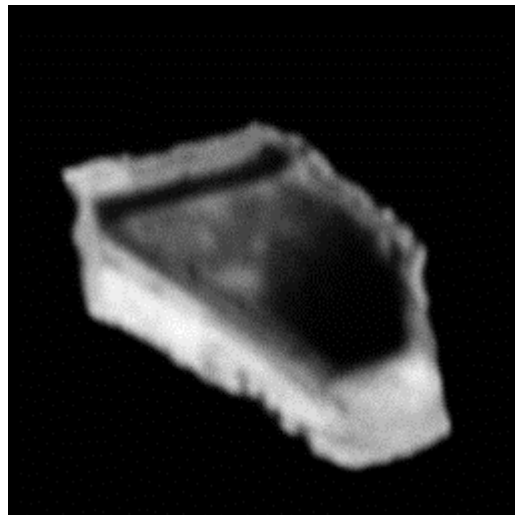


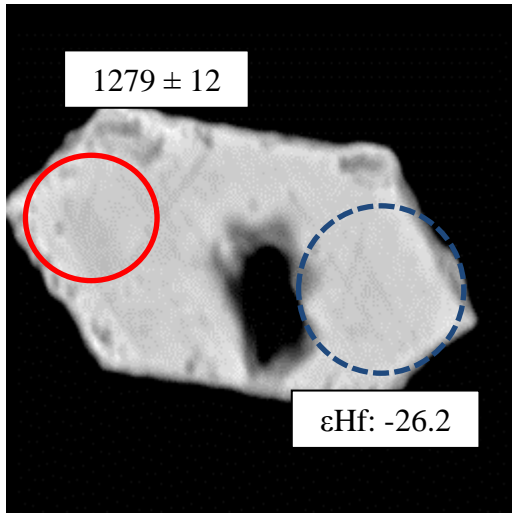


SL-3-23

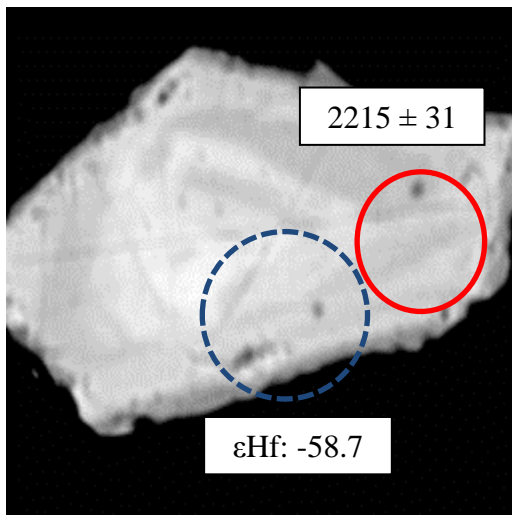
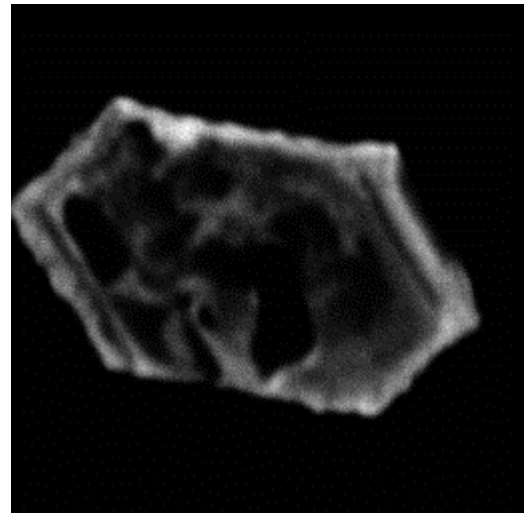


SL-3-24

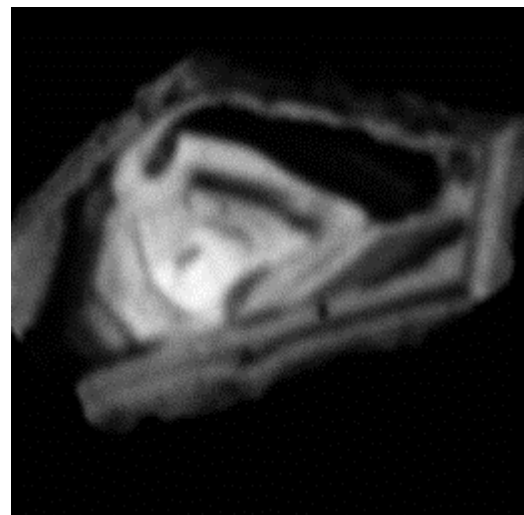


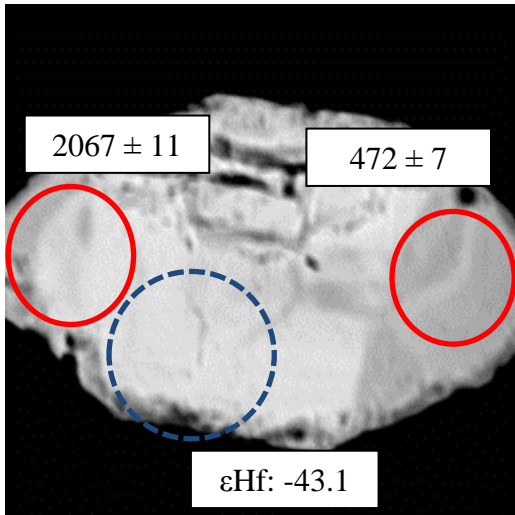


**SL-3-25**

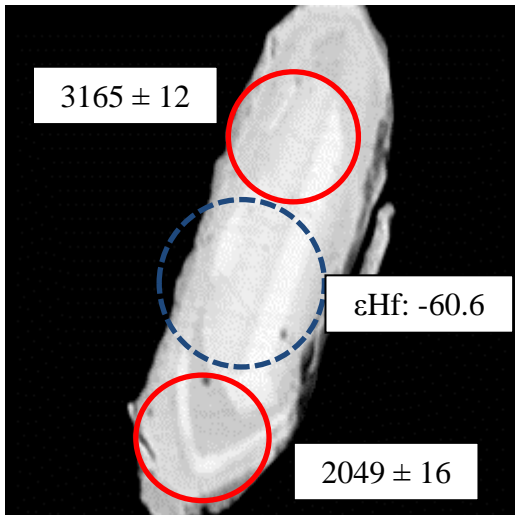
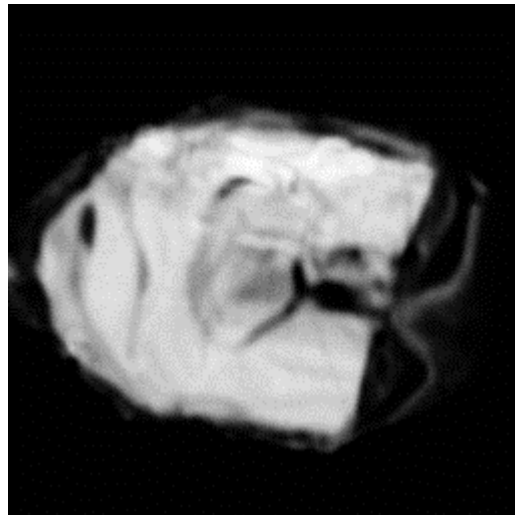


**SL-3-26**

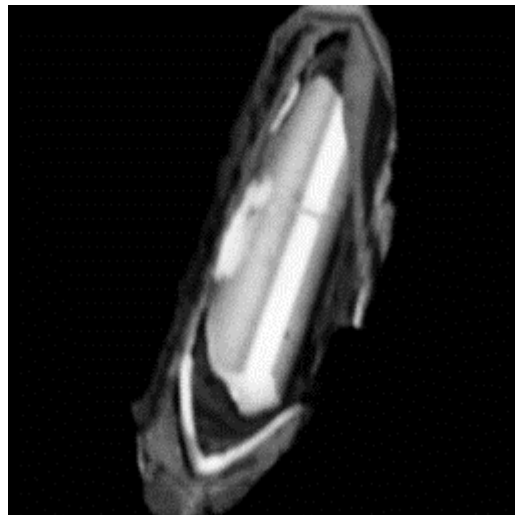


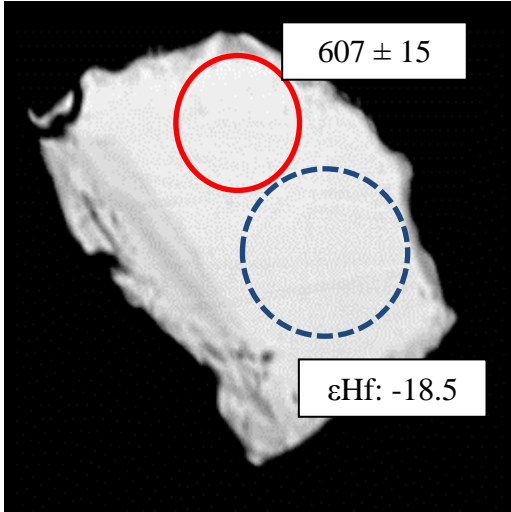


SL-3-27

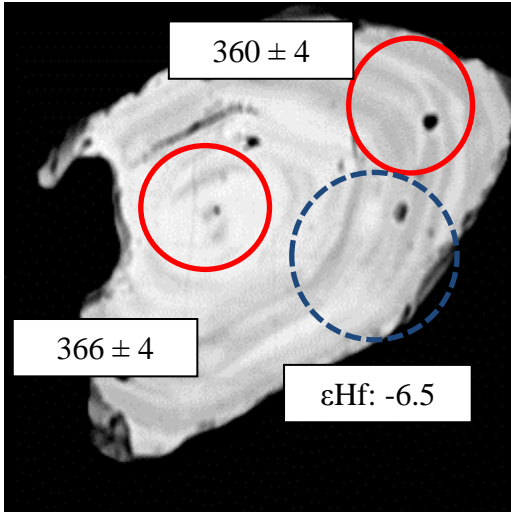
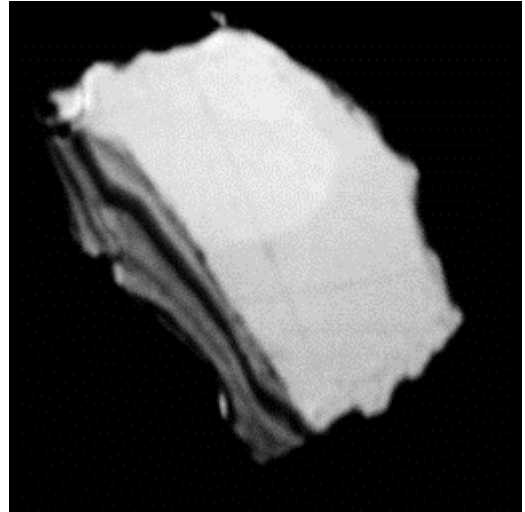


SL-3-28

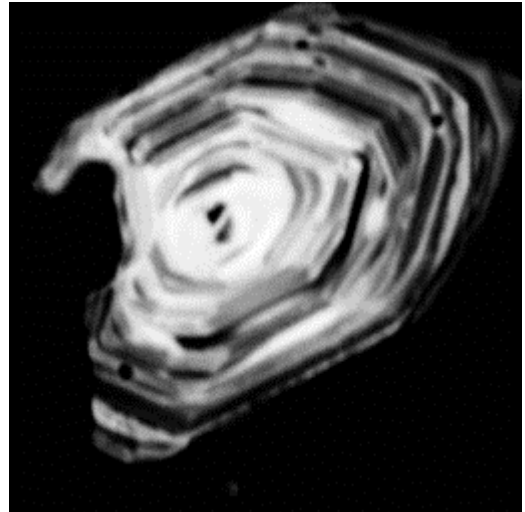


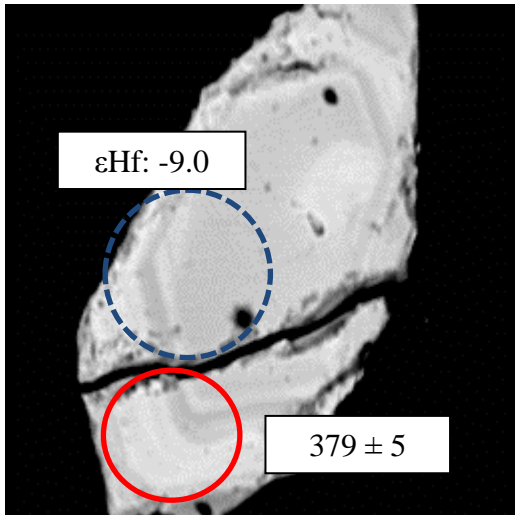


SL-3-29

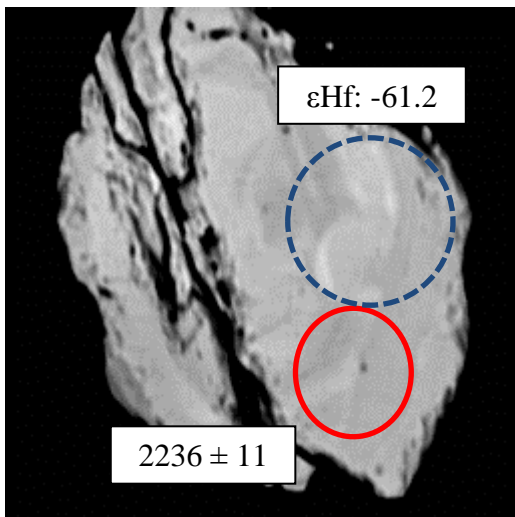
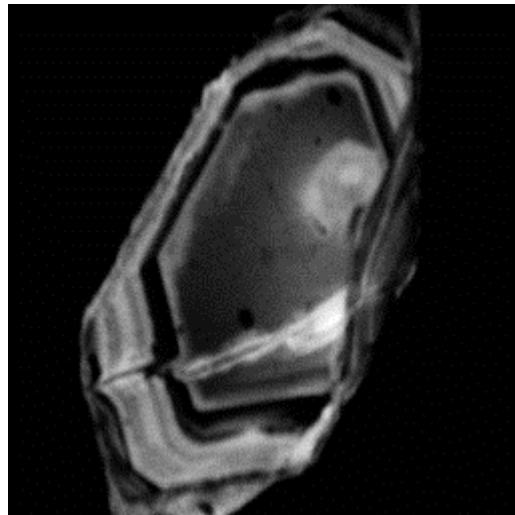


SL-3-30

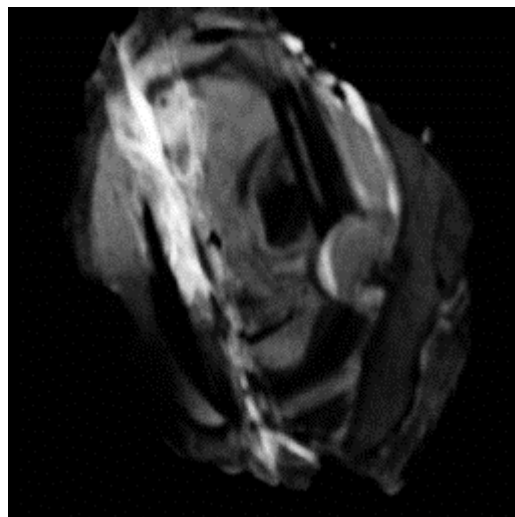


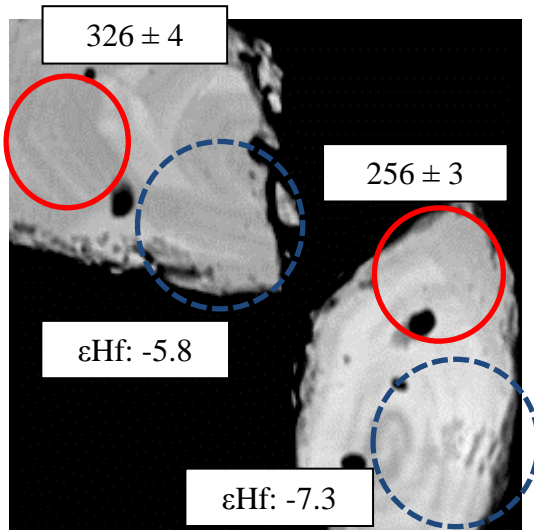


SL-3-31

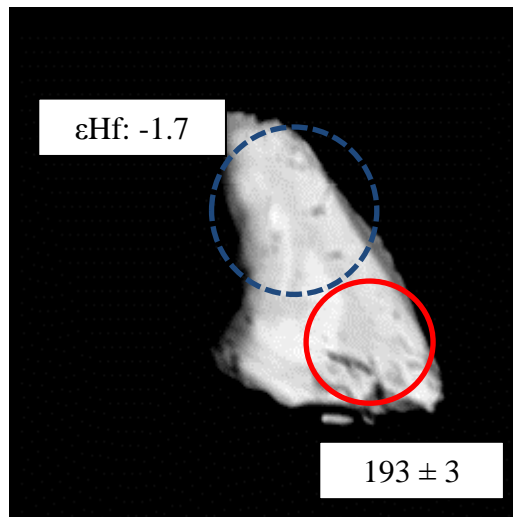
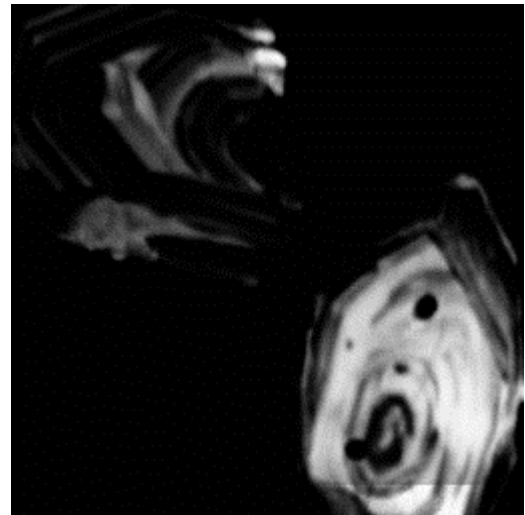


SL-3-32

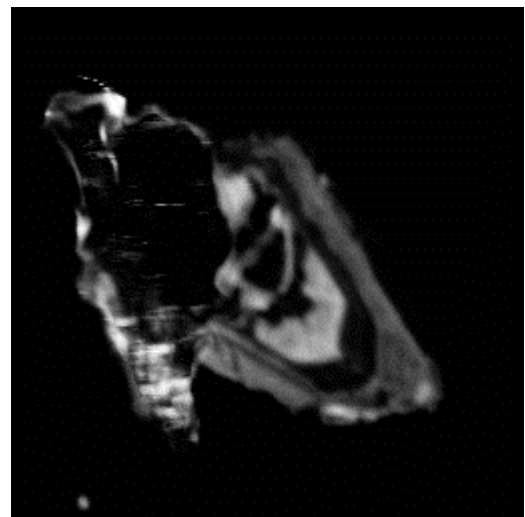


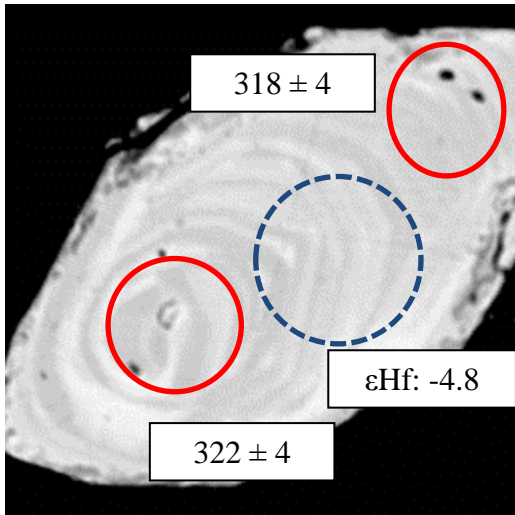


**SL-3-33**

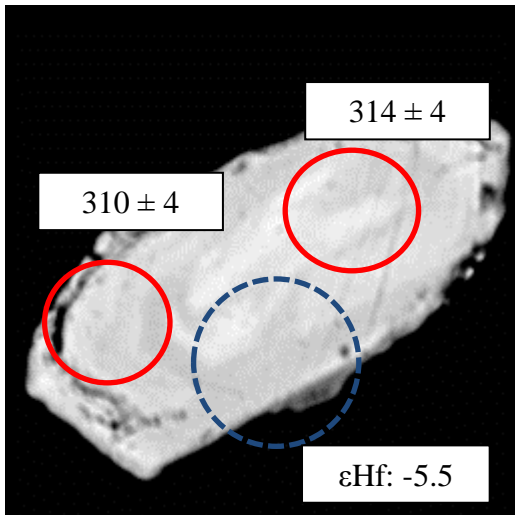
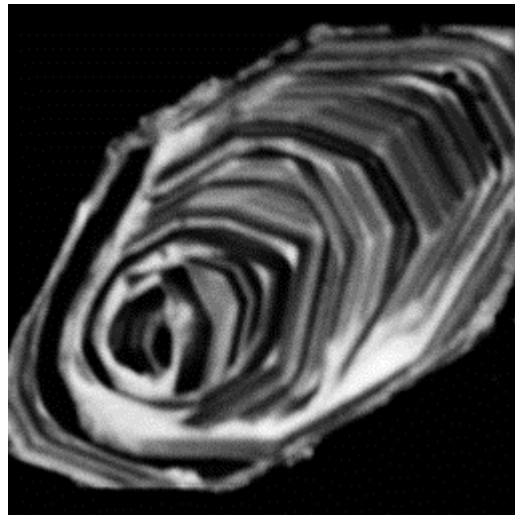


**SL-3-34**

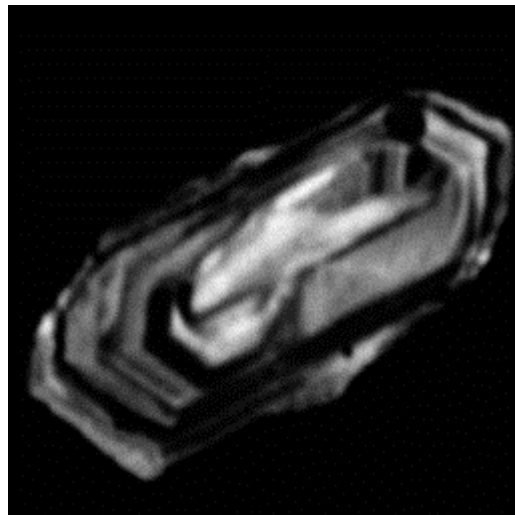


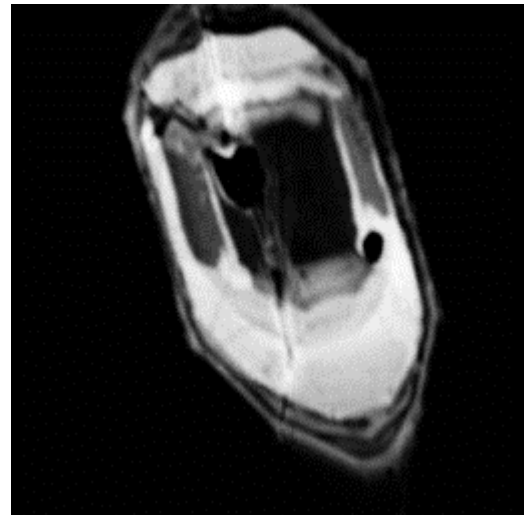
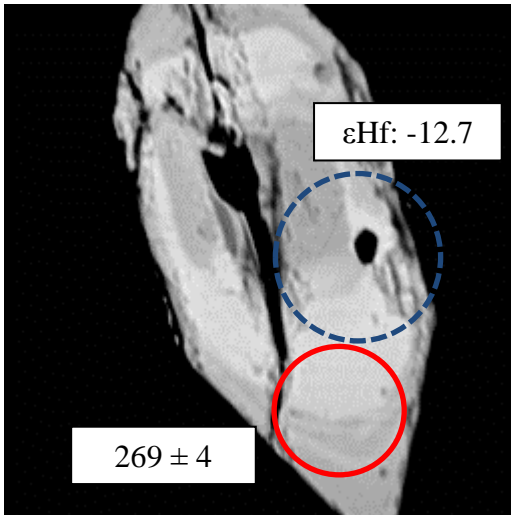


SL-3-35



SL-3-36





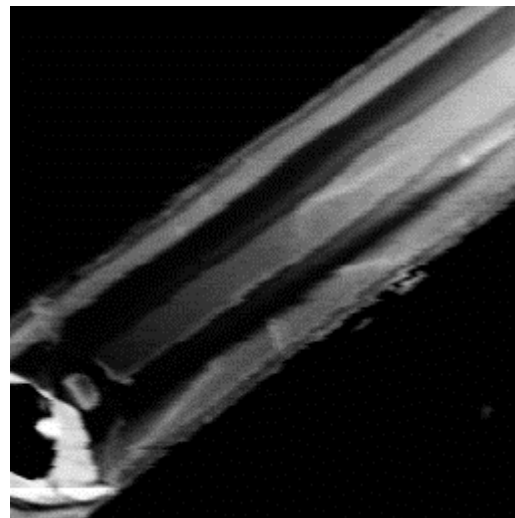
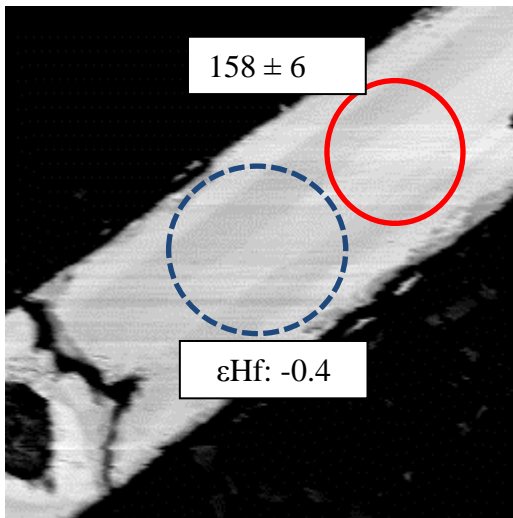
SL-3-37

BSE and CL images of the zircons from the **CN-3** (Çangaldağ Pluton, Dacite Porphyry)

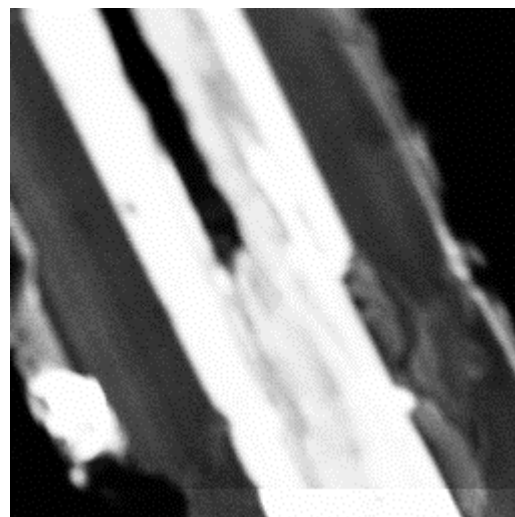
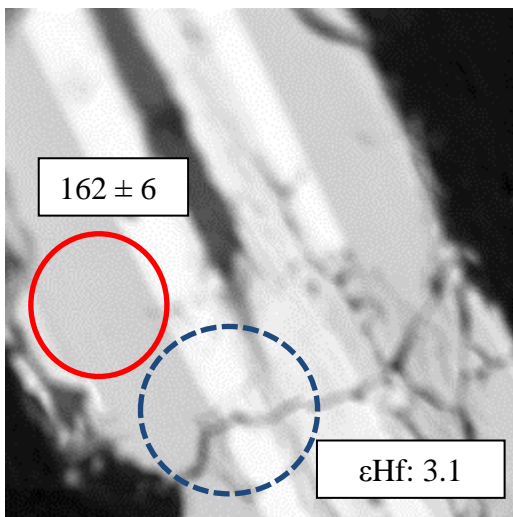
Circle: U-Pb age (Ma, laser spot size 25 micron), dash circle Hf isotope (laser spot size 35 micron)

**BSE**

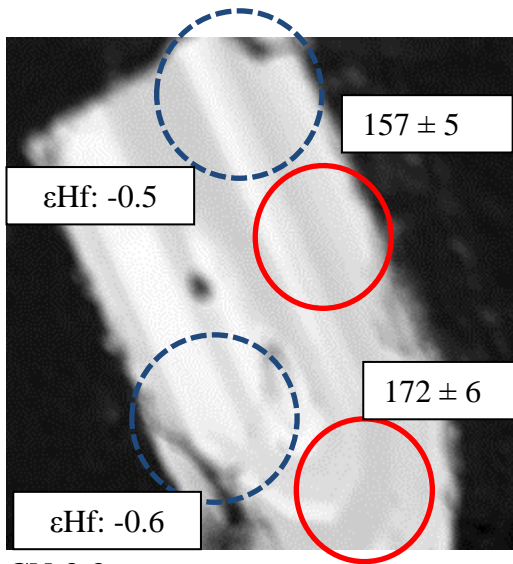
**CL**



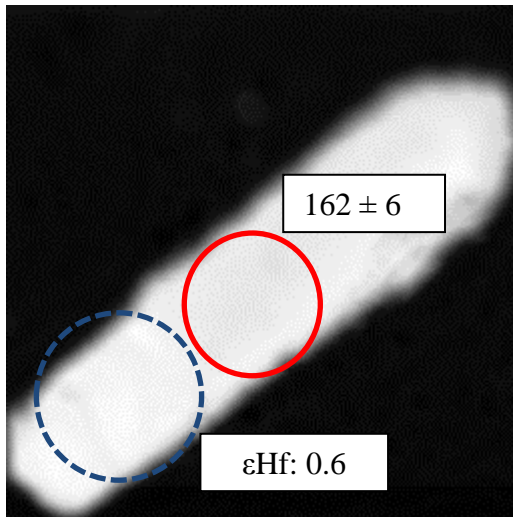
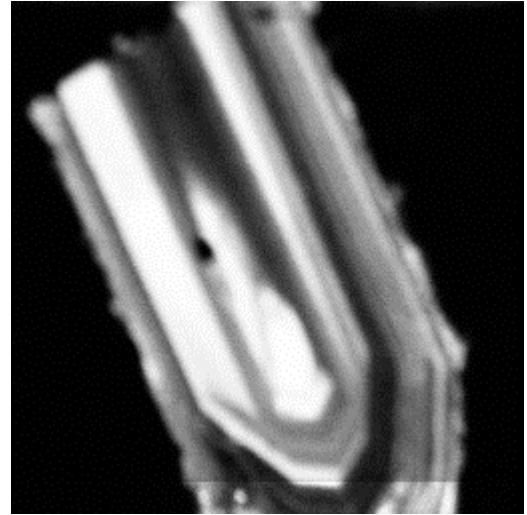
**CN-3-1**



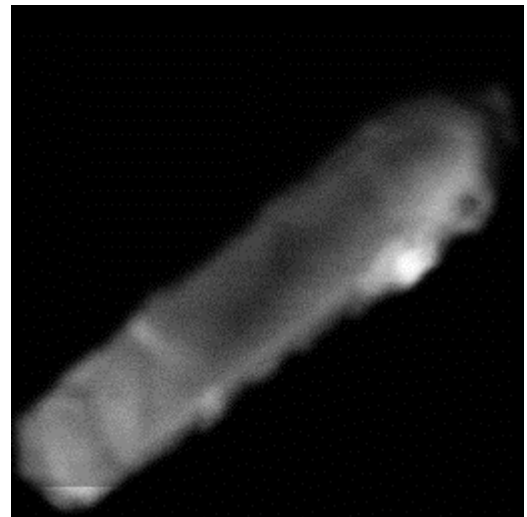
**CN-3-2**

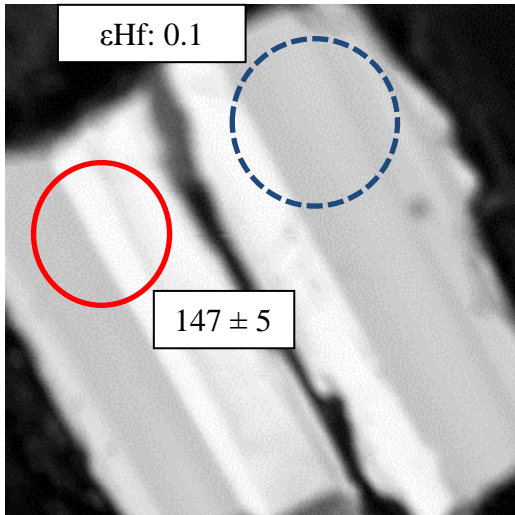


CN-3-3

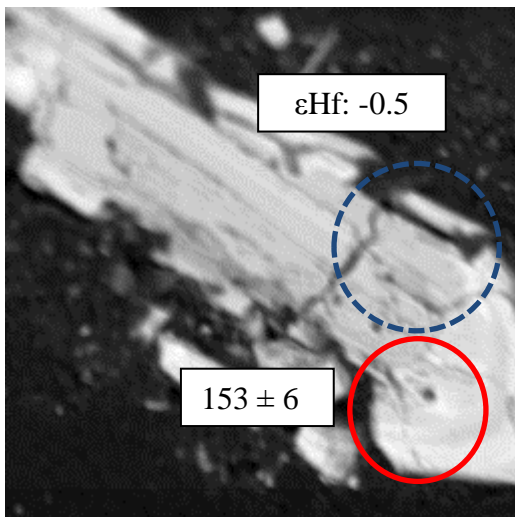
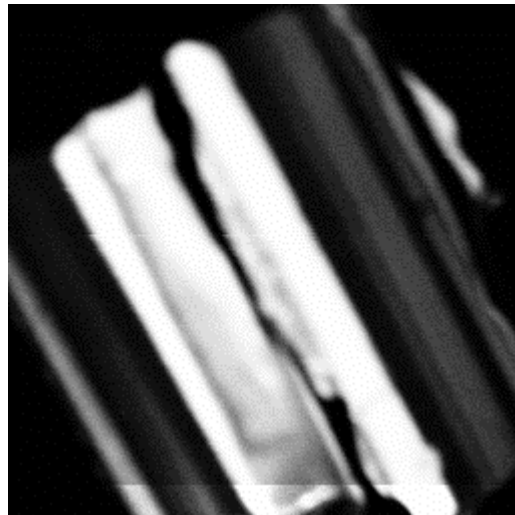


CN-3-4

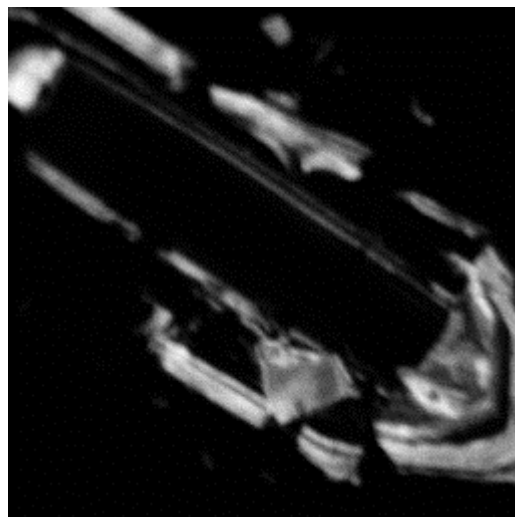


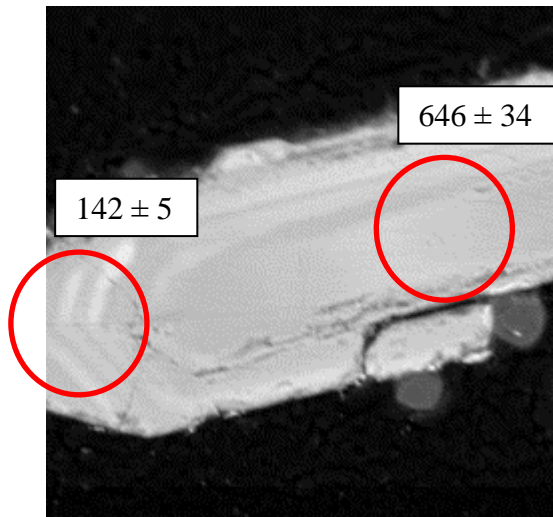


CN-3-5

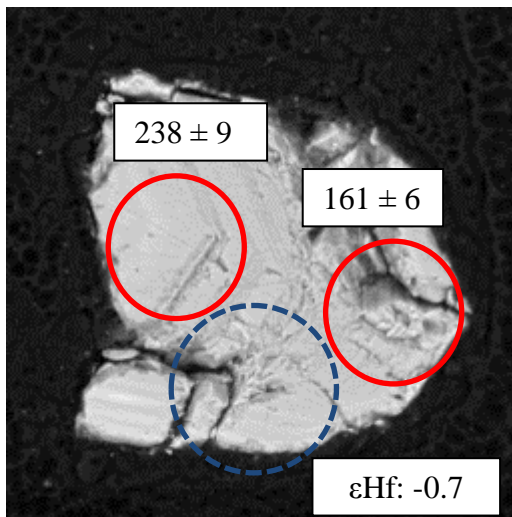
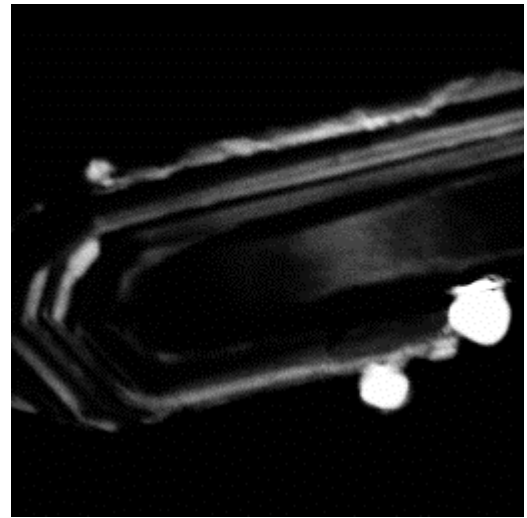


CN-3-6

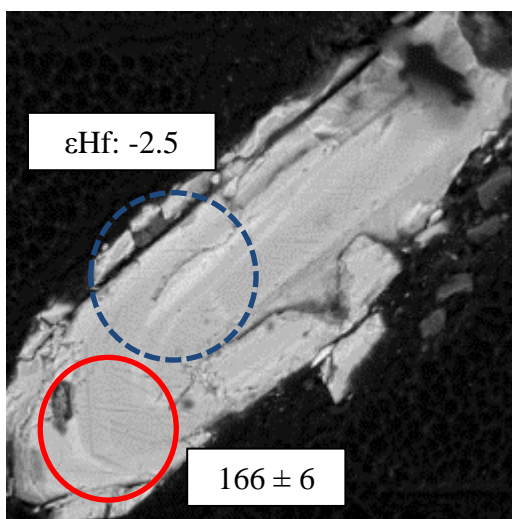
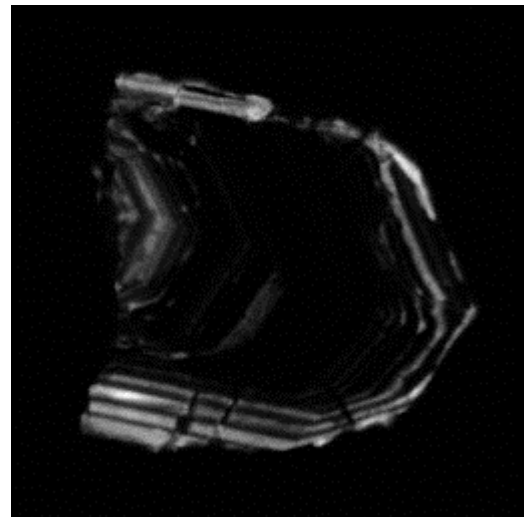




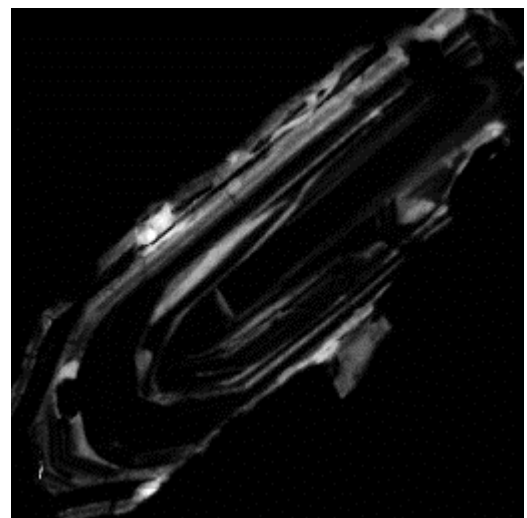
CN-3-7

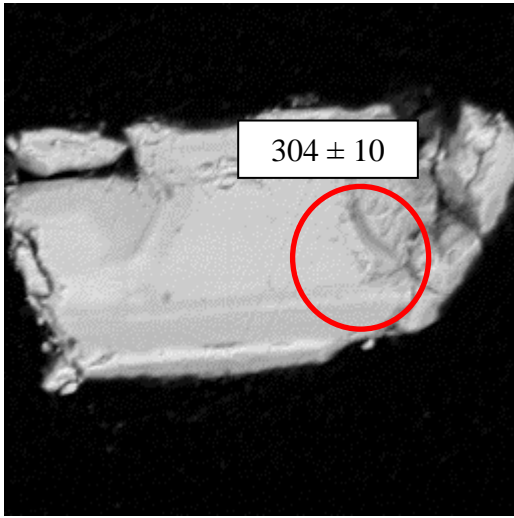


CN-3-8

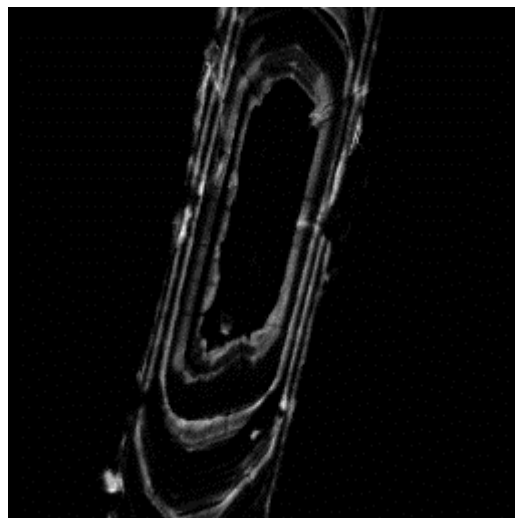
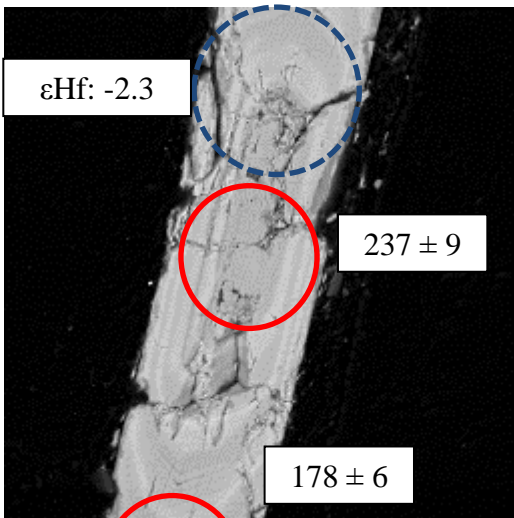
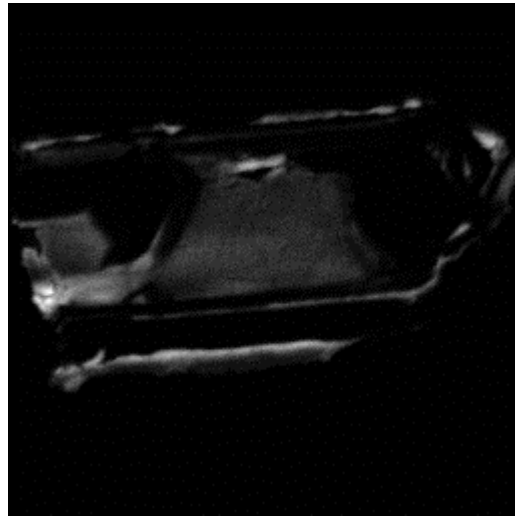


CN-3-9





CN-3-10



## APPENDICES E

### Laser Ablation Conditions for U-Pb Geochronology

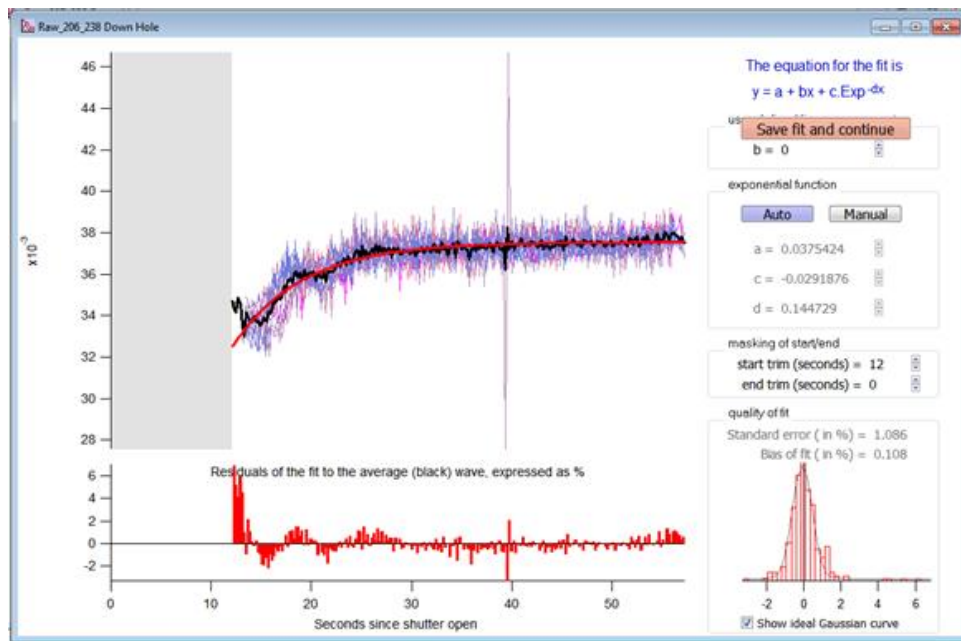
These conditions are as follows: energy density of 4-6 J/cm<sup>2</sup>, spot sizes were either 25 or 35 microns depending on the Pb concentrations of targeted areas within the zircons, and a repetition rate of 4 Hz. The ablation time was 60 seconds, which followed a 45 seconds background intergration interval. The washout time was ~120 seconds in between sample analyses.

As employed in Chen and Simonetti (2014) and Simonetti and Neal (2010), all of the ablations were conducted using a 1000 mL/min He flow rate. <sup>202</sup>Hg, <sup>204</sup>(Pb+Hg), <sup>206</sup>Pb, <sup>207</sup>Pb, <sup>208</sup>Pb, <sup>232</sup>Th, <sup>235</sup>U, and <sup>238</sup>U ion signals were measured during the analytical sessions. Additionally, <sup>202</sup>Hg ion signal was measured in order to correct for the <sup>204</sup>Hg interference on <sup>204</sup>Pb (<sup>204</sup>Hg/<sup>202</sup>Hg=0.229883). Five ion counters (Pb and Hg) and two Faraday cups (U and Th) were used to acquire all of the ion signals. The collector configuration of the NuPlasmaII MC-ICP-MS instrument provides simultaneous acquisition of the ion signals ranging in mass from <sup>238</sup>U to <sup>202</sup>Hg, which plays a critical role in obtaining highly precise and accurate U-Pb age results. Four analyses of the Plesovice and 91500 zircon standards were performed both prior and subsequent each 10 unknown analyses in order to monitor instrumental drift and laser induced elemental fractionation (LIEF).

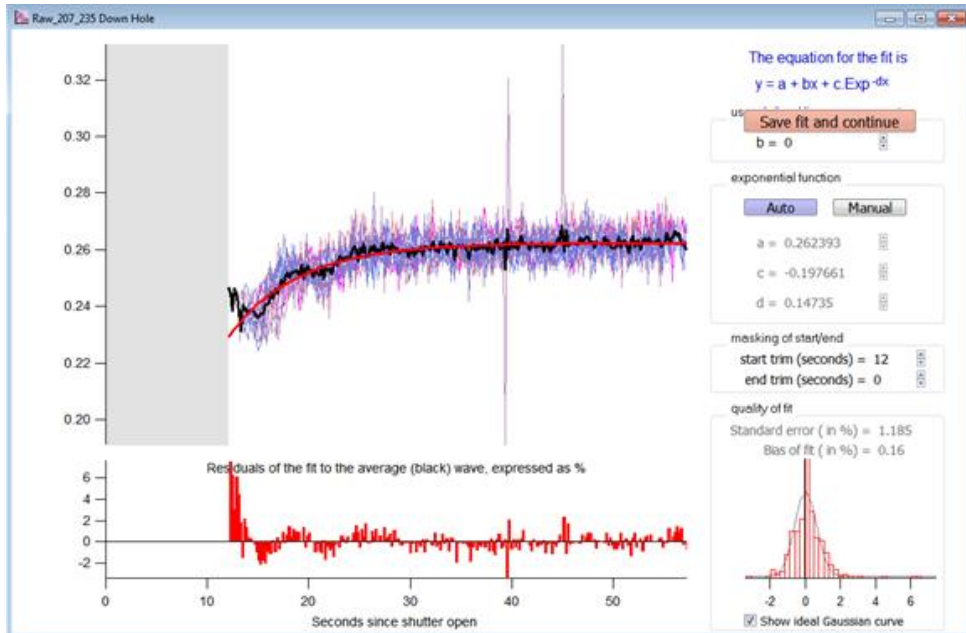
Hg, Pb, and U ion signals were acquired using the Time-resolved Analysis (TRA) software (Nu Instruments) and these (excel compatible csv files) were imported into Iolite (v3.1) software (Iolite Team, School of Earth Sciences, and University of Melbourne). All of the processed data were subsequently imported into the excel-based macro IsoPlot 4.11 (Ludwig, 2008) for plotting of data on Concordia diagrams (Tera and Wasserburg, 1972), and calculation of either concordant, lower intercept, and/or <sup>206</sup>Pb/<sup>238</sup>U weighted mean ages.

Down-hole elemental fractionation can occur during laser ablation and it refers to the change in the measured elemental ratios with time (Paton et al., 2010). Several parameters such as laser wavelength, spot size, cell volume, gas flows, and choice of ablation gas can affect the down-hole fractionation (Paton et al., 2010; Jackson et al., 2004; Horn et al., 2000).

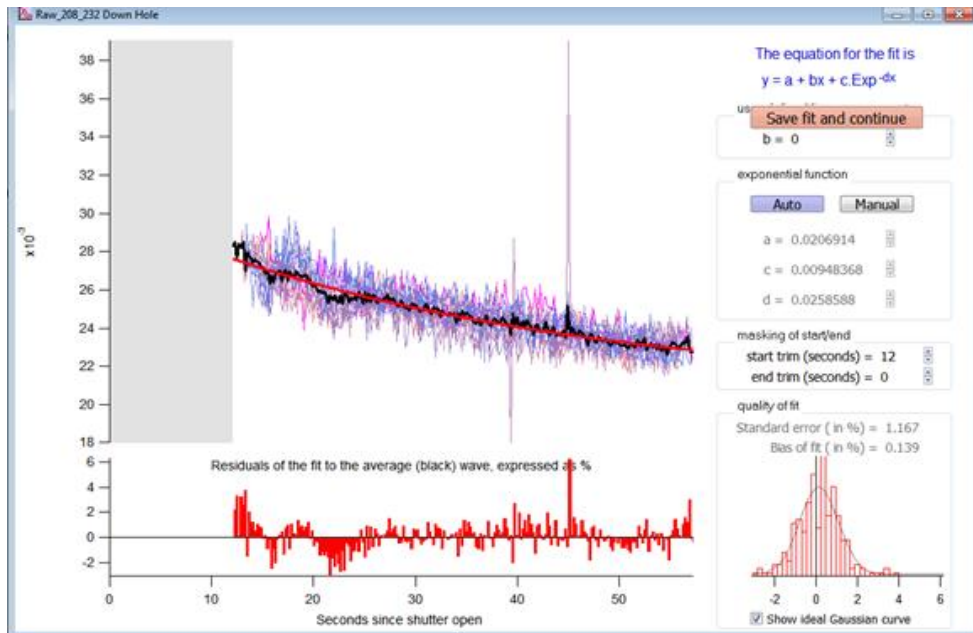
To improve the accuracy of analyses and reduce the associated uncertainty, correction of down-hole U-Pb fractionation was performed by Iolite (v3.1) software for each ablation conducted during this study. For example, the following figures display corrections for the down-hole fractionation of  $^{206}\text{Pb}/^{238}\text{U}$ ,  $^{207}\text{Pb}/^{235}\text{Pb}$  and  $^{208}\text{Pb}/^{232}\text{Th}$  ratios, respectively.



Example of the interactive window for modelling of down-hole fractionation ( $^{206}\text{Pb}/^{238}\text{U}$ ) within the Iolite data reduction software.



Example of the interactive window for modelling of down-hole fractionation ( $^{207}\text{Pb}/^{235}\text{Pb}$ ) within the Iolite data reduction software.



Example of the interactive window for modelling of down-hole fractionation ( $^{208}\text{Pb}/^{232}\text{Th}$ ) within the Iolite data reduction software.

## Laser Ablation Conditions for Hf Isotope Analysis

The laser ablation conditions employed are as follows: energy density of 4-6 J/cm<sup>2</sup>, spot sizes was 35 micron and a repetition rate of 7 Hz. The ablation time was 60 seconds which followed a 30 seconds background intergration interval. The washout time was ~120 seconds in between sample analyses.

All of the ablations were conducted using a 1000 mL/min He flow rate. <sup>183</sup>Ta, <sup>181</sup>W, <sup>180</sup>Hf, <sup>178</sup>Hf, <sup>176</sup>Hf, <sup>175</sup>Lu, <sup>176</sup>Hf, <sup>173</sup>Yb and <sup>171</sup>Yb ion signals were measured simultaneously on nine Faraday collectors. The <sup>175</sup>Lu ion signal was measured in order to correct for the <sup>176</sup>Lu interference on <sup>176</sup>Hf (<sup>175</sup>Lu/<sup>176</sup>Lu=37.61). Moreover, the <sup>176</sup>Yb ion signal interference was determined by assuming the mass bias fractionation factor of Yb was equal to that of Hf (e.g., Pearson et al., 2008).

Ion signal intensity data were processed using the Time-Resolved Analysis (TRA) software (Nu Instruments). Lastly, the εHf and T<sub>DM</sub> age values were calculated using the following formulas;

$$\epsilon\text{Hf} = [({}^{176}\text{Hf}/{}^{177}\text{Hf})_{\text{SMP}} / ({}^{176}\text{Hf}/{}^{177}\text{Hf})_{\text{CHUR}} - 1] \times 10^4$$

$$\text{Hf } T_{\text{DM}} = 1/\lambda \times \text{Ln} \times [({}^{176}\text{Hf}/{}^{177}\text{Hf})_{\text{SMP}} - ({}^{176}\text{Hf}/{}^{176}\text{Hf})_{\text{DM}} / ({}^{176}\text{Lu}/{}^{177}\text{Hf})_{\text{SMP}} - ({}^{176}\text{Lu}/{}^{176}\text{Hf})_{\text{DM}} + 1]$$

$$\text{For age correction: } {}^{176}\text{Hf}/{}^{177}\text{Hf}_{\text{in}} = {}^{176}\text{Hf}/{}^{177}\text{Hf}_{\text{meas}} - {}^{176}\text{Lu}/{}^{177}\text{Hf}(e^{\lambda t} - 1)$$

$$\lambda = 1.867 \times 10^{-11} \text{ yr}^{-1} \text{ (Scherer et al., 2001)}$$

$$\text{In order to calculate } {}^{177}\text{Hf}_{\text{meas}} = 1.88667 / {}^{180}\text{Hf}_{\text{meas}}$$

Here,

$${}^{176}\text{Lu}/{}^{177}\text{Hf}_{\text{DM}} = 0.0384 \text{ (Griffin et al. 2002)}$$

$${}^{176}\text{Hf}/{}^{177}\text{Hf}_{\text{DM}} = 0.28325 \text{ (Griffin et al. 2002)}$$

$${}^{176}\text{Hf}/{}^{177}\text{Hf}_{\text{CHUR}} = 0.282785 \text{ (Bouvier et al., 2008)}$$

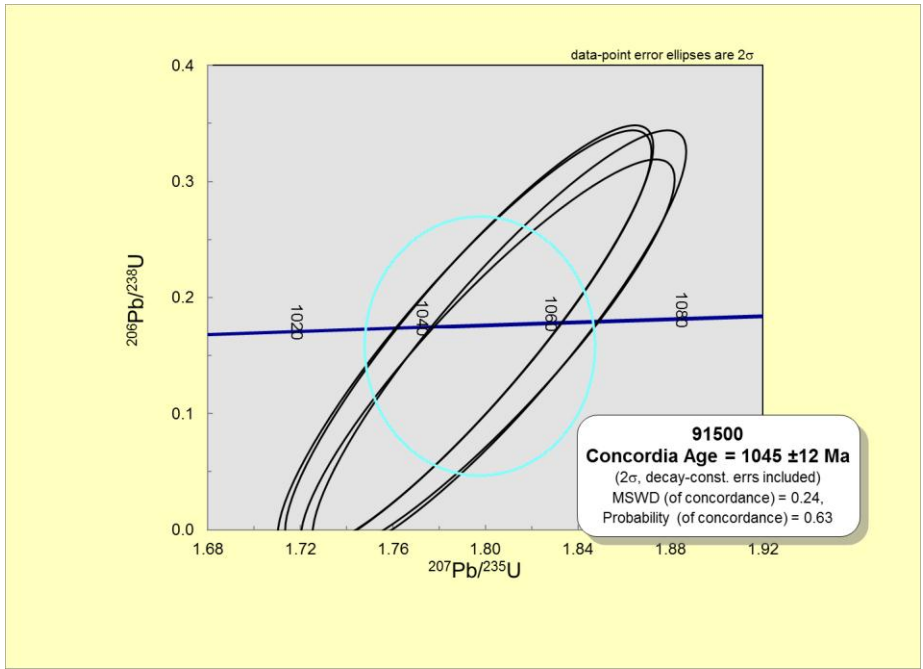
In the age correction calculations, the  $^{175}\text{Lu} / ^{176}\text{Hf}$  ratios and  $^{173}\text{Yb} / ^{177}\text{Hf}$  ratios are very low for all analyses. Due to the extremely low  $^{175}\text{Lu} / ^{176}\text{Hf}$  ratios in the zircons, initial  $^{176}\text{Hf} / ^{177}\text{Hf}$  ratios are almost identical to those at the time of magmatism and the correction for radiogenic decay is smaller than the internal precision for individual analyses.

### **Standards for U-Pb Geochronology**

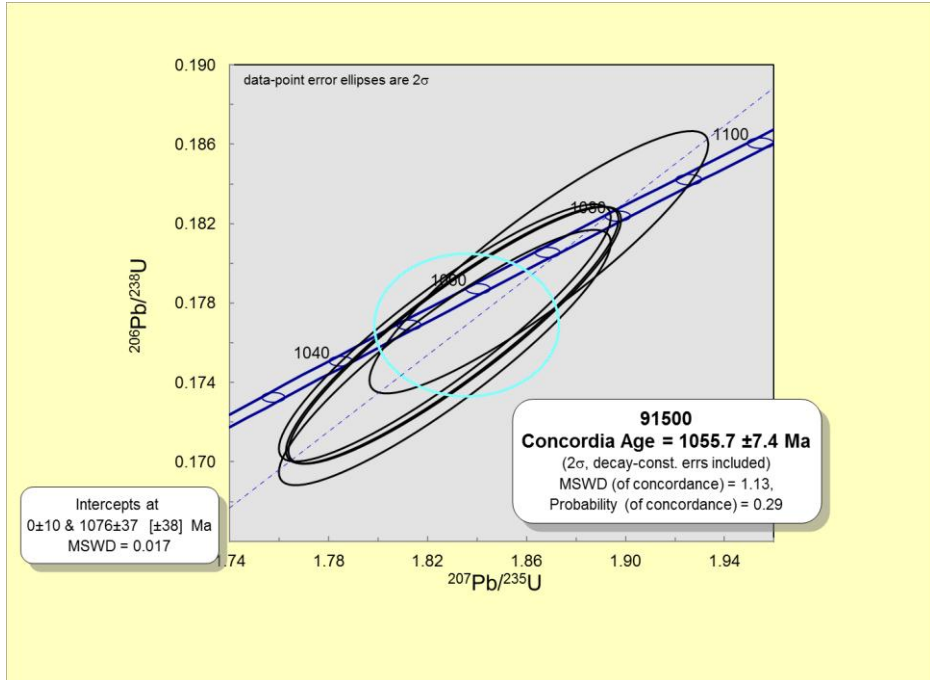
Several well established zircon standards (e.g., Plešovice, 91500, and GJ-1) were analyzed during the analytical sessions in order to ensure the accuracy of the results reported here. These yielded age results that are consistent and agree with those reported in the literature for these zircons. Moreover, these corroborating results confirm that instrumental drift and laser induced elemental fractionation have been monitored and corrected to a satisfactory level. Please see Appendices 2 and 4 file for the detailed U-Pb data for the standards.

#### **91500**

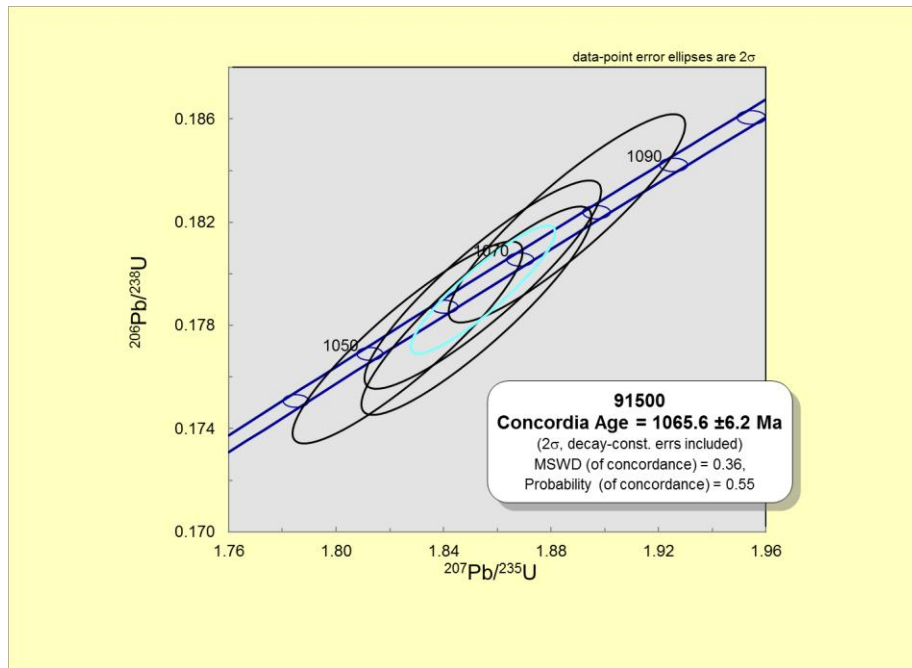
The 91500 is a well-established zircon standard and is derived from a single large crystal within a syenite from Renfrew Country, Ontario (Jackson et al., 2004). The age of this standard is reported as  $1065.4 \pm 0.6$  Ma by Wiedenbeck et al. (1995). As seen in the following figures; consistent ages were obtained here.



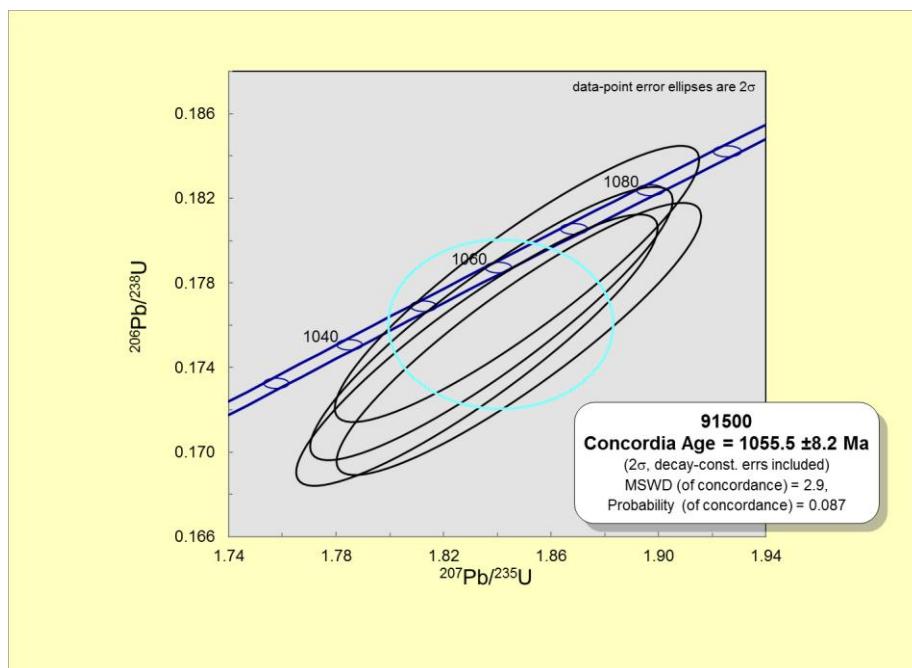
$^{206}\text{Pb} / ^{238}\text{U}$  vs  $^{207}\text{Pb} / ^{235}\text{U}$  diagram and concordia age for 91500



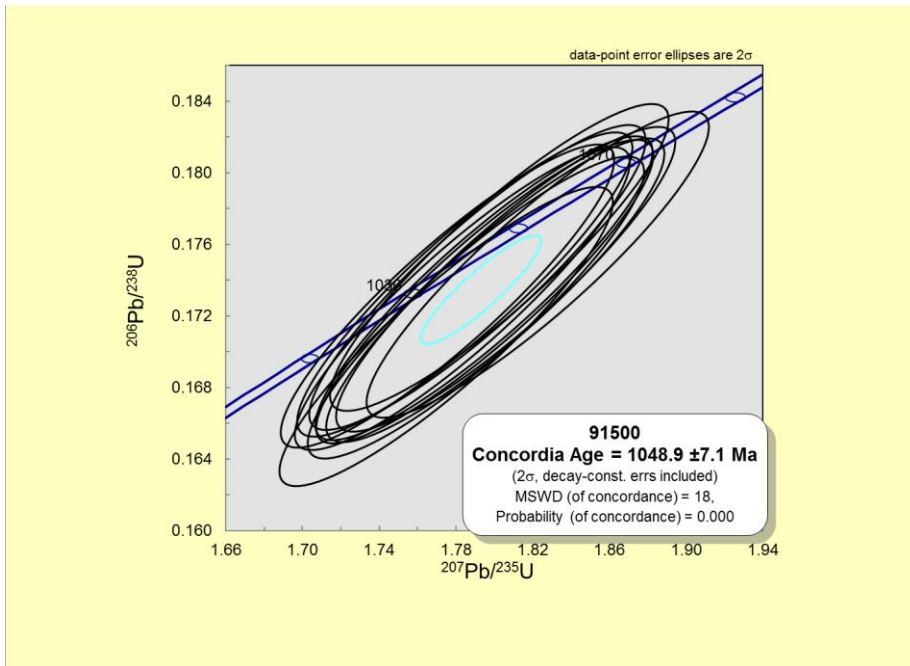
$^{206}\text{Pb} / ^{238}\text{U}$  vs  $^{207}\text{Pb} / ^{235}\text{U}$  diagram and concordia age for 91500



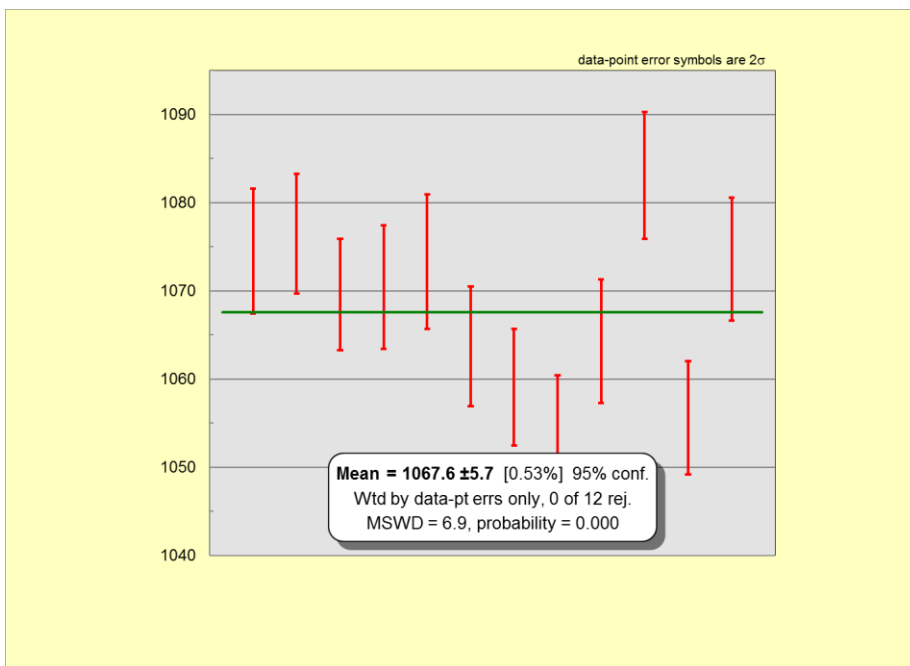
$^{206}\text{Pb} / ^{238}\text{U}$  vs  $^{207}\text{Pb} / ^{235}\text{U}$  diagram and concordia age for 91500



$^{206}\text{Pb} / ^{238}\text{U}$  vs  $^{207}\text{Pb} / ^{235}\text{U}$  diagram and concordia age for 91500



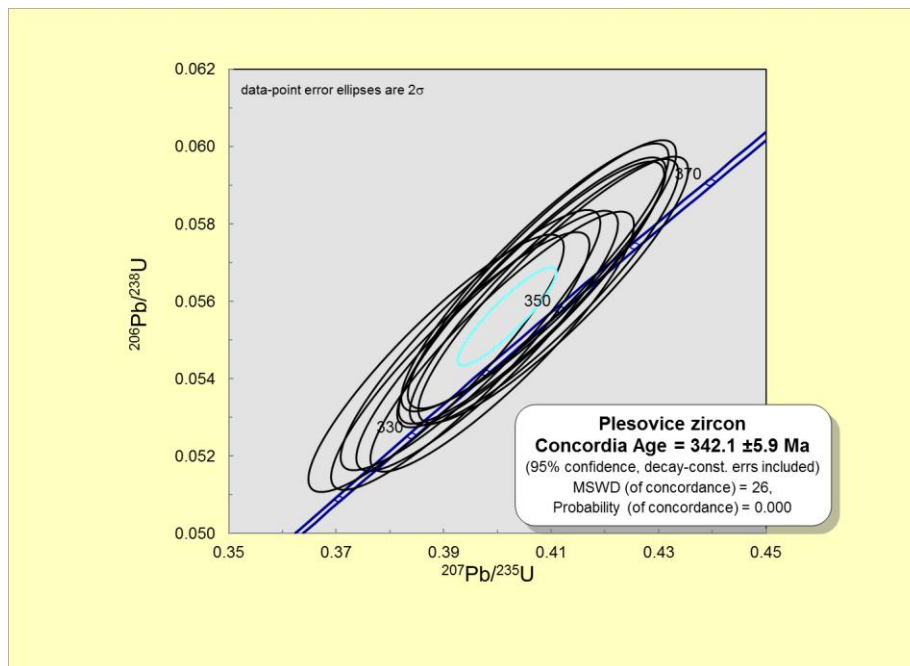
$^{206}\text{Pb} / ^{238}\text{U}$  vs  $^{207}\text{Pb} / ^{235}\text{U}$  diagram and concordia age for 91500



$^{206}\text{Pb} / ^{238}\text{U}$  vs  $^{207}\text{Pb} / ^{235}\text{U}$  diagram and weighted mean age for 91500

## Plešovice

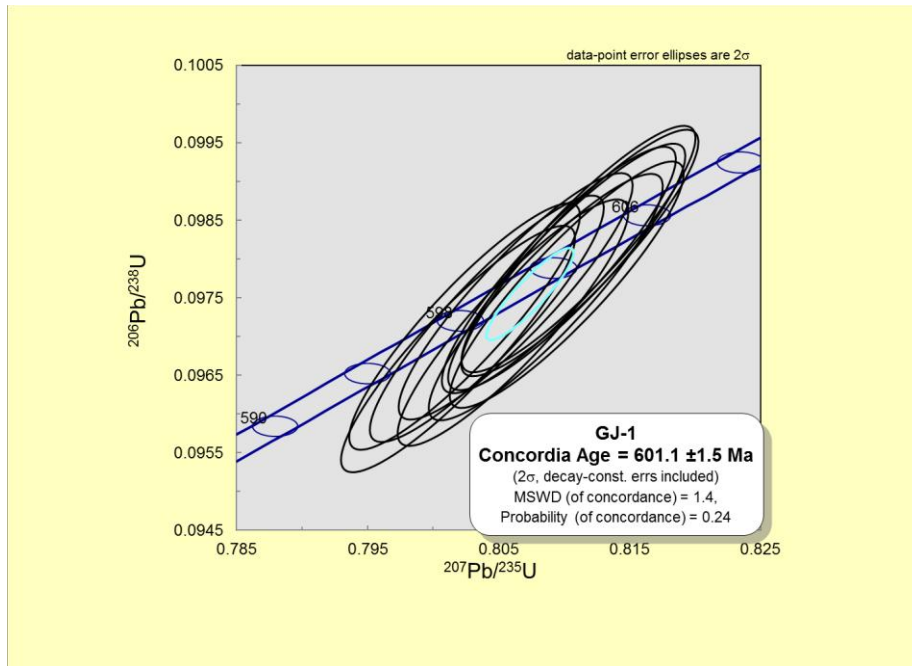
The Plešovice zircon standard is extracted from a high-temperature potassic granulite from the southern Bohemian Massif (Plešovice in the Czech Republic; Slama et al., 2008). The age of this standard is reported as  $337.16 \pm 0.08$  Ma by Slama vd. (2008). A consistent concordant age of  $342.1 \pm 5.9$  Ma (within the associated analytical uncertainty) was obtained during the course of this study.



$^{206}\text{Pb} / ^{238}\text{U}$  vs  $^{207}\text{Pb} / ^{235}\text{U}$  diagram and concordia age for Plešovice

## GJ-1

GJ-1 is a multi-color gem-grade zircon (Macquarie University GEMOC laboratory standard) from an East African pegmatite (Chen et al., 2011). The age of this standard is reported as  $608.53 \pm 0.37$  Ma by Jackson et al. (2004). The concordant age obtained here ( $601.1 \pm 1.5$  Ma) is consistent with previous results.



$^{206}\text{Pb} / ^{238}\text{U}$  vs  $^{207}\text{Pb} / ^{235}\text{U}$  diagram and Concordia age for 91500

### Standards for Hf Isotope Analysis

Three different well established zircon standards (Plešovice, 91500, and BR266) were analyzed before analytical sessions in order to ensure the accuracy of the results reported here. The obtained  $^{176}\text{Hf}/^{177}\text{Hf}$  initial ratios that are consistent and agree with those reported in the literature for these zircons. These values are for Plešovice, 0.28248 (Slama et al., 2008); for 91500, 0.28230 (Goolaerts et al., 2004); for BR266, 0.28163 (Woodhead et al., 2004).

Moreover, these corroborating results confirm that instrumental drift and laser induced elemental fractionation have been monitored and corrected to a satisfactory level.

## CURRICULUM VITAE

### PERSONAL INFORMATION

**Surname:** ÇİMEN  
**First Name:** OKAY  
**Date and Place of Birth:** February 4, 1986, Elazığ  
**Nationality:** Turkish  
**Address (office):** Middle East Technical University  
Dept. of Geological Engineering  
Ankara/TURKEY  
  
**Phone (office):** (90) 312 2105709  
**Fax:** (90) 312 2105750  
**E-mail:** [cokay@metu.edu.tr](mailto:cokay@metu.edu.tr) , okaycimen@gmail.com  
**Website:** [www.okaycimen.com](http://www.okaycimen.com)

### FOREIGN LANGUAGES

English

### EDUCATION

#### PhD.

**University:** Middle East Technical University, Ankara, Turkey, September 2011 - Ongoing

**Department:** Graduate School of Natural and Applied Sciences, Department of Geological Engineering

**Comprehensive Exam:** (6<sup>th</sup> semester of Ph.D. Program) – satisfactory - 07.06.2013.

**Cumulative GPA:** 3.69/4.00

#### MSc.

**University:** Ankara University, Ankara, Turkey, September 2009 - September 2011

**Department:** Graduate School of Natural and Applied Sciences, Department of Geological Engineering

**Thesis Title:** Rare Earth Elements Contents and Environmental Features of Organic Matter Rich Rocks in the South of Dağşeyhler Village (Bolu-Göynük). M.Sc. Thesis in Geological Engineering, Ankara University, Ankara, 96 p. (unpublished). 2011

**Cumulative GPA:** 3.71/4.00

**BSc.**

**University:** Ankara University, Ankara, Turkey, September 2005 - July 2009

**Department:** Bachelor of Science in Department of Geological Engineering

**Graduation Project:** Economic Geology of Rare Earth Elements. Graduation Project in Geological Engineering, Ankara University, Ankara, 45 p. (unpublished). 2009.

**Cumulative GPA:** 2.82/4.00

**Foreign Language (English)**

**University:** Ankara University, Ankara, Turkey, September 2004 - July 2005

**Department:** Department of Basic English

**High School**

**School:** Osmangazi Anatolian High School, İSTANBUL, 1999-2003

**Cumulative GPA:** 3.54/4.00

**WORK EXPERIENCE**

University of Notre Dame – Research Scholar – 2015-2016

Middle East Technical University – Research and Teaching Assistant – 2011-2016

**RESEARCH INTERESTS**

Petrology, Geochronology, Isotope Geochemistry, Rare Earth Elements, Environmental Geochemistry

**MEMBERSHIPS**

- American Geophysical Union (AGU) –Student Membership
- European Geosciences Union (EGU) - Student Membership
- Mineralogical Society of America (MSA) – Student Membership
- Geochemical Society – Student Membership
- Turkish Association of Mining Geologists
- UCTEA Chamber of Geological Engineers of Turkey

## **AWARDS & GRANTS**

The Scientific and Technological Research Council of Turkey / Publication Encouragement Award-2016

Middle East Technical University / Publication Encouragement Award-2016

The Scientific and Technological Research Council of Turkey / Publication Encouragement Award-2015

Middle East Technical University / Publication Encouragement Award-2015

The Scientific and Technological Research Council of Turkey / Publication Encouragement Award-2013

Middle East Technical University / Publication Encouragement Award-2013

The Scientific and Technological Research Council of Turkey / Research Fellowship in USA /05.2015-11.2015

The Higher Education Council of Turkey / Participation Grant to EGU General Assembly, Vienna, Austria / 04.12-17.2015

The Higher Education Council of Turkey / Participation Grant to Goldschmidt 2014, Sacramento, California, USA / 06.08-13-2014

## **PROJECTS**

The Petrology and Geodynamic Importance of the Metavolcanic Rocks within the Çangaldağ Complex (Central Pontides) - TUBITAK-114Y422 / Researcher - *Completed*

The New Mid-Late Paleozoic Volcanism in the Eastern Taurides: Implications for the Geodynamic Evolution of the Anatolide-Tauride Terrane - METU-OYP Project / Researcher –*Completed*

The Petrogenetic Characteristics of the Chromitite Deposits from the Tunceli Province -Tunceli University BAP Project MFTUB013-09 / Researcher - *Completed*

The pollution potential assessment of the Hasangazi chromite pit (Tunceli-Turkey) - Tunceli University BAP Project YLTUB011-13, 2013 / Researcher - *Completed*

The Scientific Investigation and Determination of Economic Potential of Oil Shales around (Hatıldağ) Bolu-Göynük-Hasanlar. General Directorate of Turkish Coal – Ankara University Joint Project, 2012 / Researcher – *Completed*

## INTERNATIONAL PAPERS (SCI/SCI-Expanded)

- Çimen, O.,** Göncüoğlu, M.C., Sayıt, K. **2016.** Geochemistry of the metavolcanic rocks from the Çangaldağ Complex in Central Pontides: Implications for the Middle Jurassic arc - back - arc system in the Neotethyan Intra - Pontide Ocean. *Turkish Journal of Earth Sciences*. Accepted.
- Çimen, O.,** Toksoy-Köksal, F., Öztüfekçi-Önal, A., Aktağ, A. **2016.** Depleted to Refertilized Mantle Peridotites Hosting Chromotites within the Tunceli Ophiolite, Eastern Anatolia (Turkey): Insights on the Back Arc Origin. *Ofioliti*. 41(1), 1-20.
- Koç, Ş., Sarı, A., **Çimen, O.** **2016.** Major and Rare Earth Element Contents in Organic Matter-Bearing Rocks of the Haymana Formation, Ankara, Turkey. Energy Sources, Part A: Recovery, Utilization, and Environmental Effects, 38 (13), 1918-1928.
- Çimen, O.,** Öztüfekçi-Önal, A., Akarsu-Akyol, E. Pollution Potential Assessment of Hasangazi Chromite Pit (Tunceli-Turkey). *Ekoloji*. In Review.
- Çimen, O.,** Toksoy-Köksal, F., Öztüfekçi-Önal, A., Örgün-Tutay, Y., **2015.** Environmental Contamination of Heavy Metals and Chrysotile Asbestos in the Munzur and Pülümür Streams (Tunceli/Turkey). *Ofioliti*. 40(1), 27-36.
- Çimen, O.,** Koç, Ş., Sarı, A., **2013.** Rare Earth Element (REE) Geochemistry and Genesis of Oil Shales around the Dağhacılar Village (Göynük-Bolu, Turkey). *Oil Shale*. Vol. 30, No. 3, pp. 419-440.

## INTERNATIONAL ABSTRACTS

- Öztüfekçi Önal, A., **Çimen O.,** Toksoy-Köksal, F., Aktağ, A., Önal, A. **2015.** Petrogenetic Characteristics of the Chromite Deposits in Tunceli Province (Turkey). Symposium on Eastern Anatolian Geology. Van. Turkey. p. 152-153.
- Önal A., Aktağ A., Toksoy-Köksal F., **Çimen O.,** Öztüfekçi-Önal A. **2015.** Geological Features of the Chromite Deposits in Tunceli Province (Turkey). Symposium on Eastern Anatolian Geology. Van. Turkey. p. 206-207.
- Çimen, O.,** Sayıt, K., Göncüoğlu, M.C. **2015.** Preliminary Geological and Geochemical Data from the Çangaldağ Complex (Kastamonu-Turkey): Implications for the Geodynamic Evolution of the Central Pontides. EGU General Assembly 2015, April 12-17, Vienna, Austria.

**Çimen, O.,** Sayıt, K., Göncüoğlu, M.C., Okuyucu, C. 2014. The new Mid-Late Paleozoic volcanism in the Eastern Taurides: Implications for the Geodynamic Evolution of Anatolide-Tauride Terrane. 8<sup>th</sup> International Symposium on Eastern Mediterranean Geology. Muğla. Turkey.

Öztüfekçi-Önal A., Toksoy-Köksal F, Zaccarini, F., **Çimen, O.,** Aktağ, A., Önal, A. **2014.** First description of platinum group minerals (PGMs) in Ultramafic rocks of the Ovacık and Pülümür ophiolitic complex, Tunceli, Turkey. 11th EMAS Regional Workshop, Leoben, Austria.

**Çimen, O.,** Sayıt, K., Göncüoğlu, M.C., Öztüfekçi-Önal, A., Aktağ, A. **2014.** MORB- and SSZ-type mafic rocks from the eastern part of the Ankara-Erzincan-Sevan-Akera Suture Belt: Preliminary geochemical data. Goldschmidt. Sacramento, California, USA.

**Çimen, O.,** Öztüfekçi-Önal, A., Toksoy-Köksal F., Aktağ, A., Önal, A. **2014.** Preliminary Data on the Geochemistry of the Chromites from Tunceli (Eastern-Anatolia). VI. Geochemistry Symposium with International Participation. 14-17 May, Mersin, Turkey. p. 35-36.

Aktağ, A., Öztüfekçi-Önal, A., Sançar, T., Önal, A., **Çimen, O.,** **2013.** New Petrological Data from the Western Termination of East Anatolian Accretionary Complex (EAAC), Eastern Turkey. EGU General Assembly Vienna, Austria.

**Çimen, O.,** Öztüfekçi-Önal A., Toksoy-Köksal F, Akarsu-Akyol E., **2012.** Environmental effects of Hasangazi (Pülümür-Tunceli) Chromite Mine. International Earth Sciences Colloquium on the Aegean Region. 1-5 October, Izmir. s.180.

**Çimen, O.,** Sarı, A., Koç, Ş., **2011.** Rare Earth Elements Enrichments of Organic Matter Rich Rocks in the south of Dağşeyhler Village (Göynük/Bolu). 18th International Petroleum and Natural Gas Congress and Exhibition of Turkey. May 11th-13th, Ankara. pp.114-115.

Yurdugül, E., Sarı, A., Koç, Ş., **Çimen, O.,** Karkuş, A., **2011.** Rare Earth Elements (REEs) Enrichments in the Upper Cretaceous Haymana Formation (Haymana/Ankara). 18th International Petroleum and Natural Gas Congress and Exhibition of Turkey. May 11th-13th, Ankara. pp.182-183.

## NATIONAL ABSTRACTS

**Çimen, O.,** Göncüoğlu, M.C., Simonetti, A., Sayıt, K. **2016.** Zircon U-Pb geochronology, Hf isotopes and whole rock geochemistry of the metavolcanic rocks from the Çangaldağ Complex (Central Pontides, Turkey). *69th Geological Congress of Turkey.* Ankara. Turkey.

- Çimen, O.**, Göncüoğlu, M.C., Sayıt, K., Simonetti A. **2016.** Whole rock geochemistry, zircon U-Pb geochronology and Lu-Hf isotope systematics of the Çangaldağ Pluton (Central Pontides, Turkey). *69th Geological Congress of Turkey*. Ankara. Turkey.
- Öztüfekçi-Önal A., Örgün Tutay Y., Önal A., Aktağ A., **Çimen O.**, **2013.** The effects of the Mineralizations and Mining Operations on Water System in Tunceli. 2nd Medical Geology Workshop. 4-6 December Antalya, pp. 57-63.
- Çimen O.**, Toksoy-Köksal F., Örgün Y, Öztüfekçi-Önal A., **2012.** Geochemical Characteristics of Bottom Sediments from Munzur and Pülümür Streams feeding Uzunçayır Dam (Tunceli) and Potential Risks on Water Chemistry. 65. Geological Congress of Turkey, The Book of Abstracts, pp.140-141, 2-6 April, Ankara.

## TEACHING

- GEOE213**-Mineralogy for Geological Engineering - Lab
- GEOE207**-Mineralogy and Petrography for Mining Engineering -Lab
- GEOE210**-Petrography - Lab
- GEOE304**-Igneous and Metamorphic Petrology - Lab
- GEOE326**-Field Geology - Field Assistant
- GEOE327**-Field Geology Mapping - Field Assistant
- GEOE417**-Metamorphic Petrography - Lab
- GEOE401**-Mineral Deposits - Lab
- GEOE491**-Geological Engineering Design - Project Assistant